Near- and mid-IR fibre grating devices and applications

Zhongyuan Sun

Doctor of Philosophy

Aston University

January 2016

Aston University

Near- and mid-IR fibre grating devices and applications

Zhongyuan Sun
Doctor of Philosophy
January 2016

This thesis presents a detailed research work on the fabrication, characterisation and applications of optical fibre grating devices with operation wavelengths cover from near- to mid- infrared (IR) range.

One of the major contributions described in this thesis is the systematic investigation on the structures, fabrication methods and spectral, thermal, strain and surrounding refractive index (SRI) characteristics of near-IR fibre gratings including fibre Bragg gratings (FBGs), chirped fibre Bragg grating (CFBGs) and long period grating (LPGs). For some applications, such as special engineering sensors and high power fibre laser, the fibre gratings have been fabricated on different novel fibres (metal coated fibre and large mode field fibre), respectively.

Another important contribution from the studies is experimental investigation on 45º tilted fibre gratings (45°-TFGs) and excessively tilted fibre gratings (ex-TFGs), and their applications. 45º-TFGs with high polarisation dependent loss (PDL) in single mode and polarisation maintaining (PM) fibres have been fabricated. The 45°-TFG has been employed as in fibre polariser to obtain the single polarised laser, which has been further developed as transverse loading sensor achieving high sensitivities. Furthermore, all fibre Lyot filter with narrow bandwidth (26 pm), constructed by two 45º-TFGs with 100m long cavity in PM fibre has been demonstrated. For ex-TFGs, SRI sensor based on a surface modified 81°-TFG, showing capability to detect glucose concentration with relatively high RI sensitivity (~168nm/RIU). Finally, an all-fibre loading sensor based on a hybrid 45° and 81° TFG structure has been demonstrated.

Finally, I have fabricated fibre gratings into mid-IR 2μm range. The mid-IR FBGs have been evaluated for thermal and strain response, revealing higher temperature sensitivities than that in near-IR range. The mid-IR LPGs have been investigated for the thermal and refractive index sensitivities, also showing significant enhancement. The 45°-TFGs in mid-IR have been investigated for their PDL characteristics. The mid-IR FBGs and 45°-TFGs have been employed in Tm-doped fibre laser cavity to realize multi-wavelength continued wave (CW) and single polarisation operation.

Key words: Fibre Bragg grating, Long-period grating, Tilted fibre grating, Optical fibre sensor, Fibre lasers.

To my parents Yuqiang Sun and Shenxiang Lei.

Acknowledgements

Firstly, I would like to thank my honorific supervisor, Professor Lin Zhang, who offered me a great opportunity to do research in the field of optical fibre gratings and kindly guided me throughout my time at Aston University. I also would like to thank her for giving me meticulous care and support during my living in the UK.

Sincere appreciations are given to John Sharp, Professor, Edinburgh Napier University, who wrote reference letter to recommend me becoming a Ph.D. candidate in Aston Institute of Photonic and Technologies at Aston University. Specially, I would like to thank Dr. Xianfeng Chen, who introduce me to my supervisor and discuss the research topic throughout the entire period of my Ph.D. study.

Here, I would like to thank Dr. Zhijun Yan and Prof. Chengbo Mou, two fraternal colleagues, friends and mentors, who have taught me the fabrication of optical fibre gratings, fibre laser build up, many types of experiment measurement, and given me countless and valuable suggestions and ideas during my Ph. D studying.

Besides, I would like to thank Dr Kaiming Zhou, Dr Jianfeng Li, Dr Binbin Luo, Dr Xiangchuan Wang, Dr. Junxi Zhang, Dr. Junsong Peng, Dr. Guolu Yin and Prof. Qizhen Sun for fruitful discussion and helps through my Ph.D. I also would like to thank Dr Shi Su, Dr. Peng Li, Dr. Adedotun Adebayo, Dr. Jiangling Li, Dr. Xueting Wang, Mr. Chenyang Liu, Mrs. Xi He, Mr. Changle Wang, Dr. Mingming Tan and Mr. Ayomipo Badmos who have helped and supported me during my study at Aston University.

In particular, I am deeply grateful Lab Technician Mr Andrew Abbot, Academic Support Administrator Mrs Helen Yard, and Research Student Administrator Mrs Sandra Mosley for their friendly help and the technical and administrative support throughout my study.

Thanks must also to all of my friends I met in UK for past 7 years. Many friends here became a part of my life. Specially, I have to give my gratitude to Mr. Ning Xu and Mrs. Tingting Han, who providing me with much invaluable support, encouragement, and understanding through my hard times. Particularly, I would like to thank Mr. Tong Cui, Ms. Jialin Wei and Ms. Shu Wang for the wonderful times that we had spent together.

Finally and also most importantly, I would like to express my deepest gratitude to my parents. They financially and spiritually supported my undergraduate education in China and postgraduate education in the UK. Without their support and encourage, I cannot finish this work on time. I love them and appreciate their parental love for ever!

Contents

ACRONYMS

ASE	Amplified Spontaneous Emission
BBS	Broadband source
BER	Bit error rate
B-Ge	Boron and Germanium
CFBG	Chirped fibre Bragg grating
CW	Continuous wave
DOP	Degree of polarisation
EDF	Erbium doped fibre
EMI	Electromagnetic interference
Ex-45°TFG	Excessively 45°TFG
FBG	Fibre Bragg grating
FWHM	Full width half maximum
FSR	Free spectral range
GODC	Germanium oxygen-deficient centre

IR	Infrared ray
LP	Linear polarization
LPG	Long period grating
MCVD	Modified chemical vapor deposition
MWL	Multi-wavelength laser
NBOHC	Non-bridging oxygen hole centre
NPR	Nonlinear polarization rotation
OSA	Optical spectrum analyser
PBS	Polarization beam splitter
PC	Polarization controller
PD	Pump diode
PDL	Polarization dependence loss
PER	Polarization extinction ratio
PM	Polarization maintaining
P-OHC	Peroxy oxygen hole centre

RIU	Refractive index unit
SA	Sodium acetate
SRI	Surrounding refractive index
TDF	Thulium doped fibre
TEM	Transmission electron microscopy
TFG	Tilted fibre grating
WDM	Wavelength division multiplexer

List of figures

List of tables

Chapter 1.
Introduction and Thesis structure

1.1 Introduction

Since in-fibre gratings were demonstrated by Hill et al. in 1978 [1], a variety of application devices based on optical fibre gratings have been developed. So far, fibre Bragg gratings as the most common in-fibre devices have been used in many applications, such as telecommunications and sensing [2, 3], fibre laser systems and pump laser stabilizers [4], gain flattening filters [5], WDM systems [6] and chromatic dispersion compensators [7]. In the earlier development period, optical fibre gratings were mostly classified into two categories: (i) fibre Bragg gratings (FBGs), based on forward to backward core mode coupling which are characterized by wavelength selective reflection function in form of filtering and (ii) long-period gratings (LPGs), based on forward core to cladding mode coupling which are characterized by loss filter function.

In the last ten years, optical fibre gratings with tilted structure have gained more attention from researchers due to their distinctive optical properties. The ability to couple light from the core mode to cladding and radiation modes by the tilted fibre gratings (TFGs) was first reported in 1990 by Meltz et al. [8]. Subsequently, Erdogan & Sipe [9] gave a theoretical analysis of TFG structures and also pointed out the in-fibre polarization characteristic function of 45°-TFG structure, which enable it to couple s-polarized light from the guided core-mode to the radiation mode and propagate the p-polarized light through the fibre. Basically, fibre grating devices are a periodic form of modulation of the refractive index (RI) of the fibre core. This RI modulation structure can be introduced by exposing a silica glass fibre to an ultraviolet laser (UV) with a typical wavelength in the range of 244nm-248nm [10].

In recent years, the optical fibre devices operating in the mid infrared (mid-IR) spectrum have attracted growing interests due to their application potentials in defence [11], health [12, 13] and the environment [14]. Optical fibre gratings are useful in-fibre components, therefore, there are high demands for their wavelength extension from near-IR to mid-IR. Moreover, laser sources within eye-safe (2μm) region, especially for operation wavelengths in the atmospheric transmission window between 2.05μm and 2.3μm, have been attracting special attention. However, most of the reported mid-IR fibre lasers used the bulk mirrors in the cavities, inducing high insertion loss and limiting the structure compactness. FBGs can be used as intra-cavity resonators for all fibre lasers to eliminate these disadvantages. Therefore, the fabrication of FBGs extending to mid-IR wavelength range is the key factor for the development of all fibre mid-IR lasers. Besides, the 45°-TFG can be employed as an in-fibre polarizer in a mid-IR mode-locked fibre laser providing the effect of nonlinear polarization evolution (NPE) [15] and as well as low insertion loss and high compactness.

1.2 Structure of thesis

The thesis consists of seven chapters and the detailed contents of each chapter are listed below:

Chapter 1 provides a brief introduction and describes the structure of the thesis.

Chapter 2 will begin with a historical perspective about the development of optical fibre gratings. Subsequently, mechanism photosensitivity of optical fibre and photosensitivity enhancement techniques are reviewed in details. As the second major part of this chapter, the theory concerning the mode coupling mechanisms and phase match conditions are discussed systematically. Finally, a brief description of the three major fibre grating fabrication methods for FBG, LPG and TFG is given.

Chapter 3 presents the research outcome on the fabrication and characterisation of different types of optical fibre grating. The chapter will first describe two inscription methods for producing FBGs with central wavelengths covering the range from 800nm to 1550nm, and their thermal and strain sensing characteristics. Then, the chapter will introduce the chirped fibre Bragg grating made in large mode fibres with the discussion on the fabrication and spectral response. A short section has been devoted to the FBGs fabricated in metal coated fibre and the evaluation of their thermal property. Finally, the chapter gives a systematic investigation of LPGs with different periods, including the characterization of their spectral, thermal and surrounding refractive index (SRI) response. Chapter 4 presents the fabrication, spectral characteristics and applications of 45°-TFGs. The first part of this chapter introduces the structure and phase matching conditions of

TFGs. Then, the second part gives a theoretical review on the polarization characteristics of 45°-TFG and introduces the fabrication methods for tilted fibre grating. As one unique type of application, the power tapping experiment based on 45°-TFG is described. Finally, the applications of 45°-TFGs based all fibre interferometer in laser systems are discussed.

Chapter 5 reports the experimental investigation of excessively tilted fibre gratings (ex-45°TFGs) and their temperature and refractive index sensing function in detail. Firstly, this chapter gives a detailed description of the structure and mode coupling mechanism of ex-45°TFGs. Then, the inscription methods and characterisation of the thermal and SRI sensitivity for ex-45°TFG are discussed. In the final part, two applications employing ex-45°TFGs are presented; one is the implementation of a novel glucose sensor based on an ex-45°TFG and the other is the demonstration of loading and temperature sensing using a hybrid 45°- and 81°-TFG to simplify the measurement process.

Chapter 6 presents the fabrication and applications of optical fibre gratings in the mid-IR wavelength range. First of all, the characteristics of mid-IR FBGs, LPGs and 45°-TFGs in terms of spectral, thermal, strain and RI response, as well as polarization dependent loss (PDL) are discussed, respectively. Secondly, the results on a multi-wavelength continuous wave mid-IR fibre laser utilizing a set of FBGs with Bragg wavelengths in the mid-IR range as reflectors are reported. Finally, a thulium-doped fibre laser employing a 45°-TFG and Sagnac loop mirrors as cavity elements is demonstrated, which can operate with tuneable single-wavelength lasing around 2000nm.

Chapter 7 will present the thesis conclusions and some detailed suggestions for future works.

Chapter 2.

Background review (history, photosensitivity, grating theory and fabrication methods)

2.1 Fibre grating history

Optical fibre photosensitivity was first discovered in germanium-doped silica fibre at the Communication Research Centre (CRC) in Canada by Hill and co-workers [1] in 1978. During an experiment performed to research scattering phenomenon in special optical fibre, the visible argon ion laser radiation light was launched into the core of the fibre. It was noticed that as a function of time, an increase in the fibre attenuation was observed. The spectral measurements displayed that a weak standing wave intensity pattern formed by the 4% back reflection from the cleaved end of the fibre interacting with the forward propagating light. It was determined that a permanent refractive index grating was photo-induced into the core of this special fibre, which operated as a type of distributed reflectors that coupled the forward- to the counter-propagating light beam. This scientific discovery that subsequently called "Hill gratings" was a milestone in researching on the nonlinear properties of germanium-doped silica fibre. Although scientists realized the importance of this discovery in future research development at that time, this curious phenomenon confused a few researchers [16, 17], for about ten years. The main reason for this is that it was difficult to repeat the original experiments and also because the phenomenon observed only from the experiments which was limited to the one "magic" fibre at the CRC. Moreover, the writing wavelength of the spectral region of the "Hill gratings" is confined in the visible part of the spectrum, which was no use for telecommunication and signal processing and sensing in near-IR region.

During 1980s, scientists were already researching in second-harmonic generation phenomenon in germanium-doped silica optical fibres, which has a zero second-order nonlinear coefficient responsible for second-harmonic generation. Sasaki, Ohmori[18] and Hill et al.[19] reported another nonlinear phenomenon of sum frequency generation. Stolen [20] and Farries [21] set up some experiments to support a mechanism for phase-matched generation of second harmonic (SH) light in the fibre. Afterwards the observation from Stone [22] demonstrated virtually any germania-doped silica fibre is sensitive to argon ion laser radiation light, recommenced activity in the field of fibre gratings.

The major technical breakthrough came from Gerry Meltz et al.'s paper[23], which reported that Bragg gratings have been produced by holographic technique using the ultraviolet laser at 244nm single-photon absorption. They demonstrated the two interfering 244nm single-photon UV laser beams could be used to carve the grating that would reflect a wide wavelength range light (750nm~1650nm) by illuminating the fibre core from the side. The Bragg resonance wavelength is dependent on the angle between the two interfering beams. So the wavelength for reflection gratings can be extended to fabricate at 1530nm, which is an interesting wavelength in telecommunications field. R. Kashyap et al. [24] demonstrated the first fibre laser operating from the reflection of the erbium-doped germane-silicate fibre grating at 1500nm afterwards. Normally, UV induced index changes in standard single mode optical fibres have been limited to - 3×10^{-5}. Since then, several treatment methods for increasing index changes in optical fibres have been developed. However, these treatment methods make it possible to create efficient reflectors only a hundred wavelengths long. Lemaire and his colleagues [10] reported a simple fibre treating

technique which can sensitise fibres using a low temperature and high pressure hydrogen treatment before the UV exposure. In the same year Hill and Anderson et al. [25] invented the phase mask method to write the FBGs, which made FBGs commercial fabrication becoming a reality.

At the beginning, the observation of photosensitivity in fibres was only a scientific curiosity without more researchers' attention, but over time it has become to play an important role in sensing technology and optical communication engineering. Nowadays, research into mechanisms of fibre photosensitivity and its applications have sprung up in many universities and industrial laboratories all over the world. Thousands of articles in regard to photosensitivity and fibre gratings have been published in the scientific journals and in the proceedings of conferences, and workshops.

2.2 Photosensitivity in optical fibre

The photosensitivity in optical fibre refers to a permanent refractive index change of the fibre core after exposure to UV light with specific wavelength. Photosensitivity was first discovered in an optical fibre where it was exposed to visible argon ion laser radiation at 488nm launched into its core. The photosensitivity is mainly determined by the core material. It was initially discovered in the germanium doped fibre and photo-excited with 240-250nm ultraviolet (UV) light. Actually, following many years of research, varying degrees of photo-sensitivities have been observed through photoexcitation at different UV wavelengths in other element doped fibres, such as europium[26] , cerium [27], phosphorus [28] and erbium: germanium [29]. Nevertheless, the germanium doped fibre shows more sensitivity than the others. Therefore, most of optical fibre core we used is doped with germanium, which is widely employed in both the optical sensor applications and the telecommunications fields. In this section, we will only present the germanium induced photosensitivity mechanism.

2.2.1 The point defects in germanium-doped fibre

The point defects in optical fibre are usually produced by ionizing radiation [30] and the fibre fabrication process [31]. In the 1980's, point defects is related to the phenomenon of second harmonic generation [20, 32-35]. The one-photon process that causes the photo-induced variation at 240nm is below the band gap at 146nm, thereby the point defects in ideal glass tetrahedral network are reasonable for the observation of photosensitivity. In order to better understand the

photosensitivity at UV region, it is necessary to study the point defects in the germanium doped fibre.

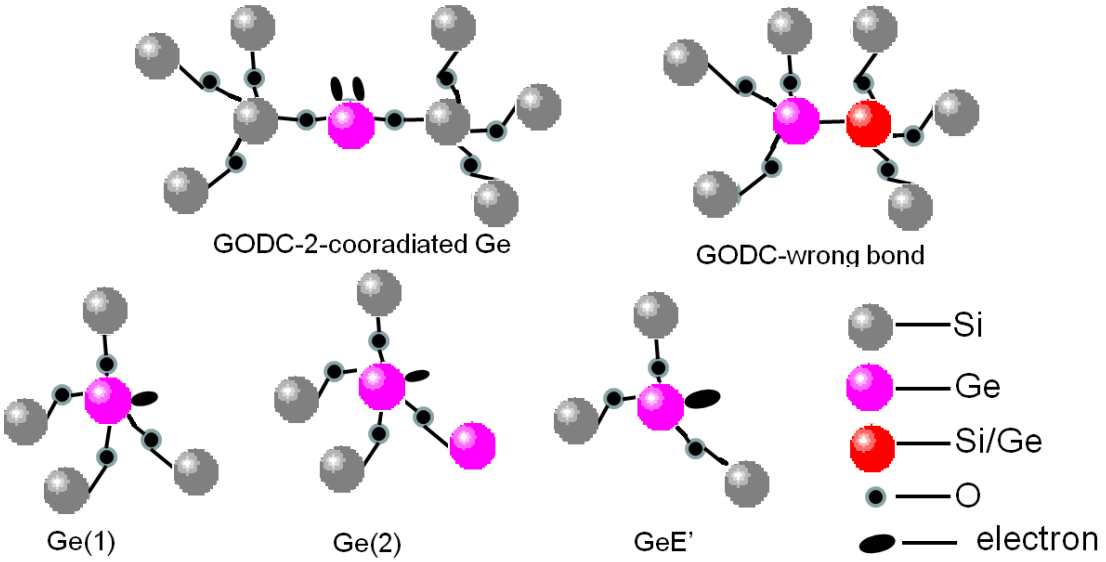

Figure 2.1 The schematic of proposed point defects of germanium doped silica.

Germanium can be considered as both GeO2 and GeO in the glass, due to it having two stable oxidation states (+2 and +4). As is known, the germanium doped preform is prepared by using the modified chemical vapor deposition (MCVD) technique. It is also well known that GeO becomes more stable than GeO2 at high temperature [36, 37]. Therefore, during the high – temperature gas-phase oxidation process of MCVD, GeO2 dissociates to the GeO molecule. When GeO is incorporated into glass, this molecule displays itself in the forms of 2-coordiated Ge or the Ge-Si (or Ge-Ge) wrong bonds, which are considered the defects precursors [38]. This point defect is related to the 240-250nm absorption band and its centres are named as germanium oxygen-deficient centres (GODCs), which are responsible to the photosensitivity of optical fibre. Figure 2.1 shows the schematics of the proposed point defects in germanium doped optical fibre.

In Figure 2.1, the Ge(1) and Ge(2) are ensnared electron centres, which have the absorption wavelength at 281nm and 213nm, respectively [38].

2.2.2 Photosensitivity mechanisms

Photosensitivity in optical fibres denotes a modification in the refractive index of the fibre core, which [1] was first discovered in an optical fibre where it was exposed to visible argon ion laser radiation at 488nm launched into its core. Although the mechanism of photosensitivity has not been illustrated clearly and the processes details are not yet fully explained by now, there are also several theories that have been published to explain it, such as: colour-centre model [39], compaction model [40], stress-relief model [41], electron charge migration model [42], permanent electric dipole model [43], ionic migration model [44] and Soret effect [45]. Among all these models, the first three mechanisms were involved in photosensitivity for the most common germanosilicate fibre. In this section, we will describe these three models associated with refractive index changes: colour centre, compaction/densification and stress relief models.

2.2.2.1 Colour centre model

The colour-centre model was firstly proposed by Hand and Russell [39]. It is well known that in many germanium-doped optical fibres there are two dominant absorption bands at 195nm (6.35eV) and 240nm (5.1eV)), which is associated with point defects GeE' and GODC induced by the chemical reactions. Under the UV irradiation, the Ge-Si wrong bond is broken by absorbing one UV photon at about 240nm, or by two-photon absorption at 480nm, forming a GeE' centre and

releasing the electron freely into the glass matrix until electrons are extracted from neighbouring Ge sites to create additional absorption centres in the glass. Thus, the other absorption band has been generated as well, which leads to a refractive index change following the Kramers-Kronig relationship [46]. After that, many experiments [47, 48] supported the colour-centre model for photosensitivity effect.

As we discussed in the last section, two possible candidates of GODC are listed as follow: Ge^{2+} ions coordinated by two oxygen atoms and getting the Ge-Ge or Si-Ge wrong bonds or two lone pair electrons (see in Figure 2.1) [49]. Two photochemical reaction paths for colour centre model were firstly proposed by Hosono et al. [50] through their experiment results. One reaction path is the single-photon process that the wrong bond based GODC absorbs a photon (5.16eV) and converts into GeE', GeO^{3+} and an electron (see in Figure 2.2(a)); another reaction path is two-photon process that the 2-coordinated Ge based GODC absorbs two photons and generates a self-trapped hole centre (STH) and a Ge electron centre (GEC) and finally the GEC is converted to GeE' (see in Figure 2.2(b)).

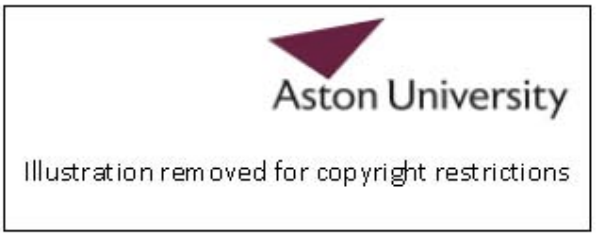

Figure 2.2 The two photochemical reaction paths: (a) single photon process and (b) two-photon process[50].

In the colour centre model, the changes of refractive index are associated with the photo induced changes of absorption in UV region through Kramers-Kronig relation, which is expressed as [46] :

Equation 2.1 $$\Delta n_{eff}(\lambda) = \frac{1}{2\pi^2}\rho\int_0^{\infty}\frac{\Delta\alpha_{eff}(\lambda)}{1-(\lambda/\lambda')^2}d\lambda$$

Where P is the principal part of the integral, λ is the wavelength at which the refractive-index change was calculated, and α_{eff} (λ) is the effective change in the absorption coefficient of the defects.

For colour centre model, Kramers-Kronig relationship indicates that the UV absorption of silica is connected to the refractive index change in the infrared and visible spectrum. Although this model can explain UV-induced low value refractive index change accurately, which has been verified by several experimental results [51-55], it is unable to fully account for the experimental investigations especially in higher value of refractive index changes.

2.2.2.2 Compaction/densification model

The compaction/densification model assumes that the UV laser exposure induces density modulation which leads to refractive index variation. The amorphous silica film [40] has been shown to have linear compaction effect that results in refractive index change which is illuminated under the KrF excimer laser, and its thermal reversibility. In their experiment, a KrF excimer laser was employed to irradiate thin-film amorphous silica samples grown on Si wafers. There was about 16% reduction in the film thickness after irradiation and an increase of refractive index

during laser irradiation. After the samples were annealed for one hour at 950°C, the compaction disappeared and the thickness and refractive index value were recuperated to the original state. However, if continued accumulation of UV irradiation is applied beyond the compaction threshold, it will become irrecoverable [56]. They also measured the refractive index change in hydrostatically compressed silica and the experiment results were consistent with laser-compacted, amorphous silica. This result confirmed that the variation of refractive index caused by laser and hydrostatically induced compaction growth have similar physical mechanisms, which means internal structure rearranged resulted in compaction of amorphous silica processing and not through a processing of defect creation. Afterwards, in order to comprehensively understand the formation dynamics of FBG, the UV-induced compaction in the Ge-doped fibre was also observed in the experiments by using transmission electron microscope (TEM) [57].

2.2.2.3 Stress relief model

The stress relief model claims that the refractive index change depends on the relief of built-in thermo-elastic stress caused in the fibre core by the UV-illumination [58]. During the fibre drawing and cooling process, the different thermal expansion coefficients of fibre cladding and core region lead to the fibre core being under tension [59]. It is known the tension can reduce the refractive index because of the stress-optic effect. Therefore, during the UV irradiation process, the wrong bonds break and the relaxation in the tensioned fibre core induced by the thermal effect could cause the increasing of refractive index. Although the stress relief model explains the large index change in the fibre core, the growing of fibre Bragg grating induces very strong tension,

which contradicts this model [51]. Moreover, the stress relief model can't explain the thermal reversibility of grating inscription.

2.2.3 Photosensitivity enhancement techniques

The standard single mode telecom fibres which doped 3 mol% germanium dioxide have shown very poor photosensitivity (typically only indicates index changes of 3×10^{-5}) [60]. Thus, the researchers have tried to understand and increase the photosensitivity in optical fibres since the beginning of grating inscription in optical fibre and the discovery of photosensitivity. Normally, increasing concentration of germanium dopant can improve the photosensitivity of fibre (large index changes of 5×10^{-4}) [61]. However, the higher germanium doping level also leads to some drawbacks such as significant transmission loss and reduced mechanical strength. Therefore, three main methods have been developed to increasing the photosensitivity of fibre: hydrogen loading, flame brushing and appreciated co-doping method.

2.2.3.1 Hydrogen loading technique

Lemaire and co-workers [62] firstly reported hydrogen loading technique which achieving the high UV photosensitivity in optical fibres. The permanent index change of hydrogenated fibre after UV exposure has been increased to 3.43×10^{-3}, which is almost 100 times higher than non-hydrogenation fibre. In this method, the treating process is that the optical fibres are soaked in hydrogen gas within a pressure ranging from 20~750atm at a temperature ranging from 25°C to75°C for several days (the loading time depends on the temperature and pressure). One

advantage of this technique is that the hydrogen in unexposed fibre areas will release out, which can cause critical loss at communication windows.

The achieved increased photosensitivity in hydrogen loading technique process is due to the capability of hydrogen to create additional GODCs from germanium atoms in the lattice in the following fashion. The research results from Douay et al. have demonstrated that the concentration of GODCs in the fibre core is significantly increased after loading hydrogen treatment [63]. In hydrogenation process, H_2 molecules can diffuse into the fibre core through the cladding where the fibre is placed in a high pressure hydrogen gas tube. UV exposure or any intense heat will result in dissolving H_2 to thermally react with Si-O-Ge glass sites and subsequent formation of additional GODCS, Si-OH and Ge-OH bonds which cause the large permanent index changes in the fibre core [64]. However, involving hydroxyl broadband absorption peak at 1.39μm and 1.41μm can causes critical loss in the communication windows [65, 66]. Thus, some researchers have tried to load the fibre with deuterium instead of hydrogen, which appeared to move the infrared loss band away from the tele-communication transmission window [67].

2.2.3.2 Flame brushing technique

The flame brushing is another simple and effective photosensitization technique for germanosilicate optical fibre, which can achieve high photosensitivity with small absorption loss [68]. The designated region of fibre is brushed repeatedly in a flame fuelled with hydrogen and oxygen at the temperature of approximate 1700 ºC for around 20mins. The flame brushing and

hydrogenation technique have the same photosensitizing principle, by which the hydrogen molecules dissolve quickly into the fibre and chemically react with germanosilicate glass to induce the GODC bands that are the main reason for the fibre photosensitivity, sensitising the fibre with Δn reaching 10^{-3} [68].

Comparing with the hydrogenation technique, there are several advantages for fibre photosensitivity enhancing by this technique, such as permanent photosensitivity enhancement, strong FBGs fabrication in normal standard telecom fibre, localization of photosensitivity and short treating time. However, the major shortcoming of this technique is that the high temperature treatment by flame brush can weaken the fibre, which could seriously shorten the service life of the optical fibre device fabricated using this approach.

2.2.3.3 Co-doping technique

The photosensitivity can be enhanced by adding additional materials (co-dopants) into the germanosilicate fibre, such as boron (B) [43] and tin (Sn) [69].In 1993, Williams's et.al demonstrated a highly photosensitive fibre which was co-doped with boron and germanium in the fibre core. In their experiment, three type fibres (1- standard telecom fibre with 3mol% GeO_2, 2- fibre with highly Ge concentration of 20 mol% GeO_2 and 3- B/Ge co-doping fibre with 15 mol% GeO_2) have been exposed to UV-beam until their index modulation became saturated. They achieved the saturated index modulation of approximately 7×10^{-4} for B co-doped fibre over about 10 minutes while for other two fibres, it took about 2 hours to reach the saturated index modulation of 3×10^{-5} and 2.5×10^{-4} respectively. The systematic study shows the B co-doping

can significantly increase the index change, which is around 4 times larger than that of the standard single mode fibre. Meanwhile, the UV exposing time to reach saturated reflectivity was sharply decreased from more than 2 hours for the pure germanosilicate fibre to only around 10 mins for co-doped fibre [70]. As we known, the doping of boron to silica could decrease refractive index of the glass and make it softer than original material [71]. Although these investigations evidently indicate a much better photosensitivity response from B co-doped fibre than the fibre with only equivalent Ge concentration, boron doping causes extra loss about 0.1 dB at 1550 nm range, which is not satisfying. However, for short length gratings, this may not be of concern.

In another approach to enhance the photosensitivity of the fibre by adding other material as co-dopants, Dong *et.al* [69] reported that tin (Sn) co-doped fibre exhibits the saturated refractive index change of 3 times bigger than of the normal germane-silicate fibre. And comparing with B co-doping, Sn co-doped fibre has some advantages including not introducing significant loss at the telecommunication transmission window and the grating survival at high temperature [72].

The nitrogen (N_2) co-doping germanosilicate fibre also exhibited extremely high photosensitivity, where the refractive index change is around 2×10^{-3} for non-hydrogenation fibre, and 1×10^{-2} index change for hydrogenated fibre [73]. However, hydrogenated N-doped fibres induce very high intrinsic loss at the level of 1000dB/km at the third telecommunication window, because the N-H bond has extraordinary strong absorption loss band at the wavelength of 1506nm [74, 75].

.

2.3 Coupled mode theory

Coupled mode theory is a mathematics tool for analysis of the propagation of electromagnetic waves in periodic layered mediums. Nowadays, it becomes one of most popular solutions utilized in obtaining quantitative information about the diffraction efficiency and spectral dependence of optical fibre gratings (including FBG, LPG, and TFG). There are a number of different coupled-mode formulations produced by mathematicians [76, 77]. Here, the coupled-mode theory that will be discussed is based on the model provided by Erdogan [78-80].

Erdogan pointed out that in the ideal-mode approximation to coupled-mode theory the transverse component of the electric field can be written as a superposition of ideal modes which are in an ideal waveguide without grating perturbations.

Equation 2.2 $$\vec{E}_t(x,y,z,t) = \sum_j [A_j(z)\exp(i\beta_j z) + B_j(z)\exp(-i\beta_j z)].\vec{e}_{jt}(x,y)\exp(-i\omega t)$$

Where the coefficients $A_j(z)$ and $B_j(z)$ are the slowly varying amplitudes of the $_j$th mode travelling in the +z and -z directions, respectively. $\vec{e}_{jt}(x,y)$ is the transverse mode field with the time dependence exp(-iωt), which might describe; bound-core, cladding or radiation LP modes. The propagation constant β means:

Equation 2.3 $$\beta = \frac{2\pi}{\lambda} n_{eff}$$

where n_{eff} represents the effective refractive index of jth mode.

The presence of a dielectric perturbation causes the various modes to be coupled. The amplitudes $A_j(z)$ and $B_j(z)$ of the *j*th modes to evolve along the *z* direction. This can be explained in the following equations:

Equation 2.4 $$\frac{dA_j(z)}{dz} = i\sum_k A_k\left(K_{kj}^t + K_{kj}^z\right)\exp\left[i\left(\beta_k - \beta_j\right)z\right] + i\sum_k B_k\left(K_{kj}^t - K_{kj}^z\right)\exp\left[-i\left(\beta_k + \beta_j\right)z\right]$$

Equation 2.5 $$\frac{dB_j(z)}{dz} = -i\sum_k A_k\left(K_{kj}^t - K_{kj}^z\right)\exp\left[i\left(\beta_k + \beta_j\right)z\right] - i\sum_k B_k\left(K_{kj}^t + K_{kj}^z\right)\exp\left[-i\left(\beta_k - \beta_j\right)z\right]$$

Where K_{kj}^t and K_{kj}^z are the transverse and longitudinal coupling coefficients between the j and k modes respectively. The transverse coupling coefficient K_{kj}^t can be written as;

Equation 2.6 $$K_{kj}^t(z) = \frac{\omega}{4}\int_\infty\int\left[\Delta\varepsilon(x,y,z)\vec{e}_k^t(x,y).\vec{e}_j^{t*}(x,y)\right]dxdy$$

Where ω is the waveguide frequency. The longitudinal coefficient K_{kj}^z has similar equation format as K_{kj}^t, but K_{kj}^z is usually neglected because generally $K_{kj}^z(z) \langle\langle K_{kj}^t(z)$ (nearly 2 orders of magnitude smaller) for fibre modes. $\Delta\varepsilon(x,y,z)$ is the permittivity perturbation.

Most Fibre gratings are fabricated by exposing a photosensitive fibre to a spatially varying pattern of UV light. The refractive index n_{eff} change can be expressed as:

Equation 2.7 $$\delta n_{eff}(z) = \bar{\delta} n_{eff}(z)\left[1 + \nu\cos\left(\frac{2\pi}{\Lambda}z + \phi(z)\right)\right]$$

where *v* is the fringe visibility of the index change; Λ is the grating period; $\varphi(z)$ is the grating chirp and $\bar{\delta} n_{eff}(z)$ is the "dc" index change spatially averaged over a grating period. The UV-induced index change $\delta n_{eff}(x,y,z)$ in most fibre gratings is approximately uniform across the core and negligible outside the core. Therefore, the core index change can be written by

substituting $\bar{\delta} n_{eff}(z)$ in equation 2.7 by $\bar{\delta} n_{co}(z)$. Then, the general coupling coefficient (Equation 2.8) can be rewritten as:

Equation 2.8 $$K_{kj}^{t}(z) = \sigma_{kj}(z) + 2\kappa_{kj}(z)\cos\left[\frac{2\pi}{\Lambda} z + \phi(z)\right]$$

Where σ_{kj} is the "dc" coupling coefficient and κ_{kj} is the "ac" coupling coefficient

Equation 2.9 $$\sigma_{kj}(z) = \frac{\omega n_{eff}\, \bar{\delta} n_{eff}(z)}{2} \iint_{core} \vec{e}_k^{\,t}(x,y)\vec{e}_j^{\,t*}(x,y)dxdy$$

Equation 2.10 $$\kappa_{kj}(z) = \frac{\nu}{2}\sigma_{kj}(z)$$

2.3.1 Fibre Bragg gratings (FBGs)

For an FBG, the dominant interaction is close to the wavelength for which a mode of amplitude A(z) is coupled into an identical counter-propagating mode of amplitude B (z). The Equation 2.4 and 2.5 may simplified by keeping the terms that involve the amplitudes of the particular mode and by synchronous approximation. The resulting equations can be written as:

Equation 2.11 $$\frac{dR}{dz} = i\hat{\sigma}R(z) + i\kappa S(z)$$

Equation 2.12 $$\frac{dS}{dz} = -i\hat{\sigma}S(z) - i\kappa^{*}R(z)$$

where the amplitude R and S are

Equation 2.13 $$R(z) \equiv A(z)\exp\left(i\delta z - \frac{\varphi}{2}\right)$$

Equation 2.14 $$S(z) \equiv B(z)\exp\left(-i\delta z + \frac{\varphi}{2}\right)$$

In Equation 2.11 and 2.12, κ is the "ac" coupling coefficient and a σ the general "dc" self-coupling coefficient defined as

Equation 2.15 $$\hat{\sigma} \equiv \delta + \sigma - \frac{1}{2}\frac{d\varphi(z)}{dz}$$

In above Equation 2.15, the derivative (1/2)dφ(z)/dz describes possible chirp of the grating period, the detuning δ is assumed to be constant for all gratings along the z axis, this becomes:

Equation 2.16 $$\delta \equiv \beta - \frac{\pi}{\Lambda} = \beta - \beta_D = 2\pi\Delta n_{eff}\left[\frac{1}{\lambda} - \frac{1}{\lambda_D}\right]$$

Where $\lambda_D = \Delta n_{eff}\Lambda$ is the "design wavelength" (initial resonance wavelength) for Bragg scattering by a very weak grating (i.e. $\delta n_{eff} \to 0$).

In a single-mode Bragg grating case, the relations for coupling coefficients κ and σ can be simplified as:

Equation 2.17 $$\sigma = \frac{2\pi}{\lambda}\overline{\delta n_{eff}}$$

Equation 2.18 $$\kappa = \kappa^{*}$$
$$= \frac{\pi}{\lambda}\nu\overline{\delta n_{eff}}$$

If there is a forward coupling grating with no chirped, then $\overline{\delta n_{eff}}$ is a constant and $d\phi / dz = 0$. Therefore, κ, σ and $\hat{\sigma}$ are constants, and thus Equations 2.13 and 2.14 are simplified into

coupled first-order ordinary differential equations with constant coefficients, for which closed-form solutions will be calculated out when appropriate boundary conditions are specified.

For a FBG with length L, the reflectivity could be recognised as a forward-propagating wave from the negative infinite (z= -∞), while assuming that no backward-propagating wave exists for z ≥ L/2. The amplitude ρ and the power reflection coefficient R can be expressed as follow:

Equation 2.19 $$\rho = \frac{-\kappa \sinh\sqrt{(\kappa L)^2 - (\hat{\sigma} L)^2}}{\hat{\sigma}\sinh\sqrt{(\kappa L)^2 - (\hat{\sigma} L)^2} + i\sqrt{\kappa^2 - \hat{\sigma}^2}\cosh\sqrt{(\kappa L)^2 - (\hat{\sigma} L)^2}}$$

And

Equation 2.20 $$R = \frac{\sinh^2\sqrt{(\kappa L)^2 - (\hat{\sigma} L)^2}}{-\frac{\hat{\sigma}^2}{\kappa^2} + \cosh^2\sqrt{(\kappa L)^2 - (\hat{\sigma} L)^2}}$$

Using the equation 2.20 the maximum reflectivity of FBG can be given as:

Equation 2.21 $$R_{\max} = \tanh^2(\kappa L)$$

By plotting equation 2.20 for κL=0.88 and κL=3, the reflection spectra of a uniform Bragg grating are illustrated as below:

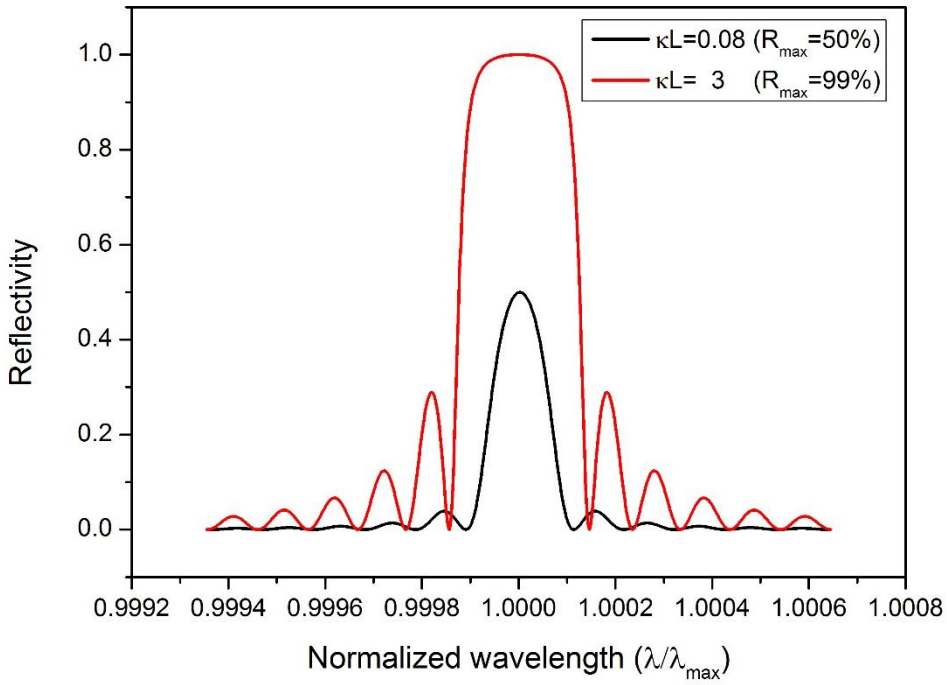

Figure 2.3 Simulated reflection spectra of 5mm long FBGs with κL=0.88 and κL=3.

In figure 2.3, the normalized wavelength is

Equation 2.22 $$\frac{\lambda}{\lambda_{\max}} = \frac{1}{1+\hat{\sigma}L/\pi N}$$

Where λ_{max} is the wavelength at maximum reflectivity, and N is the grating period number (N=L/Λ).

2.3.2 Long period gratings (LPGs)

For LPGs, the dominant interaction is close to the wavelength for which a mode of amplitude $A_1(z)$ is coupled into an identical co-propagating mode of amplitude $A_2(z)$. Therefore, this simplifies equation 2.4 and equation 2.5 to the following;

Equation 2.23 $$\frac{dR}{dz} = i\hat{\sigma}R(z) + i\kappa S(z)$$

Equation 2.24 $$\frac{dS}{dz} = -i\hat{\sigma}S(z) + i\kappa^{*}R(z)$$

The new amplitudes R and S are:

Equation 2.25 $$R(z) \equiv A_1 \exp\left[-i(\sigma_{11}+\sigma_{22})\frac{z}{2}\right]\exp\left(i\delta z - \frac{\varphi}{2}\right)$$

Equation 2.26 $$S(z) \equiv A_2 \exp\left[-i(\sigma_{11}+\sigma_{22})\frac{z}{2}\right]\exp\left(-i\delta z + \frac{\varphi}{2}\right)$$

In above equations, the "ac" components are σ_{11} and σ_{22}, and the "ac" cross-coupling coefficients are $\kappa = \kappa_{21} = \kappa_{12}^{*}$. The "dc" self-coupling coefficient can be described as:

Equation 2.27 $$\hat{\sigma} \equiv \delta + \frac{\sigma_{11}-\sigma_{22}}{2} - \frac{1}{2}\frac{d\phi}{dz}$$

In above equation 2.27, the detuning δ is assumed to be constant for all gratings along the z axis, this becomes:

Equation 2.28 $$\delta \equiv \frac{1}{2}(\beta_1 - \beta_2) - \frac{\pi}{\Lambda} = \pi\Delta n_{eff}\left[\frac{1}{\lambda} - \frac{1}{\lambda_D}\right]$$

Where $\lambda_D = \Delta n_{eff}\Lambda$ is the "design wavelength" (Initial resonance wavelength) for an infinitesimally weak grating. As for Bragg gratings, the grating conditions corresponds to δ =0 or $\lambda = \lambda_d = \Delta n_{eff}\ \Lambda$.

For a uniform grating, κ and $\hat{\sigma}$ are constants. Similar as the case of the FBG, the forward-coupled grating Equations 2.25 and 2.26 are coupled first-order ordinary differential equations with constant coefficients. Thus, closed-form solutions will be calculated out when appropriate initial conditions are specified.

2.3.3 Tilted fibre grating (TFGs)

TFGs are gratings photo-induced index modulation tilted by an angle θ with respect to the fibre axis z' (see in Figure 2.4). The index perturbation could be expressed as:

Equation 2.29 $$\delta n_{co}(\mathrm{x},\, z) = \overline{\delta n_{co}}(z')\left\{1 + s\cos\left[\frac{2\pi}{\Lambda_{\mathrm{G}}} z' + \varphi(z')\right]\right\}$$

Where, z'=xsinθ+zcosθ shown in Figure 2.3. However, the grating period along the fiber axis (z-direction) is simply $\Lambda=\Lambda_G/\cos\theta$. Here, $z'\approx z\cos\theta$ is used in Equation 2.29. the general coupling coefficient described in Equation 2.26 will becomes:

Equation 2.30 $$C_{\pm\mp}^{T}(\mathrm{z}) = \zeta(\mathrm{z}) + 2\kappa_{\pm\mp}(\mathrm{z})\cos\left[\frac{2\pi}{\Lambda} z + \varphi(z\cos\theta)\right]$$

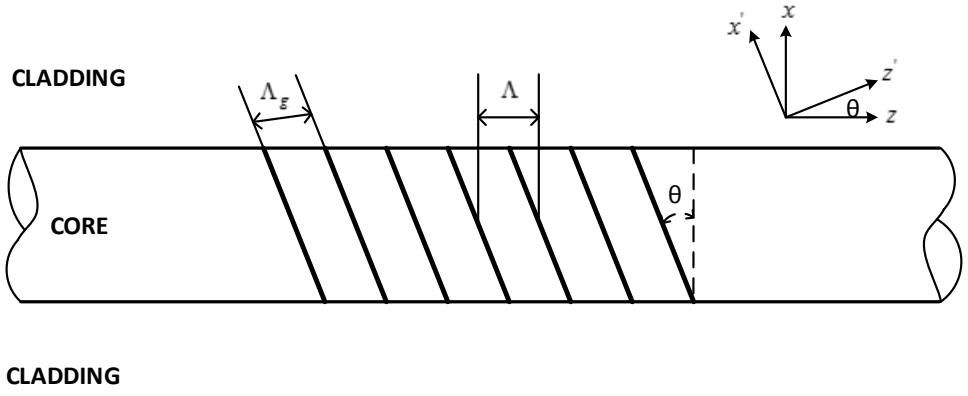

Figure 2.4 Diagram of a tilted fibre grating in the fibre core.

Where the subscripts m and q actually describe the forward travelling mode (+) and backward travelling mode (-), respectively. The self and cross coupling coefficients are modified as follows [79]:

Equation 2.31 $$\zeta(\mathrm{z}) = \omega \frac{\mathrm{n}_{\mathrm{co}}}{2} \overline{\delta n_{co}}(z\cos\theta) \iint_{core} e_{\pm}^{T}(x,y) \cdot e_{\mp}^{T^*}(x,y) dxdy$$

Equation 2.32 $$\kappa_{\pm\mp}(\mathrm{z}) = \frac{\mathrm{s}\omega \mathrm{n}_{\mathrm{co}}}{4} \overline{\delta n_{co}}(z\cos\theta) \iint_{core} e_{\pm}^{T}(x,y) \cdot e_{\mp}^{T^*}(x,y) \cdot e^{\pm i\frac{2\pi}{\Lambda} x\tan\theta} dxdy$$

Finally, the tilted fringe effect can be expressed by an effective fringe visibility[9], $S_{\mp\pm}(\theta)$ can be defined as

Equation 2.33 $$\frac{s_{\pm\mp}(\theta)}{s} = \frac{\iint_{core} \exp(\pm i \frac{2\pi}{\Lambda} x\tan(\theta)) e_{\mp}^{T}(x,y) \bullet e_{\pm}^{T^*}(x,y) dxdy}{\iint_{core} e_{\mp}^{T}(x,y) \bullet e_{\pm}^{T^*}(x,y) dxdy}$$

2.4 Phase matching conditions

Normally, the bound wave can be coupled to the counter-propagating or co-propagating modes in perturbed optical fibre. According to the mode coupling direction, optical fibre gratings will be divided into two types. One is a backward-coupled grating, in which the incident light is coupled into the opposite direction, such as FBGs and small angle TFGs. The other type is forward-coupled gratings, such as LPGs and large angle TFGs, which couple the light to the same directions.

For the transfer of energy from a mode into another propagating mode, the phase mismatch factor $\Delta\beta$ is referred to a detuning, which is written as:

Equation 2.34 $$\Delta\beta = \beta_i \pm \beta_d - \frac{2\pi}{\Lambda_g} N\cos\theta$$

Where β_i is the propagation constant for the incident mode, β_d signifies the diffracted mode propagation constant, Λ_g is the grating period, θ is the tilt angle of grating and letter N express an integer number(0,1,2…). The sign ' ± ' represents the situation thereof the mode propagates in $\mp z$ direction.

The transfer energy is significant when $\Delta\beta = 0$, Equation 2.34 can be rewritten as:

Equation 2.35 $$\beta_i \pm \beta_d = \frac{2\pi}{\Lambda_g}\cos\theta$$

Both β_i and β_d share the same sign for counter-propagating modes. In contrast, they have opposite signs for co-propagating mode. The first-order diffraction is dominant with regards to most cases, hence N=1[77]. The resonant wavelength should be:

Equation 2.36 $$\lambda = (n_{eff}^{i} \pm n_{eff}^{d})\frac{\Lambda_g}{\cos\theta}$$

In the case of normal FBG (θ=0), the Bragg wavelength is shown by:

Equation 2.37 $$\lambda_B = 2n_{eff}\Lambda$$

Where n_{eff} is the effective index of the core.

Figure 2.5 below shows a diagram of the light coupling from the forward-propagating core mode to the backward-propagating core mode.

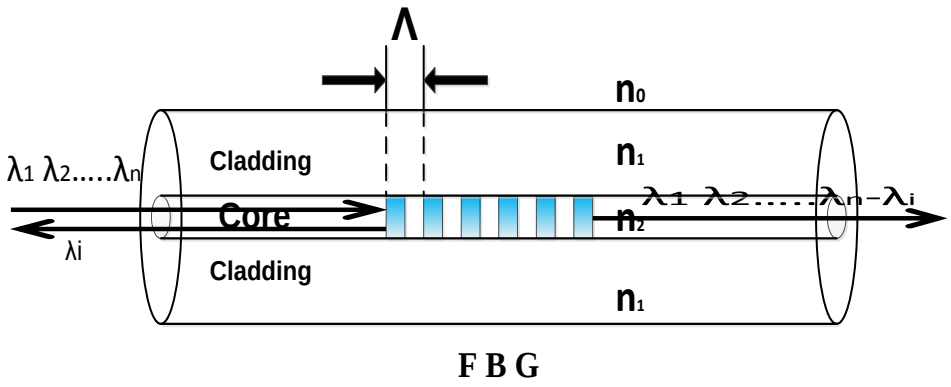

Figure 2.5 Schematic of mode coupling of an FBG structure.

The phase matching condition of an LPG (coupling from the core mode into the co-propagating cladding mode) is given by:

Equation 2.38 $$\lambda_{res} = (n_{co} - n_{cl,m}) \bullet \Lambda$$

Where n_{co} is the effective index of the core mode and $n_{cl,m}$ is the effective index with the m^{th} cladding mode. Λ is the period of the grating, usually in the region at several hundred microns[81].

Figure 2.6 shows a diagram of mode coupling by an LPG structure.

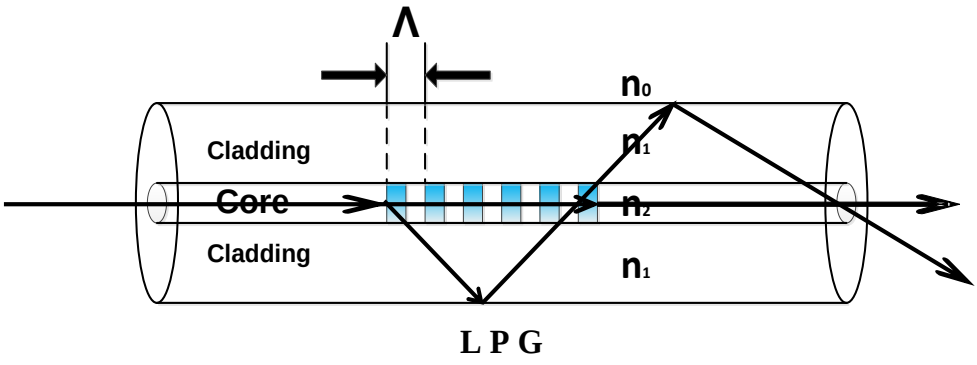

Figure 2.6 Schematic of mode coupling of an LPG.

In the case of a TFG, the mode couplings are possible in both coupling directions (the core mode can be coupled to the counter-propagating modes or to the co-propagating modes, which depends on the magnitude of the grating tilt angle. The resonant wavelengths are shown as below [79, 82]:

Equation 2.39 $$\lambda_{co-cl} = \left(n_{co} \pm n_{cl,m}\right) \cdot \frac{\Lambda_g}{\cos\theta}$$

Where n_{co} is the effective index of the core and $n_{cl,m}$ is the effective index with the m^{th} cladding mode. The "+" indicates the coupling to the counter-propagating modes where as "-" to the co-propagating modes. The grating period along the fibre axis can be simply expresses as:

Equation 2.40 $$\Lambda = \frac{\Lambda_g}{\cos\theta}$$

Where Λ_g is the normal period of the grating and θ is the grating tilt angle.

The schematics of mode coupling to opposite directions by TFGs are shown in Figure 2.7.

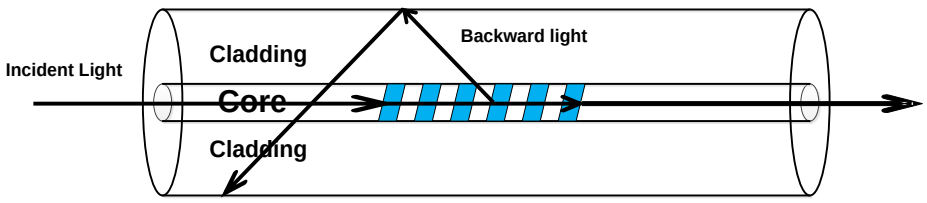

T F G (a)

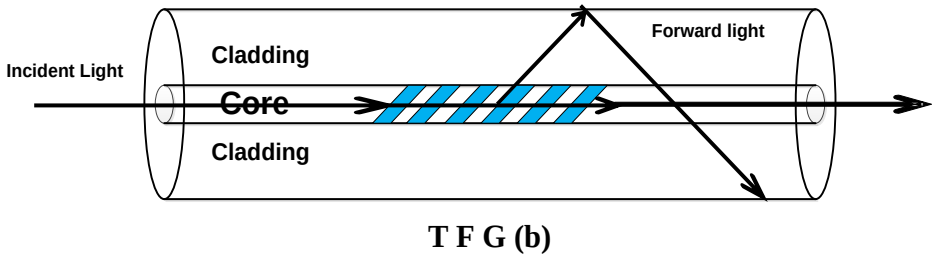

Figure 2.7 Schematic of TFG mode coupling: a) backward coupling; b) forward coupling.

2.5 Fabrication techniques of optical fibre grating

2.5.1 Internal inscription technique

The internal fiber grating writing technique was firstly invented by Hill and co-workers in 1978 by using germanium-doped silica fibre and visible argon ion laser radiation [1].Hill's experimental setup is shown in Figure 2.8.

Figure 2.8 Schematic of Hill experiment set up of fibre Bragg grating fabrication by internal inscription technique. [1]

As shown in Figure 2.8, a 488nm argon ion laser is employed as the source launching into core of the fibre. The standing wave was formed by 4% Fresnell reflection occurred at the cleaved end of fibre interfering with initial incident laser light. The high intensity points modified the refractive index in the germanium-doped photosensitive fibre in period to form a Bragg grating structure in the fibre core. However, the FBG fabricated by this technique is limited to the central wavelength coinciding with the excitation laser wavelength. Thus, the period of grating is determined by the wavelength of incident laser and effective index of fibre core, which is:

Equation 2.41 $$\Lambda = \frac{\lambda_{UV}}{2n_{eff}}$$

This technique has almost no use for real application devices as the structure can be generated for one fixed Bragg wavelength without any tuneability.

2.5.2 Two-beam holographic side-inscription technique

The two-beam holographic technique was first demonstrated by Meltz *et al.* in 1989 [23]. The disadvantages in the original Hill gratings were overcome by Meltz's work due to improved writing efficiency and the ability to write gratings with arbitrarily designed Bragg wavelength by the angle adjustment of the interfering beams. Figure 2.9 shows a basic schematic of transverse holographic technique experiment set up.

Figure 2.9 Schematic of an amplitude-splitting interferometer used by Meltz et al. which demonstrated the first externally fabricated Bragg grating [23].

As shown in Figure 2.9, the 244nm UV beam was divided into two equal intensity beams through a 50:50 beam splitter and reflected by two symmetric mirrors. Then the two reflected beams recombined to form an interference pattern illuminating on the fibre, and the period of the interference pattern depends on the half angle (θ/2) of the two beams and the irradiation wavelength (λ_{UV}), and the relation is expressed as:

Equation 2.42 $$\Lambda = \frac{\lambda_{UV}}{2\sin\left(\frac{\theta}{2}\right)}$$

As we see from Equation 2.37, the Bragg resonance wavelength of the grating is related to period of the grating, which is: $\lambda = 2n_{eff}\Lambda$. Thus, the equation 2.38 can be rewritten as the relation between the FBG wavelength and irradiation wavelength and beam angle:

Equation 2.43 $$\lambda = \frac{n_{eff}\lambda_{UV}}{sin\left(\frac{\theta}{2}\right)}$$

where n_{eff} is the effective refractive index of the core.

2.5.3 Phase mask scanning technique

Phase mask scanning technique is considered as an alternative method, which is one of the most efficient approaches to produce fibre gratings with high quality and reproducibility. This technique was simultaneously proposed by Anderson and Hill [25, 83] in 1993, and is based on near contact exposure through a phase mask. Figure 2.10 shows the schematic of a phase mask inscription method that was first demonstrated by Hill *et al*.

Figure 2.10 The schematic of phase mask inscription method that was first demonstrated by Hill et al [25].

The phase mask is a one-dimensional periodic surface relief pattern with period Λ_{pm} etched into fused silica substrate that is transparent to ultraviolet light (see Figure 2.11). A near-field fringe patter is thereby produced on the fibre core due to the interference of the ±1 order diffracted beams. The phase masks have been optimized to suppress the light diffraction energy in 0 order (<5%) by controlling the depth of corrugation and choosing the amplitude of the periodic surface-relief pattern with π phase modulation at the wavelength of incident UV beam, and maximize diffraction efficiency in each of the ±1 diffracted orders.

The depth of corrugations of minimum 0 order diffraction is expressed as:

Equation 2.44 $$d = \frac{\lambda_{UV}}{2(n_s(\lambda_{UV})-1)}$$

Where λ_{uv} is the wavelength of the UV beam and $n_s(\lambda_{uv})$ is the refractive index of fused silica substrate at the wavelength of incident UV beam.

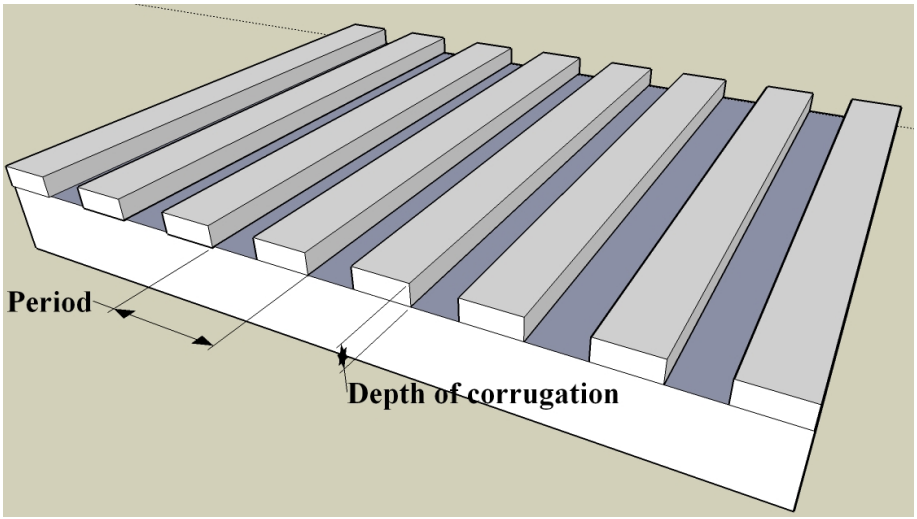

Figure 2.11 One-dimensional periodic surface relief pattern of a phase mask.

The period of the grating written by phase mask method is

Equation 2.45 $$\Lambda_G = \frac{\Lambda_{PM}}{2}$$

The main advantage of the phase-mask technique is its capabality of producing high quality and complex grating structures such as chirped grating[84], apodized grating [85], Moiré grating [86], sampled grating [87] and phase-shifted grating [88]. Another advantage of phase mask inscription technique is the ability to inscribe gratings with sophisticated structures and angles. However, the drawback of this technique is that gratings of different wavelengths require different phase masks.

2.5.4 Point by point inscription technique

Point by point inscription technique is a non-interferometric method of grating inscription which was first demonstrated by Malo *et al*. and Hill *et al*.[89, 90]. It involves the exposure of a small section of fibre to UV beam, the refractive index of only the UV exposed fibre area changes at a time, and the UV beam is laterally translated to expose other sections of the fibre.

Since these gratings are inscribed on the fibre section by section, it's not an efficient technique to write long length gratings which require large index perturbation. In addition, as the UV beam cannot be focused to less than one micron, it is not feasible to write first order Bragg gratings by point-by-point method. This technique cannot be used for inscribing the TFG structures, and thus only used for LPGs with the period ranging from 10μm to 600μm. Recently, with the development of the femtosecond laser, the point-by-point technique is employed more widely in grating and microstructure fabrication using femtosecond laser inscription.

2.5.5 Optical fibre grating inscription by femtosecond laser

Since femtosecond laser micro-structuring of silica was first reported in 1994 [91], the use of ultrashort laser pulses in the femtosecond regime to directly induce refractive index changes in transparent dielectric materials has attracted a lot of attention within the last decade. The first LPG fabricated by femtosecond laser was demonstrated in 1999 [92]. In that paper, an LPG was inscribed by point-by-point inscription technique using IR femtosecond laser. However, the transmission spectrum of this LPG was noisy and not regular like UV written gratings. The spectra of femtosecond laser inscribed LPGs in both germano-silica and pure silica fibres were

successfully improved by Hindle *et al* [93] afterwards. FBGs fabricated using 800nm femtosecond laser and point-by-point technique was firstly reported by Martinez *et al* in 2004 [94]. In their experiments, FBGs with first, second and third order resonance at 1550nm were inscribed in telecom fibres without any photosensitisation. Phase-mask technique was also employed as another method to write FBGs using femtosecond laser, by which FBGs of different orders were first inscribed by Mihailov *et al* in 2003 [95].

Although optical fibre gratings fabricated using femtosecond laser have some drawbacks (poor spectra and large transmission loss [96]), their extraordinary properties can be realized as below:

a. Fibre gratings can be inscribed in any fibre material without photosensitivity.
b. The fibre gratings can be operated at high temperatures (up to 1000 °C).
c. The fibre gratings writing can extend far into the fibre cladding.
d. Birefringent reflection can be induced or controlled.

2.6 Chapter conclusion

In this chapter, a comprehensive review on fibre grating development history and the UV photosensitivity of optical fibre has been given, including the three models of colour centre, compaction/densification and stress relief. Following that, the techniques based on hydrogen loading, flame brushing and co-doping to increase photosensitivity of the silicate glass fibre have been discussed. As the second main part of this chapter, the theory of mode coupling mechanism and phase match condition and the structure of fibre gratings including FBG, LPG and TFG have been discussed in detail. Finally, fibre gratings inscription methods such as internal, two-beam holographic, phase mask and point-by-point inscription techniques have been reviewed.

Chapter 3.

Fabrication and sensing characteristics of UV laser inscribed fibre Bragg gratings and long period gratings

3.1 Introduction

In this chapter, the three main in-fibre grating fabrication techniques - two-beam holographic, phase-mask, and the point-by-point technique, which have been employed to fabricate all the gratings used in the work presented in this thesis, will be discussed. This will be followed by a detailed discussion on thermal, strain and refractive index sensing properties of three different types of fibre grating (FBG, CFBG and LPG) which were designed and fabricated using the three techniques. In addition, FBGs and CFBGs have been fabricated on two novel fibres (metal coated fibre and large mode filed fibre) requested by project collaborators – Strathclyde University and JK Lasers for applications in high temperature sensing and high power fibre laser, and their spectral properties have been presented and discussed.

3.2 Fibre Bragg gratings inscription and sensing characteristics

3.2.1 FBG inscription

Employing the optical fibre grating fabrication methods described in Chapter 2, the FBGs can been inscribed by placing the fibre in the interference fringe area formed by two intense UV laser beams. The two main different methods producing the interfering fringes are two-beam holographic inscription technique and phase mask inscription technique. The following will discuss the FBGs fabricated using two UV inscription methods.

a. Two-beam holographic inscription

Figure 3.1 shows the two beam holographic UV fabrication system in our laboratory at Aston University. The UV laser beam is transmitted through and divided into two beams with equivalent power by a 50:50 beam splitter. Then, these two beams are reflected by two mirrors and intersected together on the fibre core to generate interfering fringes.

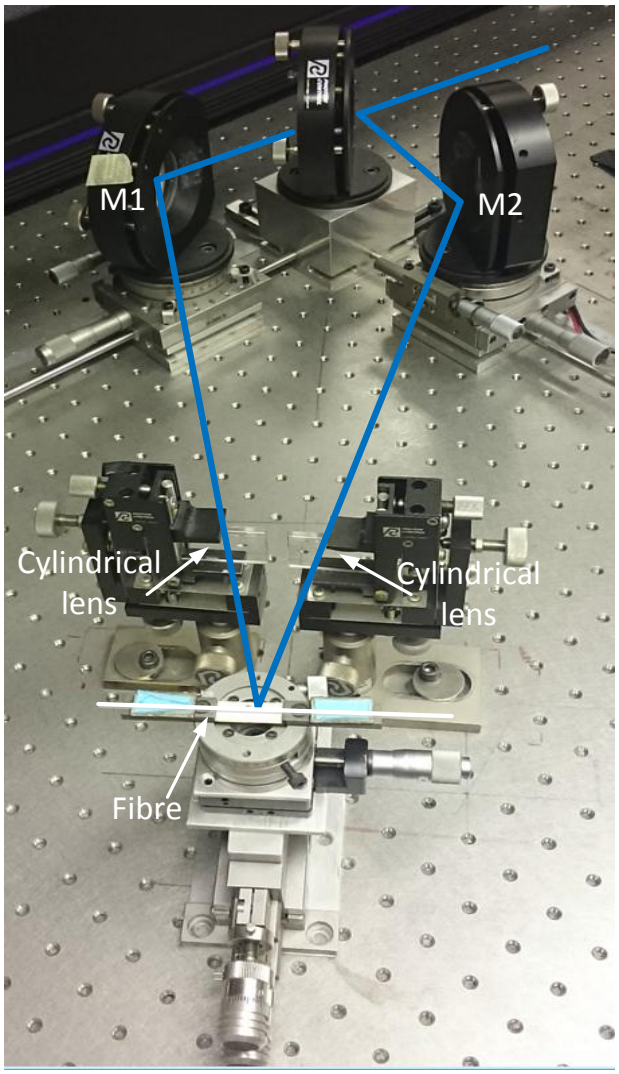

Figure 3.1 Two beam holographic FBGs inscription system in the laboratory at Aston University.

As the fibre core become exposed to the UV intensity fringes, the refractive index of the core is periodically modified along the fibre length. The main advantage of the two-beam holographic method is that it is possible to write selected wavelength gratings by changing the angle (2α) between the two beams. The major disadvantage of this technique is that it is susceptible to mechanical vibration and limited grating length, thus the grating quality may not be as good as those inscribed by phase-mask technique.

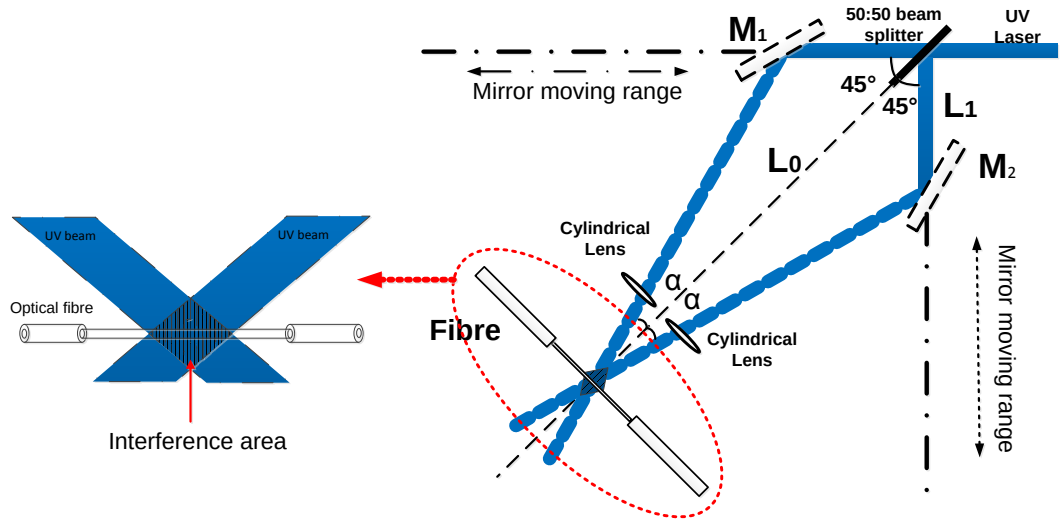

Figure 3.2 Schematic diagram of optical set-up using the two-beam holographic technique.

As shown in the schematic diagram in Figure 3.2, the Bragg wavelength of an FBG is set by changing the angle between the two incident UV beams (i.e. by changing the distance between mirrors M1 and M2 and the beam splitter) when using two-beam holographic technique. A range of FBGs with Bragg responses in four different wavelength ranges (800nm, 1060nm, 1310nm and 1550nm) have been designed and inscribed using the two-beam holographic method. The fibre we selected is the standard single–mode fibre (SMF-28e, Corning) with a core diameter of 8.2μm and cladding diameter of 125±0.7μm. The core and cladding refractive indices are 1.461 and 1.456, respectively. The spectrum measurement set up is shown in Figure 3.3, where a Broad Band Source was employed as a light source and the HP86142A OSA (optical spectrum analyser) was used to display the transmission spectrum of FBG.

Figure 3.3 Diagram of FBG transmission spectrum measurement set up.

FBGs can be inscribed easily using two-beam holographic method with designed wavelength and reflectivity. The typical transmission spectra of FBGs in four different wavelength ranges written by the two-beam holographic technique are shown in Figure 3.4. Although all four gratings of different wavelengths showed the reflectivities around 10dB in the figure, much higher reflectivity (up to 30 to 40dB) is achievable by increasing the UV laser power or the exposure time.

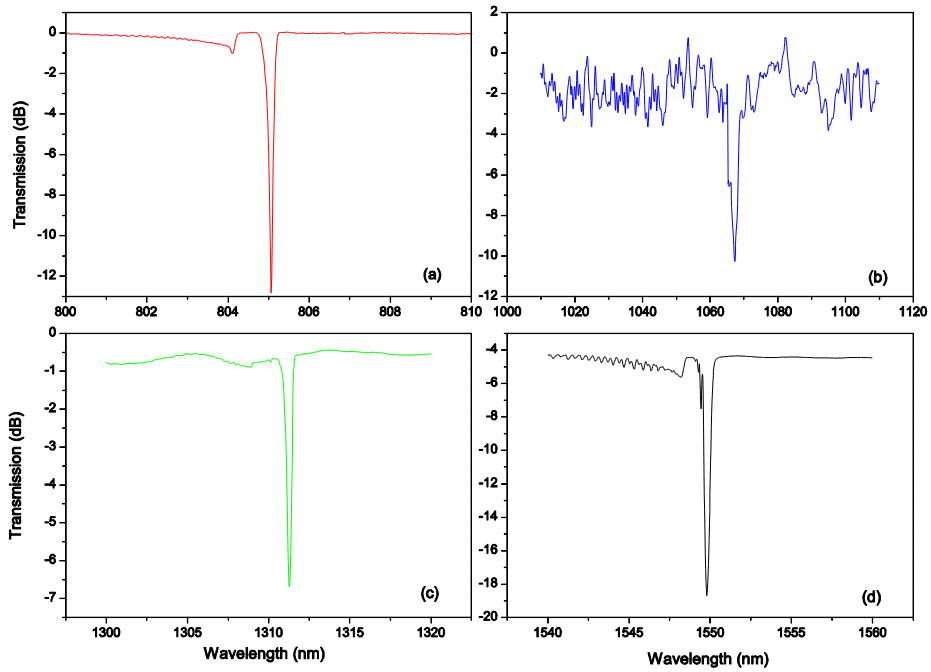

Figure 3.4 Transmission spectra of FBGs UV-inscribed in SMF by holographic method with designed wavelengths in four ranges: (a) 800 nm, (b) 1060 nm, (c) 1310 nm, and (d) 1550 nm.

b. Phase mask inscription technique

The phase mask technique was first demonstrated by Hill [25] and Anderson et al. [83] in 1993. Although this method is just for fixed wavelength grating fabrication, it is widely used as one of the most effective techniques for reproducible FBG inscription. The phase mask is a corrugated surface-relief grating etched in a fused silica plate. With UV beam at normal incidence, the radiation is diffracted into several orders, m=±1, ±2….. The phase masks have been optimized to suppress the light diffraction energy in 0 order and maximize diffraction efficiency in each of the

±1 diffracted orders. As shown in Figure 3.5, an interference pattern is produced by the superposition of ±1 orders diffracted beams, which can be used for writing FBGs.

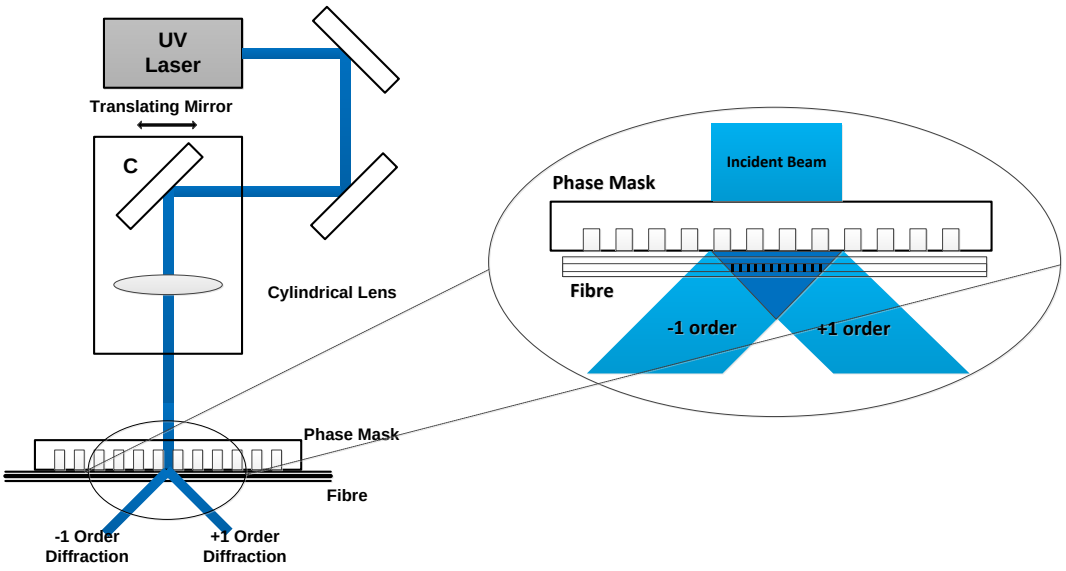

Figure 3.5 A schematic experimental arrangements for fabricating complex structure gratings using the UV beam scanning across a phase mask.

Figure 3.5 also shows the experimental arrangement of the phase-mask fibre grating fabrication system in our research group lab. The UV beam is focused by a cylindrical lens (which transversely-mounted on a PC-controlled translation stage) through the phase mask which is placed in close proximity to the fibre. With the movement of the mirror mounted on the translation stage, the UV beam can be scanned along the fibre length to produce the grating structure in the core of fibre.

When a phase mask is used, the Bragg wavelength is fixed by the phase mask period. In other words, FBGs with different wavelengths are inscribed by different phase masks. The structure and specifications of a multi-wavelength phase mask which been used to fabricate the FBGs of five 5 different wavelengths are shown in Figure 3.6.

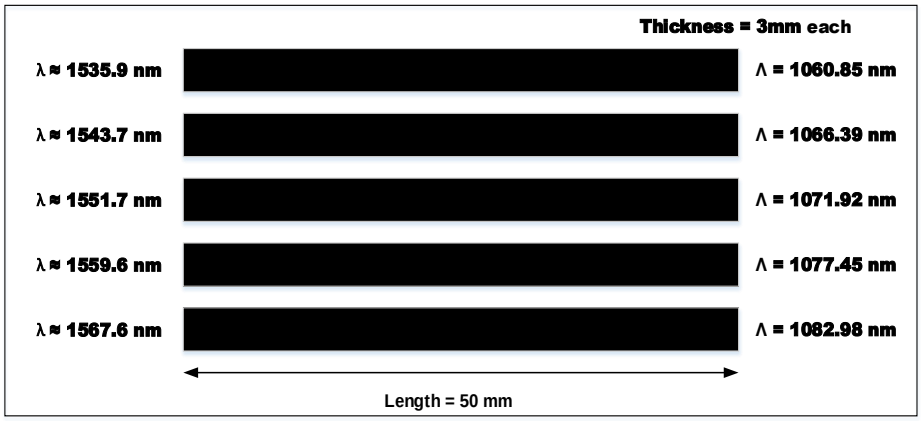

Figure 3.6 Schematic of phase mask structure with five pitch patterns.

From the figure we see this mask contains five mask lines with five different periods (1065.85nm, 1066.39nm, 1071.92nm, 1077.45nm and 1082.98nm) can be used to produce FBGs with responses at 1535.9nm, 1543.7nm, 1551.7nm, 1559.6nm and 1567.6nm, respectively. Five FBGs were UV-inscribed using this phase mask and the transmission spectra are shown in Figure 3.7.

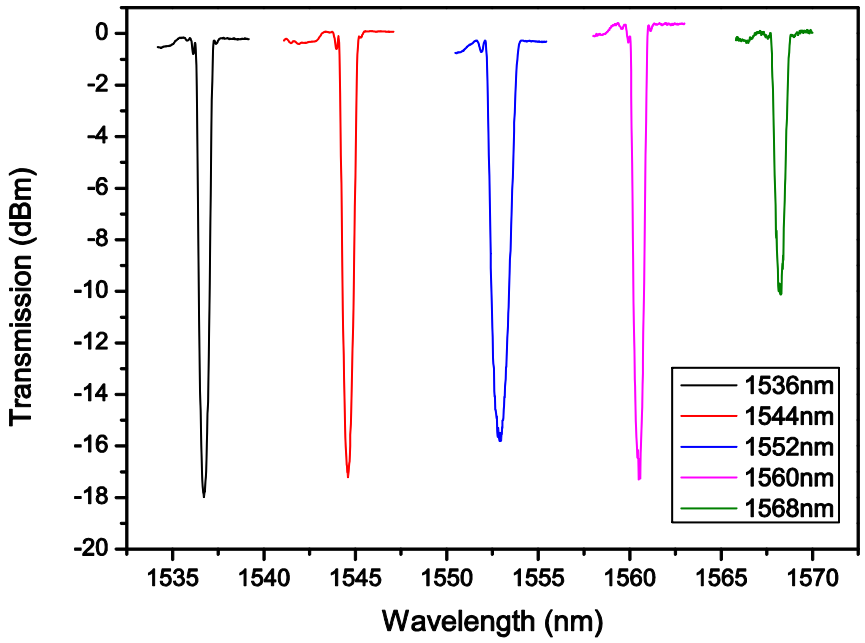

Figure 3.7 Transmission spectra of FBGs with five different wavelengths (1535.9nm to 1567.6nm) fabricated by a phase mask with multiple lines.

In order to enhance photosensitivity in silica optical fibre, fibre samples can be hydrogen-loaded by storing them into hydrogen gas chamber at temperatures 20-70°C and pressure 150atm typically, which results in diffusion of hydrogen molecules into the fibre core. After being UV

exposed, hydrogen will diffuse out of the fibre. This leads to a shift with central wavelength of a UV-written grating. A thermal annealing process (at 80°C for 48 hours) is implemented to out-gas hydrogen from the fibre quickly and to stabilize the grating properties. Figure 3.8 shows the spectra of an FBG with Bragg wavelength at 1550nm written in an SMF-28 telecom fibre before and after annealing. We can see that it is about 0.5nm wavelength blue shift when returned to room temperature compared to before annealing.

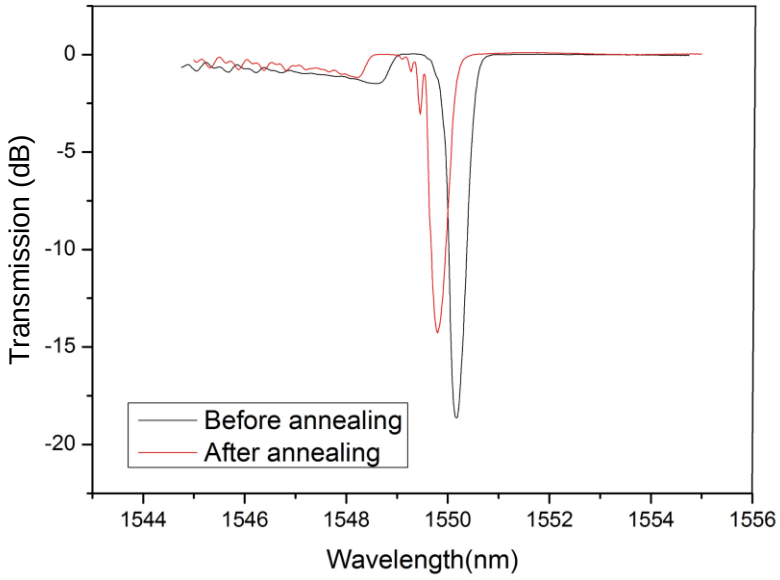

Figure 3.8 Spectra of the FBG inscribed in SMF-28 fibre before and after the annealing.

3.2.2 FBG sensing characteristics

The effective refractive index (RI) and the period space between each grating plane will be affected by temperature and strain changes. The FBG central wavelength depends on effective RI of the core and the periodicity of the grating. So we can deduce that the FBG centre wavelength shifts due to temperature and strain changes. Equation 3.1 gives the relationship between Bragg wavelength shift and strain and temperature changes.

Equation 3.1 $$\Delta\lambda_B = 2\left(\Lambda\frac{\partial n_{eff}}{\partial T} + n_{eff}\frac{\partial\Lambda}{\partial T}\right)\Delta T + 2\left(\Lambda\frac{\partial n_{eff}}{\partial l} + n_{eff}\frac{\partial\Lambda}{\partial l}\right)\Delta l$$

The first term in above equation represents the thermal effect on an FBG. This corresponds to the thermal expansion induced grating space change and the thermo-optical effect induced change in the effective RI. The first term also can be written as:

Equation 3.2 $$\Delta\lambda_B = \lambda_B(\alpha_\Lambda + \alpha_n)\Delta T$$

Where $\alpha_\Lambda = (1/\Lambda)(\partial\Lambda/\partial T)$ is the fibre thermal expansion coefficient; $\alpha_\Lambda = (1/n_{eff})(\partial n_{eff}/\partial T)$ is the thermo-optical coefficient.

In the thermal sensing evaluation experiment, three FBGs with different wavelengths, which were fabricated by the two-beam holographic technique, were investigated. The temperature sensing experimental set up is shown in Figure 3.9. The grating region, which is usually around 10mm long, of the fibre is placed in the heating device controlled by a temperature controller (Light wave LDT-5910B). The temperature can be varied from 0°C to 80°C at a step of 5°C. For each temperature, the FBG's resonance is measured and recorded by the Optical Spectrum Analyser (OSA).

Figure 3.9 Experimental setup for FBG thermal characterisation.

From Figure 3.10, it can be seen that the three FBGs with responses in three different wavelength ranges exhibit different thermal sensitivities. Figure 3.10(a) shows the thermal response for the 800nm FBG, giving a temperature sensitivity of 6.30 ± 0.07 pm/^{0}C (in temperature increasing cycle) and 6.2 ± 0.1 pm/^{0}C (in temperature decreasing cycle), respectively. In Figure 3.10 (b) and (c), we see the temperature sensitivities are 9.90 ± 0.07 pm/°C (increasing cycle) and 10.1 ± 0.2 pm/°C (decreasing cycle) and 12.60 ± 0.06 pm/°C (increasing cycle) and 12.5 ± 0.3 pm/°C (decreasing cycle) for the FBGs with the central wavelengths in 1310nm and 1550nm ranges, respectively. Extraordinarily, the temperature sensitivity of the FBG with the central wavelength in 1550nm (12.60 ± 0.06 pm/°C) is twice as that of only 6.2 ±0.1 pm/°C at the 800nm FBG. These results clearly indicate that the longer the FBG central wavelength is, the higher the temperature sensitivity is.

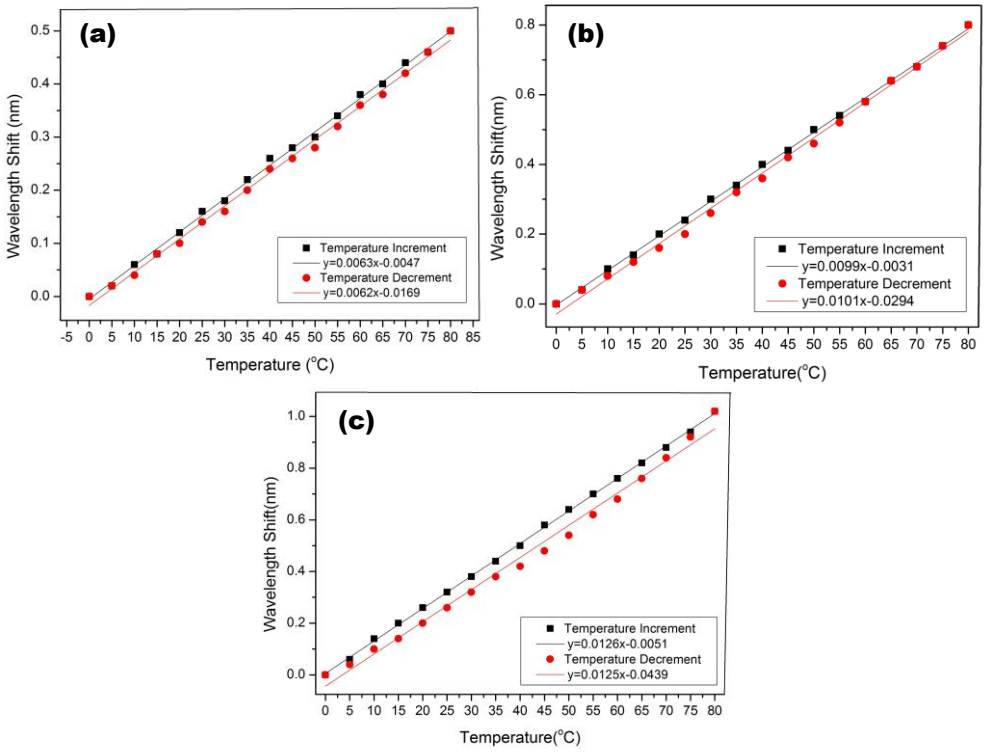

Figure 3.10 FBG thermal responses with designed wavelengths at three different ranges: (a) 800 nm, (b) 1310 nm, and (c) 1550 nm.

The second term in Equation 3.1 represents the strain effect on an FBG. The strain expansion leads to the change of the effective refractive index and the period of the FBG, resulting in the wavelength shift which can be written as

Equation 3.3 $$\Delta\lambda_B = \lambda_B(1-p_e)\varepsilon_z$$

where p_e is an effective strain-optic constant defined as

Equation 3.4 $$p_e = \frac{n_{eff}^2}{2}[p_{12} - v(p_{11} + p_{12})]$$

Where P_{11} and P_{12} are components of strain-optic tensor, v is the Poisson's ratio.

Figure 3.11 Experimental setup for FBG strain characterization

The experimental setup for FBG strain characterization is shown in Figure. 3. 11. The FBG was straightly clamped on two 3D translation stages separated at a distance of 40cm. The varied strain was supplied to the grating by moving the right-hand stage from 0mm to 0.35mm at a step of

0.05mm, which give a strain range of 750με. Figure 3.12 presents the strain responses of the three FBGs with different Bragg wavelengths. From the figures, it can be seen that the strain sensitivities are 0.40 ± 0.01 pm/με, 1.00 ± 0.06 pm/με and 1.10 ± 0.06 pm/με for the FBGs with the central wavelength at 800 nm, 1310 nm, and 1550 nm, respectively, which demonstrates that the FBG with the Bragg resonance in longer wavelength range also exhibits higher strain sensitivity than that in shorter wavelength range. It is in good agreement with earlier report in [89].

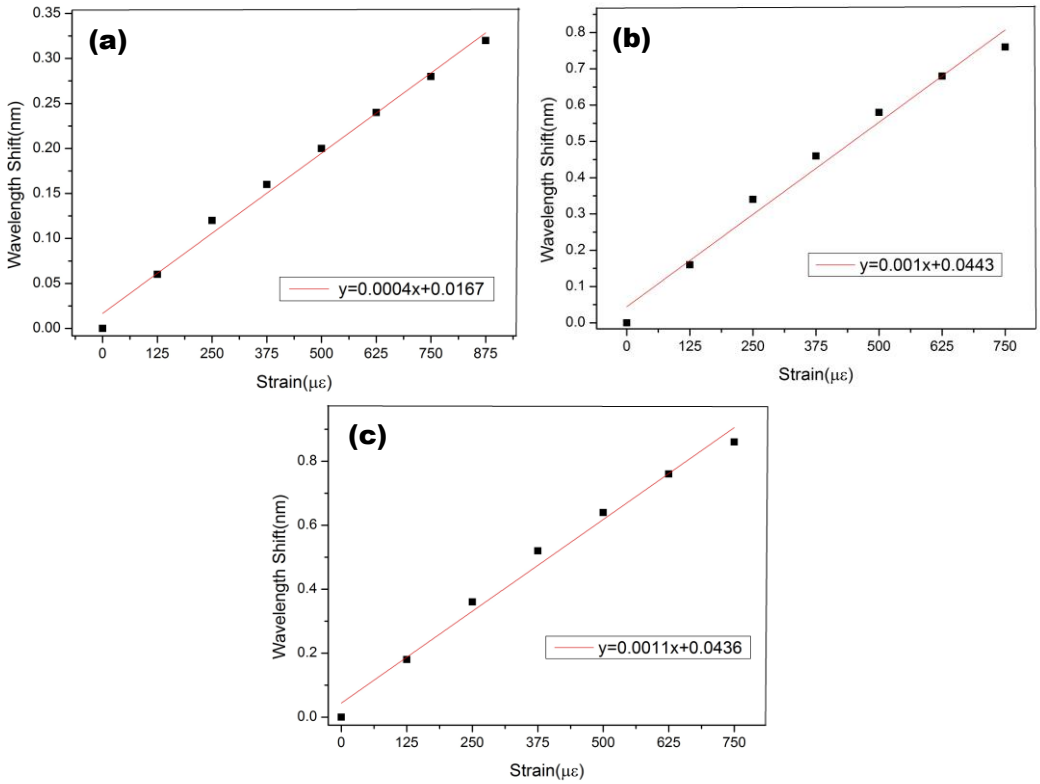

Figure 3.12 FBG strain responses with designed wavelengths at: (a) 800nm, (b) 1310nm and (c) 1550nm.

3.3 Fibre Bragg gratings with chirped structure

Chirp usually refers to the phenomenon of a frequency change. If the period of the fibre Bragg grating varies monotonically along the grating length direction, its Bragg response wavelength will be changed along the same direction resulting in a chirped structure. Thus, this kind of gratings known as chirped fibre Bragg grating (CFBG), which is illustrated schematically in

Figure 3.13. CFBG can be classified into two types by grating period change rate: linear and non-linear. So far, the CFBGs have been applied in a wide range of applications: optical fibre dispersion compensation [7], ultrashort optical pulse amplifier[97], coder (encoder) in optical code division multiple access (CDMA) system[98], time-delay component in phased array antenna [99, 100] and optical fibre sensor [101].

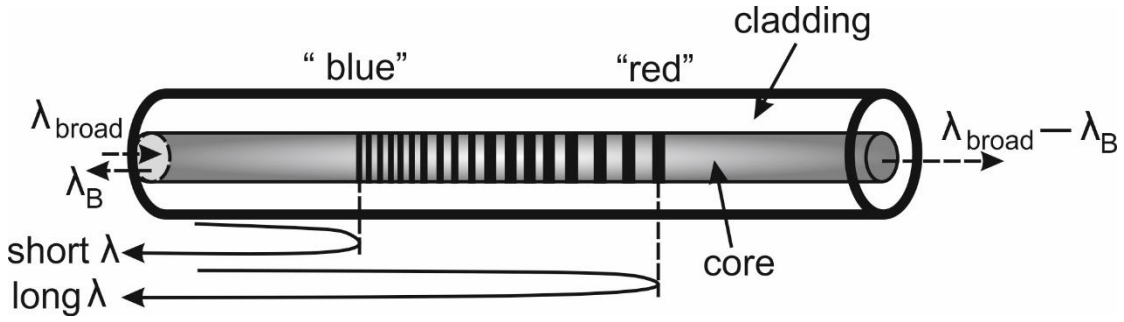

Figure 3.13 A schematic diagram of a chirped fibre Bragg grating.

The CFBG can be considered as either the grating period Λ or the refractive index of the fibre or both monotonically varying along the fibre length axis, as shown in Equation 3.5.

Equation 3.5 $$\lambda_B(z) = 2n_{eff}(z)\Lambda(z)$$

The CFBGs reported in this thesis are all linearly chirped in period as:

Equation 3.6 $$\Lambda(z) = \Lambda_0 + \Lambda_1 z$$

Where Λ_0 is the initial period and Λ_1 is the linear variation rate along the length of the grating. However, one may consider a CFBG structure consists of a group of small length uniform Bragg gratings increasing in period. The primary function of a CFBG is an in-fibre broad-band reflector. Normally, the chirp rate (Λ_1) of a linear CFBG is defined by bandwidth/grating-length.

The CFBGs discussed in this thesis are inscribed by using the phase mask technique. The phase masks for CFBG fabrication were purchased from Ibsen, which were designed for 244nm illumination. Wavelength with Figure 3.14 (a) shows the broad reflection spectrum of a 15mm long CFBG inscribed using a phase mask with period of 1069.32nm and chirped rate of 1.2 nm/cm.

Figure 3.14(b) shows the group delay measured as a function of wavelength of this CFBG. The group delay of CFBG is the time required for the pulse of light to propagate along its length.

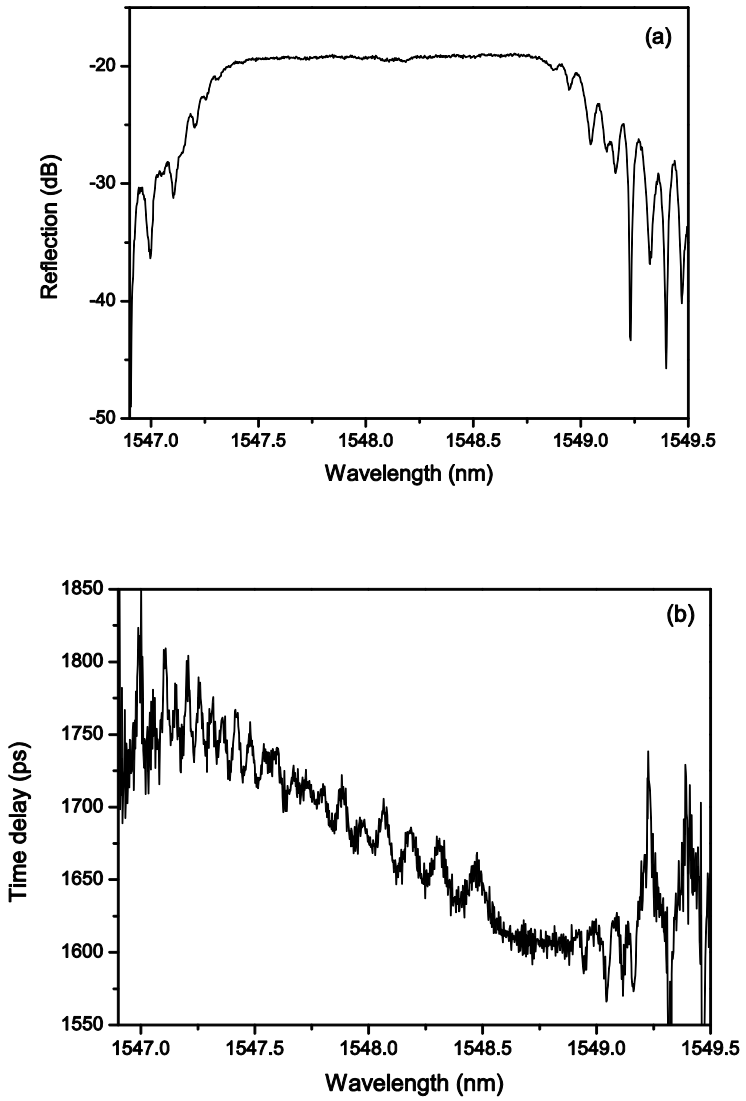

Figure 3.14 (a) Typical reflection spectrum of CFBG with 15mm grating length, (b) Time delay spectrum.

From Figure 3.14 (b), we found that the time delay curve exhibits strong fluctuations in the reflection band, which is caused by the FP effect from both of grating ends. The group delay ripple are critical in determining the ultimate systems performance of CFBG [102]. They can manifest in inter-symbol interference, and result in variations in Bit error rate (BER) across the grating spectrum, which may be eliminated by applying for an apodisation function to the chirped structure [103]. The typical technique used to produce an apodisation profile is by introducing a

time dependent phase shift during fabrication, using a periodical triangle wave to dither the phase mask to erase the grating fringes partly or completely.

3.4 Optical fibre gratings inscribed in novel fibres

3.4.1 Inscription of FBG on metal coated fibres

The optical gratings have been requested to be fabricated on different novel fibres, depending on applications. As mentioned previously, FBG sensors have been developed for application in monitoring the health of large-scale civil and industrial structures, such as skyscrapers, bridges, machines and vehicles. FBG sensing techniques have also brought the technical challenges in embedding and installation of the sensors. This is because the normal fibre buffer (jacket) is made of polymer, which causes problems when the sensors are sealed in concrete and metal structures. With the development of fibre coating techniques, metal coated fibres have become available and may solve these problems. Moreover, with metal buffer protection, FBG sensors can operate at high temperature and in harsh environment.

In collaboration with Strathclyde University and in order to develop fibre-optic sensors, FBGs were UV-inscribed in metal coated fibre - IVG Cu/Al 1300nm Fibre - whose structure is shown in Figure 3.15.

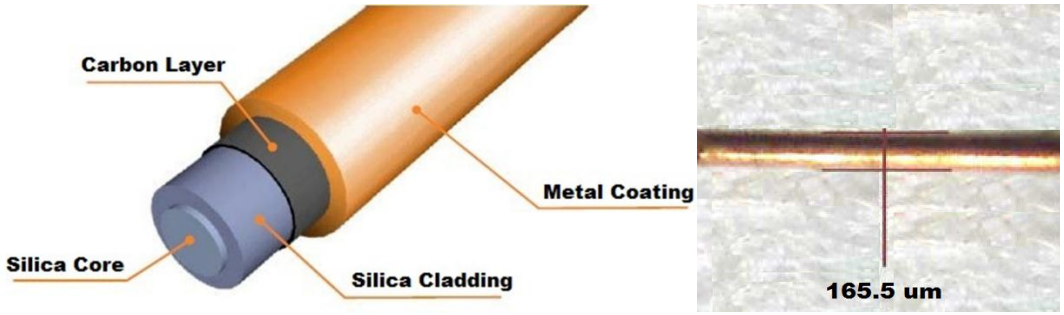

Figure 3.15 Left: Schematic of metal coated fibre structure; Right: Microscope view of metal coated fibre.

This metal coated fibre (IVG Cu/Al 1300nm) has a core diameter of 6.5um and cladding diameter of 165.5um. There are four layers in the metal coated fibre: silica core, silica cladding, carbon layer and metal coating. Here, the additional inner carbon layer is used to improve metal-to-silica adhesion (< 1μm thick).

We inscribed the FBGs in metal-coated fibre by using phase mask fabrication technique. As discussed earlier in this chapter, all the fabrication methods are side-exposing the fibre. Therefore, before the UV exposure, the fibre jacket (buffer) of about 1cm length has to be removed. For removing the metal coating, the fibre was immersed into 70% nitric acid (HNO3) that filled in a glass dish for a period up to 5 minutes. The inner carbon layer can be either burned off with the splicer arc in "cleaning" mode or dissolved in warm sodium hydroxide (NaOH), which takes several hours.

In order to increase the photosensitivity, the metal coated fibre with 1cm coating removed was hydrogen loaded at normal condition. Then the fibre was mounted in the phase mask or two-beam holographic system for FBG fabrication. Figure 3.16 shows the typical transmission spectrum for the FBGs UV-inscribed in the metal coated fibre, which is similar to the FBGs made in normal fibre.

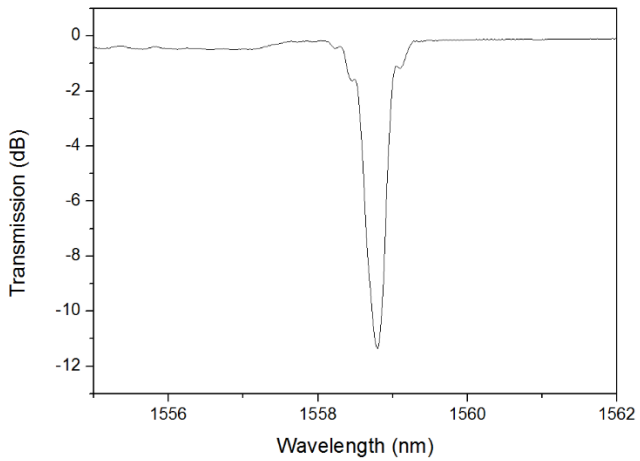

Figure 3.16 The typical transmission spectrum for the FBGs UV-inscribed in the metal coated fibre

The fabricated FBGs in metal coated fibre were evaluated for temperature sensing for two temperature ranges: low temperature range (0 - 80°C) and high temperature range (120 - 900°C). For sensing in low temperature range, the experiment setup is the same as FBG in normal fibre which is showed in Figure 3.9. For high temperature sensing, a high temperature chamber furnace was used and the experiment arrangement is shown in Figure 3.17.

Figure 3.17 High temperature sensing experimental arrangement for FBG in metal coated fibre.

A broadband light source (HP 83437A) was used as the signal source, and the optical spectra of the FBG were captured by an OSA (Yokogawa AQ6373). The FBG was positioned in a laboratory chamber furnace (Carbolite CWF 1100). To avoid the effects of vibration caused by hot air flow, the FBG was fixed in the chamber furnace. The FBG was heated from 120°C to 300°C in steps of 30°C and from 300°C to 900°C in steps of 50°C using the temperature control panel of chamber.

For the temperature sensing, FBGs UV-inscribed in metal coated fibre have a typical sensitivity of 11.6 pm/°C in the low temperature range (0-80°C), as shown in Figure 3.18 (a), and 13.8 pm/°C in high temperature range (120-900°C), as shown in Figure 3.18 (b). In the high temperature range, the sensitivity increases and the response become slightly nonlinear with increasing temperature that it is in good agreement with earlier report in [89]. The reason for this phenomenon may be due to the coefficient of thermal expansion changing for different temperature ranges. Normally, we regard the fibre thermal expansion coefficient is a constant, which is true for a small

temperature range. However, we can't ignore the effect caused by the dependence of thermal expansion coefficient on temperature for a wide range temperature sensing.

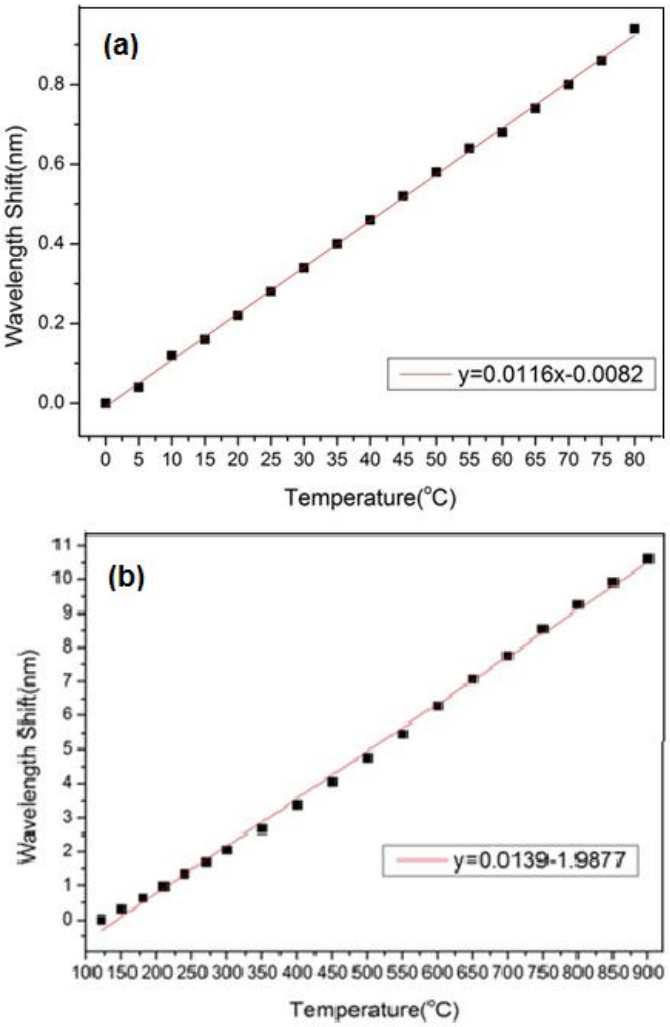

Figure 3.18 The thermal response of the FBG UV-inscribed in metal coated fibre in: (a) low temperature range (0-80°C) and (b) high temperature range (100-900°C).

The strain response of the FBG in metal coated fibre was also experimentally evaluated and the results are shown in Figure 3.20, giving a strain sensitivity of 1.2pm/με, which is slightly different to the FBGs in normal fibre that discussed in earlier chapter. This is because the effective strain-optic constant is variated between the different type fibres.

The FBGs UV-inscribed in metal fibre were supplied to Strathclyde University and have been used in high stress monitoring of pre-stressing tendons in nuclear concrete vessels and the results are published in Journal of Nuclear Engineering and Design [104].

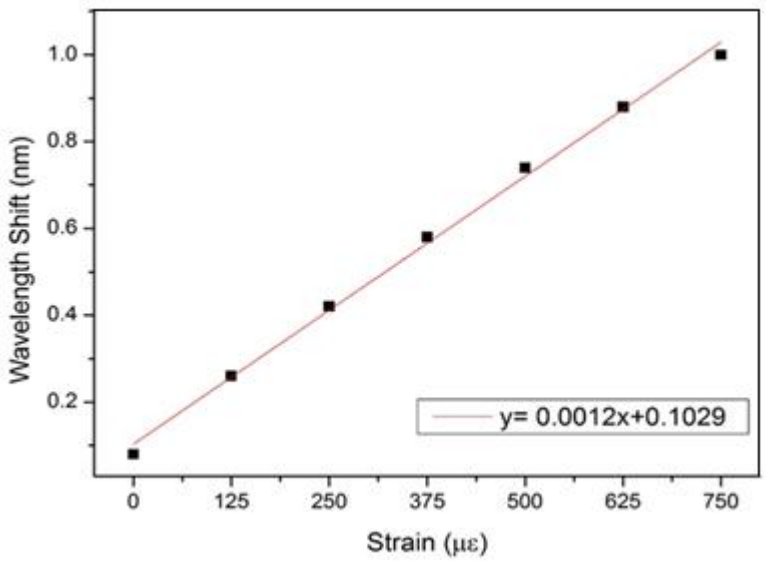

Figure 3.19 The strain response of the FBG UV-inscribed in metal coated fibre.

3.4.2 Inscription of FBGs and CFBGs on large mode field fibre

In a high power fibre laser system, the damage threshold of fibre material (around 5 W/μm^2) limits the highest output power. To increase output power, large mode field fibre may be used. For 1kW output power level, the radius of core is at least around 8μm. Conventionally, the optical fibre gratings are employed as reflectors (FBGs), dispersion compensation component (CFBGs) and polarised device (45°-TFGs) in the fibre laser system. In this section we will discuss the optical fibre gratings fabrication on the large mode field fibre.

In this section, the FBGs and CFBGs inscribed on large mode field fibres will be discussed. The large mode field fibre supplied by JK Lasers was investigated for inscription of FBG and CFBG structures. This fibre can handle high optical power of 1.5kW/μm^2 and its detailed information of fibre parameters is listed in Table 3. 1.

Fibre parameter	Value
Core diameter (micron)	20 ± 2
Core NA	0.065 ± 0.005
Clad diameter (micron)	390 ± 2
Clad NA	0.46 ± 0.02
Coating diameter (micron)	550 ± 10

Table 3.1 Specific parameters of the large mode field fibre for grating inscription.

According the table 3.1, the large mode field fibre has 20μm core and 390μm cladding. The cross section of fibre was observed under a microscope (shown in Figure 3.20). As it shown, the diameters of core and cladding are measured 20.43μm and 396.37μm, which are in good agreement with the values given in the data sheet.

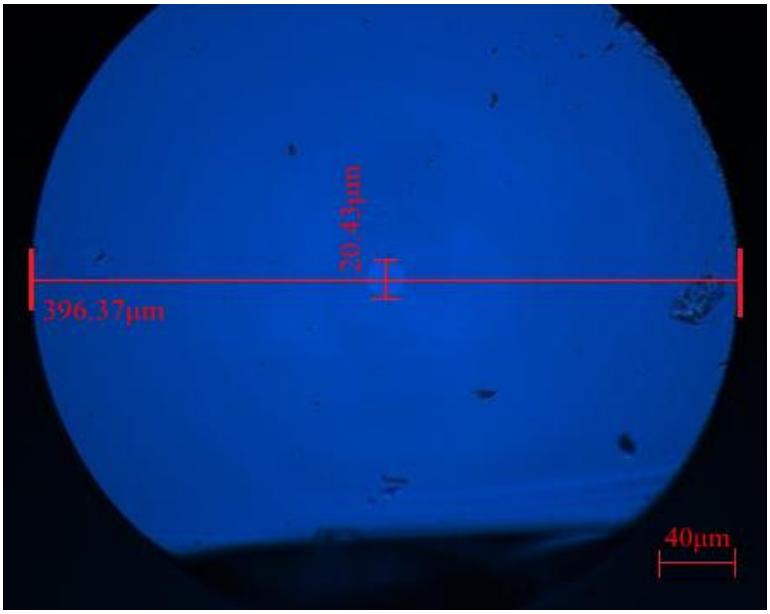

Figure 3.20 The cross section of fibre with 20.43μm diameter core and 396.37μm diameter cladding.

The numerical aperture of fibre given in the data sheet is 0.065. When the operation wavelength is at 1060nm, the normalized frequency V can be calculated out by equation as follow:

Equation 3.7 $$V = \frac{2\pi}{\lambda} \bullet a \bullet NA$$

Where α is the radius of core, λ is the operation wavelength and NA is the numerical aperture of the fibre. The normalized frequency V of this fibre is around 4.4. According to the theory of optical waveguide, when v is large number, the mode capacity could be roughly evaluated as $V^2/2=10$. The mode field diameter (MFD) for 20/390 fibre operating at 1060nm wavelength is 16.511μm, which could be simulated out by Matlab as shown in Figure 3.21:

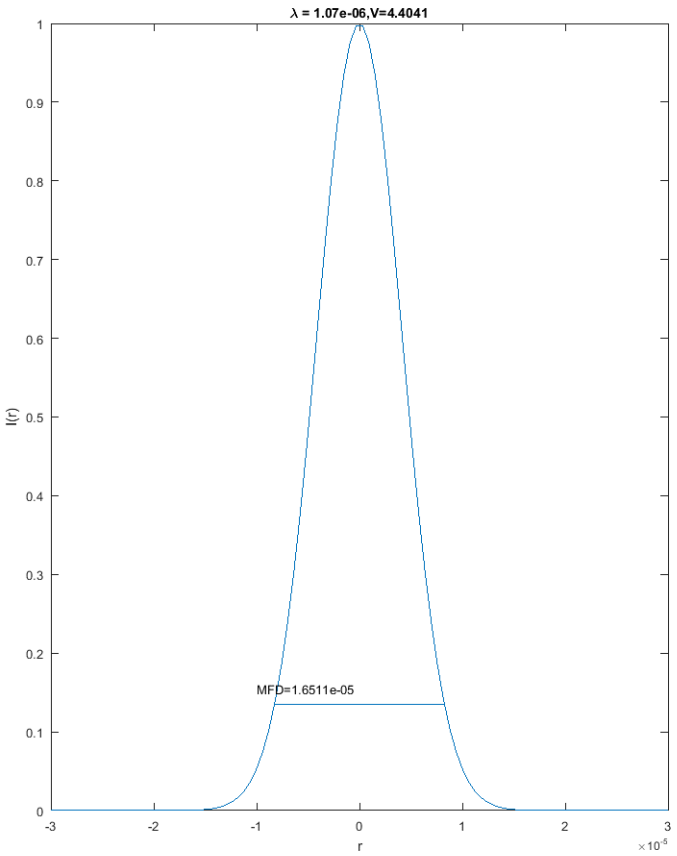

Figure 3.21 Simulation result of mode field diameter (MFD) for 20/390 fibre operating at 1060nm.

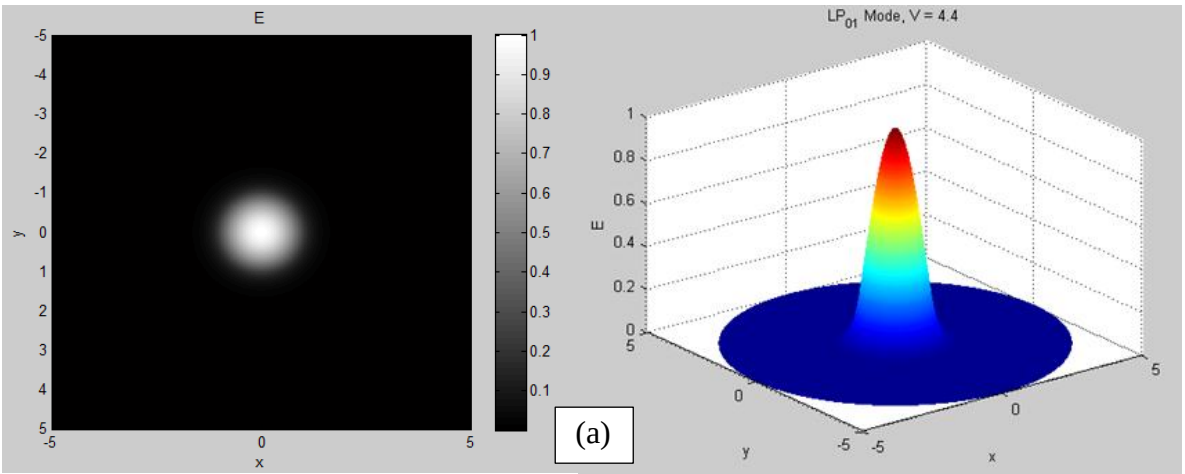

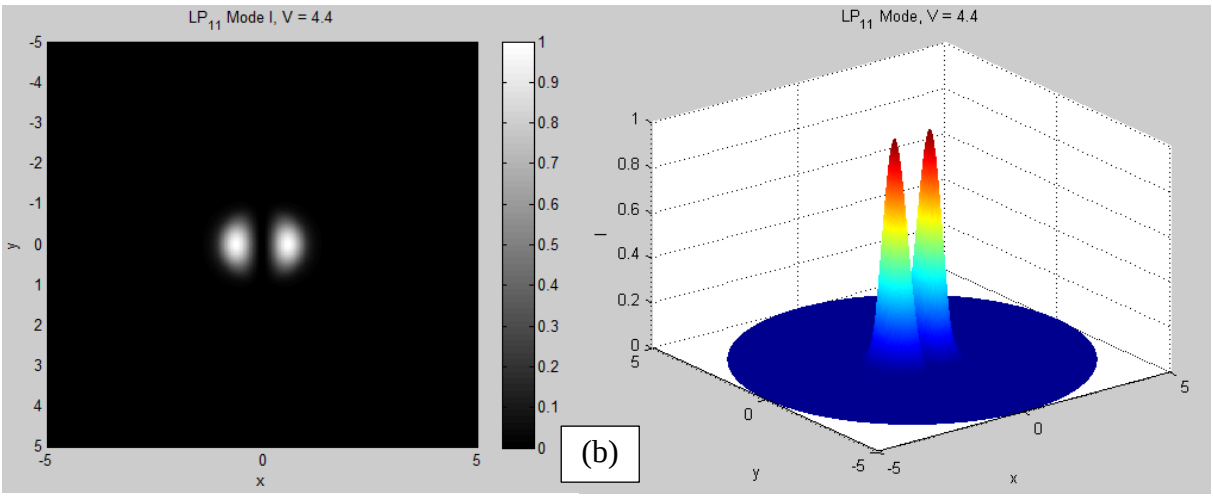

Figure 3.22 Matlab simulated near field patterns of 20/390 fibre: (a) LP01 mode, (b) LP11 mode.

A designed chirped phase mask was purchased for CFBGs in this large mode field fibre. We have first tested the phase mask, which is designed for 244nm UV laser by Ibsen Photonics. The specifications of the phase mask are: period of mask 736.94nm and chirped rate 0.8nm/cm. Figure 3.23 shows the image of the UV diffraction pattern of the phase mask with and without optical fibre. It can be seen from Figure 3.24, 0 order diffraction pattern is noticeably weak.

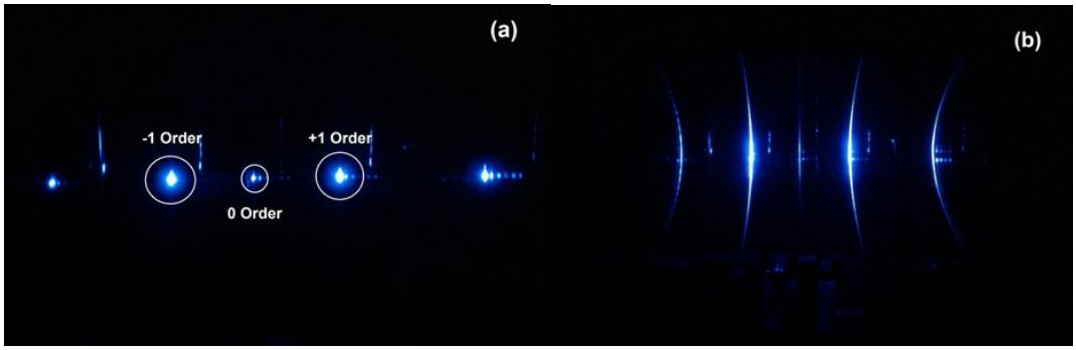

Figure 3.23 Image of UV diffraction pattern by phase mask without (a) and with (b) optical fibre.

We also calculated the diffraction efficiency of 0 and ±1 order diffraction beams by measuring the intensity of diffraction beam using a power meter. The equation of diffraction efficiency is listed as following:

$$\textbf{Diffraction Efficiency} = \frac{\textbf{Diffracted power}}{\textbf{Incident UV beam power}}$$

The measured diffraction efficiencies of 0 and ±1 order of the chirped phase mask are listed in table 3.2.

Diffraction Efficiency (%)	Diffraction Efficiency (%)	Diffraction Efficiency (%)
-1 order	0 order	+1 order
33.40 ± 0.01	3.34 ± 0.01	32.40 ±0.01

Table 3.2 Measured phase mask diffraction efficiency.

From table 3.2 we can see the 0-order suppression (only 3.34 ± 0.01 % diffraction efficiency) is reasonable, because the 0-order diffraction of phase mask is usually suppressed to less than 4% diffraction efficiency.

We firstly inscribed a 1060nm FBG in the hydrogen loaded 20/390 fibre by using a 20mm long phase mask with 742nm pitch period from Aston University. As the 20/390 fibre core diameter is around 20μm, which is more than double of the core size of standard single mode fibre (8μm), a butt-coupling measurement technique was required to characterize the spectral profiles of the FBG in this large mode field fibre. Figure 3.24 shows the schematic diagram of the butt-coupling system we used in the experiment.

Figure 3.24 Schematic diagram of butt-coupling system for the measurement of FBGs in 20/390 fibre.

The measured transmission spectrum of 1060nm FBG in 20/390 fibre is shown in Figure 3.25. In the figure, there are three peaks: the strongest one is fundamental mode LP01, which shows a 9dB (90%) reflectivity, and the other two relatively weak peaks are LP11 and LP21.

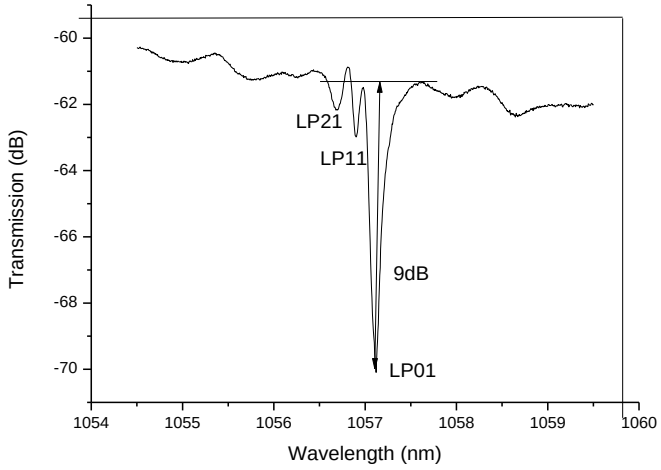

Figure 3.25 The transmission spectrum of the FBG at 1057nm in 20/390 fibre.

We have fabricated the FBG with chirped structure on 20/390 fibre by using the chirped phase mask. The transmission spectra of CFBG are measured using OSA at different resolutions (0.06nm and 0.5nm). From the Figure 3.26, it can be clearly seen that the reflectivity is increasing with reducing OSA resolution. Because the 20/390 fibre is not a single mode fibre, the most percentage of light is butt-coupled into the fibre fundamental mode, but there is still a part of light coupled into the high order modes, which will affect the measurement accuracy of FBG reflectivity of the fundamental mode. In 20/390 fibre, the power of light couple in is sum of the power of LP_{01}, LP_{11} and LP_{21}. If the P_{LP01} is 90% of P_{in} and the sum of P_{LP11} and P_{LP21} is 10% of $P_{in,}$ then we will only measure 10dB reflection of the multimode FBG, although the actual reflectivity is higher than 10dB. However, in the experiment, we noticed when we reduced the resolution of OSA, the percentage of the light measured in the fundamental mode was increased, as shown by the results in Figure 3.26.

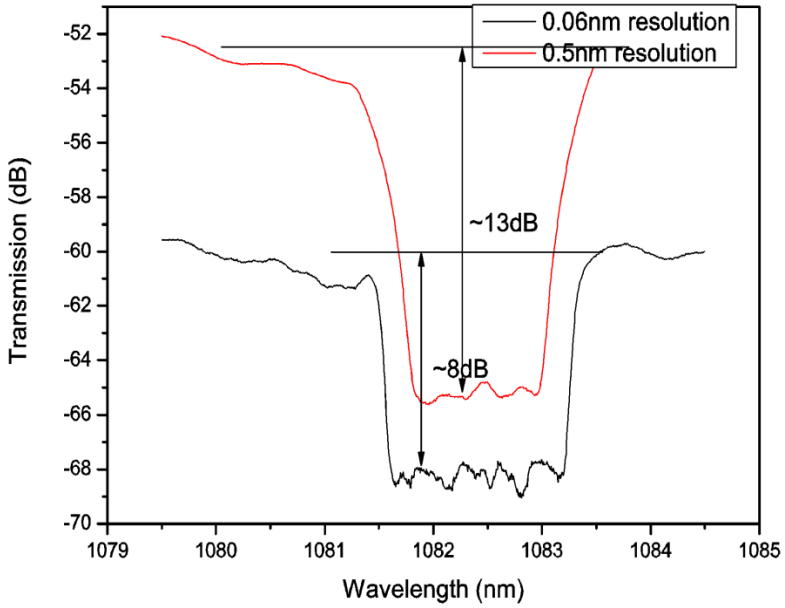

Figure 3.26 The reflection spectra of the CFBG in 20/390 fibre at 1060nm measured with different OSA resolutions.

3.5 UV-inscribed Long Period Grating

Long period gratings (LPGs), which can couple the light from the fundamental core mode to co-propagating cladding modes in the fibre, have attracted much attention for their applications in fibre-optic sensors and communication systems. They can be used as in–fibre, low–cost, band rejection filters. The multiple bands of LPG can be used to effectively separate strain and temperature effects acting simultaneously on the grating[105]. Additionally, because the light coupling involves cladding modes, LPGs are sensitive to the surrounding medium and thus can be employed as refractive index sensors[81]. The phase matching condition and mode coupling theory for LPGs are discussed in detail in Chapter 2.

3.5.1 Fabrication of long period gratings

The common fabrication method for LPGs is the point-by-point technique, which is usually used to fabricate LPGs with periods ranging from 10μm to 600μm. Due to the limit of the focused size

of the UV beam spot, it is difficult to write 1st order Bragg gratings which have normal periods of ~0.5μm at 1550nm by this method [25].

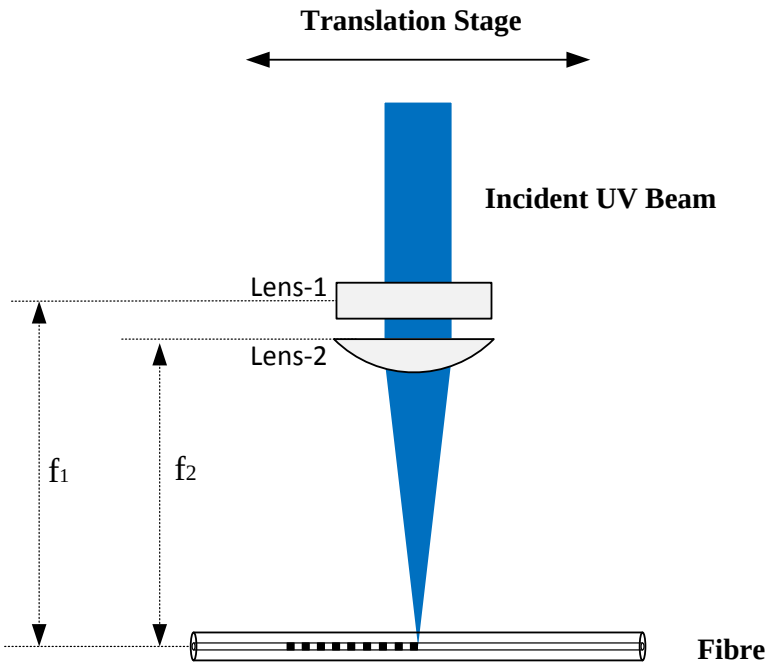

Figure 3.27 Schematic diagram of the point-by-point technique system employed in Aston University lab to UV-inscribe LPGs.

As shown in Figure 3.27, compared to the phase-mask inscription system, one more cylindrical lens is added to focus the writing beam along the fibre length. The PC controlled shutter modulates the laser power by switching on/off with a 50:50 duty cycle to achieve point by point print. This technique is widely used for LPG fabrication.

The LPGs used in the research presented in this report were fabricated by the same 244nm UV laser and the point-by-point inscription method. The optical fibre used for most LPG fabrication is single-mode standard telecom fibre (SMF-28e, Corning). Similar to FBG fabrication, the fibre samples were hydrogen loaded at temperatures (20-70℃) and pressure 150atm for 48 hours to enhance the fibre photosensitivity. All the fabricated LPGs were characterized using a broad band source, covering the wavelength range from 1250nm to 1650nm, and the HP86142A OSA. The LPGs were UV-inscribed with three different periods: 300μm, 350μm and 400μm for the investigation. The typical experimental spectra for these three periods LPGs are shown in Figure

3.28. It can be clearly seen from the figure that the 300µm and 350µm LPGs have 3 transmission loss bands in the wavelength range from 1250nm to 1650nm, whereas the 400µm LPG has shown 4 loss bands in the same range. By controlling the UV exposure time, the individual loss band will grow with certain strength. As shown in Figure 3.28, the strongest coupled mode in each structure has reached 20dB attenuation and other coupled cladding mode peaks are about 10dB.

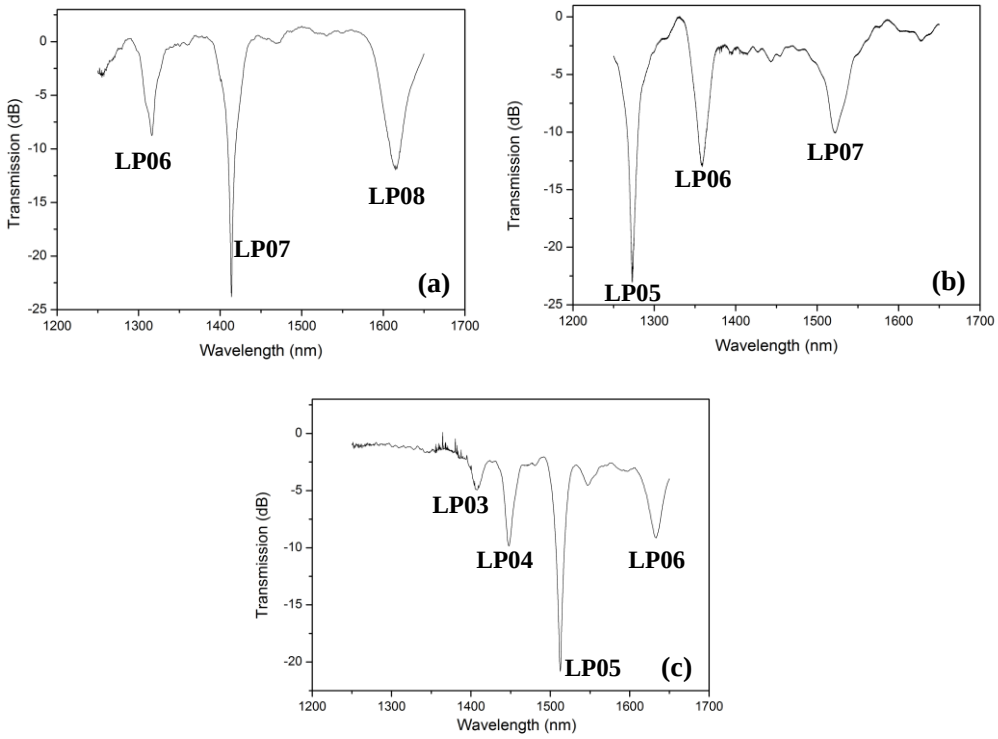

Figure 3.28 Transmission spectra for LPGs with different periods: (a) 300µm (b) 350µm and (c) 400µm.

To stabilize the structure, the LPGs have been annealed at 80°C for 48 hours to remove the residual molecular hydrogen in SMF-28 fibre, which was not completely used in the photochemical reaction during the grating fabrication. Figure 3.29 shows the comparison between the transmission spectra of the two LPGs of 300µm and 400µm periods before and after annealing.

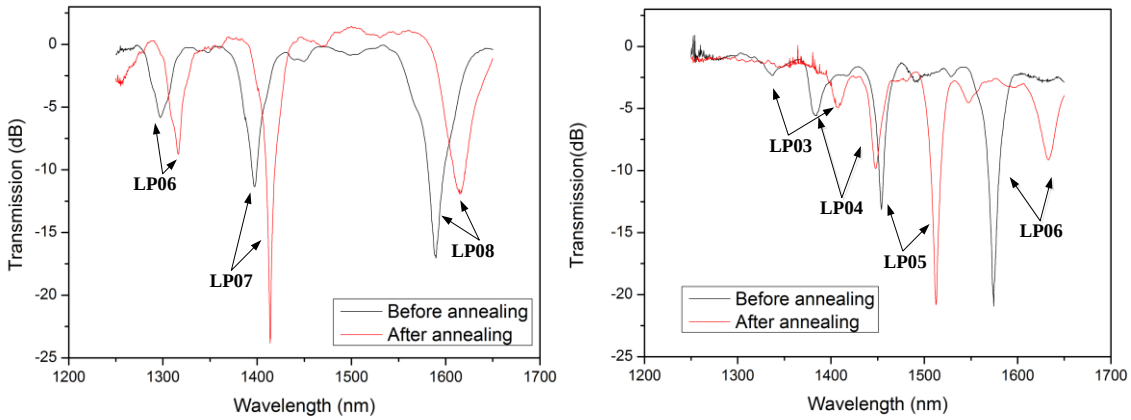

Figure 3.29 Spectrum of the annealing effect of LPGs inscribed in SMF-28 fibre left: 300 period; right: 400 period.

From the results shown in Figure 3.29 we can see it is about a 40nm wavelength red shift for 300μm period LPG and an 80nm wavelength red shift for 400μm period LPG before and after annealing treatment. Compared with FBGs (0.5nm), the wavelength shift of LPG is much more significant before and after annealing. From Equation 2.34, we can reason that the resonant wavelength is determined by the effective refractive index and grating period. Assuming the effective refractive index variation is the same; the resonant wavelength peaks for LPG will shift more than for FBG due to their grating periods in different order of magnitude, as has been discussed in Chapter 2. The peaks shift direction by temperature change depends on fibre dispersion factor γ and the temperature dependence of the waveguide dispersion Γ_{temp}. If the cladding mode order is less than or equal to 7, the value of fibre dispersion factor must be positive. So the peak shift direction only depends on the value of the temperature dependence of the waveguide dispersion ($m \leq 7$). The temperature dependence of the waveguide dispersion can be expressed as [106]

Equation 3.9
$$\Gamma_{temp} = \frac{\xi_{co} n_{co}^{eff} - \xi_{cl} n_{cl,m}^{eff}}{n_{co}^{eff} - n_{cl,m}^{eff}}$$

Where ξ_{co} and ζ_{cl} are the thermo-optic coefficients of the fibre core and cladding materials, respectively. In the hydrogenated fibre, the effective refractive index of core is always larger than the refractive index of cladding, so $n_{co}^{eff} - n_{cl,m}^{eff}$ will be always positive. After annealing, the

hydrogen gas will be released from the core. The core effective RI n_{co}^{eff} will decrease more sharply than the cladding effective RI $n_{cl,m}^{eff}$. Therefore, $\xi_{co} n_{co}^{eff} - \xi_{cl} n_{cl,m}^{eff}$ will be positive and the Γ_{temp} will be positive. Thus, all the LPG resonant wavelength peaks for mode order $m \leq 7$ will red-shift after annealing.

Figure 3.26 shows the attenuation of each peak of the LPG also changes before and after annealing. This is due to the change of the coupling coefficient as the UV-induced index modulation has been changed after the annealing. The transmission of the attenuation band of the LPG is governed by Equation 3.10 as follows [79]:

Equation 3.10 $$T_i = 1 - \sin^2(k_i L)$$

where L is the length of the LPG and k_i is the coupling coefficient for the ith cladding mode. According to Equation 3.10, the intensity of LPG resonant wavelength peak is determined by LPG length L and the coupling coefficient k_i. The LPG transmission dependence on grating length has been experimental evaluated by three UV-inscribed LPGs with the same period of 400μm, but different gating lengths: 10mm, 15mm and 20mm. Figure 3.27 shows the transmission spectra of these three LPGs and we can clearly see that the longest LPG has the strongest attenuation bands. More specifically, for LP06 band, the transmission loss is around 25dB for 20mm long LPG, whereas only 5dB for 10mm long LPG. Thus, it is possible to control the response wavelength and the strength of the LPG attenuation band by controlling the period, the length and UV exposure time.

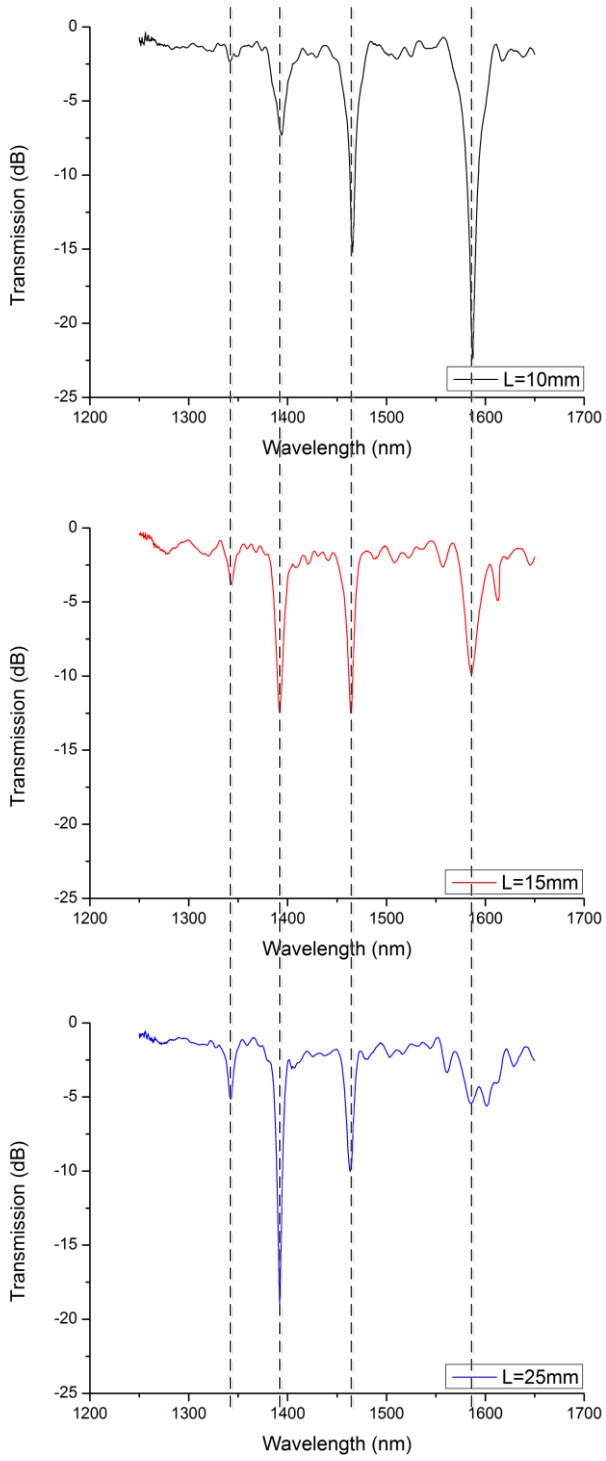

Figure 3.30 Spectra of three LPGs of 400 μm period with different lengths (10mm, 15mm and 20mm).

3.5.2 Thermal sensing property

One of the most important applications of LPGs is sensing for different physical conditions (temperature, strain and surrounding refractive index). In this section, the results on temperature sensing by LPGs are presented.

By differentiating the LPG phase-matching Equation 2.34 with temperature, we may obtain LPG temperature sensitivity expression[106]:

Equation 3.11 $$\frac{d\lambda_{res}}{dT} = \lambda_{res} \cdot \gamma \cdot (\alpha + \Gamma_{temp})$$

Where α is the thermal expansion coefficient of fibre, γ is waveguide dispersion as below;

Equation 3.12 $$\gamma = \frac{\frac{d\lambda_{res}}{d\Lambda}}{n_{co}^{eff} - n_{cl,m}^{eff}}$$

The LPG temperature sensing experiment was conducted using the set up shown in Figure 3.31, where the LPG is housed on a thermal Peltier with a temperature controller to vary the temperature from 0°C to 80°C.

Figure 3.31 Experimental setup for LPG thermal response evaluation using a Peltier with temperature controller.

To avoid the effects of strain and bending, the LPG was fixed on the metal heated plate on the Peltier by thermo stable tape.

Three LPGs with different periods (300μm, 350 μm and 400 μm) were employed as sensors for the temperature sensing experiment. During the temperature response study, all readings were taken with air as the surrounding medium. The initial temperature was selected at room temperature ($20^{\circ}C$). The LPG was then heated from $20^{\circ}C$ to $80^{\circ}C$ in step of $10^{\circ}C$ using the temperature controller device. We observed a spectral shift to longer wavelength with temperature increase.

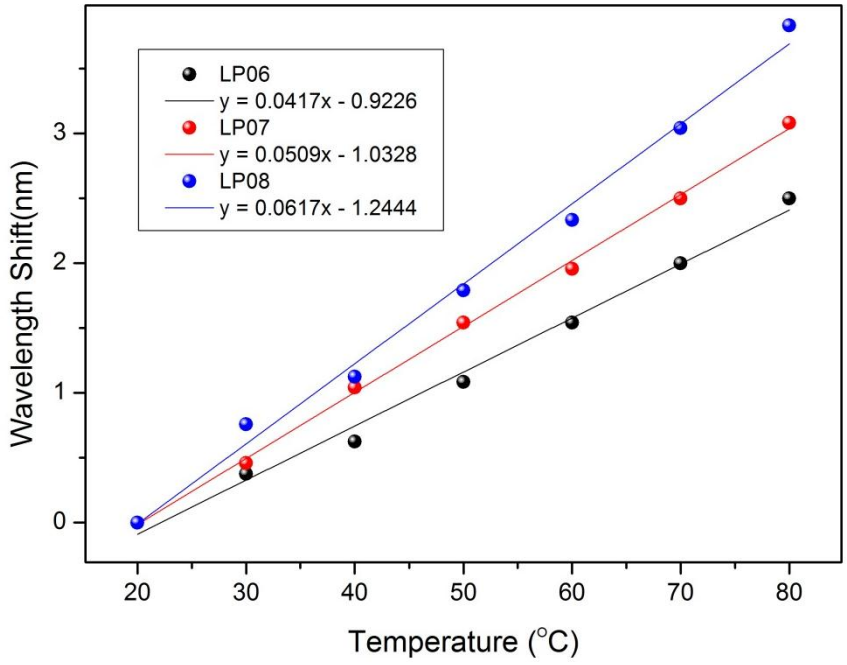

Figure 3.32 Thermal response of the LPG of 300 μm period for different order cladding modes: (LP06, LP07 and LP08).

The temperature response of 300 μm period LPG is plotted for LP06, LP07 and LP08 cladding modes, as shown in Figure 3.29. As seen in the figure, all three loss bands shift to the longer wavelength with increasing temperature. For temperature change from 20°C to 80°C, the temperature sensitivities for LP06, LP07 and LP08 are 41.7 pm/°C, 50.9 pm/°C and 61.7 pm/°C, respectively. Here we see the temperature sensitivity of LP08 mode is almost 50% higher than the LP06 mode.

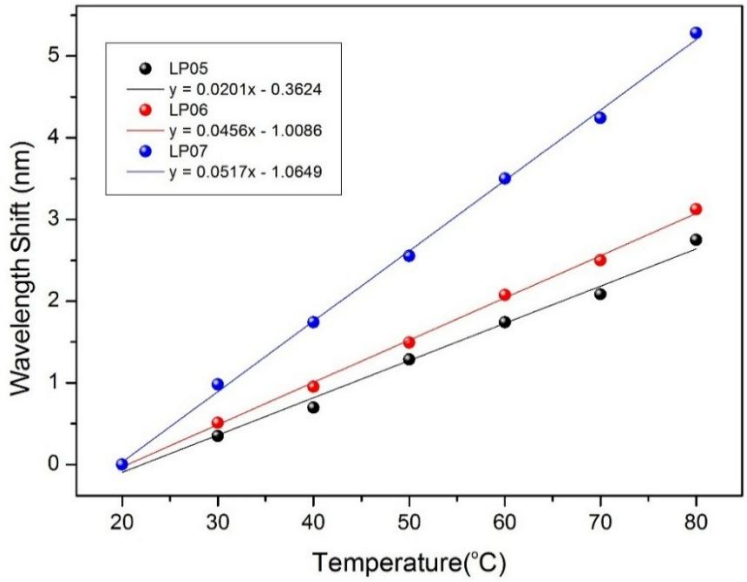

Figure 3.33 Thermal response of the LPG of 350 µm period for different order cladding modes: LP05, LP06 and LP07.

Figure 3.33 shows the temperature sensitivities of 350µm period LPG for different order cladding modes: LP05, LP06 and LP07, which are 20.1 pm/°C, 45.6 pm/°C and 51.7 pm /°C respectively.

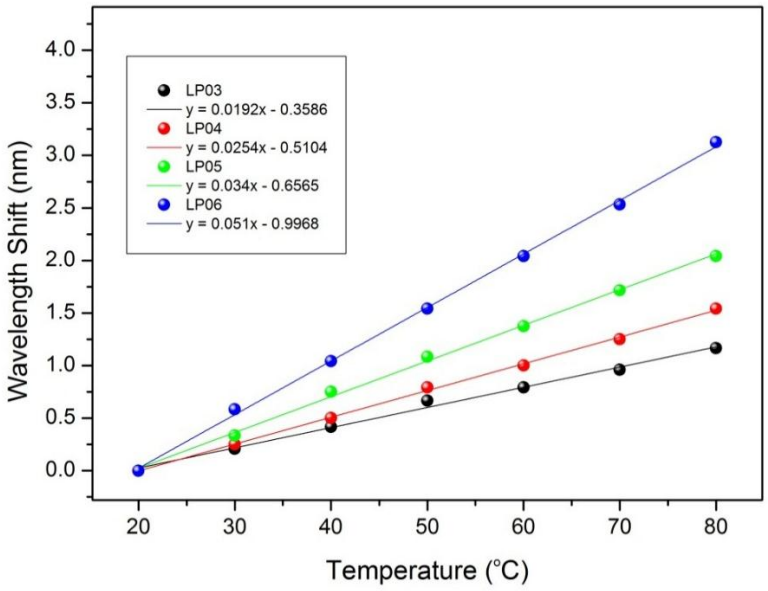

Figure 3.34 Thermal response of the LPG of 400µm period for different order cladding modes: LP03, LP04, LP05 and LP06.

Figure 3.34 plots the thermal response of the LPG of 400 μm period for the LP03, LP04, LP05 and LP06 cladding modes, showing temperature sensitivities of 19.2pm/°C, 25.4 pm/°C, 34

pm/°C and 51pm/°C, respectively. Here we also see the temperature sensitivity is higher for the cladding mode with higher order, but the difference is not as larger as shown for the LPG of 300μm period and 350μm period. For same cladding modes (LP 06), the thermal sensitivity is increasing by the period of LPG.

3.5.3 SRI sensor based on long period grating

In Chapter 2, the phase matching condition of LPG has been formulated through Equation 2.34. Re-writing equation 2.34, we can derive analytic expressions for the surrounding refractive index (SRI) sensitivity $d\lambda_{res}/dn_{sur}$ of the resonant wavelength as

Equation 3.13
$$\frac{d\lambda_{res}}{dn_{sur}} = \lambda_{res} \bullet \gamma \bullet \Gamma_{sur}$$

Where Γ_{sur} is the SRI dependence of the waveguide dispersion, which can be expressed as [106]:

Equation 3.14
$$\Gamma_{SRI} = -\frac{u_m{}^2 \lambda_{res}^3 n_{sur}}{8\pi r_{cl}^3 n_{cl} (n_{co}^{eff} - n_{cl,m}^{eff})(n_{cl}{}^2 - n_{sur}{}^2)^{3/2}}$$

Where u_m is the mth root of the zeroth-order Bessel function of the first kind, and r_{cl} and n_{cl} are the radius and refractive index of the fibre cladding, respectively.

To evaluate the SRI sensing capability of the LPGs, we applied a series of index oil (from Cargille laboratory) with different RIs from 1.305 to 1.444 to the gratings and measured their spectral evolution using the setup shown in Figure 3.35. To avoid wavelength shift induced by the bending and axial strain, the grating was straightly clamped on two stages set at the same height. The index oil was placed on a flat glass substrate, which can be raised by a vertical micrometre to submerge the grating into the index oil without imposing any force to the grating. Once the grating was surrounded by the index oil, the shift of wavelength was almost instantaneously observed on the optical spectrum analyser. After each index oil measurement, the grating was rinsed with methanol to remove the residual oil till the original spectrum in air was restored.

Figure 3.35 The experiment setup for surrounding refractive index sensing.

Figure 3.36 shows the comparison of SRI responses of different cladding modes of the 300μm period LPG. As is shown in the figure, each cladding mode has a different SRI sensing range. The maximum detectable SRI is 1.444, and the sensitivities for LP06 mode at 1220nm, LP07 mode at 1300nm and LP08 mode at 1450 nm are -8.26nm/RIU, -18.4nm/RIU and -56.3nm/RIU, respectively. As shown in Figure 3.33, the wavelength shift against SRI is not linear, but exponentially increasing with the SRI and reaching the maximum when approaching the cut-off mode index. Table 3.3 lists the measured SRI sensitivity of the three cladding modes of the 300μm period LPG at 1220nm, 1300nm and 1450nm.

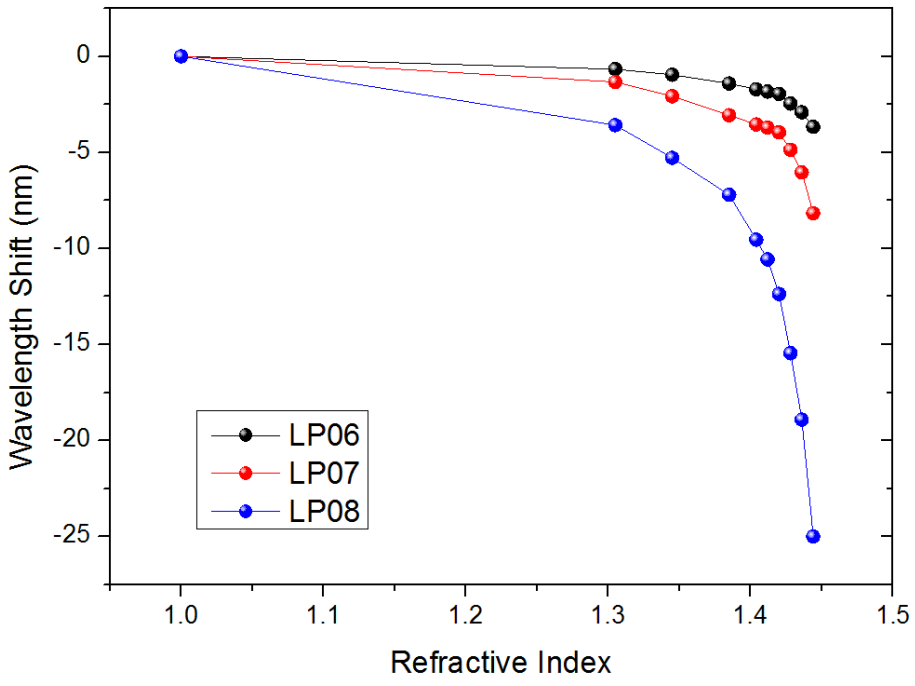

Figure 3.36 SRI responses of different cladding modes of 300μm period LPG

Resonance wavelength	Mode order	RI sensitivity
1220nm	LP06	-8.26nm/RIU
1300nm	LP07	-18.4nm/RIU
1450nm	LP08	-56.3nm/RIU

Table 3.3 The measured SRI sensitivities for different cladding modes of 300μm period LPG.

In the experiment, we also have evaluated SRI response for the other two LPGs (with periods of 350μm and 400μm. For comparison, Figure 3.37 plots the wavelength shift of the cladding resonance peaks at around 1500nm region against SRI for all three LPGs. From the measurement results, we can estimate the SRI sensitivities are -56.3 nm/RIU of peak LP08, -24.82nm/RIU of peak LP07 and -22.37 nm/RIU of peak LP06, for the three LPGs with period at 300μm, 350μm and 400μm, respectively. These results clearly indicate that at the same wavelength range, the higher order mode presents higher SRI sensitivity.

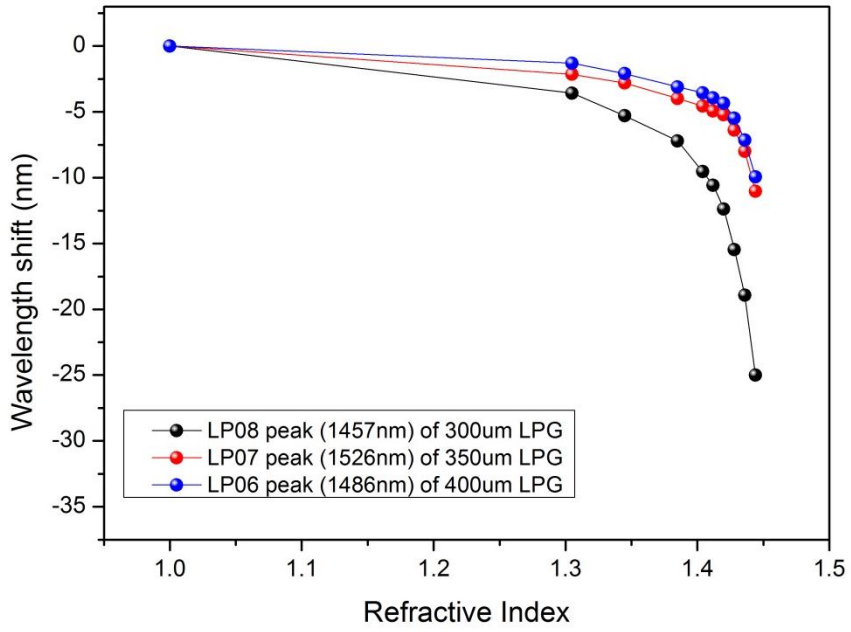

Figure 3.37 The SRI responses of the cladding modes (at around 1550nm) of LPGs with period 300μm, 350μm and 400μm for SRI range from 1 to 1.44.

According to the equation 3.14, the SRI sensitivity of an LPG could be improved by using small cladding radius fibre. To verify this, we inscribed 350μm LPG on SM1500 (4.2/80) fibre (from Fibercore company) with 40μm cladding radius and investigated their SRI sensitivities. The experiment setup and procedure for this experiment have already been introduced in earlier section. The transmission spectrum of 350μm LPG on SM1500 (4.2/80) fibre is plotted in figure 3.38, and we only see one resonance peak in 1200nm to 1600nm region.

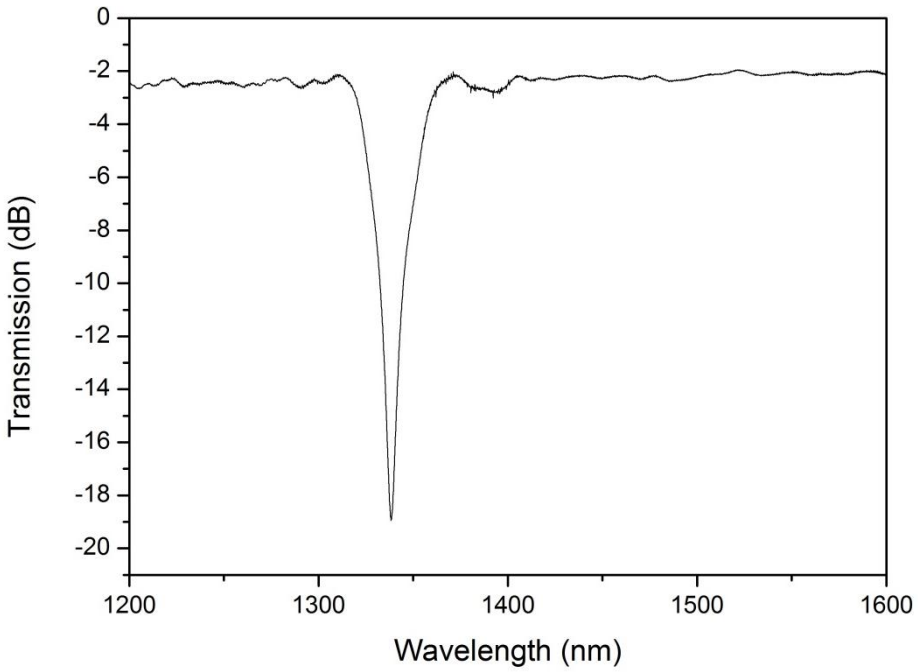

Figure 3.38 The transmission spectrum of 350μm LPG on SM1500 (4.2/80) fibre.

We have investigated the thermal and SRI sensitivity of 350μm LPG on SM1500 (4.2/80) fibre (sample 1) and compared with LPG on the SMF28 fibre (sample 2), who has two resonances (1340nm and 1360nm) in this region. Figure 3.39 depicts the results, showing the thermal sensitivity is -277.1pm/°C for the LPG made in small cladding fibre (sample 1) and 45.6pm/°C for the LPG in normal cladding fibre (sample 2). According to the Equation 3.9 to 3.11, the value and sign of thermal sensitivity for an LPG is determined by the cladding mode order and thermal coefficient ξco. Here we clearly see that with increasing temperature, the wavelength of LPG in small cladding fibre red-shifts whereas the LPG in normal cladding fibre blue-shifts.

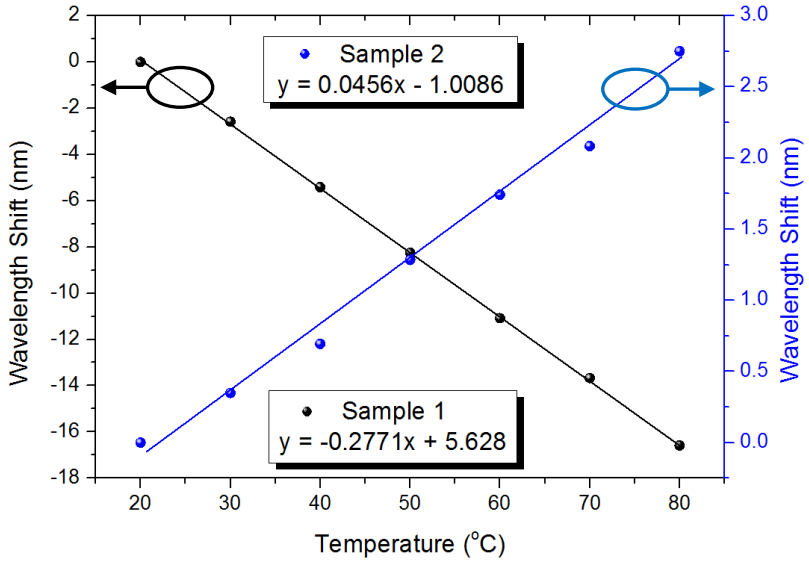

Figure 3.39 Comparison of temperature response of 350μm inscribed into SM-28 fibre with 62.5μm cladding radius (blue) and SM1500 (4.2/80) fibre with 40μm cladding radius (black).

Figure 3.40 plots the SRI response for the two LPGs, showing the SRI sensitivity is much higher for the LPG made in small cladding fibre then that in normal fibre. Quantitatively, the SRI sensitivity is only 10.43nm/RIU for LPG in normal fibre, but reached 59.64nm/RIU for LPG in small cladding fibre, which indicates that the SRI sensitivity is almost increased by 6 times when the cladding radius reduced by 1/3.

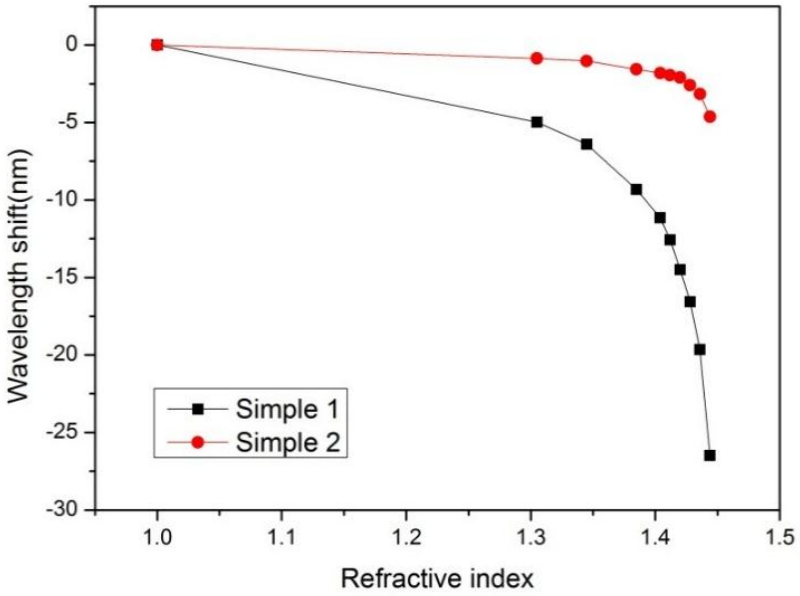

Figure 3.40 Comparison of SRI response of 350μm inscribed into SM-28 fibre with 62.5μm cladding radius (red) and SM1500 (4.2/80) fibre with 40μm cladding radius (black).

3.6 Chapter conclusion

At the beginning of this chapter, we have presented three optical fibre grating fabrication techniques which have been used to fabricate all the Near-IR fibre grating devices described in this chapter. The FBGs have been inscribed by two main different methods: two beam holographic inscription technique and phase mask inscription technique. The holographic technique has been employed to write FBGs with arbitrary wavelengths in the near- and mid-IR range. The phase mask inscription technique is the most effective grating inscription technique due to the simplicity of the optical system and its stability compared to the two-beam holographic technique. LPGs with period ranging from 10μm to 600μm normally were fabricated by point-by-point technique.

The FBGs and LPGs are remarkable for different sensing applications: temperature sensor, strain sensor and SRI sensor. Both FBGs and CFBGs UV-inscribed in metal coated and large mode fibres fibre have been presented with their unique spectral responses. With metal buffer protection, FBG sensors can operate at high temperature and harsh environment. FBGs in metal coated fibre have a typical sensitivity of 11.6 pm/°C in low temperature range (0-80°C) and 13.9 pm/°C in high temperature range (120-900°C). The optical fibre gratings fabrication on the large mode field fibre can be employed in high power fibre laser system with up to 1 kW output power level. Finally, to improve and enhance the RI sensitivity in the aqueous solution, the LPG structures were inscribed into a 40μm cladding radius fibre and a standard fibre (62.5μm cladding radius). The experiment results the RI sensitivity at the index is increased from 10.43nm/RIU to 59.64nm/RIU.

Chapter 4.

Fabrication, Spectral Characteristics and Applications of 45° Tilted Optical Fibre Gratings

4.1 Introduction

Tilted fibre grating (TFG) is a special type of grating which was first reported by Meltz *et al.*[8] in 1990. In 1996, Erdogan and Sipe performed a theoretical investigation of TFG structures[9]. TFG grating planes are tilted at angles to the fibre axis instead of perpendicular to it, thus resulting in the incident light guided in the fibre core being coupled into cladding or radiation modes. In 2005, Kaiming Zhou *et al.* reported a UV-inscribed TFG with 45° tilted structure (45°-TFG), showing high polarisation-dependent-loss (PDL) by theoretical and experimental investigation. Since then, many applications based on 45°-TFG were wildly reported including PER equalizer [107], in-line Polari meter[108] and polarization filters [109].

In this chapter, the inscription and characterization of UV-inscribed TFGs with tilted structures at 45° will be presented and discussed. Furthermore, we will demonstrate different applications based on 45°-TFGs. Finally, we will present 45°-TFGs inscribed in polarization maintaining (PM) fibre and demonstrate an all-fibre Lyot filter theoretically and experimentally.

4.2 Structure and phase matching condition of TFG

TFGs are capable of coupling the light from forward-propagating core mode to backward-propagating, radiation and forward-propagating cladding modes when the tilt angle is at <45°, =45° and >45°, respectively. Figure 4.1 shows the schematic diagram of a TFG structure in fibre core. In this figure, Λ_G is the grating period, Λ represents the grating period along the fibre axis and θ is the angle of the tilted structure.

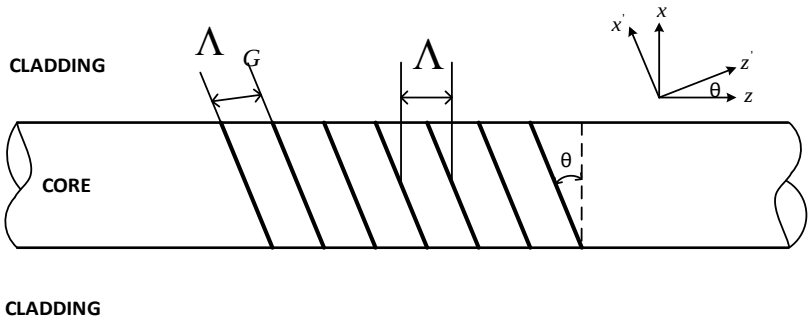

Figure 4.1 Schematic diagram of a tilted grating structure in fibre core.

As we discussed in Chapter 2, the strongest coupling wavelength for a TFG can be given by the phase matching condition:

Equation 4.1 $$\lambda_{strongest} = (\mathrm{n}_{co}^{eff} \pm \mathrm{n}_{cl,m}^{i,eff}) \times \frac{\Lambda_G}{\cos\theta}$$, i = TE or TM

Where n_{co}^{eff} and $\mathrm{n}_{cl,m}^{i,eff}$ are the effective refractive index of core mode and *m*th TE/TM cladding mode, and the signs of "+" and "-" describe the cases wherein the mode propagates in the –z or +z direction, respectively.

4.2.1 Phase matching conditions for TFG

The phase matching condition can be expressed by using the principles of conservation of momentum, which make us understand intuitively the mode coupling mechanism in the tilted fibre gratings. Conservation of momentum requires that the sum of the wave vector of core mode $\vec{K}_{core}$ and the vector of grating $\vec{K}_G$ must be equal with the wave vector $\vec{K}_x$ of reflected core, cladding, or radiation mode according to the equation 4.2.

Equation 4.2 $$\vec{K}_x = \vec{K}_{core} + \vec{K}_G \qquad \mathrm{x}: \text{core, cladding, radiation}$$

Where $\vec{K}_{core} = n_{core}\frac{2\pi}{\lambda}$, $\vec{K}_G = n_{core}\frac{2\pi}{\Lambda}\cos\theta$ and $\vec{K}_x = n_x\frac{2\pi}{\lambda}$.

As we descried earlier in of this section, the direction of the mode coupling depends on the tilted angle of the grating structure. Due to the total internal reflection effect at the boundary between the silica fibre cladding and air, if the tilt angle of a TFG at the boundary is less than the critical angle of the silica and air interface, the light will be tapped out from the side of the TFG by the radiation modes. However, if the tilted angle is below or beyond this total internal reflection angle range, the light will be confined in backward- and forward-propagating cladding modes respectively without tapping out from the grating fibre side. When the TFG is placed in the air, the critical angle of the fibre cladding boundary can be written as

Equation 4.3 $$\alpha_c = \arcsin\frac{n_1}{n_2}$$

where n_1 and n_2 are refractive indices of air (n_1=1) and fibre cladding (n_2=1.45), respectively. As shown in figure 4.2, φ is the incident angle of radiation beam which is related to tilted grating angle θ by $\varphi = \left|\frac{\pi}{2} - 2\theta\right|$. If $\varphi < \alpha_c$, the tilted grating angle range for the radiation mode out-coupling will be given as $\theta_{1c} < \theta < \theta_{2c}$, where θ_{1c} and θ_{2c} can be expressed as:

Equation 4.4 & 4.5 $$\theta_{1c} = \frac{1}{2}(\frac{\pi}{2} - \alpha_c), \theta_{2c} = \frac{1}{2}(\frac{\pi}{2} + \alpha_c)$$

Based on equation 4.3, the critical angle can be calculated as $\alpha_c = 43.8°$. Therefore, this range can be calculated as from 23.1° to 66.9° in air surrounding-medium. So the phase matching conditions for TFGs can be classified into three types: (a) the tilted angle of TFG is θ<23.1°, at which the forward-propagating core mode is coupled to backward-propagating cladding mode; (b) the tilted angle of TFG is within 23.1°<θ<66.9°, at which the core mode is coupled to radiation modes; (c) the tilted angle of TFG is θ>66.9°, at which the core mode is coupled to the forward-propagating cladding modes. Figure 4.2 shows the phase match conditions for TFGs with tilted angles in three different ranges.

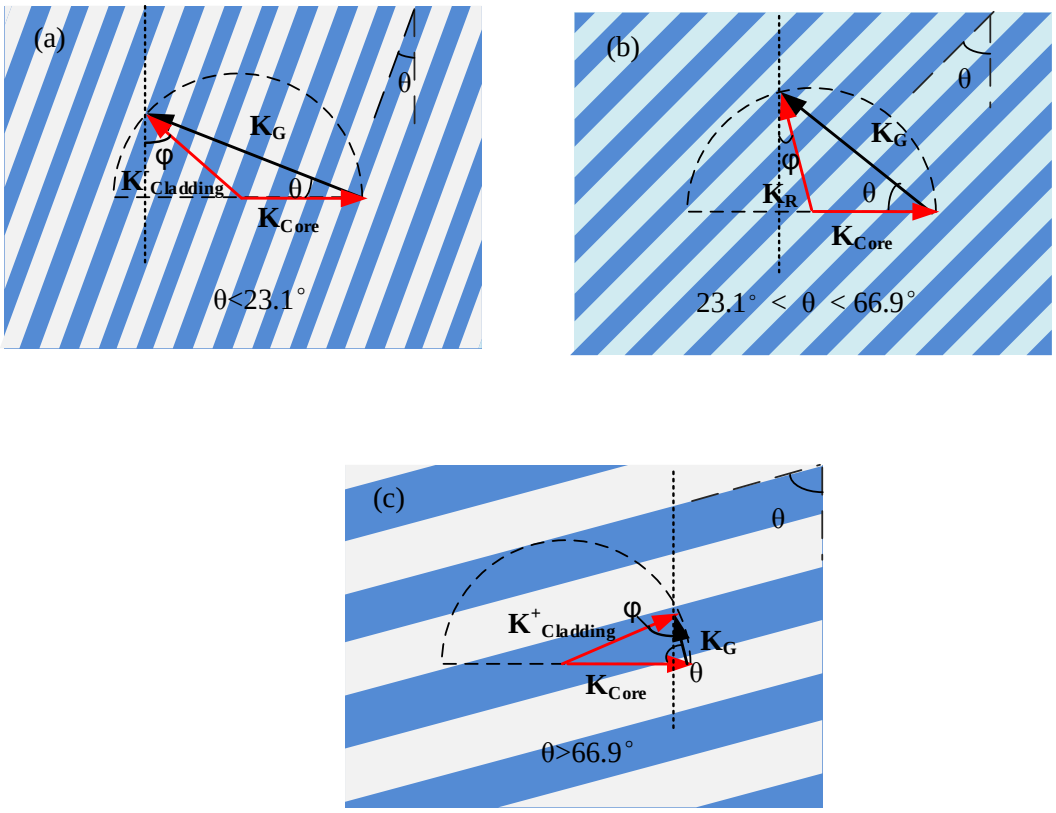

Figure 4.2 Sketch of tilted fibre grating structures with different angles and their phase-match conditions: (a) TFG with θ<23.1°; (b) TFG with 23.1°<θ<66.9°; (c) TFG with θ>66.9°.

4.3 Inscription and characteristics of 45°-TFGs

4.3.1 Polarization characteristics of 45°-TFGs

It is well-known that when unpolarised light is incident on a boundary between two media with different refractive indices at the Brewster angle [110], the light that is reflected from the boundary is totally polarized and the refracted light will be partially polarized. By using Snell's Law and Fresnel equations, the Brewster angle can be calculated as:

Equation 4.6 $$\theta_B = \arctan(\frac{n_2}{n_1})$$

Where n_1 is the refractive index of the initial medium and n_2 is that of the second medium. In a fibre grating, n_1 will be equal to effective refractive index of core, and n_2 is equal to the effective refractive index of the core mode after UV modification. However, because the UV induced index

modulation is so small (the order of $10^{-5} \sim 10^{-3}$), n2 ≈ n1. Thus, in a UV-inscribed fibre grating, the Brewster angle may be estimated as $\theta_B = \arctan(\frac{n_2}{n_1}) = \arctan(1) = 45^\circ$. Hence, a 45°-TFG can be recognized as an ideal in-fibre polarizer, which couples the s-polarized light out of fibre core and leaves the p-polarized light propagating through the fibre (see figure 4.3).

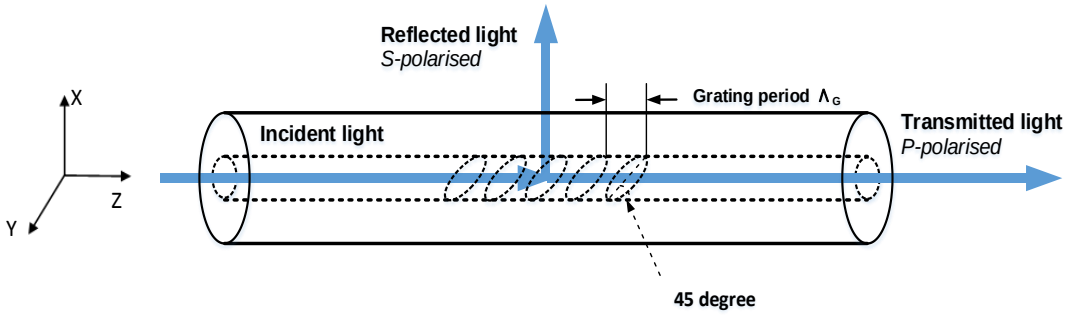

Figure 4.3 Schematic of a 45°-TFG structure, showing in-fibre polarizer function.

Zhou *et al*. [111] gave the simulation of transmission spectra of TFGs with different tilted angles for s-polarization and p-polarization light (see figure 4.4). From both figures, it is clearly noted that the transmission loss of p-polarization light is almost eliminated when the tilted angle is at 45°, whereas the transmission loss of s-polarization light still remains high at this angle. In other words, the polarization dependent loss (PDL) of 45°-TFG reaches the maximum at 45°.

Figure 4.4 (a) Simulated transmission spectra of TFGs with various tilting angles. P-light (dashed curves); s-light (solid curves). (b) Transmission losses of TFGs for s-light and p-light versus tilting angles. The peak wavelength is set to 1.55μm [111].

Based on the discussion in section 4.2.1, the strongest coupling wavelength for a 45°-TFG can be given as

Equation 4.7 $$\lambda_{strongest} = 2n\Lambda_G \cos 45°$$

Where n is the refractive index of the fibre core, Λ_G is the grating period, and the 45^0 is the tilting angle of the TFG in the fibre core.

The bandwidth (λ_B) of 45°-TFG has been given by Ref [112] as follow:

Equation 4.8 $$\lambda_B = \frac{\sqrt{2\ln 2}}{\pi n_0} \bullet \frac{\lambda_R^2}{\omega_0}$$

Where n_0 is effective refractive index of fibre core, λ_B is resonance wavelength and ω_0 is a fibre core radius.

4.3.2 Inscription of 45°-TFGs by phase mask technique

TFGs can be fabricated using the methods similar to normal FBG fabrication, for which the refractive index of the fibre modulation is induced by an interference pattern composed of two intense UV laser beams. There are two ways generally used to fabricate TFGs: (1) holographic technique and (2) phase mask scanning technique. As shown in Figure 4.5, a TFG can be inscribed by rotating the fibre at the angle θ_{ext} which is the angle between the fibre normal axis and the interference fringe pattern (Figure 4.5 (a)). For phase mask technique, a TFG structure can be inscribed by rotating a normal phase mask (Figure 4.5 (b)) or directly using a tilted phase mask with a tilted grating pattern, as shown in figure 4.5 (c). In order to fabricate high quality gratings, all TFGs reported in this thesis were written by phase mask technique.

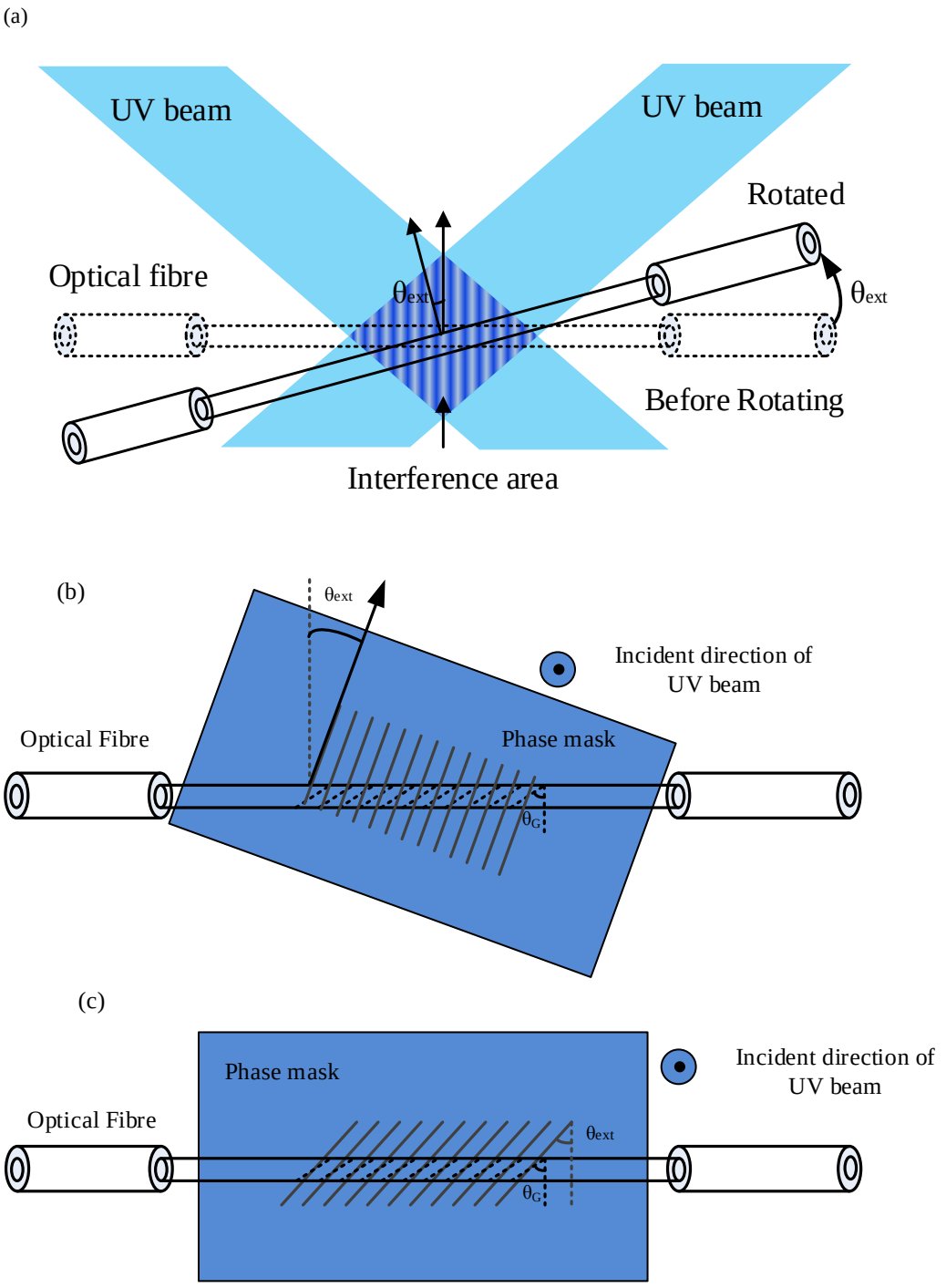

Figure 4.5 Schematic for the TFG inscription by (a) two-beam holographic technique, (b) rotating phase mask with respect to the optical fibre and (c) phase mask with tilted pattern.

The optical fibre for grating fabrication can be regarded as a cylindrical lens due to its own geometry. This cylindrical lens effect leaves the UV interference fringes unaltered in the direction parallel to its centre axis, but compresses the fringes in the direction perpendicular to centre line. Therefore, the tilted angle of the grating is not the same as the fibre rotated angle or external

phase-mask angle θ_{ext}. The difference in the internal and external tilt angles is illuminated in Figure 4.6.

Figure 4.6 Schematic diagram of a TFG showing the difference between the internal and tilt external angle θ_{ext} and internal angle θ_{int}.

Thus, the internal grating tilt angle θ_{int} is related to the external tilted angle θ_{ext} described in ref. [107] as follows:

Equation 4.8
$$\theta_{\text{int}} = \frac{\pi}{2} - \tan^{-1}\left[\frac{1}{n_{UV}\tan(\theta_{ext})}\right]$$

Where n_{uv} is the refractive index of the fibre at wavelength of the UV laser. The relationship between the internal and external angles is plotted in Figure 4.7.

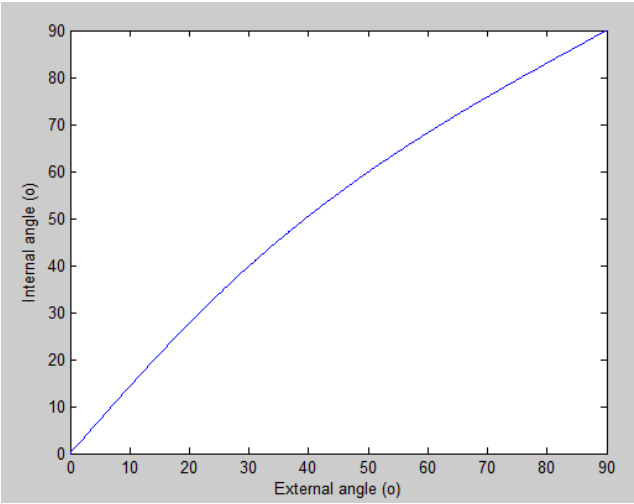

Figure 4.7 Plot of relationship between internal angle and external tilt angle.

All 45°-TFGs reported in this thesis were UV inscribed into single mode fibre by using a tilted phase mask. The phase mask was purchased from Ibsen Photonics with a special design for the period and tilted angle. The mask period is of 1830nm which ensures the central response is at 1550nm region, and the tilted angle is at 33.7° to ensure the UV-induced fringes will tilt at exact by 45° in the fibre core. All 45°-TFGs were inscribed using a 244nm UV light source from a frequency doubled Ar^+ CW laser (Coherent Sabre Fred ®) and the phase mask scanning technique. In order to enhance photosensitivity of silica fibre, before the 45°-TFG inscription, all fibre samples were hydrogen-loaded by storing them into hydrogen gas chamber at temperature 80°C and under pressure 150bar for two days. Most of fabricated 45°-TFGs were UV inscribed in the standard telecom single mode fibre (SM-28) from Corning and some were in high photosensitive fibre (PS1250/1500) and PM fibre (PM 1550) from Fujikura®.

After inscription, a high magnification microscope system (Zeis Axioskop 2 mot plus) with a 100× oil immersion objective lens was employed to examine the grating structure. Figure 4.8 shows a micro-image of a 45°-TFG in the SM_28 fibre core. It can be seen clearly from the micro-image that the tilt angle of grating pattern is measured at 45.04° and the diameter of fibre core is 8.77μm.

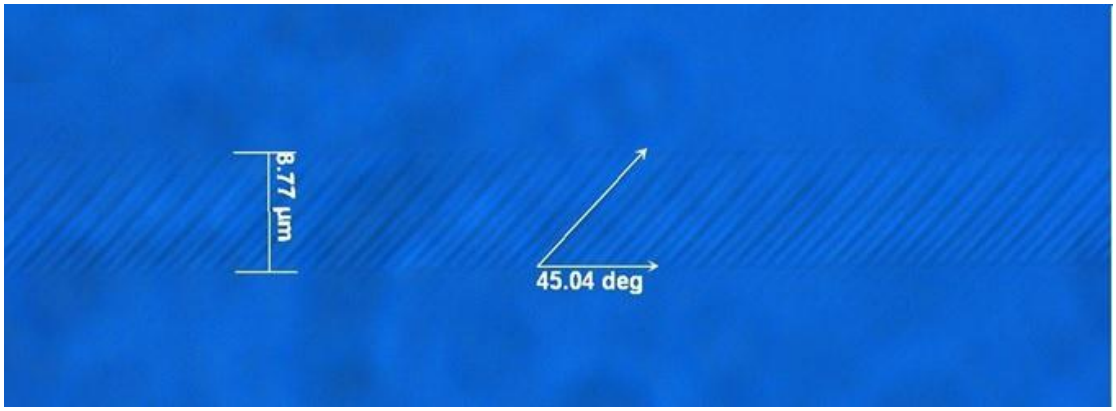

Figure 4.8 Microscopy image of a 45°-TFG taken under a 100x oil objective lens.

4.3.3 Polarisation dependent loss of 45°-TFG

As discussed in earlier section, the 45°-TFG can be recognised as an in-fibre polarizer. Thus, polarization dependence loss (PDL) or the polarization extinction ratio (PER) is the important parameter of a 45°-TFG. The definition of PDL is a measure of the peak-to-peak difference in transmission of an optical component or the ratio of the maximum and the minimum transmission of a system with respect to all possible states of polarization[113]. The PDL mathematic expression of a 45°−TFG was given in Ref. [114] as follow:

Equation 4.9 $$PDL = -10(\alpha_{\max} - \alpha_{\min})\log(e) \times l$$

where $\alpha_{\max}$ and $\alpha_{\min}$ are the maximum and minimum light transmission loss coefficients in 45^0-TFG, e is the natural exponential and l is the grating length.

The PDL of 45°-TFG could be measured by using the polarization scanning technique. A typical experimental setup for measuring PDL by the polarization scanning technique is illustrated in Figure 4.9, which involves the use of a tuneable laser, a commercial fibre polarizer, a fibre polarization controller (PC) placed in front of the 45°-TFG and a power meter (or an optical spectrum analyser).

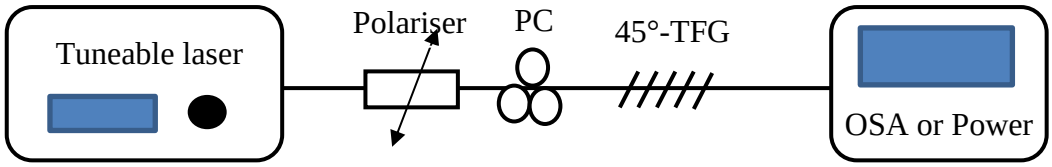

Figure 4.9 Diagram of the setup used for characterising the PDL of 45°-TFGs.

The polariser and the PC used in the PDL measurement setup are operating in 1550nm region. The maximum and minimum transmission spectra of the 45°-TFG at each wavelength can be

obtained by adjusting the PC. The PDL can then be calculated using Equation 4.9. Figure 4.10 shows the measured PDL spectra at 1550nm of one of the 45°-TFGs inscribed in SM-28 fibre with a grating length of 24mm. From the figure we can see the PDL, i.e. the difference between the maximum and minimum transmission, at 1550nm is about 22.1dB. This PDL value corresponds to a percentage value of 99.38%, which means that the 45°-TFG couples out 99.38% of s-polarized light from the fibre.

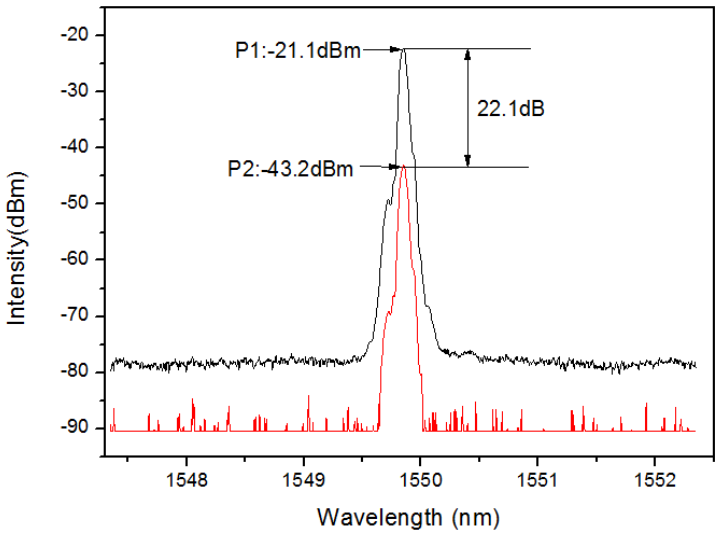

Figure 4.10 Transmission spectra of a 24mm-long 45°-TFG measured using a single wavelength at 1550nm at two orthogonal polarization states (P1 and P2).

The PDL of a 45°-TFG over a broad wavelength range can also be measured by using commercial LUNA Vector Analyser system based on Mueller method [115]. Figure 4.11 shows the overall PDL result for the same 45°-TFG measured in the range of 1525nm to 1610nm. From the figure we can see that the PDL monotonically decreases from the short wavelength to the long wavelength. This can be explained as follows. As calculated in ref [111], the PDL spectral response of a 45°-TFG has a Gaussian shape that is symmetric to certain wavelengths manifesting a broadband polarizing behaviour. In our experiment, due to the limit range of the measurement system, we are unable to measure the full wavelength range of PDL. However, it can be clearly seen in Figure 4.11 that the other half of the Gaussian shape should be within the range of 1530nm to 1610nm. One may notice that there are spectral ripple of the grating overall PDL profile when

the device is exposed to air (black solid line). This is because the cross coupling between the forward propagating core mode and radiation modes resulting from the refractive index mismatch between the air and cladding. In order to eliminate this resonance effect, the grating area of this 45°-TFG was immersed into index matching gel to achieve an infinite cladding boundary condition. As clearly shown in Figure 4.11, all ripples have been eliminated and the overall PDL profile is a smooth curve as shown by the red-line plot. Quantitatively speaking, we can see the PDL is about 15 dB around wavelength 1550nm and dropped to 12dB at 1600nm.

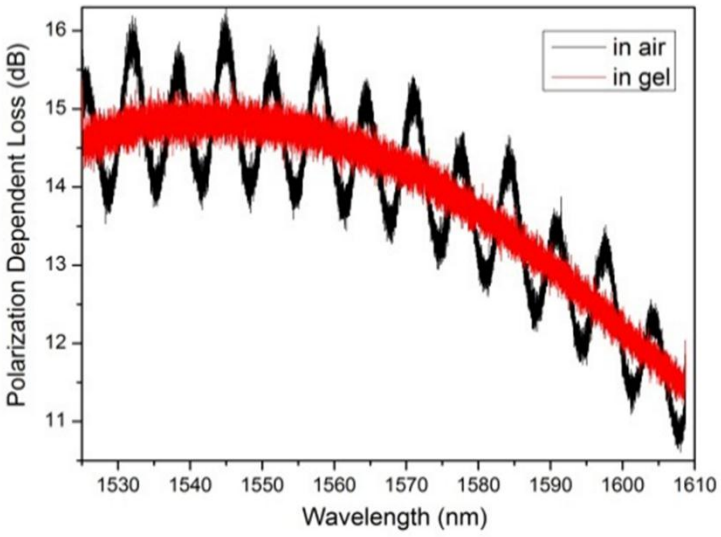

Figure 4.11 The overall PDL spectral response of the 45°-TFG measured in air (black curve) and in index matching gel (red curve).

From equation 4.9, it is easy to find out that the PDL is linearly proportional to the grating length. In order to verify this co-relation experimentally, we fabricated five 45°-TFG samples with different grating lengths (5mm, 10mm, 15mm, 20mm and 24mm) under the same fabrication parameters. The measured PDL results for all five 45°-TFG samples are plotted in Figure 4.12. As clearly shown from the figure, the PDL increases with the grating length at a rate of almost 0.986 dB/mm.

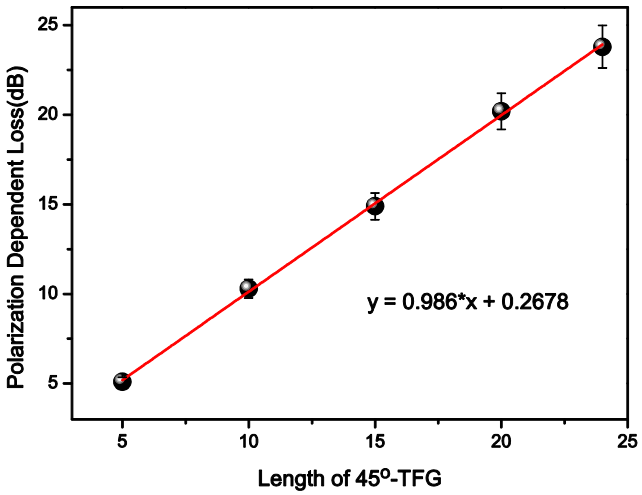

Figure 4.12 The PDL of 45°-TFG against grating length.

The 45°−TFG has a linear polarization response, which works as described earlier by coupling out the s-polarised light and propagating the p-polarised light through the tilted grating fibre. If the linearly polarised light from the 45°-TFG is aligned with either the slow- or fast-axis of a PM fibre, the output will show a minimum and a maximum power [114]. To evaluation the polarisation distribution of 45°-TFGs, we measured the grating using the experimental set up shown in Figure 4.13, by changing the polarisation state of the light launched to the 45°-TFG.

Figure 4.13 Experimental setup for measuring polarization distribution of 45°-TFG.

The set-up shown in Figure 4.13 consists of a single wavelength light source (from a tuneable laser), a fibre polarization controller (PC), a fibre polarization beam splitter (PBS), a fibre rotator and a power meter with dual-channel. The two outputs of the PBS are two pieces of PM fibre, therefore, the light coming out from the two ports are linearly polarized with orthogonal polarization states. The polarization distribution was measured by rotating the PM fibre 2 output port from 0^0 to 360° with a step of 10° for three 45°-TFGs and a pristine fibre for comparison. While for the pristine fibre without grating, the output power measurement shows a perfect circle in Figure 4.14 (a), indicating no polarisation effect at all. For the three 45°-TFGs with PDLs of 10dB, 15dB and 22 dB, the polarization distribution plots show a figure 8 shape as seen in Figure 4.14 (b), (c) and (d). Comparing the polarization distribution figures for the three 45°-TFGs, we clearly see that the high PDL grating shows a narrower waist than the low PDL one.

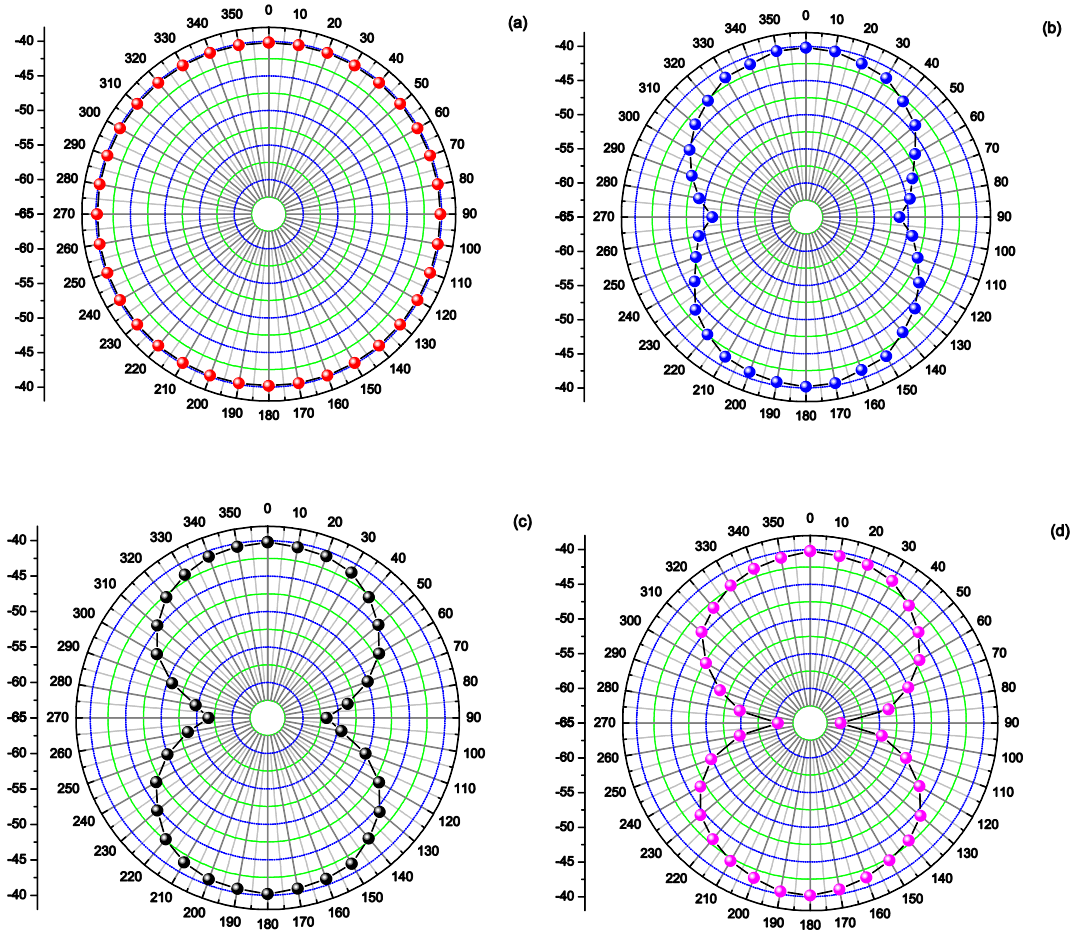

Figure 4.14 Polarization distribution measurement: (a) for a prestige fibre with 0dB PDL; (b) for a 45°-TFG of 10dB PDL; (c) for a 45°-TFG of 15dB PDL; (d) for a 45°-TFG of 22dB PDL.

4.4 Power tapping function of 45°-TFG

4.4.1 Principle of power tapping based on TFG with 45° tilted angle

As we discussed in an earlier section, if the tilted angle of TFG is within 23.1°<θ<66.9°, the core mode is coupled to radiation modes. The tilt angle of the grating plane and the index modulation strength will determine the radiation coupling efficiency of the light that is tapped out. The 45°-TFG is an ideal device for side-tapping power out of fibre due to its radiation light coupled out of the fibre perpendicularly.

The spectrum of a TFG can be simulated by the Green's function method [116]. Thus, the loss of a core mode of a TFG in a single-mode fibre can be expressed as $-\alpha\delta l$, where α is the loss coefficient of TFG , and is given in ref. [111] as below:

Equation 4.10

$$\alpha = -\frac{k_0^3 \delta n^2}{4n(1+(\frac{u^2}{w^2}))} \frac{k_1^2(a\omega)}{k_0^2(a\omega)} \int_0^{2\pi} \left[1-\sin^2\theta_0 \cos^2\theta(\frac{\pi}{4}-\varphi)\right] \times \left[\frac{R_s J_0(au)J_1(aR_s)-uJ_0(aR_s)J_1(au)}{R_s^2-u^2}\right]^2 d\phi$$

where $k_0=2\pi/\lambda_0$ is the wave vector of light in vacuum; n and δn are the original and the perturbation refractive indices of the core, respectively; u and ω are the fibre waveguide parameters; a is the core radius; K and J are Bessel function.

In Equation 4.10, $R_s = \left(R_t^2 + k_0^2 n_{cl}^2 \sin\theta_0^2 + 2R_t k_0 n_{cl} \sin\theta_0 \times \cos\varphi\right)^{\frac{1}{2}}$, where θ_0 is the angle between the radiation beam and the fibre axis, which satisfies $R_g - n_{eff}k_0 + k_0 n_{cl}\cos\theta_0 = 0$; φ denotes the polarization of the core mode; Rt and Rg are wave vectors of the grating along the fibre axis and across the fibre cross section and are defined as $Rt=2\pi/\Lambda_g \sin 45°$ and $Rg=2\pi/\Lambda_g \cos 45°$.

From Equation 4.10, we can calculate the ratio of radiated and input power of *s*- and *p-polarised* light for a 45°-TFG. Figure 4.15 shows the simulated ratio of radiation power in percentage with different modulation index changes. It can be clearly seen from the figure that we can design the tapping power efficiency for 45˚-TFGs by controlling appropriate index modulation strength during the grating fabrication.

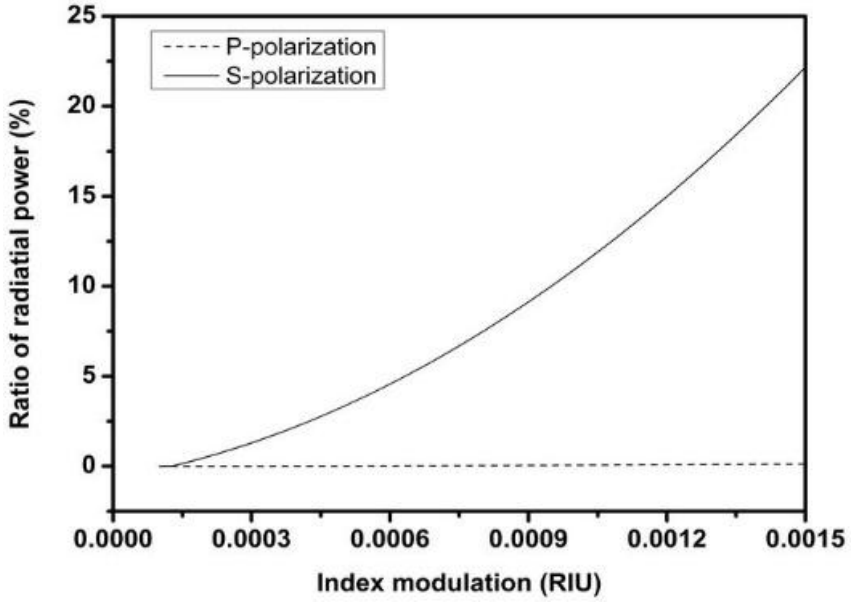

Figure 4.15 Simulated ratio of radiation power of *s*- (solid line) and *p-polarization* (dash line) for a 45˚-TFG.

4.4.2 Experimental results for power tapping using 45°-TFGs

Power tapping experiment setup is shown in Figure 4.16, which consists of a tuneable laser from HP, an InGaA amplified detector (700 nm - 1800 nm) from Thorlabs, an oscilloscope and a power-meter. The tuneable laser was operating at 1550nm wavelength and launched into the 45°-TFG. The detector was amounted on a translation stage for examining the side-tapped power distribution along grating axial direction. The oscilloscope which was connected to a detector was used to measure the light power tapped out from the side of the 45°-TFG. The power metre was employed to measure the remaining light power transmitting along the fibre core.

Figure 4.16 Experimental setup for power tapping measurement.

It can be seen clearly from the experiment, the power tapping out from the 45°-TFG side varies along the grating length. Choosing the 12 mm long 45˚-TFG, by moving the translation stage in 0.5 mm step, the power distribution over the entire grating length was measured. The result is plotted in Figure 4.17, which clearly shows that the side-tapped power is the highest at the start position of the grating and decreased exponentially along the grating length. As we known, the loss of a core mode of a TFG depends on the length of grating. Thus, the side tapped power from 45°-TFG decreased along the grating length.

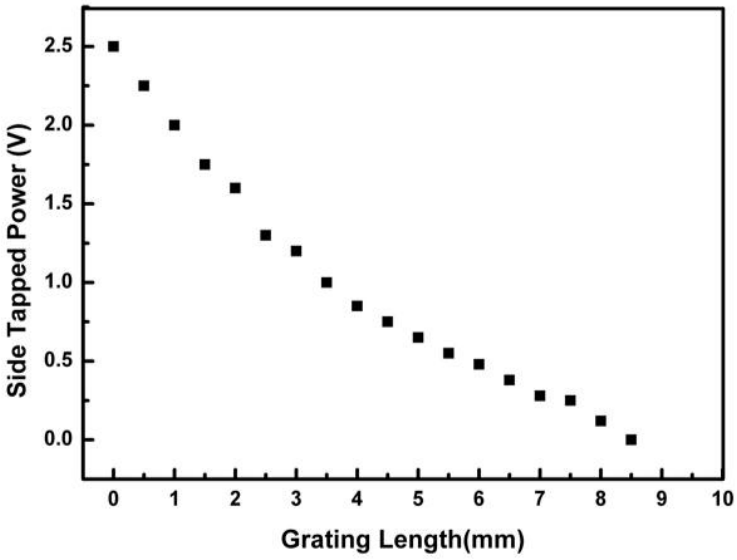

Figure 4.17 Measured side-tapped out power along the length of the 12mm 45°-TFG.

The side-tapped and transmitted power of the 45˚-TFG can be measured simultaneously by placing a photo diode at the beginning position of the 45°-TFG and a power meter at the fibre end. The side-tapped power and transmitted power were recorded respectively by changing the tuneable laser wavelength. The results are plotted in Figure 4.18. It can be seen clearly from the figure that the shorter wavelength gives more transmitted and less side-tapped power, and vice versa with the longer wavelength.

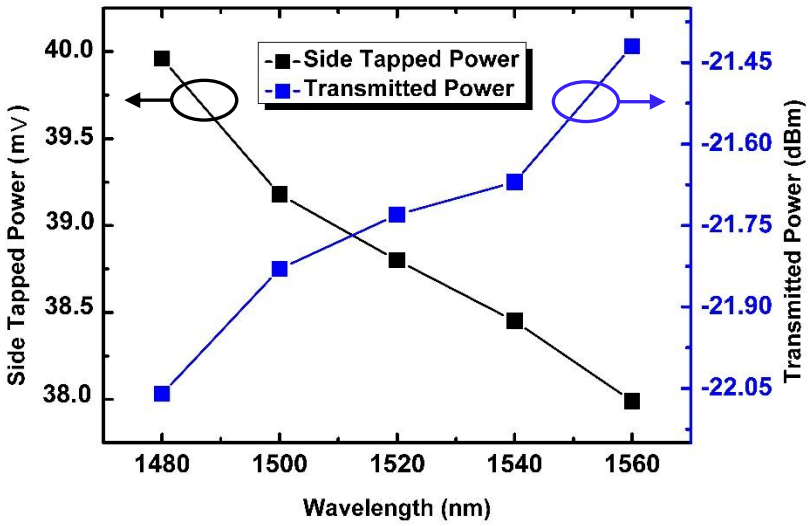

Figure 4.18 The side-tapped and transmitted power from a 45°-TFG probed with a light source at different wavelengths.

4.5 Application of 45°-TFG in laser systems

As a high PDL in-fibre polariser, the 45°-TFG can play an important role in fibre laser systems to achieve the single polarization and mode-locking pulse output [15, 117]. This section will focus on using the 45°-TFG as an intra-cavity functional element to obtain the single polarisation and soliton mode locking lasers. Furthermore, a novel loading sensor based on single polarization fibre laser using a 45°-TFG will also be discussed.

4.5.1 Single polarization single wavelength fibre laser

The optical fibre laser can be used as an important light source in both optical communication [118] and sensing applications [119]. Polarisation is one of the most important proprieties of laser light. The single polarised laser is more desirable for applications. Due to the effect of low birefringence of the passive and active fibre, most of laser systems can just generate unpolarised or a very low degree of polarization (DOP) output. To achieve fibre laser output with high DOP, several methods [120, 121] have been proposed. Because the 45°-TFGs can be successfully fabricated in standard single mode fibre with high PDL, it is now possible to achieve single polarization fibre laser by using 45°-TFG as intra-cavity polarizer.

In order to achieve the single polarization laser output, we constructed a fibre ring laser and inserted a 45°-TFG into the laser cavity. The experimental setup of the single polarization ring laser based on 45°-TFG is illustrated in Figure 4.19. As shown in the figure, a 4-metres length of EDF (from Fibercore, absorption at 1530nm is 11dB/m) is inserted in the ring cavity and pumped by a grating stabilized 976nm laser diode (LD) which can provide up to 200mW pump power though a 980/1550 wavelength division multiplexing (WDM) coupler. A 10:90 coupler is employed to couple 10% of light out of the laser cavity. A uniform FBG with reflectivity larger than 90% and 3-dB bandwidth of 0.19nm at the wavelength of 1550nm is incorporated in the cavity through an optical circulator, which defines the laser seeding wavelength while maintaining unidirectional oscillation. A 45°-TFG is inserted between the circulator and the coupler to

achieve single polarization oscillation. A polarization controller (PC1) is used to optimize the cavity birefringence. Figure 4.20 provides a typical output with 0.08nm linewidth of the ring laser measured by an OSA.

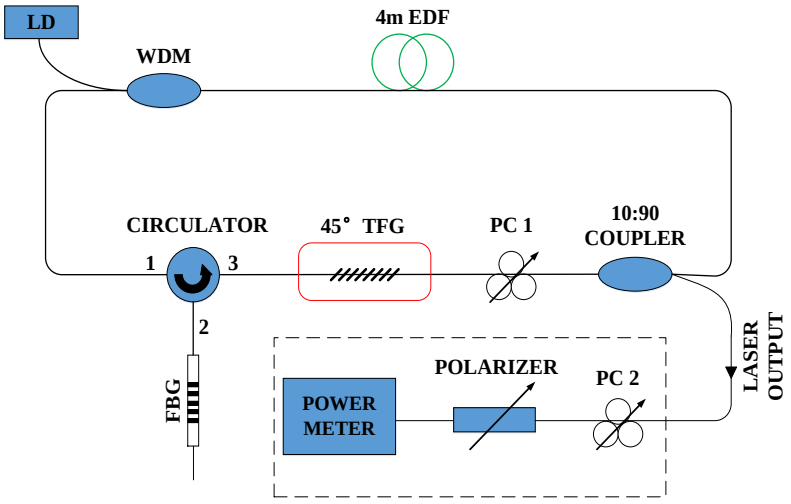

Figure 4.19 Schematic diagram of the single polarization fibre ring laser structure. The degree of polarization (DOP) of the laser output is measured using the setup shown in dashed line box.

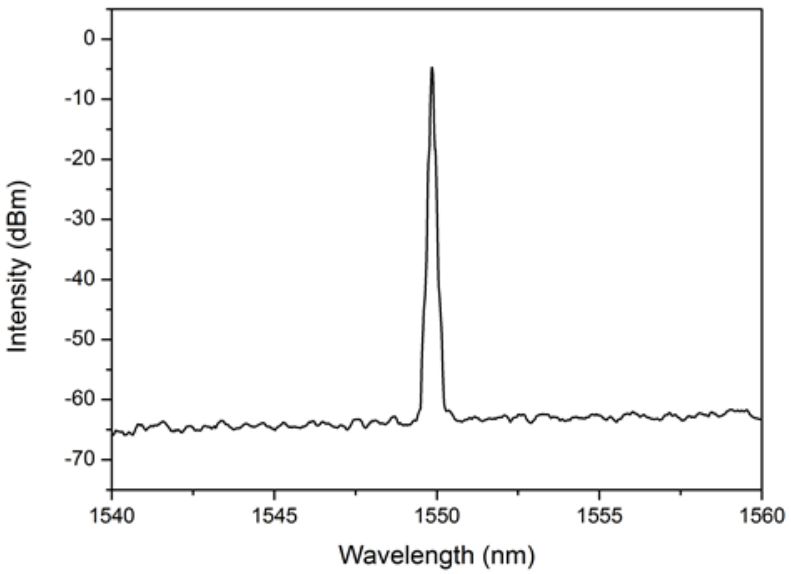

Figure 4.20 Typical output spectrum of the fibre laser.

The degree of polarization (DOP) measurement of the output of the fibre laser is conducted by the setup shown in the dashed line box in Figure 4.19. The DOP of laser light is expressed as below:

Equation 4.11 $$DOP = \frac{P_{polarized}}{P_{polarized} + P_{unpolarized}} \times 100\%$$

where $P_{polarized}$ is the polarized part of the laser and $P_{unpolarized}$ is the unpolarised part. By properly adjusting polarization controller (PC2) in the setup shown in Figure 4.19, either the maximum power (power of polarized light plus half unpolarised light) or the minimum power (power of half polarized light) of the laser output can be obtained. Therefore, the DOP can be calculated by using Equation 4.11. The 45°-TFG used as the intra-cavity polarizer has a PDL of 22.1dB. The measurement showed that without the 45°-TFG in the ring cavity, the fibre ring laser output has a DOP of only about 19.7%, which suggests that the laser output is almost un-polarized. After inserting the 45°-TFG into the laser cavity, the DOP of the laser output significantly increased to 99%, which clearly indicates that the output of the laser is highly polarized and almost single polarization. The slope efficiency of the fibre laser has also been examined before and after incorporating the 45°-TFG into the cavity. Figure 4.21 clearly shows the slope efficiency decreased from 11.93 % to 8.06 % after the 45°-TFG had been inserted into the laser cavity. This is owing to the PDL of 45°-TFG and splicing loss in the laser cavity.

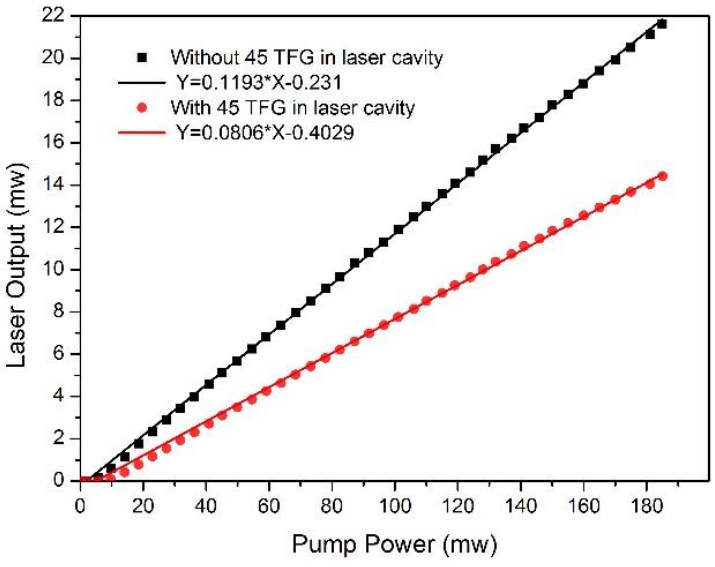

Figure 4.21 Slope efficiency of the fibre ring laser with and without the 45°-TFG.

We also measured the stability of the fibre ring laser output with the 45°-TFG in cavity. Figure 4.22 displays typical output spectra of fibre ring cavity laser measured over half an hour at a 5 minutes interval. No noticeable spectral variation has been observed over this period.

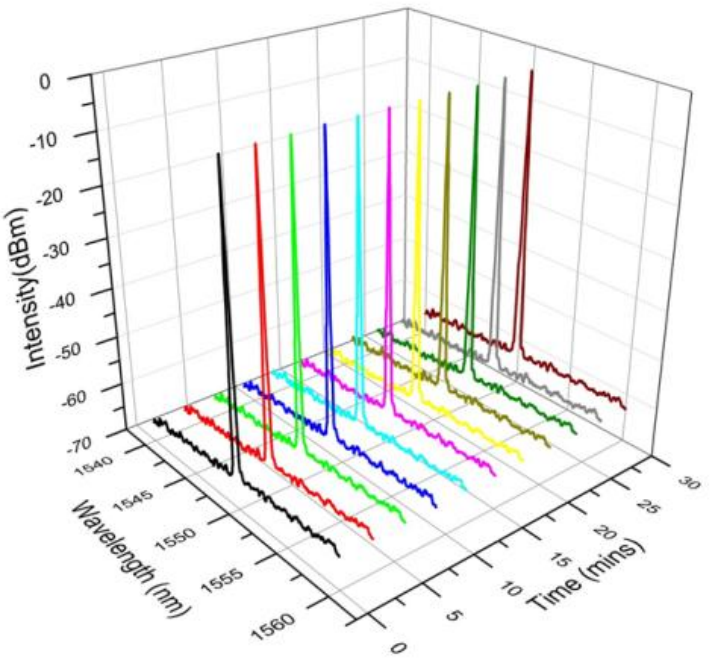

Figure 4.22 The stability of fibre ring cavity laser output spectra measured over half an hour at the laboratory condition.

4.5.2 Mode-locked fibre laser using 45º-TFG and FBG

Ultrafast picosecond fibre lasers are useful light sources that have found many applications in the field of telecommunication, micro-machining, medical imaging and fundamental research. An efficient approach to achieve picosecond pulses is laser passive mode locking using an element or scheme called a saturable absorber. Various methods have been implemented to mode-lock a fibre laser, including semiconductor saturable absorber mirror (SESAM) [122], carbon nanomaterial [123], and nonlinear polarization evolution (NPE) [124]. The picosecond pulse output can be achieved by inserting a narrow band filter, such as a fibre Bragg grating (FBG). The pulse duration and wavelength can then be tailored by the filter bandwidth and central wavelength. NPE mode-locked lasers use the intrinsic fibre nonlinearity as an effective saturable absorber, which could avoid such problems. As 45º-TFG has been proved to be an efficient in-

fibre polarizer for fibre laser systems [15, 125], we have proposed and demonstrated an NPE mode-locked EDF fibre laser using a 45°-TFG as an in-fibre polarizer to manipulate the nonlinearity and dispersion property of the laser to achieve the mode-locking. Similarly to the CW fibre ring laser, a standard FBG is used to tailor the output pulse duration and lock the centre wavelength.

The experimental setup of a passively mode-locked laser using a 45º-TFG and an FBG is illustrated in Figure 4.23. As shown in the figure, a 4-meters length of conventional erbium doped fibre (EDF M12, from FiberCore) is inserted in the ring cavity with nominal absorption coefficient of ~17.92 dB/m at 1530nm and normal dispersion +23 ps^2/km. The rest of the cavity consists of 10.5 meter standard telecom fibre with dispersion of -22 ps^2/km at 1550nm and a one meter HI 1060 fibre coming with 980/1550 wavelength division multiplexer (WDM) coupler, with dispersion -17.8 ps^2/km at 1060nm. Thus, the net-anomalous dispersion of the laser cavity is -10.12 ps^2/km. This ensures soliton pulse shaping of the laser. The pump and output arrangement is the same as the CW fibre laser in section 4.5.1, while the uniform FBG used as seeding has a reflectivity larger than 90% and 3-dB bandwidth of 0.5 nm at the wavelength of 1567nm. The 45°-TFG with a PDL of 22.1 dB is inserted between two polarization controllers (PC1 and PC2) to achieve the effect of nonlinear polarization evolution (NPE), as it can provide the necessary intensity discrimination for mode locking.

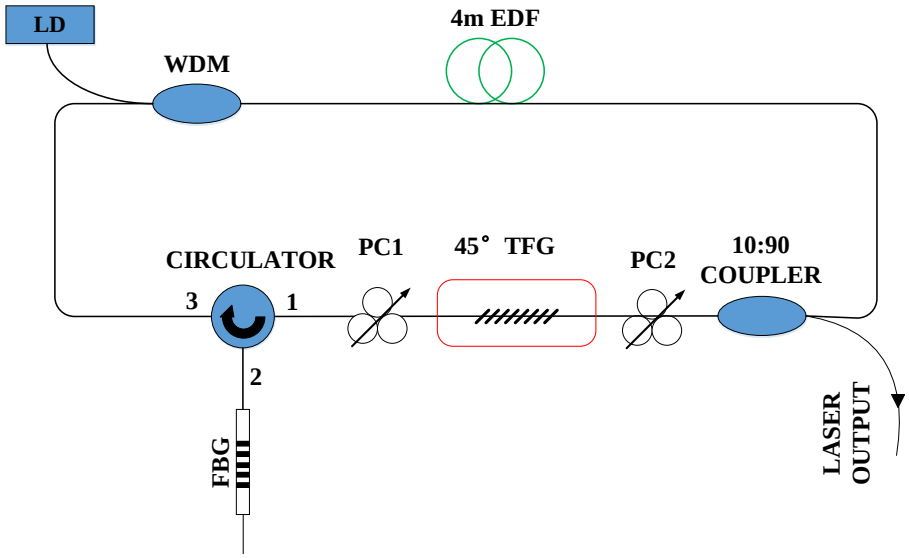

Figure 4.23 Schematic configuration of the 45°-TFG and FBG based mode-locked fibre laser.

The stable passively mode-locked pulses were observed by carefully adjusting the polarization controllers (PC1 and PC2) in the system. Figure 4.24(a) shows the measured optical spectrum of the soliton pulses at the launched pump power of 73.2mW with a resolution of 0.05nm. The central wavelength of optical spectrum profile is 1567nm with a spectral bandwidth at full-width half maximum (FWHM) of 0.55nm. A typical pulse train is shown in Figure 4.24 (b) with an 86.9ns interval between two adjacent pulses, giving a repetition rate of 10.34MHz. The average output power was measured to be 2.5mW and the pulse energy was calculated to be 0.2nJ. Figure 4.24(c) shows the measured FWHM autocorrelation trace at 26ps corresponding to the pulse duration of 16ps – a typical ps laser pulse. The measured time bandwidth product is 0.33 which is similar to the theoretical value of 0.32 for soliton pulses indicating the output laser pulses are transform limited.

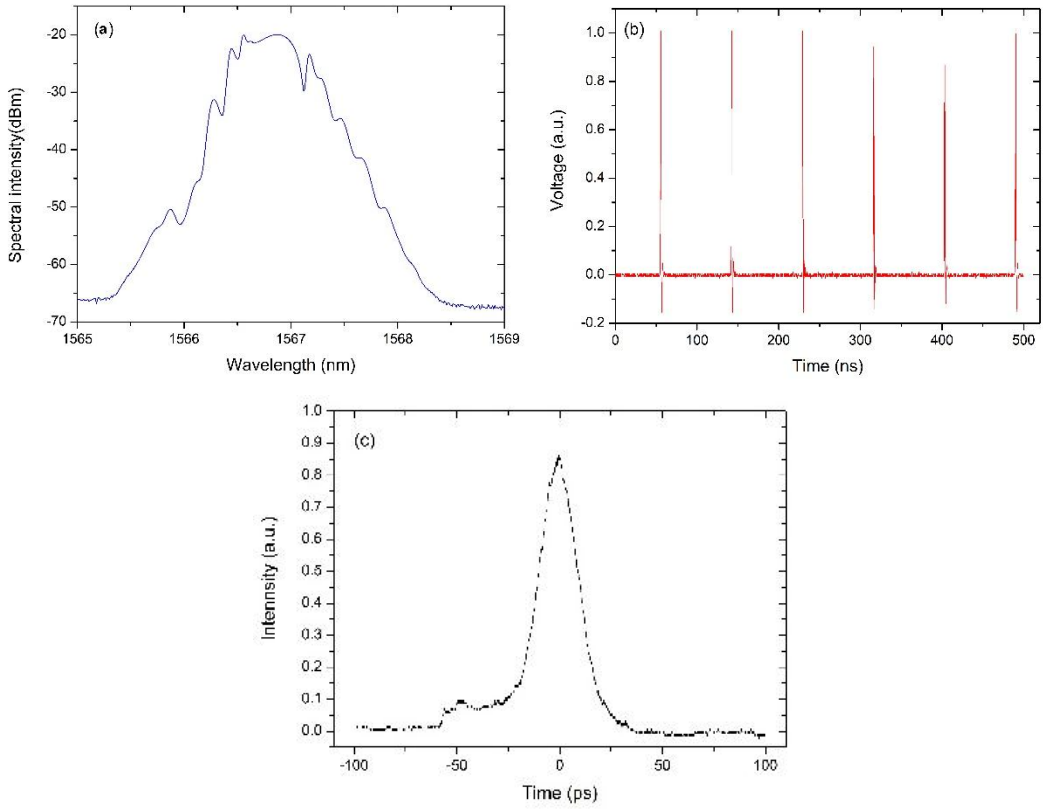

Figure 4.24 (a) Optical spectrum of the ~ 26ps output pulse; (b) a typical output pulse train of the mode-locked fibre laser showing interval between two adjacent pulses of ~ 86.9ns; (c) Measured auto-correlation trace.

The 45°-TFG based mode locking fibre laser can be tuned over a certain wavelength range generating single polarization output as well, as the polarization response of the 45°-TFG is quite broad. In our mode locking laser system, the seeding FBG was thermally tuned from 0°C to 80°C, shifting the laser output from 1567nm to 1568nm, giving ~1nm tuning range. Figure 4.25 shows the output spectra when the FBG is under temperature tuning from 0°C to 80°C.

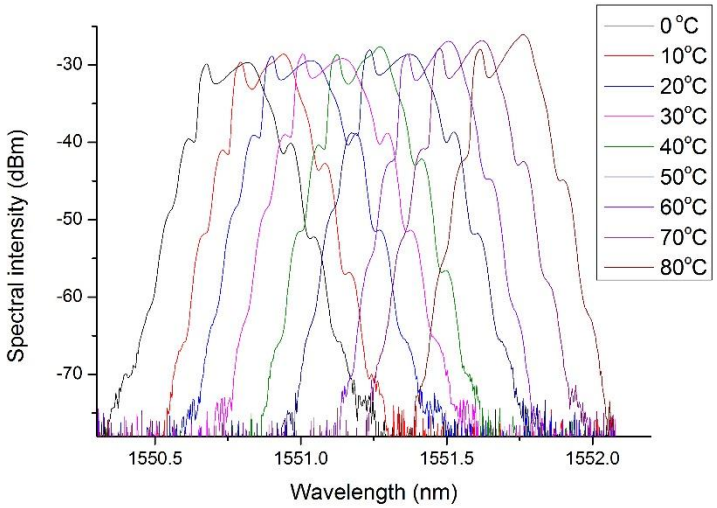

Figure 4.25 Output spectra of all fibre erbium doped fibre soliton ring laser tuned by temperature.

4.5.3 Loading sensor based on single polarization single wavelength fibre laser

Most fibre loading sensors proposed so far are based on their passive operation with expensive spectrometer for signal demodulation. External light source will also be required in such types of sensors. The above issues can be resolved by using fibre laser based sensors because the laser itself is a light source and signal demodulation can be obtained by relatively low cost power measurement. Thus, the laser sensors [126] have become more attractive due to their high signal-to-noise ratio, narrow bandwidth and low threshold power. Conventionally, the fibre laser sensor is formed by a section of EDF as the gain material and FBGs as reflectors. The FBG in such a laser system can also be used as a sensing element which leads to the wavelength shift of the laser [127] by some environment parameter variation, such as temperature, strain and so on. The following section will discuss a loading sensor based on single polarization single wavelength fibre laser incorporating a 45°-TFG.

4.5.3.1 Loading sensing principle

The EDF laser system can be generally regarded as a quasi-three-level system[128] , the output laser power can therefore be written as below:

Equation 4.12 $$P_{out} = \frac{\Omega_b \cdot (1+B)}{\varepsilon_e + \varepsilon_a} \cdot \frac{h \cdot \nu}{\tau} \cdot \frac{\delta_2}{2} \cdot (\frac{P_p}{P_{th}} - 1)$$

where we have set $B = \frac{\varepsilon_a \cdot N_t \cdot l_m}{\delta_{loss}}$, and

Ω_b the beam area in the active medium,

ν the frequency of the emitted photon,

h the Planck constant, l_m the length of the active medium,

N_t the total number of the population in the laser level and ground level,

ε_e the effective stimulated emission cross section,

ε_a the effective absorption cross section,

δ_2 s the logarithm loss due to the output coupler of the laser system,

τ effective life time of the upper laser level,

δ_{loss} the total logarithm loss of the laser system including cavity loss and mirror loss,

P_p the pump power

P_{th} the threshold pump power.

The threshold pump power P_{th} also can be expressed as:

Equation 4.13 $$P_{th} = \frac{\delta_{loss} \cdot (1+B)}{\mu} \cdot \frac{h \cdot \nu_p}{\tau} \cdot \frac{\Omega}{\varepsilon_e + \varepsilon_a}$$

where μ is the pump efficiency, v_p the frequency of pump light and Ω cross section area of the active medium. The substitution of Equation 4.12 into Equation 4.13 gives the more intuitive form of output laser power:

Equation 4.14 $$P_{out} = (\mu \cdot \frac{\Omega_b}{\Omega} \cdot \frac{1}{h \cdot \nu_p} \cdot P_p - \frac{\Omega_b \cdot \varepsilon_a \cdot N_t \cdot l_m}{\varepsilon_e + \varepsilon_a} \cdot \frac{1}{\tau}) \cdot \frac{\delta_2}{2} \cdot (h \cdot \nu) \cdot \frac{1}{\delta_{loss}} - \frac{\Omega_b}{\varepsilon_e + \varepsilon_a} \cdot \frac{h \cdot \nu}{\tau} \cdot \frac{\delta_2}{2}$$

It can be seen clearly from Equation 4.14, since our laser system has a fixed setup, only the intra-cavity loss is a variable and the other parameters are constant while the laser cavity configuration remains unchanged.

As a result of the polarizing property of the 45º-TFG, the proposed fibre laser cavity could eliminate one polarization state thus giving out single polarization output. The single polarization oscillation will be formed after certain roundtrips in the cavity. In the laser system, because we use standard single mode fibre, not PM fibre, the light polarization will not be preserved after the light passing through the 45°-TFG. Only light beams with specific polarization state that are able to transform to linear polarization state prior to reaching the 45°-TFG have the minimum cavity loss. Therefore, any alternation in the cavity that could induce birefringence change leading to the intra-cavity polarization state change will be filtered by the 45°-TFG. This polarization state filter effect will result in a laser output power variation which can be detected. As shown in Figure 4.26, we assume an elliptically polarized light travels in the laser cavity when stable laser oscillation established. We now define the logarithm intra-cavity loss induced by the loading induced birefringence change as:

Equation 4.15 $$\delta_{loss} = \ln\left(\frac{I_{Trans}}{I_{in}}\right)$$

where I_{in} is the intensity of single polarized light incident into the 45°-TFG, I_{Trans} is the intensity of single polarized light transmitted through the 45°-TFG.

Figure 4.26 Birefringence induced by load applied to the fibre.

The principle of the intra-cavity loss induced by loading effect can be described by Jones matrix method. We may assume the fibre laser cavity single polarization light $\overrightarrow{E_{in}}$ incident into 45°-TFG could be described in Equation 4.16 using Jones vector

Equation 4.16 $$\vec{E}_{in} = E \cdot \begin{bmatrix} \cos\alpha \\ \sin\alpha \cdot e^{i\phi} \end{bmatrix}$$

where E is the amplitude of the light field, tanα is the ratio between the x and y component of the electric field and ϕ is the phase difference between the two orthogonal electric fields. The intensity of the input single polarized light can be written as Equation 4.17 by multiplying its complex conjugate.

Equation 4.17 $$I_{in} = \overrightarrow{E_{in}} \cdot \overrightarrow{E_{in}^{*}}$$

As shown in Figure 4.26, the angle between the axis of the polarizer (45°-TFG) and the y axis is θ. Thus the fibre laser cavity transmitted light $\overrightarrow{E_{Trans}}$ after the polarizer (45°-TFG) can be expressed as:

Equation 4.18 $$\overrightarrow{E_{Trans}} = \begin{bmatrix} \sin\theta & 0 \\ 0 & \cos\theta \end{bmatrix} \cdot \overrightarrow{E_{in}}$$

The intensity of the transmitted light after the polarizer can then be given by:

Equation 4.19 $$I_{Trans} = \overrightarrow{E_{Trans}} \cdot \overrightarrow{E^{*}_{Trans}}$$

Due to the photo-elastically induced birefringence, the applied loading can thus alternate the polarization state of input light $\overrightarrow{E_{in}}$ when transverse force applied onto the single mode fiber. Within the same coordinate system, the load applied to the fiber will produce linear birefringence in *x* direction. As a consequence, the light undergoing linear birefringence in *x* direction could transform to:

Equation 4.20 $$\vec{E}'_{in} = E \cdot \begin{bmatrix} e^{-i\cdot\frac{\tau}{2}} & 0 \\ 0 & e^{i\cdot\frac{\tau}{2}} \end{bmatrix} \cdot \begin{bmatrix} \cos\alpha \\ \sin\alpha \cdot e^{i\phi} \end{bmatrix}$$

where $\begin{bmatrix} e^{-i\cdot\frac{\tau}{2}} & 0 \\ 0 & e^{i\cdot\frac{\tau}{2}} \end{bmatrix}$ is the Jones matrix expression of the load induced phase change, $\tau = \delta \bullet l$ is the phase retardation due to the applied load, δ is the amount of birefringence per unit length that is proportional to the load while *l* is interaction length. Then, by increasing the applied load to the fibre in the laser cavity, τ will be varied between 0 and 2π periodically.

According to Equations 4.12-4.20, we can see that the transmitted light is governed by the load induced birefringence variation that will lead to the intra-cavity loss alternation of the laser cavity. This is the principle of our fibre laser based loading sensor.

4.5.3.2 Experimental setup of laser loading sensor and results

The schematic description of the laser loading experiment is illustrated in Figure 4.27. The laser structure is the same as the one illustrated in Figure 4.18; the dotted circle in Figure 4.27 indicates the sensing fibre section in the cavity. In the experiment, the plastic coating of the sensing fibre was removed to reduce the buffer effect. The loading setup is shown in the dotted box, which was implemented by laying the sensing fibre and a dummy fibre (SMF-28) between two flat-surface aluminium plates. During the experiment, we gradually increased the load on the top of the plate with a number of standard weights. The active loading lengths were set as 31mm and 51mm, respectively. The laser output was continuously monitored by a high sensitivity power meter.

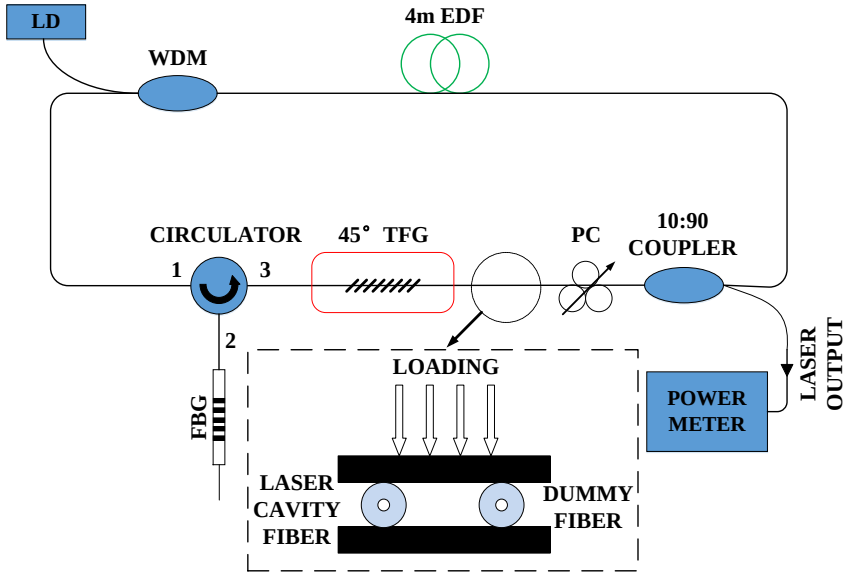

Figure 4.27 Schematic of the fibre laser loading sensor incorporating an intra-cavity 45°-TFG.

Before applying the transverse load, we maximized the laser output power by adjusting the PC to guarantee the laser working in an optimized condition. We then applied the transverse load to the sensing fibre in cavity from 0 to 6.4kg in an elevation step of 0.1kg. The laser output power changed with loading weight variation due to the alteration of intra-cavity polarization state. The measured output optical power changes against the loading weight on two different active loading lengths (31mm and 51mm) are plotted in Figure 4.28 and Figure 4.29, separately. It can be seen that the normalized output power varies with increasing load in a sinusoidal fashion with a fixed period and gradually reduced amplitude in a similar trigonometric

function which is caused by fibre deformation for a full cyclic change of the polarization state. However, in practical application, a linear relationship is more desirable. By taking the quasi-linear range from 32kg/m to 61kg/m for loading on the shorter active length fibre (31mm) and from 21kg/m to 47kg/m for the longer one (51mm), we can estimate that the loading sensitivity is approximately 0.033/ ($kg \cdot m^{-1}$) for the former and 0.042/($kg \cdot m^{-1}$) for the latter. The loading sensitivity for longer fibre is more sensitive than for the shorter one, because the load induced phase change depends on interaction length *l*, as discussed in the loading principle section. The longer loading length accelerating the phase change rate will lead to the reduction of the period of the sinusoidal curve of the laser output. Thus, it is possible to increase the active loading length so as to obtain higher loading sensitivity. From Figure 4.28 and 4.29, it can be seen that the measured experimental results correspond well to the theoretical calculation using Equation 4.14. Compared with TFG based loading sensor reported before[129], the sensitivity of our active loading sensor under the same experiment conditions has been increased by 50%. However, the laser output power is not able to return back to the initial point level with the cycles as we see the measured maximum power decreases with the cycle. The reason for this phenomenon is that the fibre deformation by transverse force induces the extra loss to the laser cavity. This loss will affect the loading sensitivity and limit the measurement range. The loading sensing based on this active configuration has shown significantly increased sensitivity compared with the TFG-based passive one [129]. The one of advantages of this sensor is that the loading signal can be measured using a low-cost power meter.

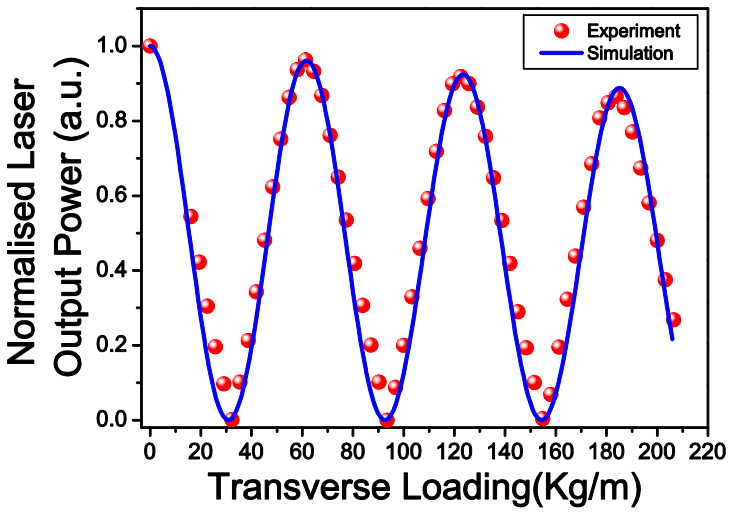

Figure 4.28 Measured output power change against loading weights for the shorter interactive fibre length (31mm).

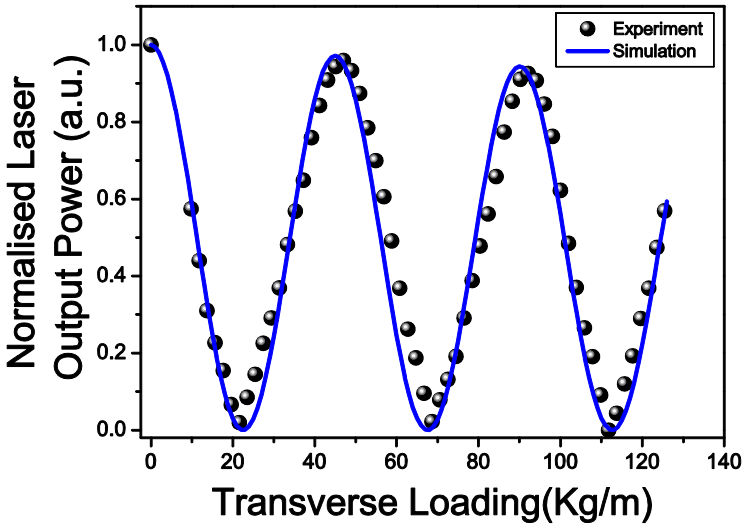

Figure 4.29 Measured output power change against loading weights for the longer interactive fibre length (51mm).

4.6 45°-TFG inscribed in PM fibre and all-fibre birefringent filter

4.6.1 45°-TFG inscribed in PM fibre

As described in the earlier section of this chapter, the 45°-TFGs have performed as in-fibre polarizers. Due to the nature of fibre configuration, the polarization status along the fibre is changing randomly. As a result, the linearly polarized light generated by the 45°-TFG cannot maintain its state of polarization while transmitted in the normal single mode fibre (such as SM28). In order to solve this issue, the 45°-TFG may be inscribed in to the polarization maintaining (PM) fibre along the fast or slow axis.

Most PM fibres are a single-mode optical fibre, which is designed to transmit light with maintained linear polarization. The PM fibre used for 45°-TFG inscription is Panda type fibre (PM1550 from Fujikura®). Figure 4.30 shows the cross-section image of the Panda type PM fibre. From figure 4.30, the diameter of the fibre core is 9.61μm and the diameter of the stress rod is about 34.83μm. This Panda structure design is used to introduce high stress-birefringence in a fibre core, resulting in fibre with excellent polarization maintaining properties.

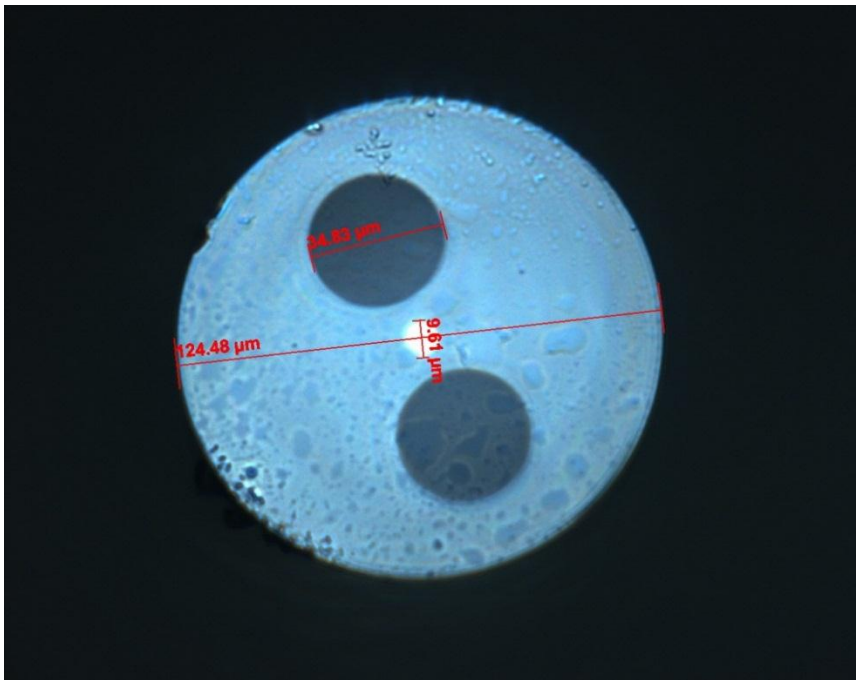

Figure 4.30 The micro-images of cross-section of the Panda type PM fibre used for 45°-TFG inscription.

In order to maintain the linear polarization state of the propagating light in the fibre, the transmitted light should be launched by the PM fibre along its principal axis (the slow- or fast-axis). Therefore, the 45°-TFG is UV-inscribed along the slow- or fast-axis of PM fibre. The PM fibre was hydrogen-loaded under 180bar at 80ºC for 72hours before the grating fabrication to enhance the photosensitivity. To inscribe 45°-TFG in the PM fibre along the slow- or fast-axis of the PM fibre was labelled under the microscope. The schematic diagram of the UV-inscription of 45°-TFG structure along the two different directions is shown in Figure 4.31. Here, we should appoint out that the polarized axis of the 45°-TFG based in-fibre linear polarizer is vertical to the inscription direction.

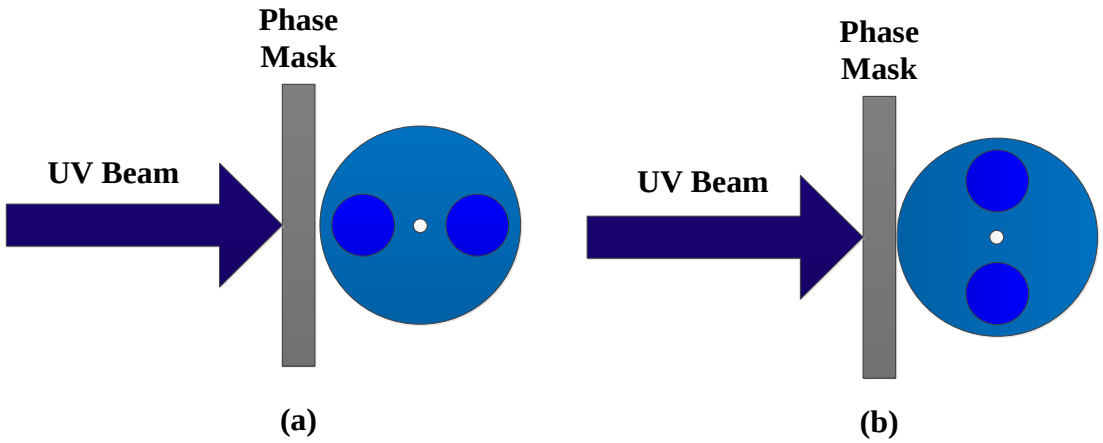

Figure 4.31 Schematic diagram of 45°-TFG inscription with respect to the (a) slow-axis and (b) fast-axis of PM fibre.

After the UV-inscription in PM fibre, the 45°-TFGs were annealed under 80 ºC for 24 hours for stabilization. The 45°-TFG structures were examined by the high magnification microscope system under a 100× oil immersion objective. As shown in Figure 4.32, the 45°-TFG structure in the core area along both the slow- and fast-axis and the stress rod of PM fibre can be clearly distinguished.

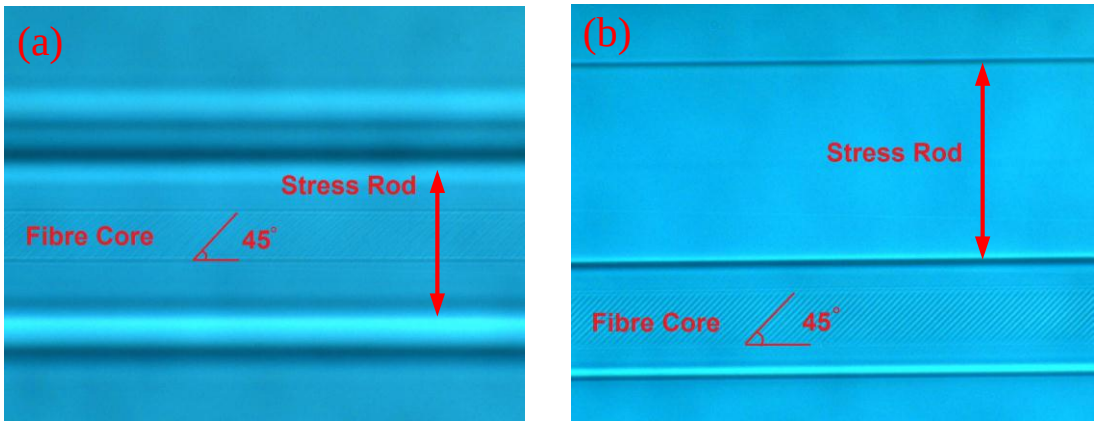

Figure 4.32 Micro-images of 45°-TFGs in PM fibre inscribed along (a) slow- and (b) fast-axis.

The 45°-TFGs in PM fibre were evaluated for the PDL by using the LUNA Vector system described in section 4.2.3. The Figure 4.33 shows the PDL of a 48mm-long 45°-TFG inscribed in the PM fibre along fast- and slow-axis .From the figure, we can see that the PDL of the 45°-TFG inscribed in PM fibre along the slow-axis is of 30dB, which is higher than that along the fast-axis

(only 18dB). This difference in PDL may be caused by the size of the effective interference area is expanded by a convex lens effect formed by the low refractive index stress rod surrounded by the high index silica [130].

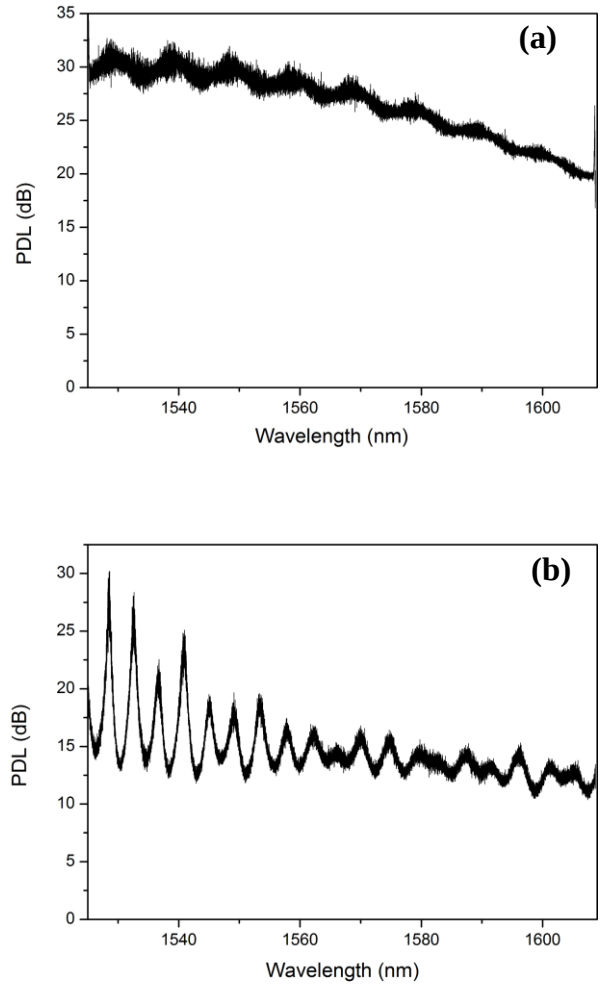

Figure 4.33 PDL profiles of the 45°-TFG in PM fibre inscribed along (a) slow- and (b) fast-axis from 1525 to 1605 nm measured by LUNA optical vector analyser 2000.

4.6.2 All-fibre polarization birefringent filter

Bornard Lyot first published the basic principle of a birefringent filter (also called as Lyot filter) operation in 1933[131]. A Lyot filter could be used as a comb filter, which is consisting of two parallel polarizers sandwiching a birefringent crystal whose axis is aligned at 45° with respect to the axes of the polarizers. As discussed in the earlier section of this chapter, 45°-TFG can be used

as a linearly polarizer. By inscribing two 45°-TFGs along a PM fibre, we may implement an all-fibre Lyot interference filter,

Figure 4.34 The schematic structure of an all-fibre Lyot interference filter based on two 45°-TFGs.

The configuration of the all-fibre Lyot filter based on two 45°-TFGs is illustrated in Figure 4.34. In experimental implementation, a length of PM fibre was spliced between two 45°-TFGs; the fast-axis of PM fibre was aligned at 45° to the fast-axis of the 45°-TFGs. In this structure, the 45°-TFGs inscribed along the fast-axis of PM fibre were used as the linear polarizers, and a section of bared PM fibre was used as the birefringence medium. The working principle of the all-fibre Lyot filter is that when light is passed through the first 45°-TFG it becomes linearly polarized, then, the linearly polarized light is incident on the PM fibre at 45°with respect to slow/fast axis, which resolves into two beams of equal intensity that travel in the fast- and slow-axes of the PM fibre. Due to the birefringence, there is a relative phase difference between these two beams, which leads to wavelength-dependent polarization state. Finally, the light with wavelength-dependent polarization state would be analysed by the second 45°-TFG and a wavelength-dependent intensity modulation is generated in the transmission. The normalized transmittance of the Lyot filter is given by [132]:

Equation 4.1 $$T = \cos^2(2\alpha + \beta) + \cos^2(\Delta\varphi / 2)\sin 2\alpha \sin 2(\alpha + \beta)$$

Equation 4.22 $$\Delta\varphi = \frac{2\pi L_{PM} \Delta n}{\lambda}$$

Where Δn is birefringence of PM fibre and L_{PM} is the length of PM fibre.

The free spectral range (FSR) of Lyot filter can be obtained [132] from Equation 4.22, as:

Equation 4.23 $$FSR \cong \frac{\lambda^2}{L_m \Delta n}$$

The full width half maximum (FWHM) of Lyot filter is half of the FSR of the filter. So the FWHM of Lyot filter can be expressed as:

Equation 4.24 $$\Delta\lambda_m \cong \frac{\lambda_m^2}{2L_{PM}\Delta n}$$

Based on Equation 4.23 and 4.24, the FSR and bandwidth of the Lyot filter transmission spectrum depends on the length of the PM fibre cavity. We have spliced three different lengths PM fibre (20m, 50m and 100m) between two 45°-TFGs in turn achieving three Lyot filters. Figure 4.35 shows the transmission spectra of the three Lyot filters, respectively. It can be clearly seen from the figure that the output from the 45°-TFG based Lyot filter exhibits comb-like transmission with sinusoidal shape and the bandwidth and FSR are PM fibre cavity length dependent. The bandwidths for 20m, 50m and 100m PM fibre cavities are 126.2pm, 57.2pm, and 28.7pm, respectively. These experiment results were found in agreement with its theoretical values (134.7 pm, 53.9 pm and 26.9pm).

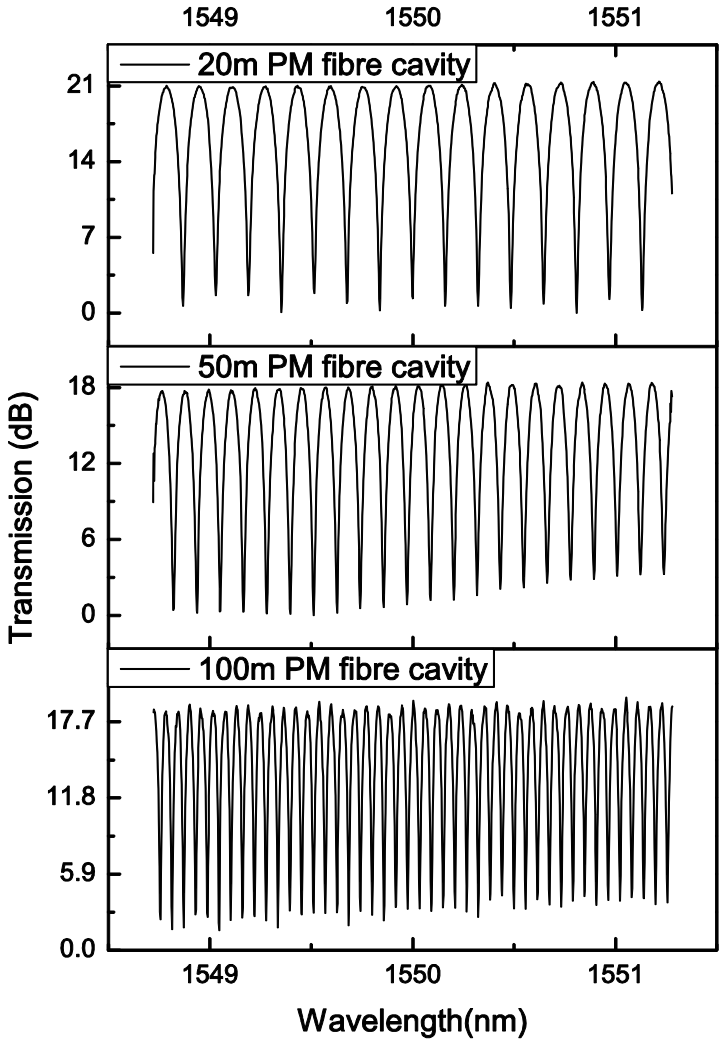

Figure 4.35 Transmission spectra of the 45°-TFG based Lyot filter with different PM fibre cavity lengths (20m, 50m and 100m).

We also compare the simulation and experimental results of the transmission spectra of Lyot filters with 50m and 100m PM fibre cavity lengths, which are shown in Figure 4.36 (a) and (b). It can be seen from figures the experimental results are in very good agreement with the simulation ones.

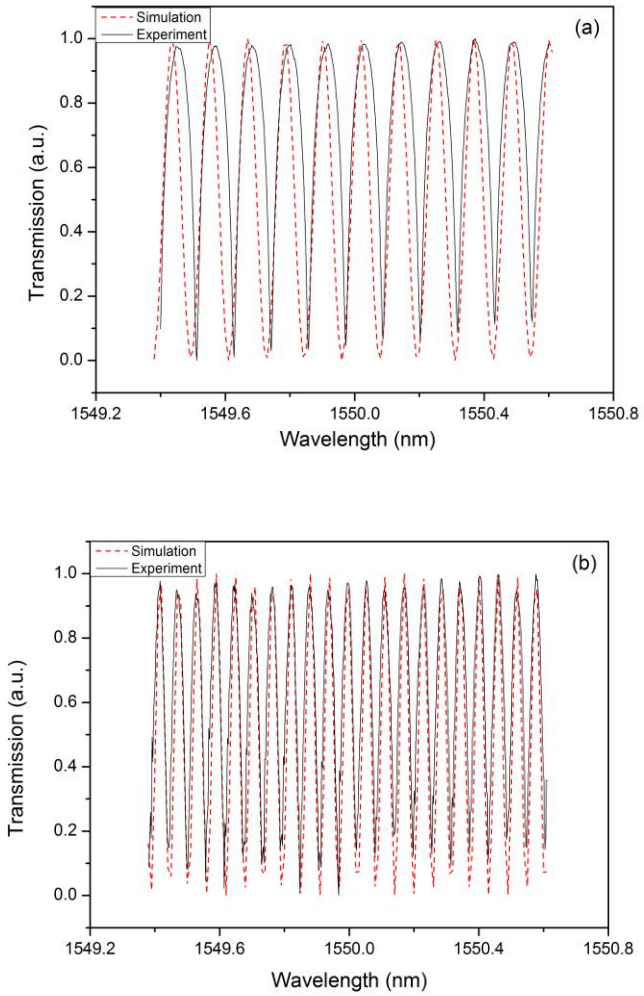

Figure 4.36 The simulated (red dash) and experimentally measured (black solid) comb-like transmission spectra of 45°-TFG based Lyot filters with (a) 50m and (b) 100m PM fibre cavity length.

4.7 Chapter Conclusion

In this chapter, systematic investigation of TFGs on the phase match condition, phase mask fabrication, spectral and polarization characteristics and applications in fibre laser systems has been presented.

For 45º-TFGs, the PDL has been discussed in the wavelength range from 1525nm to 1610nm and the maximum PDL achieved is ~21.1dB from a 24mm long grating. We also experimentally demonstrated the power tapping function of 45°-TFG and verified that the side-tapping efficiency deceases along the grating length, therefore, for a real power tapping device, a 45°-TFG of mm length may be sufficient enough. We further presents the experimental investigation of the functionality and loading application of 45º-TFG in EDFLs emitting continuous wavelength tuneable laser light of single polarisation and picosecond pulses in the region of 1.5μm. Finally, we demonstrate 45°-TFGs that were UV-inscribed along the principal axis of the PM fibre and based on 45°-TFGs in PM fibre, an all-fibre polarization interference filter can be constructed by 45°-TFG and PM fibre. All fibre Lyot filter generate comb-like transmission response and the FSR of filter can be easily designed by altering the PM fibre cavity length.

Chapter 5.

Fabrication, Spectral Characteristics and Applications of ex 45°-Tilted Optical Fibre Gratings

5.1 Introduction

The tilted fibre gratings with ex 45° tilted structures (ex 45°-TFGs) were firstly reported by Zhou et al, [133, 134]. In terms of mode coupling mechanism, an ex 45°-TFG is similar to an LPG as it couples the light from the forward propagating core mode to forward propagating cladding modes, but only to the higher order ones. Due to the asymmetric structure induced by the excessively tilted fringes in the fibre core, the light coupled into high order co-propagating cladding modes is splitting into two sets of polarization dependent modes resulting in dual-peak resonances in spectrum. Due to this unique polarization property, the large angle TFGs have been proposed as fibre sensors for the detection of loading[129], strain[134], twist[135], refractive index (RI) and liquid level[136, 137].

5.2 Principle of ex 45°-TFGs

The phase matching condition of TFG has been introduced in Chapter 4. Based on Equation 4.1, the ex 45°-TFGs phase matching condition can be written as:

Equation5.1 $$\lambda = (n_{co}^{eff}(\lambda) - n_{cl,m}^{i,eff}(\lambda))\frac{\Lambda_G}{\cos\theta} \qquad i = TE\ or\ TM$$

Where Λ_G is the normal period of grating and θ is the tilt angle of the grating and > 45°.

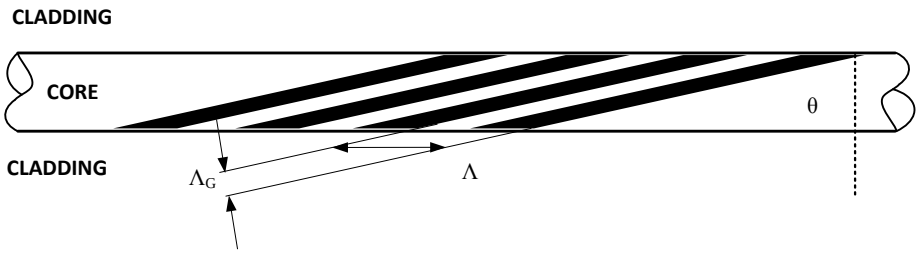

Figure 5.1 Schematic diagram of ex 45°-TFG structure in fibre core.

As shown in Figure 5.1, the geometry relation of horizontal axial period Λ, grating period Λ_G and the tilted angle θ of grating can be expressed as

Equation 5.2 $$\Lambda = \frac{\Lambda_G}{\cos\theta}$$

Using [137], ex 45°-TFG's phase matching condition can be rewritten by using the horizontal period as:

Equation 5.3 $$\lambda = (n_{co}^{eff}(\lambda) - n_{cl,m}^{i,eff}(\lambda))\Lambda \qquad \text{i} = \text{TE or TM}$$

It can be clearly seen from above equation that wavelength of ex 45°-TFG is relating to the mode index of core, m[th] order mode index of cladding and the horizontal axis period of grating. Once the ex 45°-TFG has been inscribed, mode index of core and the horizontal axis period of grating are fixed. The basic sensing theory of grating is the effective indices of the cladding modes are changing with the environmental condition. Zhijun Yan [137] gave the general sensitivity expression of cladding mode as follows:

$$\Delta\lambda = \frac{1}{1-(\frac{dn_{co}^{eff}}{d\lambda} - \frac{dn_{cl,m}^{eff}}{d\lambda})\Lambda}\left(\frac{(\delta n_{co}^{eff} - \delta n_{cl,m}^{eff})}{n_{co}^{eff}(\lambda) - n_{cl,m}^{eff}(\lambda)} + \frac{d\Lambda}{\Lambda}\right)\lambda$$

Equation 5.4

$$= \gamma(\Gamma + \alpha)\lambda$$

Where γ is the waveguide dispersion, Γ is the dependence of waveguide dispersion on environment and the material expansion α caused by the changing of environment and the λ is the operation wavelength. In Equation 5.4, the temperature and RI dependent waveguide dispersion (Γ_{TEM} & Γ_{RI}) are expressed as below, respectively:

Equation 5.5 $$\Gamma_{TEM} = \frac{(\xi_{co} n_{co}^{eff} - \xi_{cl} n_{cl,m}^{eff})}{n_{co}^{eff}(\lambda) - n_{cl,m}^{eff}(\lambda)}$$

Where ξ_{co} and ξ_{cl} are the thermo-optic coefficients of core and cladding materials, n_{co}^{eff} and $n_{cl,m}^{eff}$ are the effective index of core and m[th] order cladding mode.

Equation 5.6 $$\Gamma_{RI} = -\frac{u_m^2 \lambda^2 \Lambda n_{sur}}{8\pi^3 r^3 n_{cl,m}^{eff}(n_{cl}^2 - n_{sur}^2)^{3/2}}$$

Where u_m^2 is root of the zero order Bessel function; λ is the operation wavelength of cladding mode, n_{sur} is the RI of surrounding medium; r is the radius of fibre cladding; n_{cl} is the index of cladding .

5.3 Inscription and Characterisation of ex 45°-TFGs

5.3.1 Inscription of ex 45°-TFGs

As discussed in Chapter 4, if a TFG's tilted angle larger than 67° (for an air/glass interface), this ex 45°-TFG will couple the light from the core mode to the forward propagating cladding modes, which is similar to LPGs except the coupling to high order cladding modes. Although ex 45°-TFGs have a similar property as conventional LPGs, they could not be easily fabricated by the point-by-point technique. Because, its structure is tilted and it's period is relatively small (several microns). In order to evaluate their spectral, polarization and sensing property, a number of ex 45°-TFGs were UV-inscribed in hydrogen-loaded Corning SMF-28 fibre by the scanning mask technique using the same frequency doubled Argon ion laser. The mask used in ex 45°-TFG fabrication is a custom-designed amplitude mask with a period of 6.6μm purchased from Edmund Optics. Before ex 45°-TFGs fabrication, the SMF-28 fibre was hydrogen loaded under the standard condition to enhance its photosensitivity. The Figure 5.2 shows that the zero order diffraction of UV beam which generated by the amplitude mask for inscribing ex 45°-TFGs into the fibre core.

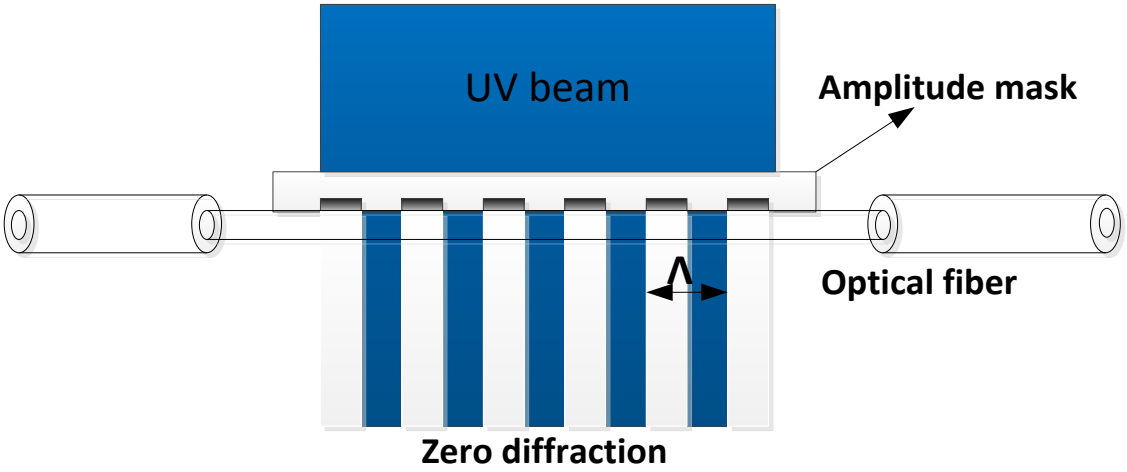

Figure 5.2 Schematic of the top view of amplitude mask and fibre with 0 order diffraction inside the fibre core.

Due to the lens effect of the cylindrical shape of the fibre, the internal tilted angle in the fibre core is different from the external tilted angle of the mask. In the experiment, the amplitude mask was tilted at 69° and 78° to produce in-fibre grating structures with tilted angles at 76° and 81°. Due to it being an amplitude mask, the ex 45°-TFGs were written by the zero order diffraction of UV laser beam which passed though the mask directly. After the UV inscription, some grating structures were examined under a microscope with 100X oil immersion objective lens. Figure 5.3 shows the image of tilted fringes in 76° and 81°-TFG and the measured angle is at 76.04° and 81.82° , which is very close to the design angle value.

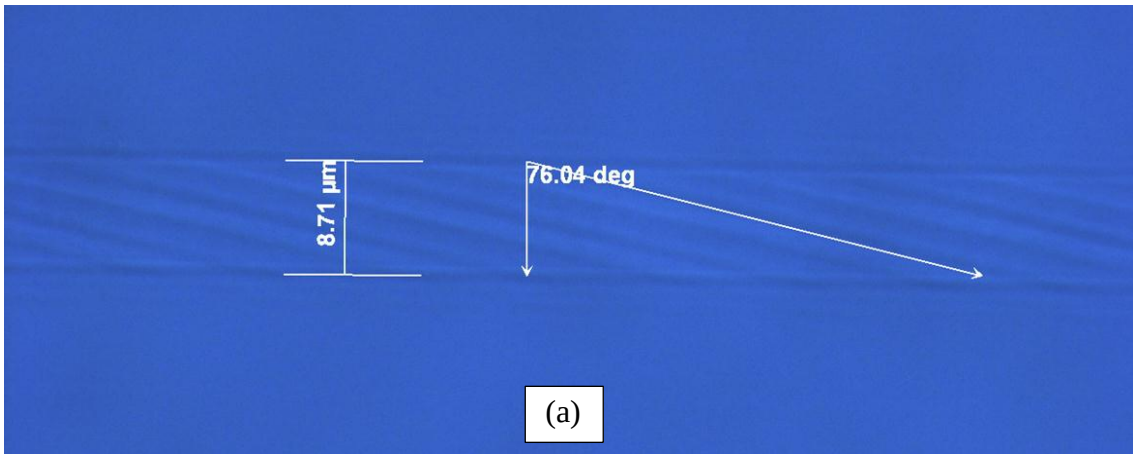

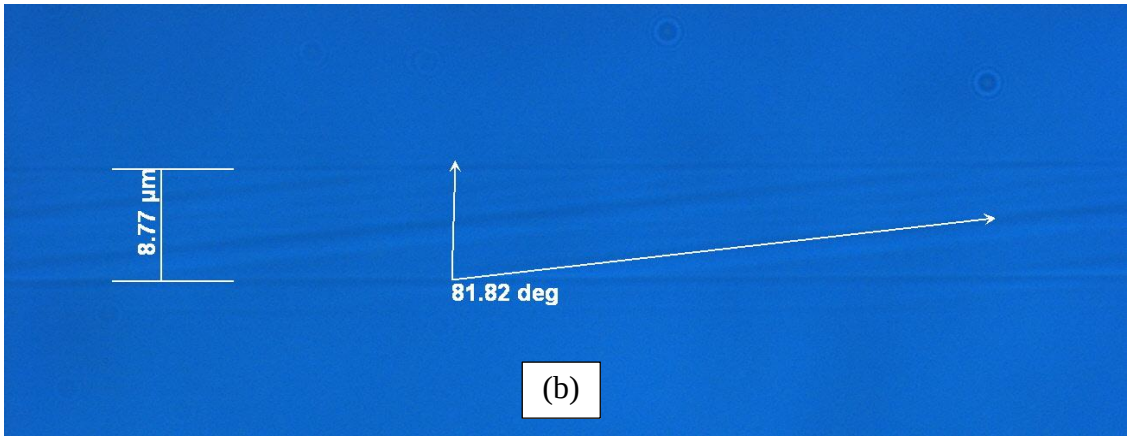

Figure 5.3 Microscope image of a TFG with tilted angle at (a) 76° and (b) 81° examined by microscope with 100X oil immersion objective lens.

5.3.2 The transmission spectra of ex 45°-TFGs

All fabricated ex 45°-TFGs were characterised using the experimental setup shown in Figure 5.4, the light from a broadband light source (from Aligent company) was launched into the one end of the ex 45°-TFG fibre and the output was monitored from the other end by an OSA. A linear polariser and a polarisation controller were inserted between the broadband light source and the ex 45°-TFG to change the polarisation state of the probing light.

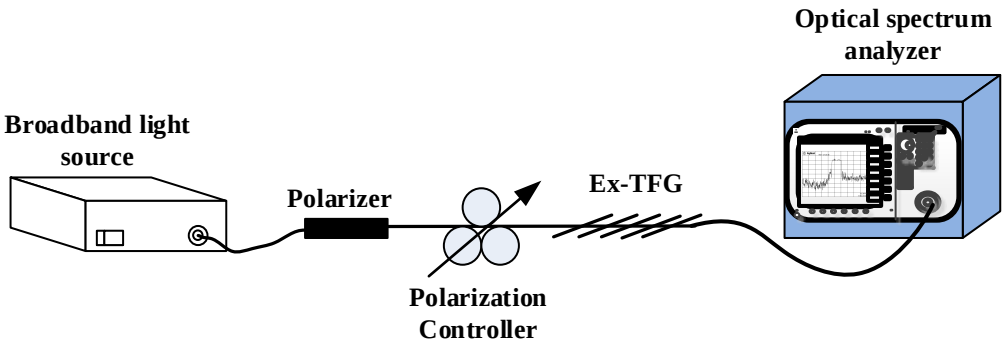

Figure 5.4 The measurement setup for ex 45°-TFGs.

As the index fringes are severely tilted in an ex-45°TFG, the asymmetric structure induces a significant birefringence to the fibre, resulting in all coupled cladding modes degenerating into two sets with orthogonal polarization states. Figure 5.5 (a) plots the typical transmission spectrum of an 81°-TFG, showing clearly the mode splitting and generating a series of dual-peak loss bands in the wavelength range from 1250 nm to 1650 nm. The zoomed transmission spectra of one of

the paired peaks for two (labelled as P1 and P2) orthogonally polarized states are shown in Figure 5.5(b). From the figure we can see that when the grating is probed with randomly polarized light, the two peaks show similar strength, e.g. 3-dB transmission loss; but when it was launched with orthogonally polarized lights (P1 or P2), one of the dual peaks grows to its full strength (~11 dB) whereas the other almost disappears.

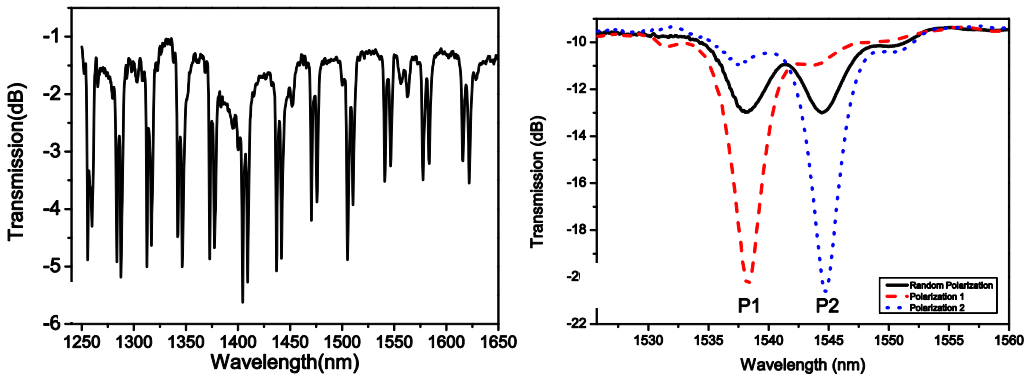

Figure 5.5 The transmission spectra of 81°-TFG: (a) a series of dual-peak resonances from 1250 to 1650 nm; (b) a paired dual peaks at around 1550nm when launched with randomly polarized light (black line) and orthogonally polarized lights (red line – TM; blue line - TE).

5.3.3 Evaluation of thermal response of ex 45°-TFGs

The thermal response of the 81°-TFG has been evaluated by the experiment setup shown in Figure 5.6. The grating was placed on the surface of a heat exchange plate while the temperature was tuned from 0°C to 80°C with an interval of 10°C. The polarizer and polarization controller were used to guarantee one of the dual peaks under measurement.

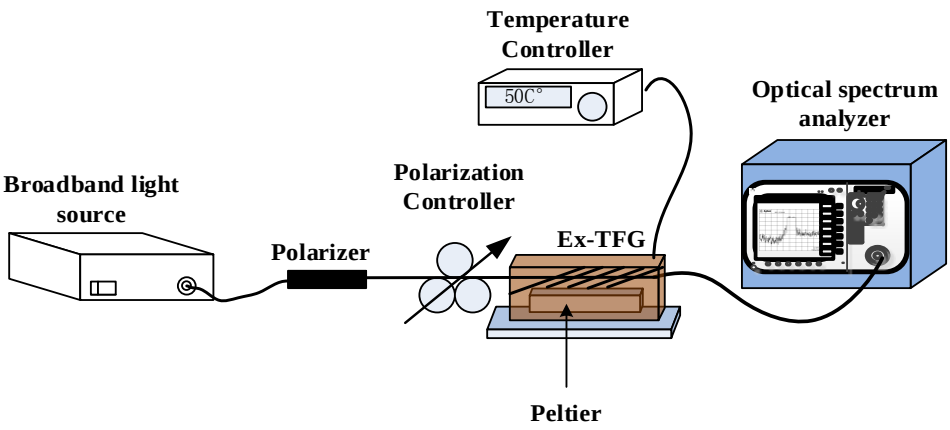

Figure 5.6 Experiment setup for temperature sensing of ex-45° TFG.

In the experiment, we examined a pair of peaks of the 81°-TFG at 1538nm and 1545nm. Figure 5.7 shows the wavelength shifts of the paired peaks against the temperature increasing from 0°C to 80°C. As clearly shown in the figure, the temperature sensitivities of the TM and TE cladding modes are 6.7pm/°C and 5.7pm/°C, which are significantly lower than that of the LPG (51.7 pm/°C) and FBG (13 pm/°C) at 1550 nm.

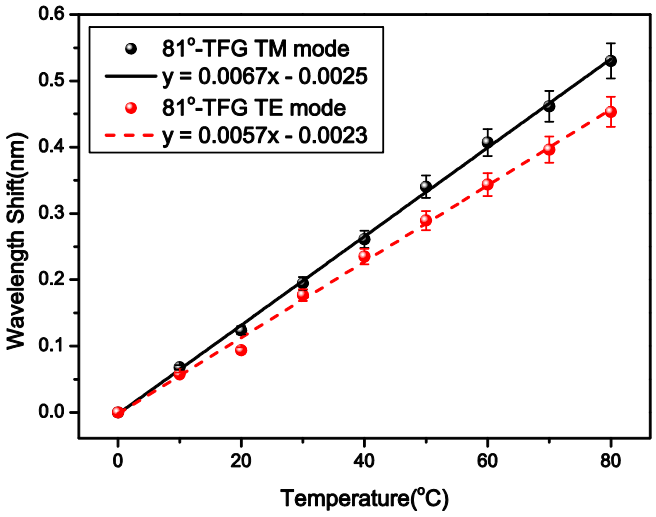

Figure 5.7 The wavelength shift of 81°-TFG against temperature change: for TM mode at 1538nm (black line) and TE mode at 1545nm (red line).

We also analysed the temperature sensitivities of TM peak at around 1550nm for 76°- and 81°-TFG. Figure 5.8 shows the wavelength shift of TM cladding mode against the temperature for these 2 ex-TFGs. From the linear fitting it can be seen clearly the temperature sensitivities are 4.2 pm/°C and 6.7pm/°C for 76° and 81° ex-TFGs, respectively. So, from the experimental results, we can see clearly that the thermal sensitivity is decreasing with decreasing of the tilted angle. However, both of 76° and 81°-TFGs sensitives are lower than the sensitivity of normal FBGs at 1550nm.

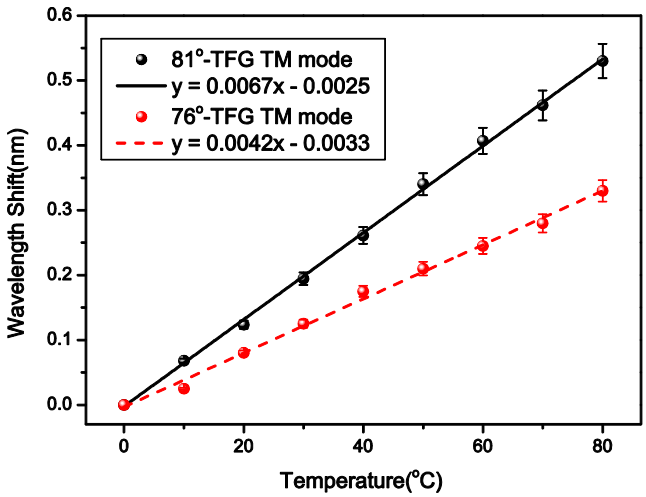

Figure 5.8 The temperature sensing results for TM cladding modes of ex-TFGs with tilted angle at 76° and 81°.

5.3.4 Surrounding medium refractive index sensing using ex 45°-TFGs

In this section, the surrounding medium refractive index (RI) sensing capability of the ex 45°-TFGs will be discussed. In the RI evaluation experiment (see set-up in Figure 5.9), the ex 45°-TFG was fixed straight on two stages to eliminate the system errors induced by bending. A series of refractive index gel (from Cargille laboratory) with different RIs from 1.305 to 1.44 were applied in turn over the grating area on the fibre sample, and the spectrum was monitored by an OSA. Once the grating was surrounded by the refractive index gel, the shift of wavelength was almost instantaneously displayed on the OSA. After each measurement, the refractive index gel adhered to the grating was washed out with methanol until the spectrum recovered to the original position on the OSA, e.g. when surrounded by air.

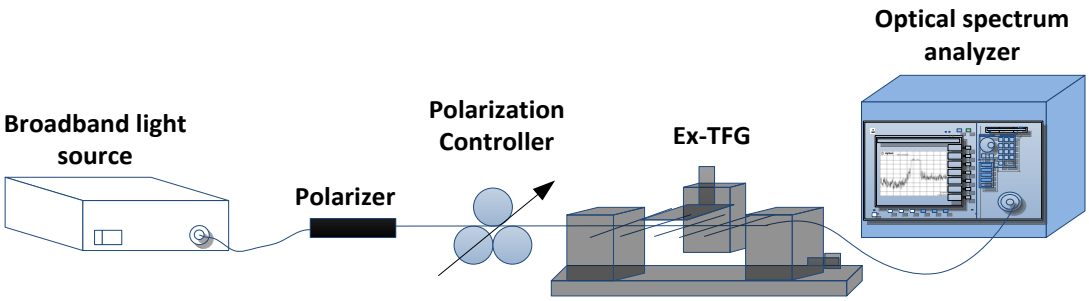

Figure 5.9 Schematic of the experimental setup for refractive index sensing of ex 45°-TFG.

Figure 5.10 plots the wavelength shift of TE and TM cladding mode peaks of an 81°-TFG responding to the RI variation from 1.305 to 1.408. It clearly shows that the RI sensitivity of TM mode is slightly higher than the TE mode. It can also be seen that the ex 45°-TFG exhibits a nonlinear RI sensitivity which differs from the linear trend of the temperature sensitivity. For the 81°-TFG, we can see from Figure 5.10, the total wavelength shifts of TM and TE mode are around 50 nm and 43.75 nm when RI changing from 1 (air) to 1.404. We also noticed that when RI was larger than 1.404, the cladding mode resonant peaks of 81°-TFG completely disappeared. This is caused by the fact that when the RI is larger than the high order cladding mode index, the light will be coupled out from the cladding to the radiation modes.

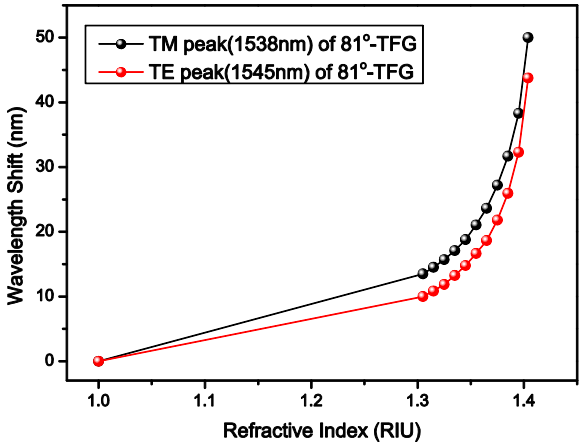

Figure 5.10 The RI response of 81°-TFG to TE mode at 1545nm (red) and TM at 1538nm (black).

Figure 5.11 shows the comparison of RI responses of TM cladding modes of 81°-TFG at different wavelengths. As it shown in the figure, each cladding mode has a different RI sensitivity. From the figure we can see, when the RI varies from 1.305 to 1.375, the RI sensitivities of TM cladding modes at 1620 nm, 1538 nm and 1310 nm are 307 nm/RIU, 196 nm/RIU and 126 nm/RIU, respectively. According to numerical analysis of ex 45°-TFG reported in Ref. [137], the cladding mode at longer wavelength is the lower order cladding mode, which is less sensitive to RI.

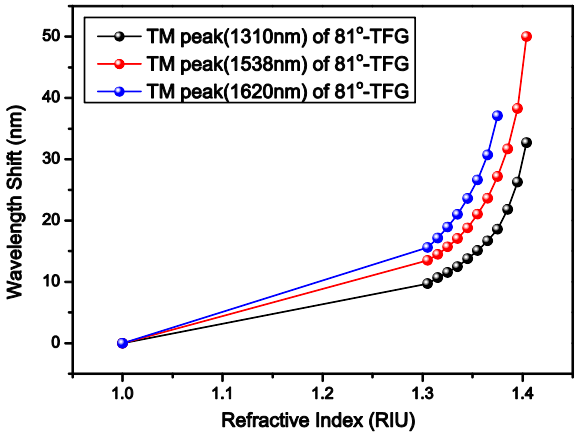

Figure 5.11 The RI responses of TM modes at 1620 nm, 1538 nm and 1310 nm.

The RI response evaluation was carried out on another TFG with slightly less tilted structure – a 76°-TFG and its response was compared with that of 81°-TFG. Figure 5.12 present the wavelength shifts of the TM peaks at around 1550nm region against RI for these two ex 45°-TFGs. From the measurement results, we can calculate out their RI sensitivities, which are at 499 nm/RIU and 396 nm/RIU covering the RI range from 1.3 to 1.4, for the two TFGs with structure tilted at 81° and 76°, respectively, indicating that the RI sensitivity increases with the tilt angle of the structure.

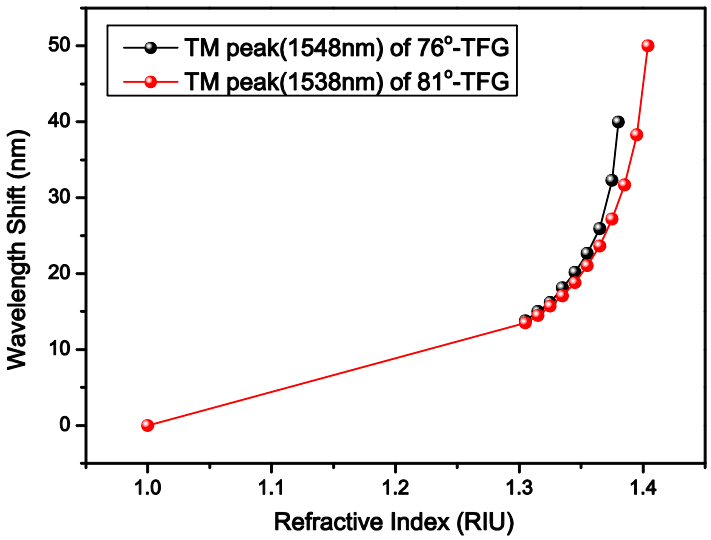

Figure 5.12 The RI responses of the TM modes (at around 1550nm) of two TFGs with structure tilted at 76° and 81° measured for the RI range from 1 to 1.4.

5.4 Novel glucose sensor based on enzyme-immobilized ex 45°-TFGs

Optical fibre biosensors have been proved as good tools for detecting specific bio-molecules in the fields of food safety, drug discovery, medical diagnosis and environmental monitoring [138-141], due to their advantages of small size, label free and high sensitivity and good selectivity. In clinic examination, it is very important to test the concentration of blood glucose, as glucose is the key source of energy of human body. Presently, only electrochemical methods are popular for the glucose analysis. In some published papers, unmodified LPG sensors have been used for non-selective analysis of very highly concentrated glucose solutions (300mg/mL) [142, 143]. Although the LPG sensor is simple to fabricate, but it suffers from the thermal and tensile cross-talk effect, because of its inherent properties of highly sensitive to the temperature and strain, and also its Q-factor is relatively low due to broad resonant spectrum. We have developed a novel sensor based on enzyme-immobilized ex 45°-TFG, offering higher bio-sensing sensitivity.

5.4.1 Grating surface modification by GOD immobilization

In order to achieve the selective method for glucose detection, the fibre surface of the grating sensor should be bio-functionalized by the glucose oxidase (GOD) firstly[144] . In this process, an 81°-TFG was initially immersed in HNO_3 solution (5% v/v) for 2h at 40°C to remove the contamination and then thoroughly washed by de-ionized water and ethanol. The cleaned fibre was then immersed in the H_2SO_4 solution (95% v/v in H_2O_2) for 1h at room temperature to activate the hydroxyl-groups (i.e., '-OH') on the glass surface followed by drying under an incandescent lamp for 18h at 40°C. An aminopropyltriethoxysilane(APTES) solution (10% v/v in ethanolic solution) is used to cultivate the -OH activated fibre for 40 min at room temperature in the silanized process, in which the NH^{3+} groups of the APTES molecules would covalently link to the -OH groups of the glass surface. Afterwards, the fibre was washed by de-ionized water and ethanol to remove non-covalently bonded silane compounds. Finally, the immobilization of enzyme molecules on the fibre surface was realized by immersed the silane fibre in 10mg/ml sodium acetate (SA) buffered solution of GOD for 2h incubation, in which the GOD's -COOH

groups would bind with the NH^{3+} groups on the surface of the silane fibre through covalent interaction. Figure 5.13 depicts the whole process of the fibre surface modification.

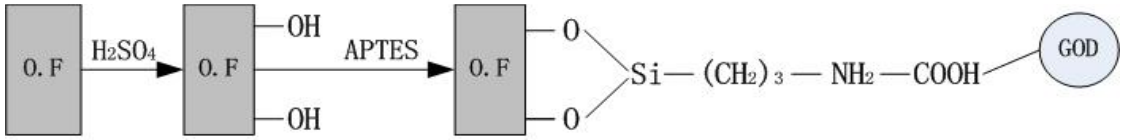

Figure 5.13 Modified process for the fibre surface of the 81°-TFG.

After the surface modification experiment, the GOD-immobilized fibre was inspected under the microscope. The micro images of the 81°-TFG showed in Figures 5.14 (a)-(c) corresponding to after cleaning, silanization and GOD-immobilization process, respectively. The comparison of Figure 5.14 (a) and (b) clearly shows that the surface of grating has been covered by a smooth silane layer. Figure 5.14 (d) shows the strong glowing fluorescence, indicating sufficient GOD molecules have been immobilized on the surface of the 81°-TFG.

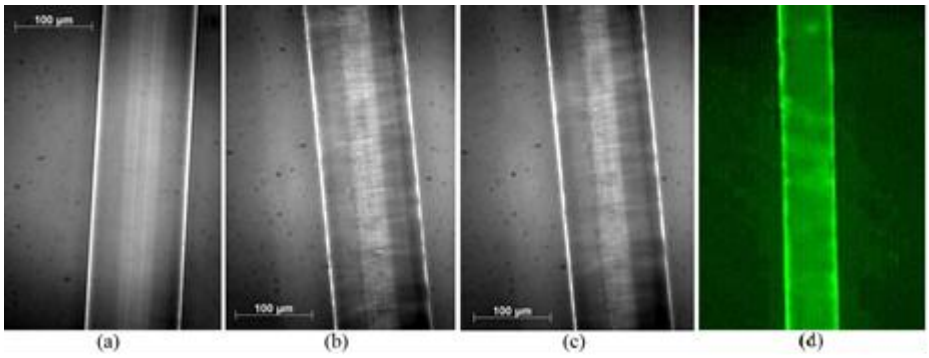

Figure 5.14 Micro image of the 81°-TFG based on (a) Cleaned fibre (b) Silane fibre (c) GOD-immobilized fibre (d) fluorescence fibre.

5.4.2 Glucose detection by GOD-immobilized 81°-TFG

The prepared GOD-immobilized 81°-TFG sensor was used for glucose detection. The selective method for glucose detection is based on the principle that the specific enzyme (i.e., GOD) immobilized on the surface of the 81°-TFG will cause the glucose (molecular weight = 180.6) to convert to the gluconic acid (molecular weight = 192.6), as shown in Equation 5.7 , leading to a relatively large RI change even in a dilute (e.g. 0.1~3mg/mL) glucose solution, which will in turn, cause a detectable shift of the resonance wavelength of the grating sensor.

Equation 5.7 $$D\text{-}Glucose + H_2O + O_2 \xrightarrow{GOD} D\text{-}Gluconic \quad acid + H_2O_2.$$

GOD used in our experiment was purchased from Sigma, and its enzymatic activity is larger than 200units/mg and one unit GOD will oxidize 1.0μ mole of β-D-Glucose to D-Gluconic acid and H_2O_2 per minute at pH 5.1 at 35°C. Thus, we prepared different concentrations of D-Glucose (0.1-5.0mg/ml) in the SA buffered solution (PH 5.2), which will provide a suitable chemical environment for this catalytic reaction. The experimental setup to investigate the correlation between D-Glucose concentration and grating spectral response is shown in Figure 5.15. Light from a broadband source (BBS, 1550A-TS, 1495~1595nm) was launched into the fibre and the transmission spectrum was recorded by an optical spectrum analyzer (OSA, AQ-6370B). A polarizer and a polarization controller (PC) were placed between the BBS and the grating to adjust and maintain the 81°-TFG to work only in the X-polarized mode.

Figure 5.15 Experimental setup for investigating the grating spectral response.

At the beginning, a pure SA buffer solution was introduced in the sample cell, and the observed resonant wavelength of the 81°-TFG was recorded as the reference. Then the prepared SA buffered solutions of D-Glucose with different concentrations were introduced into the sample cell in turn to investigate the correlation between the D-Glucose concentration and the grating spectral response. In each test, we measured the RI change induced resonance shift. After each test, the de-ionized water was used to wash the grating to guarantee its resonant wavelength

moving back to the reference point. For comparison, a non-modified 81°-TFG was also subjected to the evaluation. Figure 5.16(a) is the spectral evolution of one of the TM resonance peak with the increase of the glucose concentration from 0 to 3.0mg/ml. Because the red-shifted resonance amplitude is related to the change of average RI within the evanescence-field area surrounding the grating surface, therefore, according to Equation 4.1 and Equation 5.7, the more D-Glucose molecules (i.e., the higher the glucose solution concentration) and enough active GOD molecules exist in this evanescence-field area, the greater change of n_{cl}^{m} that affected by the change of this average RI will be. This will then result in a greater red-shift in the resonant wavelength. Figure 5.16(b) plots the resonant wavelength shift with D-Glucose concentration for the non-modified (square dots) and GOD-immobilized (circle dots) 81°- TFGs, indicating that, for the former, the resonant wavelength remains almost unchanged as the maximum variation of which is only ~0.08nm, compared with the reference point, while for the latter, it is red-shift for 0.91nm and has a good linear response with the increase of the glucose concentration from 0 to 3.0mg/ml. Linear fitting shows that the detecting sensitivity for the glucose concentration is 0.298nm·(mg/ml)−1 and the R-square ~0.99. The Q-factor of the sensor, defined by the working wavelength versus FWHM, is estimated to be ~1585nm/~4.5nm ≅ 352. However, the sensors did not respond properly in a higher concentration range from 3.0mg/ml to 5.0mg/ml. This may be due to the fact that since the activated grating length is only 10mm, above 3.0mg/ml, there were not enough active GODs to support a complete oxidation of the glucose molecules in this case, leading to a gradual decrease in the red-shifted amplitude of the resonant wavelength.

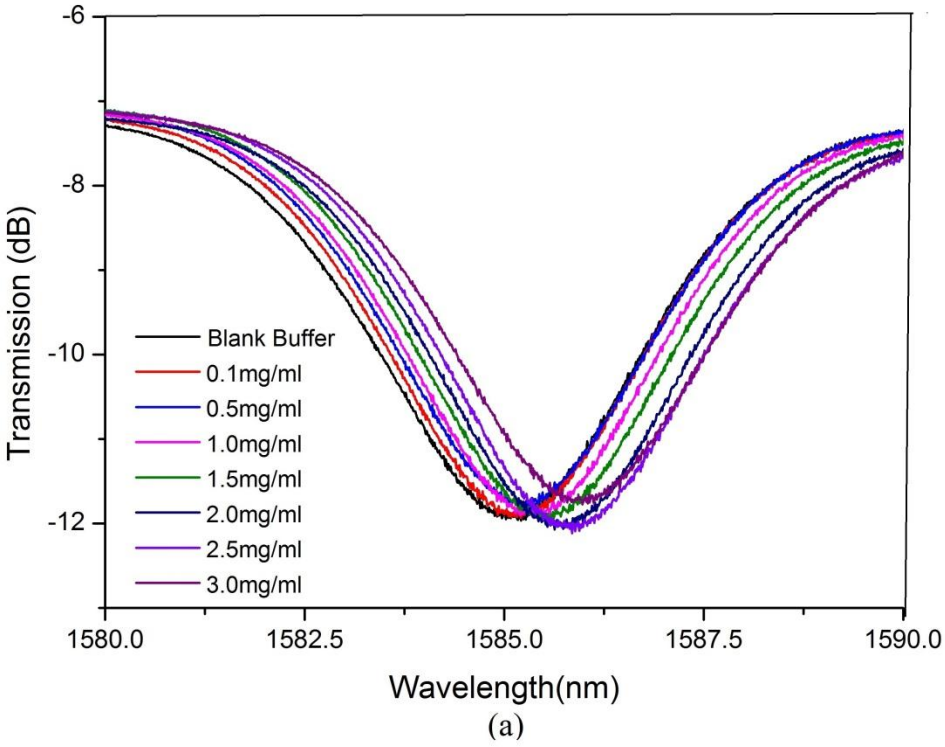

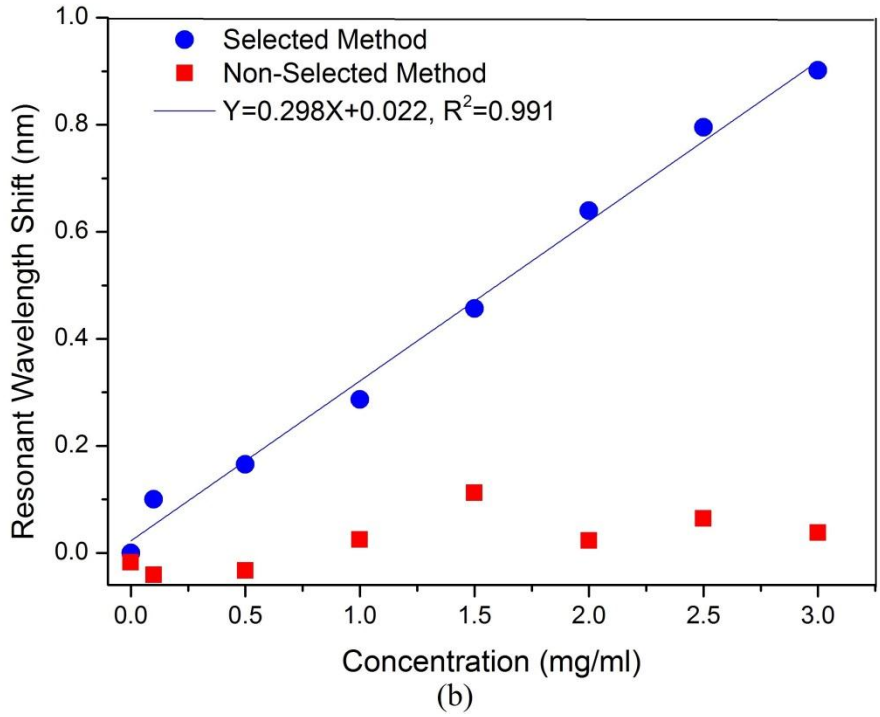

Figure 5.16 (a) Spectrum evolution of 81°-TFG with the glucose concentration; (b) Shift of the resonant wavelength of 81°-TFG by the selective method (GOD immobilized) and non-selective method (original) in the concentration range of 0~3.0mg/ml.

In order to evaluate the sensor re-usability, the GOD and silane layers on the fibre grating surface were removed by using the HNO_3 solution. Then, the above described experiment was conducted

again on the grating for three times, and the observed average variation in the resonant wavelength shift was only ±0.04nm, indicating a good reproducibility for the 81°-TFG based biosensors.

5.5 Transverse loading sensor based on hybrid 45°- and 81°-TFG

As we discussed in Chapter 4, 45°-TFG can be employed as an in-fibre polarizer. In this section we will present an all-fibre transverse loading sensor system based on a hybrid structure combining 45°- and 81°-TFG in a single piece of fibre. The use of the 45°-TFG is to polarizing the light before launching into 81°-TFG for loading sensing application.

5.5.1 Loading sensing principle and experiment

The polarization direction of the light in a fibre inevitably changes when a fibre is under loading effect. When the transverse loading is applied to the y-axis of 81°-TFG fibre as shown in Figure 5.17, the refractive index changes in the cross section due to the photo-elastic effect can be expressed by[145]

Equation 5.8 $$\Delta n = n_x - n_y = (n_{x0} - n_{y0}) + (C_1 - C_2)(\delta_x - \delta_y)$$

where n_{x0} and n_{y0} are the effective refractive indices of the fibre; C_1 and C_2 are the stress-optical coefficients; δ_x and δ_y are the stresses in x- and y-direction. For silica, the *C1* and *C2* are constant and always positive. Based on reference [146], the horizontal normal stress δ_x is always positive (tensile) and the vertical normal stress δ_y is negative (compressive), which means ($\delta_x - \delta_y$) is positive. Thus, the value of birefringence Δn is depending on the effective refractive indices of the fibre δ_x and δ_y. When the transverse load is applied to the fast axis of the 81°-TFG, we have $n_{x0} = n_s$ and $n_{y0} = n_f$ and the first term in Equation 5.8 will be positive, resulting in increase in birefringence Δn. When the transverse load is applied to the slow axis of the 81°-TFG, the birefringence Δn will be decreased. Therefore, the 81°- TFGs may be utilized to implement the optical loading sensors.

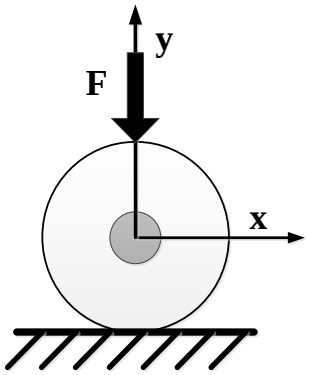

Figure 5.17 The cross section of a fibre in an assigned x–y coordinate system with transverse load applied along the y-axis.

The experimental setup of the load sensing is illustrated in Figure 5.18. Initially, the light from a broadband source (BBS) was launched into the 45°-TFG to be polarized before entering the 81°-TFG and the output was monitored from the other fibre end by an optical spectrum analyser (OSA). The 81°-TFG was laid between two flat-surface aluminium plates with a dummy fibre for balance. The active loading length between the two plates is 32 mm. In order to eliminate measurement errors from axial-strain and bending effects, the 81°-TFG was fixed on the plate with a small axial tension to maintain it straight.

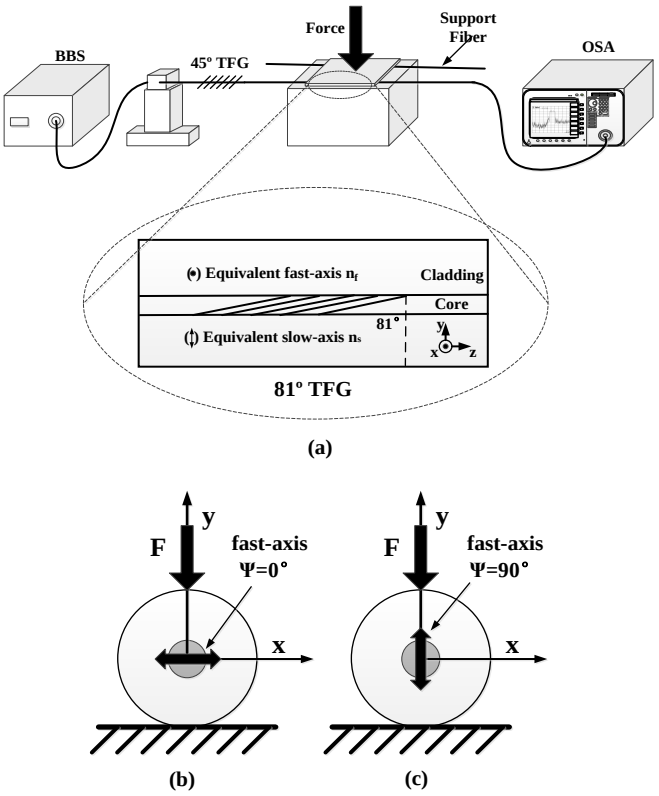

Figure 5.18 (a)The schematic diagram of the all-fibre transverse loading sensor based on a 45°-TFG and an 81°-TFG. The 81°-TFG in an x–y coordinate system showing transverse load applied to its (b) fast-axis and (c) slow-axis.

We applied the transverse load first to the equivalent fast-axis of 81°-TFG from 0 to 1.6 kg in a step of 0.1 kg by putting the weights on the top of the aluminium plate, as shown $\psi = 0°$ in Figure 5.18 (b).

5.5.2 Loading sensing results and discussion

The transmission spectrum for each applied load is plotted in Figure 5.19. As clearly seen, when the load was applied to the 81°-TFG, the P1 mode peak was gradually decreasing but P2 peak oppositely increasing, due to the load induced polarization state change. Figure 5.20 (a) plots the transmission loss against applied load for both peaks. We can see from Figure 5.20 (a) that for the loading range from 0 to 2.9 kg $m^{-1}$for peak P1 and 0 to 4.5 kg m^{-1} for P2, the transmission loss changes are almost linear, in which we estimate that the loading sensitivities are 1.902 dB/ (kg· m^{-1}) and 1.023 dB/ (kg· m^{-1}) respectively. Although we see the load-induced transmission loss goes through a cycle (maximum – minimum – maximum), however, the intensity of peak P1 is

not able to return to the initial point level with the cycles. The reason for this phenomenon is that the fibre deformation by transverse force induces the extra loss to the fibre waveguide. This loss will affect the loading sensitivity and limit the measurement range.

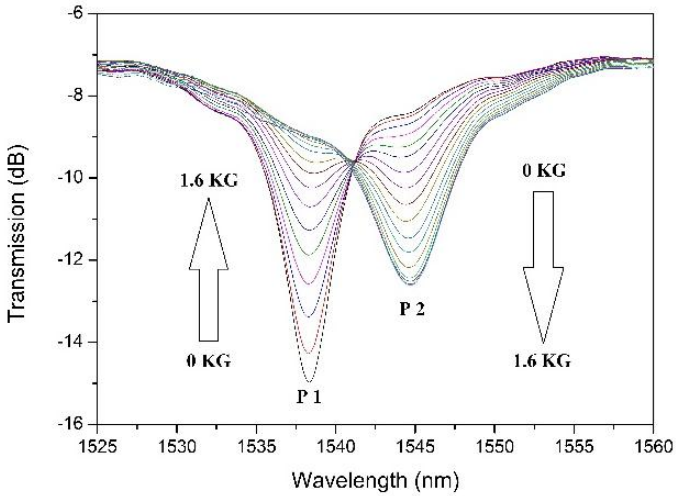

Figure 5.19 The transmission spectrum evolution of the 81°-TFG with transverse load from 0 kg to 1.6 kg applied to the fast-axis of 81°-TFG.

We then repeated the loading experiment by applying the transverse load to the grating slow-axis, as shown $\psi = 90°$ in Figure 5.19 (c). By increasing the force applied to the 81°-TFG, the P1 mode peak was decreasing, whereas the P2 peak was oppositely increasing, exhibiting a similar phenomenology to the case with the load applied to the grating fast-axis. However, it can be seen clearly from Figure. 5.20, both of the peaks of 81°-TFG will eventually disappear by further increasing the loading force. This may be explained by the fact that the birefringence Δn will decline with increasing load when the loading force is applied to the slow-axis of the 81°-TFG[134]. Thus, the low birefringence cannot maintain the light in two polarization states. As shown in Figure 5.20(b), the transmission loss changes by loading to the slow-axis are almost linear for the loading range from 0 to 4.2 kg $m^{-1}$for peak P1 and 0 to 5.2 kg m^{-1} for P2, in which we estimate that the loading sensitivities are approximately 1.365 dB/ (kg· m^{-1}) and 0.491dB/ (kg· m^{-1}) respectively. We can see for loading to the slow-axis, the initial linear response range is larger than for loading to the fast-axis, but the loading response degrades much significantly with further increased loading.

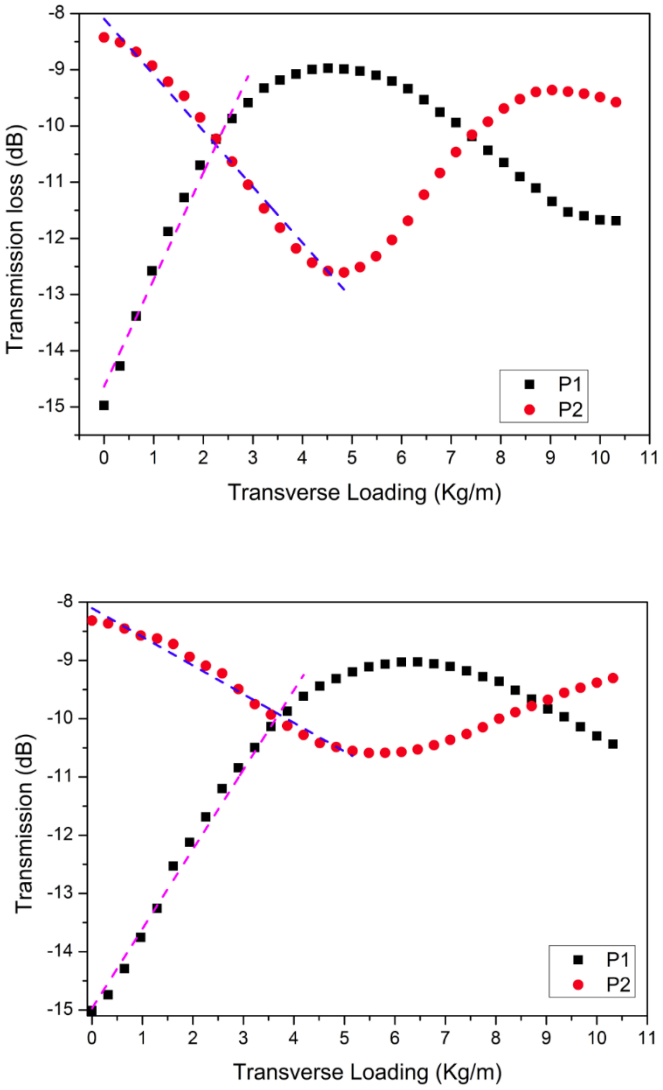

Figure 5.20 (a) Transmission losses of the two orthogonal polarization modes plotted with increasing load to fast (ψ = 0°) axis. (b) to slow (ψ = 90°) axis.

5.5.3 Loading sensing by low-cost power based interrogation

From above described experimental results, we can see the load only induces a power coupling exchange between the dual peaks with orthogonal polarization states. Thus, the hybrid TFG based loading system may be interrogated using a low cost power measurement, which is much more desirable for real applications. To this end, we have replaced the BBS and OSA in Figure 5.18 (a) with a tunable laser (in a real application, this can be a cheap single wavelength laser diode) and a power meter respectively, the schematic diagram is shown in Figure 5.21.

Figure 5.21 The schematic diagram of the transverse loading experiment system using a single wavelength source and a power meter.

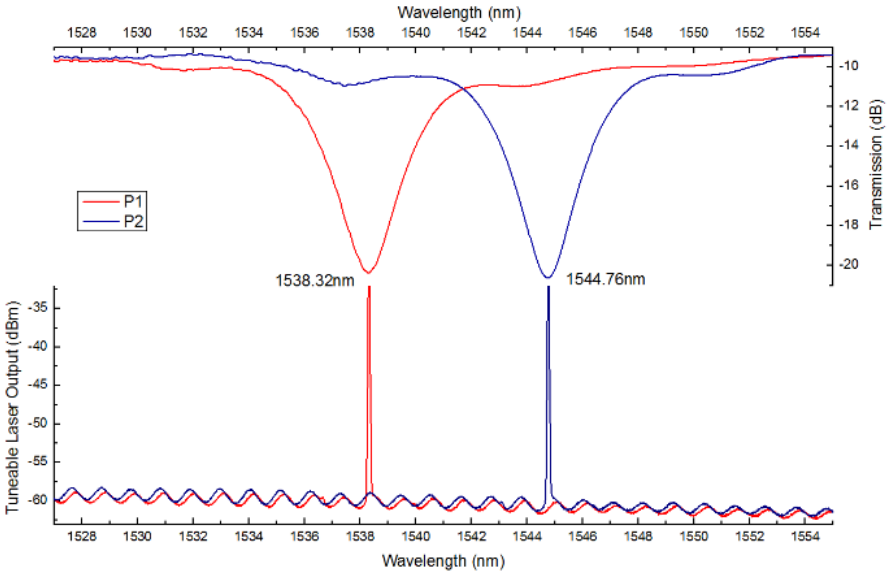

Figure 5.22 The upper plot is the transmission spectra of paired polarization peaks of 81°-TFG; the wavelength of the P1 loss peak is at 1538.32 nm and that of the P2 peak is at 1544.76 nm. The lower plot is the output spectra of the tunable laser set at the wavelengths of 1538.32 nm and 1544.76 nm, separately.

The spectra of the paired polarization peaks (1538.32 nm and 1544.76 nm) of 81°-TFG under loading are shown in Figure 5.22. In the experiment, we first tuned the laser to the P1 peak at 1538.32 nm and applied the load from 0 to 3.2 kg with an incremental of 0.1 kg to the 81°-TFG fast-axis and recorded the power reading accordingly, and then repeated this measurement by tuning the laser to match P2 at 1544.76nm. Figure 5.23 plots the measured power values against the applied load for the two peaks. Clearly, the load can be measured up to the range of 10kg/m. Although the entire plots are not linear, there is an almost linear loading response range from 0 to 3.5 $kg \cdot m^{-1}$for peak P1 and from 0 to 4.0 $kg \cdot m^{-1}$ for peak P2, in which we estimate that the loading

sensitivities are approximately 30.142 ± 1.326 μW/ (kg· m^{-1}) and 16.319 ± 0.393μW/ (kg· m^{-1}) respectively. As the load is measured in electronic signal form, this may provide a mechanism that potentially the signal may be transmitted wirelessly for remote control and monitoring.

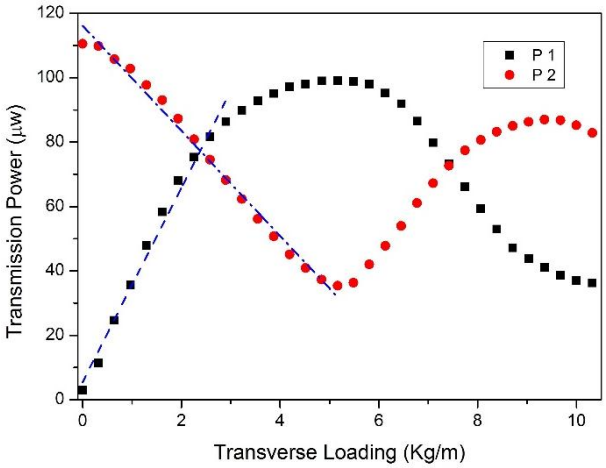

Figure 5.23 Transmission powers variation for the two orthogonal polarization peaks measured using the tuneable laser and power meter.

5.6 Chapter conclusion

In this Chapter, the principle of ex-45°TFGs have been briefly introduced and their transmission spectra characteristics have been examined, which shows paired peaks for two orthogonally polarization states. The thermal property investigation on ex 45°-TFGs with different angles (76° and 81°) was carried out, showing typical thermal sensitivities of 4pm/°C and 4.2pm/°C for the 76°-TFG and 81°-TFG at the resonance wavelength around 1550nm, which are significantly lower than that of LPGs and also lower comparing with normal FBGs. The RI response investigation shows that the sensitivity of TM mode is slightly larger than that of the TE mode, with the average RI sensitivities of 365nm/RIU and 337 nm/RIU for the TM and TE modes around 1550nm, in the index range from 1.305 to 1.404. All demonstrated ex 45°-TFG based RI sensors could be further implemented as optical biosensors by applying bio-active coating to them for potential applications in chemical, biomedical and biological detection and monitoring. We have demonstrated a cost-effective biosensor based on an 81°-TFG to detect the glucose concentration within the physiological range (0~3.0mg/ml) of human being. Comparing with the previous enzyme-immobilized LPG biosensor, the glucose sensor we proposed possesses several intrinsic advantages, including relatively higher RI sensitivity (168nm/RIU), much lower thermal cross-talk effect and higher Q-factor (352). Finally, we have demonstrated a loading sensor based on a hybrid 45° and 81° TFG, in which the two TFGs were inscribed on the same fibre adjacent to each other. Such a hybrid structure can ensure only one polarized mode is selected for detection. The evaluated loading sensitivities are 1.365 dB/ (kg· m^{-1}) and 0.491 dB/ (kg· m^{-1}) respectively at the loading range of from 0 to 4.2 kg $m^{-1}$for TM peak and 0 to 5.2 kg m^{-1} for TE peak, respectively.

Chapter 6.

Fabrication and application of optical fibre gratings in mid-IR wavelength range

6.1 Introduction

In recent years, the optical fibre devices operating at mid infrared (mid-IR) region have attracted growing interests due to their application potentials in defence[12], remote sensing [14], medical surgery [147], etc. Optical fibre gratings as useful in-fibre components are in demand to extend their operation wavelength range from near-IR into mid-IR. Moreover, laser sources locating at eye-safe 2μm region, especially for operation wavelengths in the atmospheric transmission window between 2.05μm and 2.3μm, have attracted special attention. However, most of the reported mid-IR fibre lasers use the bulk mirrors in the cavities, inducing high insertion loss and limiting the structure compactness. FBGs can be used as intra-cavity resonators for all fibre lasers to eliminate these disadvantages. Therefore, the fabrication of FBGs covering all the mid-IR wavelength range is the key factor for the development of all fibre mid-IR lasers. Besides, the 45°-TFG can be employed as an in-fibre polarizer in a mid-IR mode-locked fibre laser providing the effect of nonlinear polarization evolution (NPE)[148] and as well as low insertion loss and high compactness.

In this Chapter, we report mid-IR fibre gratings fabricated using three main in-fibre grating fabrication techniques (two-beam holographic, phase-mask, and point-by-point). Grating structures including FBGs, LPGs and 45°-TFGs have been realized in around 2μm and their thermal, strain and RI response, as well as polarization dependent loss (PDL), have been systematically characterized. In addition, we present the results on a multi-wavelength continue wave (CW) mid-IR fibre laser utilizing a set of FBGs with Bragg wavelengths in mid-IR range and a tuneable multi-wavelength fibre laser using a 45°-TFG with PDL function in mid-IR wavelength range.

6.2 Optical fibre grating in mid-IR wavelength range

6.2.1 Fabrication and characteristics of FBGs in mid-IR wavelength range

The mid-IR FBGs reported in this thesis were fabricated by a 244nm UV source from a frequency doubled Ar+ laser (Coherent Sabre Fred®) using only the two-beam holographic technique. The two-beam holographic technique for writing grating structure from the side of fibre is a flexible technique allowing inscribing FBGs with arbitrary wavelengths ranging from 750nm to 2300nm in our laboratory. We fabricated mid-IR FBGs with centred wavelengths from 1800nm to 2225nm. A super continuum broadband light source (Fianium SC480, UK) was employed to monitor the FBG growth during the UV inscription. The mid-IR FBGs were UV-inscribe in Corning SMF-28 and Thorlabs SM-2000 fibres to compare their characteristics. Note, before the FBG inscription, both SMF-28 and SM-2000 fibres were hydrogen loaded under high-temperature (80°C) and high-pressure (150 bar) for 2 days to increase their UV-photosensitivity. However, a great quantity of hydroxide ions in the hydrogen loaded fibre caused strong light absorption in the wavelength range from 1800nm to 1900nm[149]. Figure 6.1 shows the transmission spectra of SMF-28 fibre with and without hydrogen loaded and the transmission spectrum after annealing. It can be clearly seen that the strong absorption at 1850nm region has vanished after putting the SMF-28 in the oven at 80°C for 48hours as the annealing released the hydrogen in the fibre core.

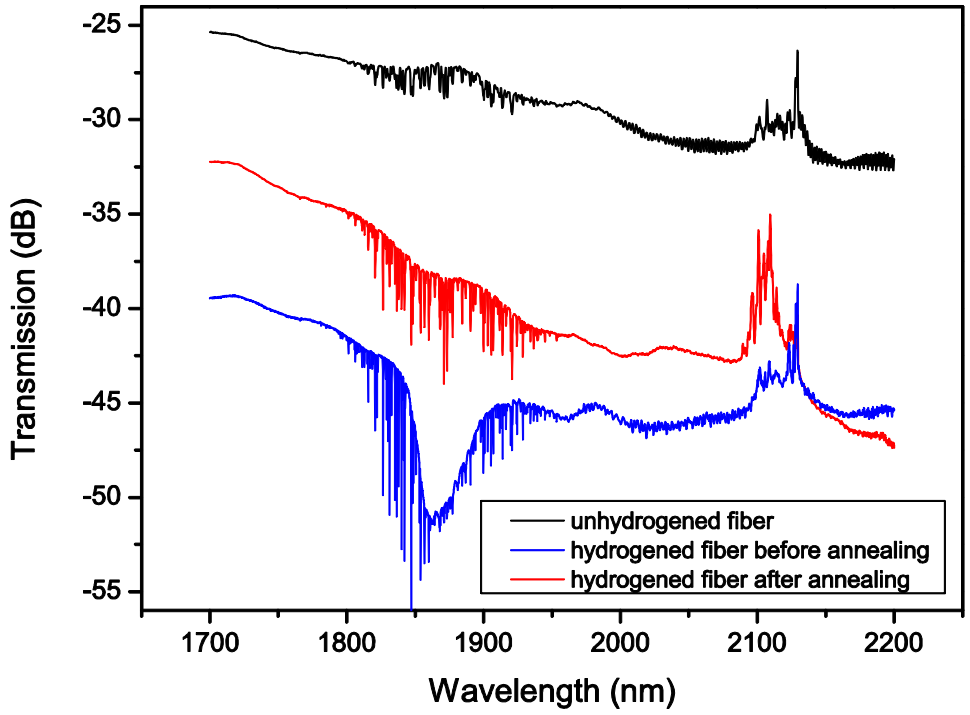

Figure 6.1 Transmission spectra of SMF-28 fibre with and without hydrogen loading and after annealing, measured using the supercontinuum light source from 1700 nm to 2200 nm.

It is clear that there is a broad absorption peak between 1830nm and 1900nm in the hydrogen loaded fibre. Therefore, the FBGs with Bragg resonances in this absorbing wavelength range were not be possibly monitored in the fabrication process, but were measured after the annealing treatment, which out-gas the hydrogen from the fibre. All mid-IR FBGs were annealed at 80°C for 48 hours to improve their long term stability. Figure 6.2 shows the measured transmission spectra of three FBGs inscribed in the SMF-28 and three in SMF-2000 fibres centred at 1800 nm, 2050 nm and 2225 nm, respectively. From Figure 6.2 we can see that the transmission loss (reflection) peaks of the six FBGs reach around 16-20dB, corresponding to a reflectivity of 96-99%; the 3dB bandwidths (FWHMs) are all less than 0.4nm. It also can be seen that the FBGs UV-inscribed in SMF-28 fibre are stronger with slightly high reflectivity and broad bandwidth than that in SMF-2000 fibre.

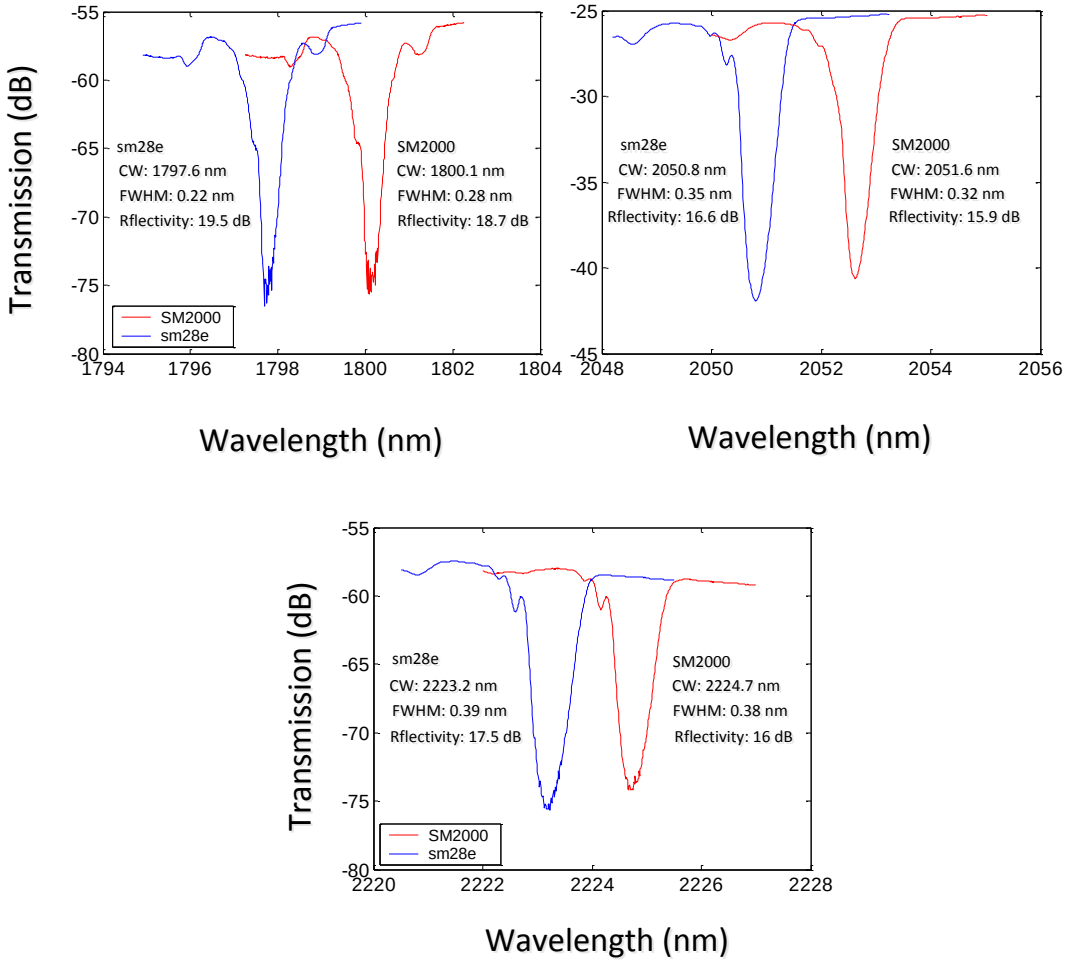

Figure 6.2 Measured transmission spectra of FBGs inscribed on SMF-28 and SMF-2000 fibres.

As we discussed in Chapter 3, the effective refractive index (RI) and the period of an FBG will be affected by temperature and strain changes. We then examined the thermal response of three FBGs with different wavelengths fabricated in SMF-28 fiber by employing the set-up described in Chapter 3 Figure 3.9. The temperature was varied from 0°C to 80°C at a step of 10°C. For each temperature, the FBG resonance was measured and recorded by the OSA. From Figure 6.3, it can be seen that the three FBGs with different wavelengths exhibit slightly different thermal responses. The temperature sensitivities are 15.4 pm/°C, 15.9 pm/°C and 16.3 pm/°C for the FBGs with the central wavelengths at 1950 nm, 2000 nm, and 2100 nm, respectively, which shows that the longer the FBG central wavelength is, the higher the temperature sensitivity.

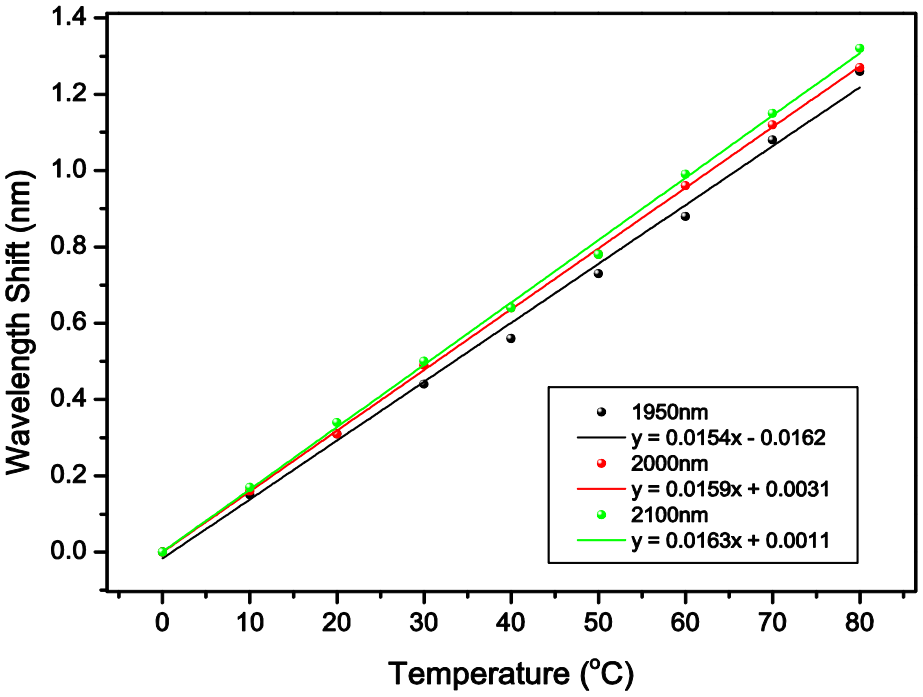

Figure 6.3 Comparison of thermal responses for three mid-IR FBGs with Bragg wavelengths at 1950nm, 2000nm and 2100nm.

The strain response of mid-IR FBGs was investigated using the experimental set up shown in Figure 3.11. The FBG was straightly clamped on two 3D moving stages set at a distance of 40cm. The varied strain supplied to the grating was realized by moving the right-side stage from 0mm to 0.35mm at a step of 0.05mm, which gives a total strain variation of 750 με. Figure 6.4 presents the strain responses of the three FBGs measured by the OSA. It can be seen that the strain sensitivities are 1.47 pm/με, 1.51 pm/με and 1.56 pm/με for the FBGs with the central wavelength at 1950 nm, 2000 nm, and 2100 nm, respectively, which demonstrates that the FBG with the Bragg resonance in the longer wavelength range also exhibits slightly higher strain sensitivity than that in shorter wavelength range.

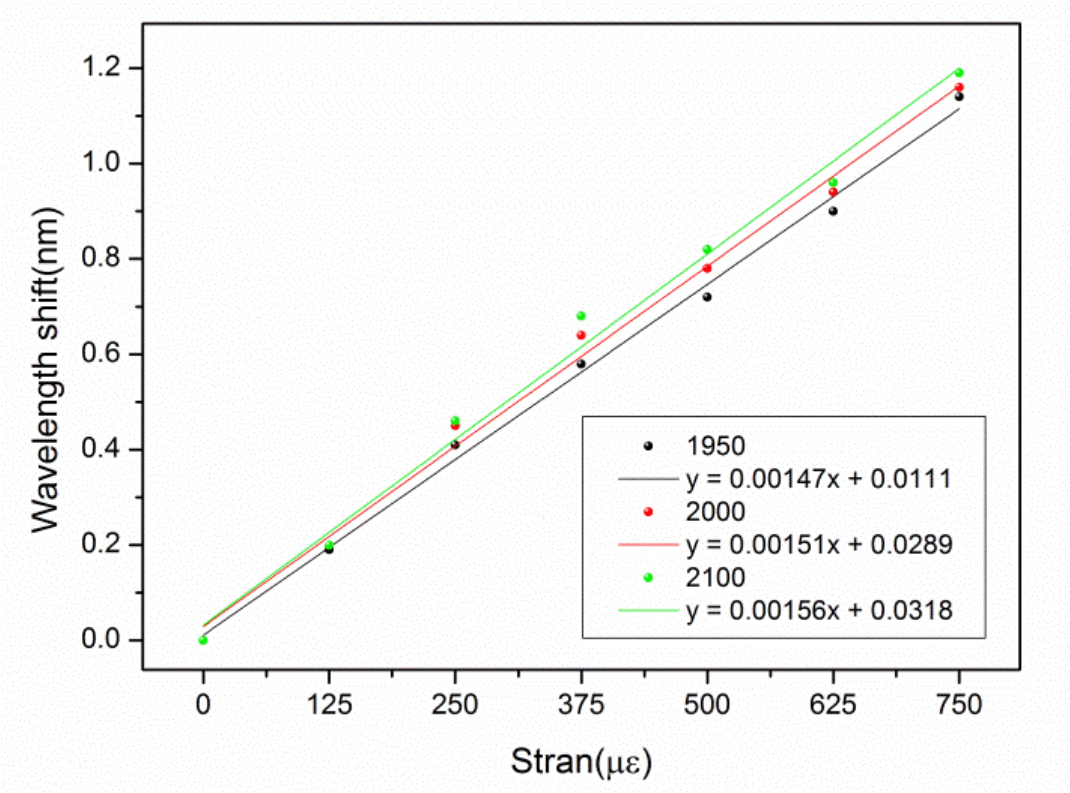

Figure 6.4 Comparison of the strain responses for three FBGs with different wavelengths.

6.2.2 Fabrication and characterization of TFGs in mid-IR wavelength range

The 45°-TFGs centred at ~2000 nm were also UV inscribed into SMF-28 fibre by using the phase-mask scanning technique and the same UV laser. The phase-mask (Ibsen, Denmark) has a 25 mm long uniform pitch and 33.7° tilted angle with respect to the fibre axis. The designed phase mask tilted angle at 33.7° is to ensure the internal tilted index fringes are at 45° in the fibre core. Before the inscription, the SMF-28 fibre was hydrogen loaded to enhance its photosensitivity. After the inscription, the grating samples were subjected to annealing treatment at 80°C for 48 hours to stabilize the grating structure. A high magnification microscope system (Zeis Axioskop 2 mot plus) under a 100× oil immersion objective lens was employed to examine the grating structure. Figure 6.5 shows a micro-image of the 45°-TFG in the fibre core of SMF-28 fibre. It can be seen clearly from the figure that the tilted angle of grating pattern is measured at 44.98° and the diameter of fibre core is 8.77 μm. The effective length of the TFG was 24 mm.

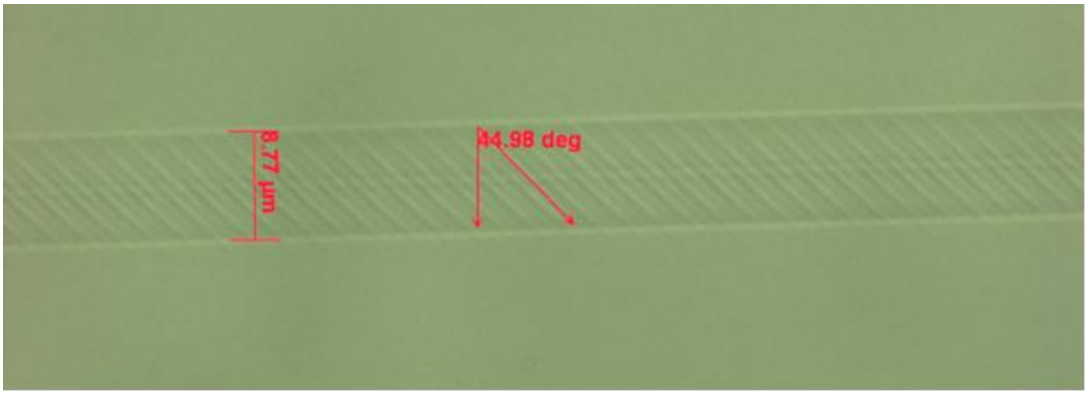

Figure 6.5 Microscopic image of the 45°-TFG taken under a 100 × oil objective lens.

As discussed before, the 45°-TFG can be recognized as an ideal in-fibre polarizer. Thus, polarization dependence loss (PDL) or the polarization extinction ratio (PER) is the important parameter of a 45°-TFG. The PDL is a measure of the peak-to-peak difference in transmission of an optical component or the ratio of the maximum and the minimum transmission of a system with respect to all possible states of polarization. The PDL of the mid-IR 45°-TFG was measured by using the polarization scanning technique. The typical experimental setup is shown in Figure 6.6 (a). In this setup, the light source is a super continuum source which can generate light from 450nm to 2400nm. The polarizer (Thorlabs LPNIRA050-MP) is a bulk component which has a high PDL of >50 dB at a range from 1550nm to 2450nm. To measure the PDL of the 45°-TFG at a specific wavelength, the central wavelength of optical spectrum analyser (Yokogawa AQ6375) was set at the measuring wavelength, and the span was set to zero. The maximum and minimum transmission through the 45°-TFG can directly be measured by adjusting the polarization controller. Figure 6.6 (b) depicts the simulated and measured PDL of the 45°-TFG within the range from 1600nm to 2400nm. The simulation method we used is volume current method, of which the details have been reported in [116]. In the simulation, the fibre core radius is set as 4.5μm, the period of grating as 0.990μm and the length of grating as 24mm. The refractive index modulation induced by the UV light was set to be 0.0017. It is observed that the simulation result agrees well with the experimental result as shown in Figure 6.6(b). The measured bandwidth of PDL is broader than 400 nm and the PDL is larger than 12dB from 1850 nm to 2150 nm. Although the maximum PDL of the 45°-TFG at 2000nm is 24dB, which is still low compared to the

commercial in-line polarizers at 1550nm (40dB), it is comparable with current commercial in-line polarizers at 2000nm (25dB). Moreover, the PDL (PER) of the 45°-TFG could be further increased by extending the length of grating and optimizing the UV scanning power and speed. This 3dB bandwidth of the mid-IR 45°-TFG is 532nm. According the equation 4.8, the 3dB bandwidth becomes broader when the operating wavelength moves to the longer wavelength. Using the same setup as shown in Figure 4.12, we also measured the insertion loss of the 45°-TFG, which was about ~0.6 dB within the range of 1850 nm to 2150nm.

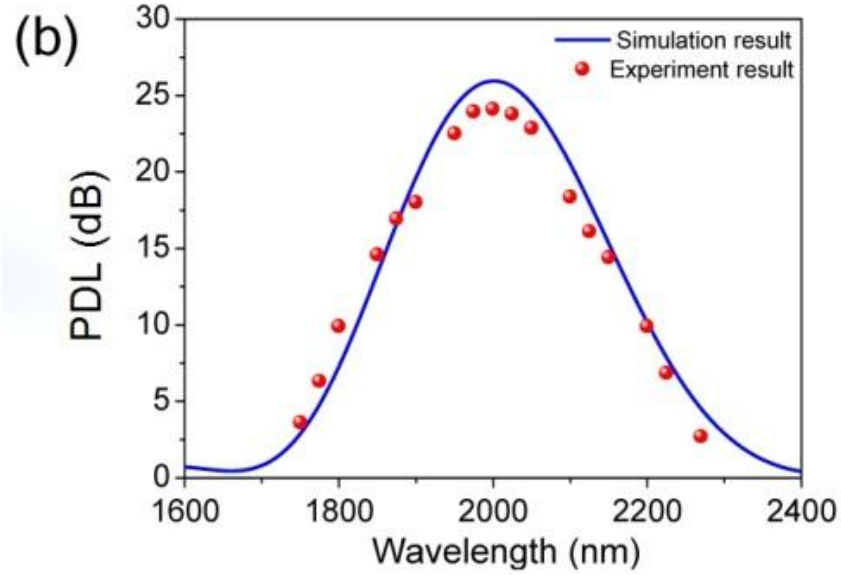

Figure 6.6 (a) Experimental setup of PDL measurement of 45°-TFG and (b) measured PDL at the range from 1800 nm to 2200 nm.

6.2.3 Characteristics and fabrication of LPGs in mid-IR wavelength range

The mid-IR LPGs of periods from 200μm to 450μm were written in hydrogen loaded Corning SMF-28 fiber by using the same 244 nm UV laser and point-by-point technique. The UV beam scanning speed was selected in the range of 0.1 mm/s to 0.3 mm/s and the duty cycles were 50%. Using the supercontinuum broadband light source and an optical spectrum analyzer with spectral range extended to 2.4 μm (Yokogawa AQ 6375), the transmission spectra of fabricated mid-IR LPGs were measured and Figure 6.7 shows the transmission spectrum of an LPG with a length of 20mm and a period of 200μm. From the figure we can clearly see that there are three broad attenuation resonant peaks distributed from near-IR (1200nm) to mid-IR (2400nm) range, and two of them are at 2μm region. The transmission loss peak at 2000 nm is relatively weak and the one at mid-IR 2183 nm (mode order m=9) exhibits a loss of 8.2 dB. The bandwidth of this resonance is >10nm, much broader than that of an FBG. LPGs are transmission loss type devices which have been employed for a range of applications in optical fiber communications and sensing, and these LPGs could translate the applications to mid-IR range.

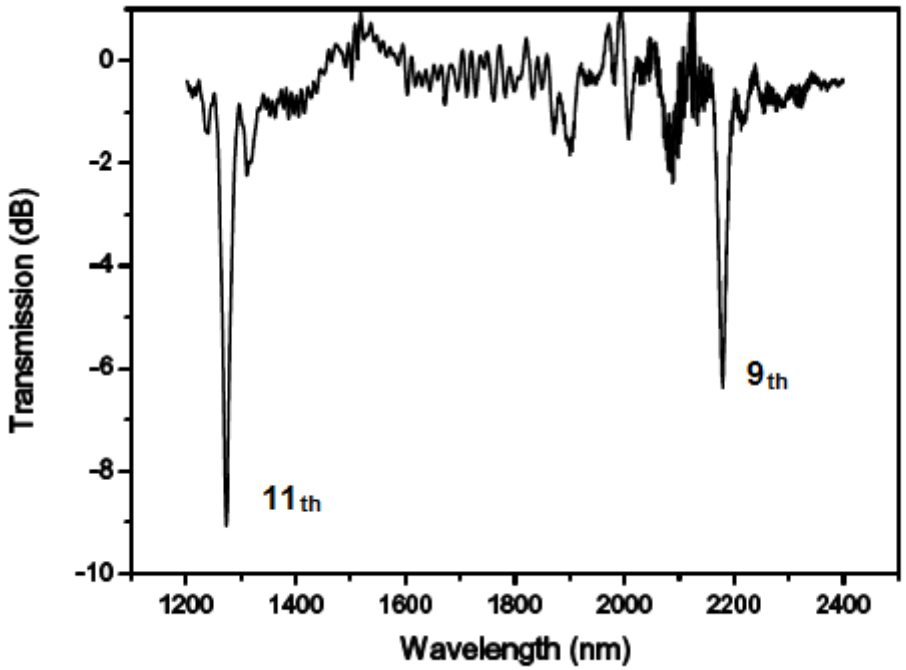

Figure 6.7 Transmission spectrum of an LPG with 200μm period UV-inscribed in SMF-28 fibre by the point-by-point method.

The light coupling from the fundamental core mode to the cladding modes of LPG generates multiple resonant peaks, which are intrinsically sensitive to the changes in environment, such as the temperature and the surrounding medium refractive index (RI). Similar to the FBG temperature sensing experiment, the mid-IR LPGs were characterized for their thermal response using the same experimental set-up shown in Figure 3.9.

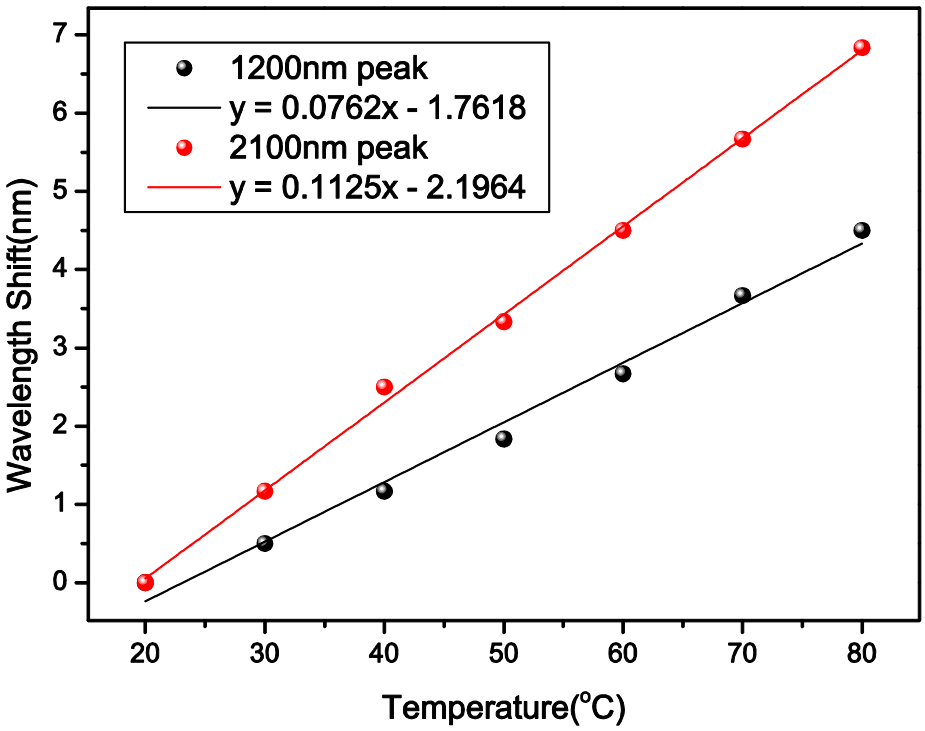

Figure 6.8 Comparison of the thermal response for two different resonant peaks of the LPG.

We have examined the thermal responses for two different resonant peaks of the LPG with the grating period of 200μm. The temperature was elevated from 20°C to 80°C with an increment of 10°C, and the experimental results of the wavelength shift are plotted in Figure 6.8. It is clear that the longer resonant wavelength corresponding to the higher order cladding mode has higher temperature sensitivity. The temperature sensitivity of the resonant peak at mid-IR 2100nm reaches to 112.5 pm/°C, which is over 50% larger than that of only 73.2 pm/°C at the 1200nm resonant peak.

Furthermore, changes of the surrounding medium RI will also affect the wavelength shift of the resonant peaks of the mid-IR LPG. To evaluate the surrounding medium RI sensing capability of

the mid-IR LPGs, we applied a series of refractive index oil (from Cargille laboratory) with different RIs from 1.3 to 1.44 to the LPG, and measured its spectral evolution using the experimental setup shown in Figure 3.30. The refractive index oil was placed on a flat glass substrate, which can be raised by a vertical micrometer to submerge the grating into the refractive index oil without imposing any force to the grating. Once the grating was surrounded by the refractive index oil, the shift of wavelength was almost instantaneously observed on the OSA. After each index oil measurement, the grating was rinsed with methanol to remove the residual oil till the original spectrum in air was restored.

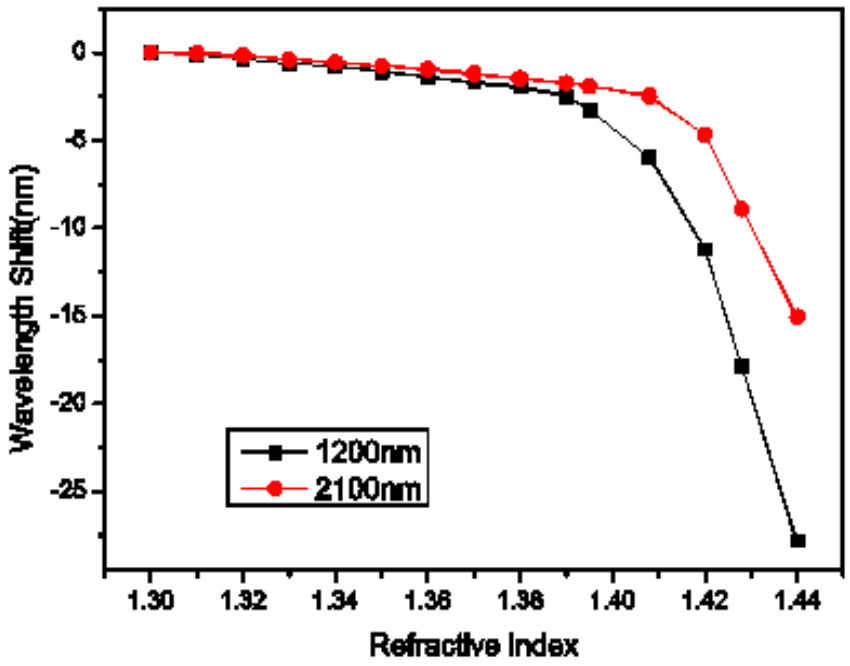

Figure 6.9 Refractive index sensing results for 20 μm LPG with 2 different resonant peaks at near-IR and mid-IR regions respectively.

Figure 6.9 plots the wavelength shifts of the near-IR and mid-IR resonant peaks for the LPG with the grating period of 200μm when subjected to 15 refractive index gels. Unlike the temperature response, the shorter wavelength resonant peak of the LPG corresponding to lower order cladding mode is more sensitive to RI change of the surrounding medium than the longer wavelength resonant peak. Quantitatively, the RI sensitivity of the shorter wavelength resonant peak of the LPG (at 1200nm) is about 198.72nm/RIU which is almost twice that at longer wavelength (2100nm) which is 107.52nm/RIU.

As we discussed in Chapter 3, the SRI sensitivity of an LPG could be improved by inscription on the SM1500 (4.2/80) fiber (from Fibercore company) with 40μm cladding radius. The LPGs of 200μm period were UV-inscribed in this thin cladding fiber and the typical transmission spectrum is shown in Figure 6.10, where we see dual resonance peaks (peak1 and peak2) in 1500nm to 1800nm region and a single resonance peak (peak 3) near 2200nm. Note, there is a dip near 2100nm which comes from the supercontinuum light source. With a selected relatively short LPG period (normally smaller than 200μm) on standard SMF-28 fibre, the light coupling between the fundamental core mode to cladding modes close to dispersion-turning-point leads to dual-peak resonances in the transmission spectrum [150]. Because thinner cladding fiber is used, we see dual-peaks occurred in 200μm period LPGs. However, when the grating period increased to 300μm, we still see dual-peak resonance, but occurred at longer wavelength region as shown in Figure 6.10.

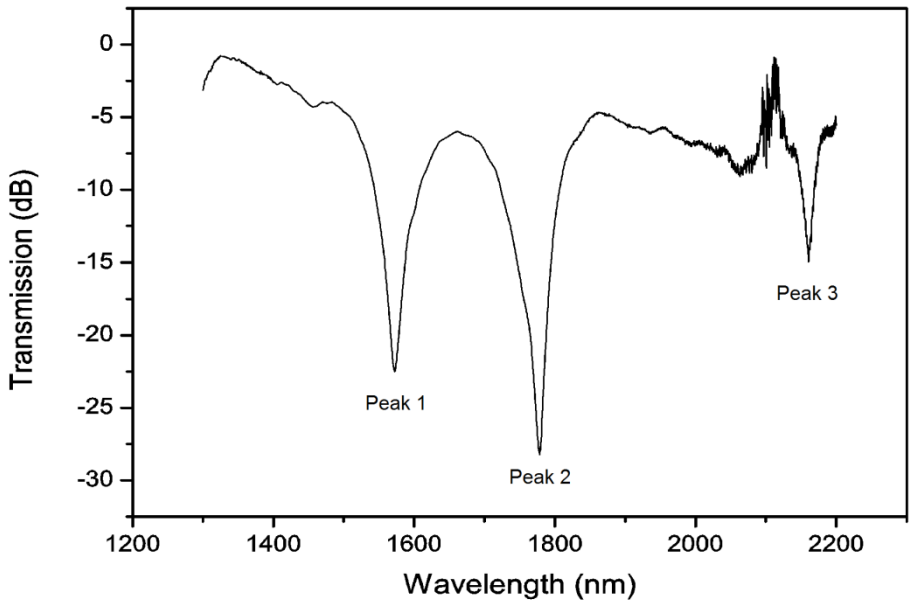

Figure 6.10 Transmission spectrum of an LPG of 300μm period UV-inscribed in SM1500 (4.2/80) fibre showing dual-peak feature and one of the dual peaks is close to mid-IR range.

By applying phase matching condition in equation 2.38, a set of phase matching curves are generated and plotted in Figure 6.11 for 9 LPG cladding modes covering a broad wavelength range from 1μm to 2.4μm: with mode order m = 1 to 9. The dispersion turning point feature is

apparent on the curves as we see that the slope direction of the phase curve changes from negative ($d\lambda/d\Lambda<0$) to positive ($d\lambda/d\Lambda>0$). From Figure 6.11, for a given LPG period (Λ=300μm), one cladding mode in the positive and the other in the negative dispersion region could meet the phase-match condition simultaneously. As a result, the conjugate cladding modes will be experimentally observed as dual-peak LPGs.

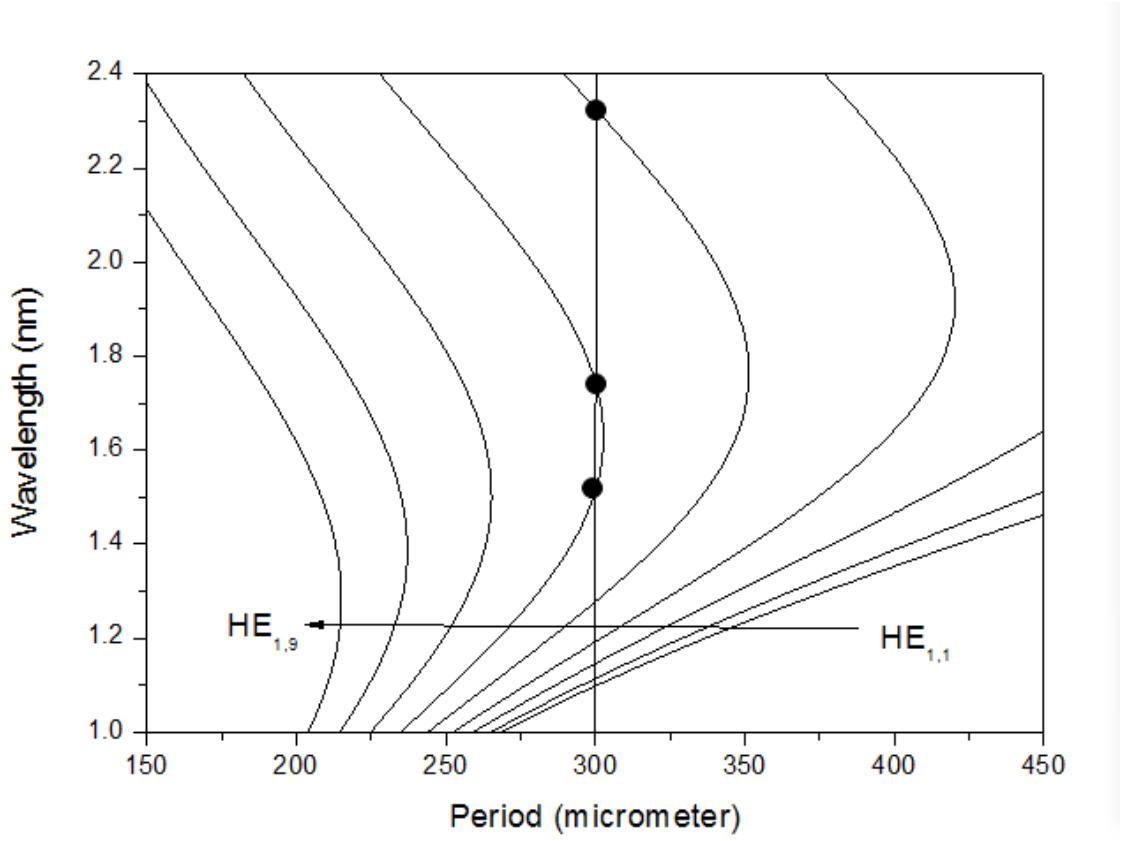

Figure 6.11 Simulated resonance wavelength versus the period of LPG on SM1500 (4.2/80) fibre with cladding modes for different orders: m = 1 to 9 (from right to left).

Theoretically, each cladding mode exhibits a turning point, providing that the observing wavelength range is sufficiently large. At each turning point, $|d\lambda res/d\Lambda|\rightarrow\infty$; thus, from Equation 3.12, we find that $|\gamma|\rightarrow\infty$ and that the turning points determine the condition of maximum sensitivity for each cladding mode. Therefore, we may design dual-peak LPGs for achieving the high sensitivity. The dual-peak property of the mid-IR LPGs UV-inscribed in thin cladding fiber was evaluated by the temperature sensing experiment and the results are shown in Figure 6.12.

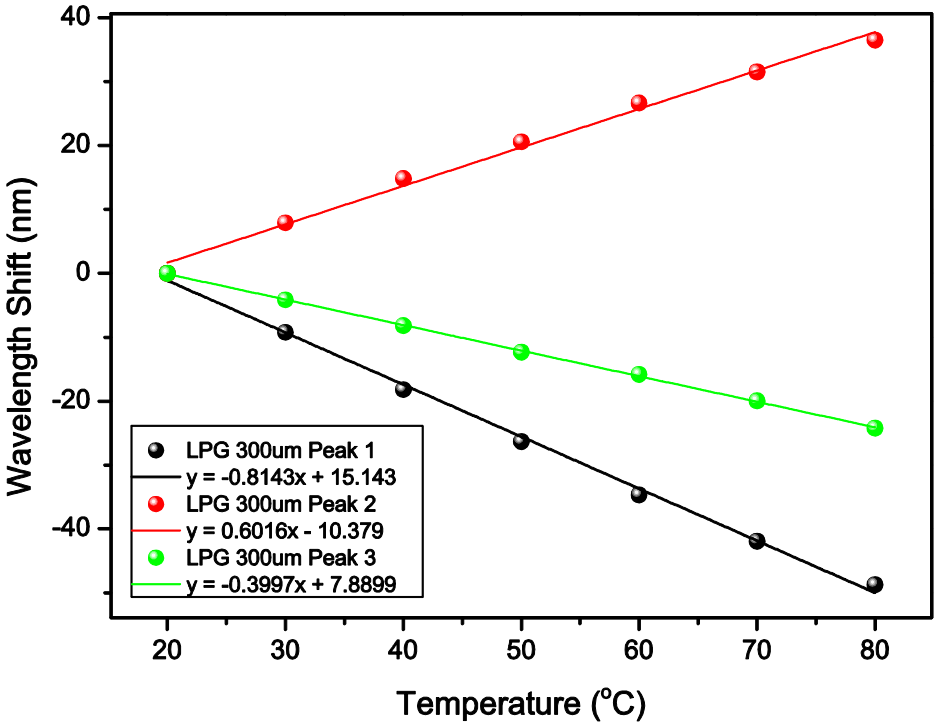

Figure 6.12 Temperature response of an LPG with 300μm period UV-inscribed in thin cladding SM1500 (4.2/80) fibre.

Figure 6.12 shows the measured thermal response of three peaks (including dual peaks) of an LPG with 300μm period over the temperature range 20°–80°C. During the experiment, we clearly saw the dual peaks were moving to opposite direction with increasing temperature, similar to the dual-peak LPGs made in normal SMF-28 fiber [106]. As shown in Figure 6.11, at 80°C, two resonance dual peaks separated by 85.2 nm (red shift +36.5 nm by the peak2 at 1800nm, blue shift −48.7 nm by the peak1 at 1600nm). The temperature sensitivities are then -814.3 pm/°C and 601.6 pm/°C for peak1 and peak 2, respectively. The wavelength shift responding to temperature changing (-399.7 pm/°C) for the single peak at 2000nm is about half of the dual peaks, but still higher than the LPG made in normal cladding SMF-28 fiber in the same wavelength range.

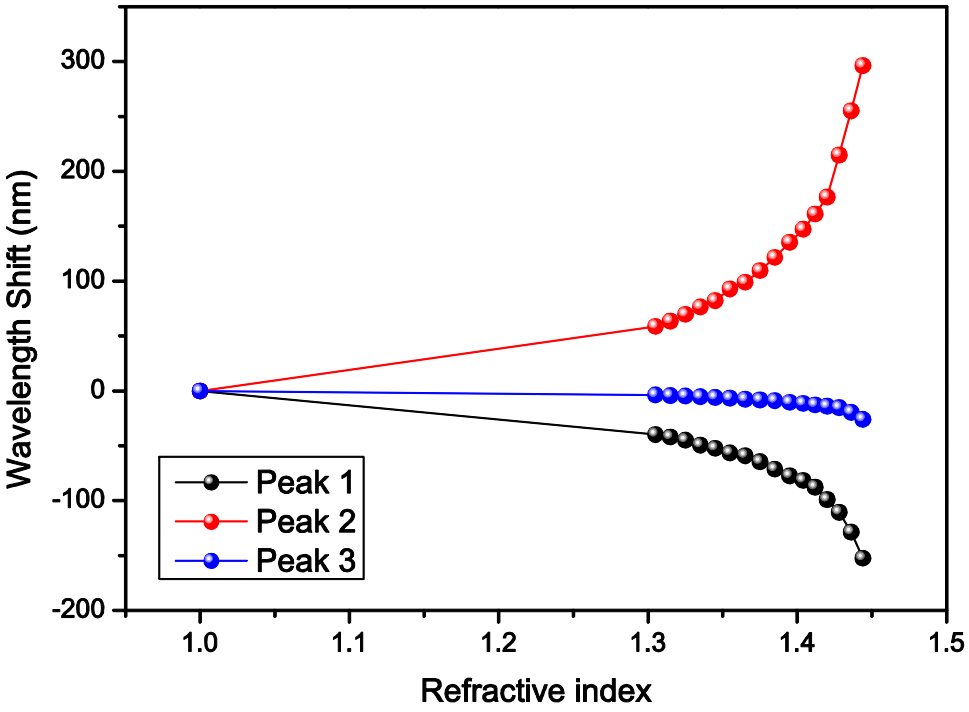

Figure 6.13 RI respond to a LPG with 300 μm period UV-inscribed in SM1500 (4.2/80) fibre.

We further investigated the RI sensitivity of the 300μm LPG UV-inscribed in thin cladding fiber by applying a set of index gels to the grating. The spectrum was measured for each RI value for all three peaks and the RI induced wavelength shifts are plotted in Figure 6.13. Over the range of RI from 1.305 to 1.444, for the dual peaks, the peak1 is blue shifted, whereas the peak2 is red shifted, and the total wavelength shifts of peak1, peak2 and peak3 are -152.42 nm, 296.2nm, and 25.79nm respectively. It is particularly noteworthy that the dual-peak resonances both showed ultrahigh RI sensitivities of -1771nm/RIU and +3722nm/RIU in the high RI range (1.404 to 1.444), respectively. The single peak at 2200nm has a measured RI sensitivity of -58.08 nm/RIU, which is more than 30 times smaller than the dual peak.

6.3 All-fibre thulium doped fibre laser using mid-IR FBGs as mirror and out-coupler

6.3.1 Introduction

Laser sources located in the eye-safe 2μm region and in the atmospheric transmission window between 2.05 μm and 2.3μm have many significant applications in medical examination, atmospheric lidar measurement, remote sensing, environment monitoring, etc [151, 152]. Compared to conventional lasers, fibre lasers have advantages of high operation efficiency, excellent heat-dissipating capability, good beam quality and compact and simple formation. Currently, the most common fibre laser technology of realizing 2-3μm emission is based on the direct energy level transitions $^3H_6 \rightarrow {}^3H_4$ from Tm^{3+} and $^5I_7 \rightarrow {}^5I_8$ from Ho^{3+}. A number of Tm^{3+} doped, Ho^{3+}-doped and Tm^{3+}-Ho^{3+} co-doped silica and fluoride fibre lasers have been reported[153-157].

In this section, we will demonstrate a broadband Tm^{3+}-doped silica fibre amplified spontaneous emission (ASE) source with up to 520 nm spanning from 1700 nm to 2220 nm. Based on the ultra-broad ASE spectrum, an all-fibre Tm^{3+}-doped laser can be realized by utilizing either a high reflective (HR) FBG-fibre end based cavity or an HR FBG- low reflective (LR) FBG based cavity. For this laser, we have investigated the wavelength selectable range for lasing, the relative thresholds, efficiencies and line width of the laser. Then, a six wavelengths switchable laser from 1925nm and 2200nm employing a mid-IRFBG array in the cavity is discussed. Finally, a thulium-doped fibre laser employing a 45°-TFG and Sagnac loop mirrors is demonstrated, which can operate with tunable single-wavelength lasing around 2000nm.

6.3.2 ASE source at 2μm range

The schematic diagrams of two Tm^{3+}-doped silica laser systems exploiting the in-fiber reflection function of mid-IR FBGs are shown in Figure 6.13, with (a) using one FBG as high reflectivity (HR) mirror and the 0°-cleaved fiber end as an output coupler and (b) using one HR FBG as mirror and one low reflectivity (LR) FBG as an output coupler. The active fiber used in these two systems is a 11-meter double cladding Tm^{3+}-doped fiber (Nufern, SM-TDF-10P/130-HE) with an octagonal shaped pump core of a diameter 130μm across the circular cross-section and a numerical aperture (NA) of 0.46. The fiber has a 10μm core diameter with a reduced NA of 0.15 by a specific pedestal around the core. The Tm^{3+} dopant concentration in the fiber core is about 5wt.% and the measured absorption coefficient at 793 nm is 3.0 dB/m. Two 793nm diode lasers (Lumics, German) with 105/125 μm core and cladding parameter multimode fiber pigtail were used as the pump source and the light was coupled into the double cladding Tm^{3+}-doped fiber through a (2+1)×1 pump combiner (ITF, USA). The maximum launched pump power was 8W. At the output end, either the fiber end facet (3.5% Fresnel reflection) (Figure 6.14(a)) or LR FBG (Figure 6.14(b)) was employed to provide laser feedback and also act as the output coupler. A number of UV-inscribed FBGs with the Bragg reflection wavelengths between 1900nm and 2200nm at a total span of 25nm were used in the laser system for multi-wavelength output operation. The HR FBG was designed with reflectivity of > 95% and a spectral FWHM of <0.4 nm, and the LR FBG was designed with reflectivity of ~50% and a spectral FWHM of <0.4 nm. Because the threshold for Fresnel-reflection-based cavity might be lower than that for the FBG-based cavity at some wavelengths of small gain, the fiber end at the FBG side was angle cleaved at 8° to reduce the reflection in order to avoid the parasitic lasing. At the output side, a germanium window was employed to remove the residual pump light.

Figure 6.14 Experimental setup of the all-fibre Tm3+-doped ASE sources based on (a) backward and (b) forward output.

Figure 6.15 shows the backward and forward ASE spectra measured using an optical spectrum analyzer (Yokogawa AQ 6375) at the launched pump power of 2W, 4W, 6W and 8W, respectively, and the measured emission and absorption cross-sections between 1700nm and 2100nm extracted from Ref. [158] were also given. It is observed that the apophysis region of both backward and forward ASE envelopes increased with raised pump power, but the peak remained essentially unchanged at the regime around 2000nm. The sharp fall of ASE envelope towards the short wavelength direction can be attributed to the strengthened ground state re-absorption induced by the increased absorption cross-section at shorter wavelength range. The similar fall of ASE envelopes towards the long wavelength direction was observed as well, resulting from the reduced emission cross-section and increased background loss with increasing wavelength. On the other hand, the optical spectrum without a spike at high launched pump power of 8W suggests that the laser operation mode was successfully suppressed with efficient angle cleaving at the fibre end. The backward ASE spectrum of over 520nm span from 1700nm to 2220nm with an FWHM bandwidth of 60nm was achieved at the maximum launched pump power of 8W, which is the

reported longest wavelength edge from the ASE of Tm^{3+}-doped fibres. Note that there were noticeable increases in the ASE spectra around 1650nm, which were clarified as ghost spectra induced by stray light of monchromator usually occurring at the shorter wavelength side of 400nm away from the original spectra in the spectrum analyser AQ6375 (this has been confirmed by Yokogawa). The stray light has no impact on the original signal and can be ignored. Besides, absorption lines caused by water vapor in the wavelength range from 1800nm to 1950nm could be clearly seen in the spectrum. Compared to the backward ASE, the forward ASE had a similar long wavelength edge of 2200nm but exhibited a narrower spectrum range spanning from 1945nm to 2220nm with a FWHM of 35 nm at the launched pump power of 8W as a result of its stronger re-absorption at the un-pumping end [159]. The red-shift of the long wavelength edge in our work can be ascribed to the comparatively long active fibre (11 m) and large rare earth ions concentration (5 wt. %). Larger Tm^{3+} concentration may enable more ground state ions to be involved in the re-absorption process per unit length, and thus stronger total re-absorption can be achieved by using longer fibre.

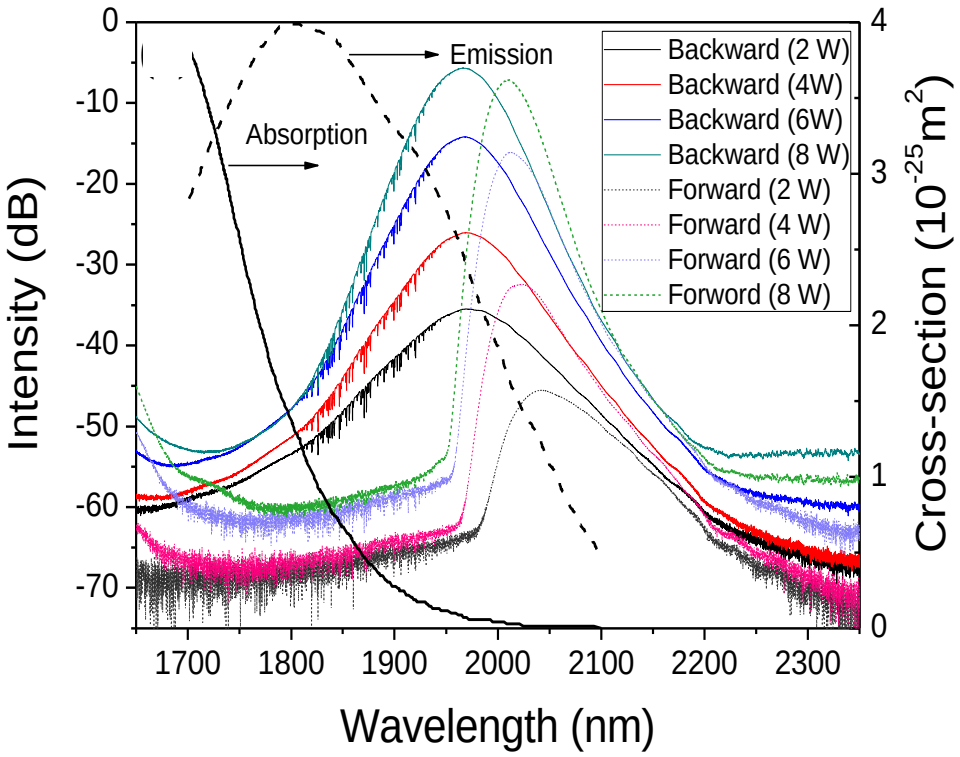

Figure 6.15 Measured backward and forward ASE emission spectra at different launched pump powers, and the absorption and emission cross-sections of Tm^{3+}-doped fibre extracted

In order to investigate the influence of fibre length on the ASE spectrum, we also measured the backward ASE spectrum using shorter fibre lengths of 5.0m and 8.0m and longer fibre of 13.0m in the system, respectively at the maximum launched pump power of 8W, as show in Figure 6.16. Compared to the system using 11.0 m fibre, the shorten fibre system exhibited shorter centre wavelength and slightly narrower FWHM bandwidth for both backward and forward ASE. For the system using 5.0m fibre, the centre wavelength blue shifted by 13.2nm and 23.8nm for the backward and forward ASE, respectively. However, the ASE centre wavelength and FWHM bandwidth of the system using 13.0m fibre were almost unchanged compared to the system using 11.0m fibre. This suggests that the fibre length of 11.0m was enough to realize the ASE with the longest edge around 2.2μm region.

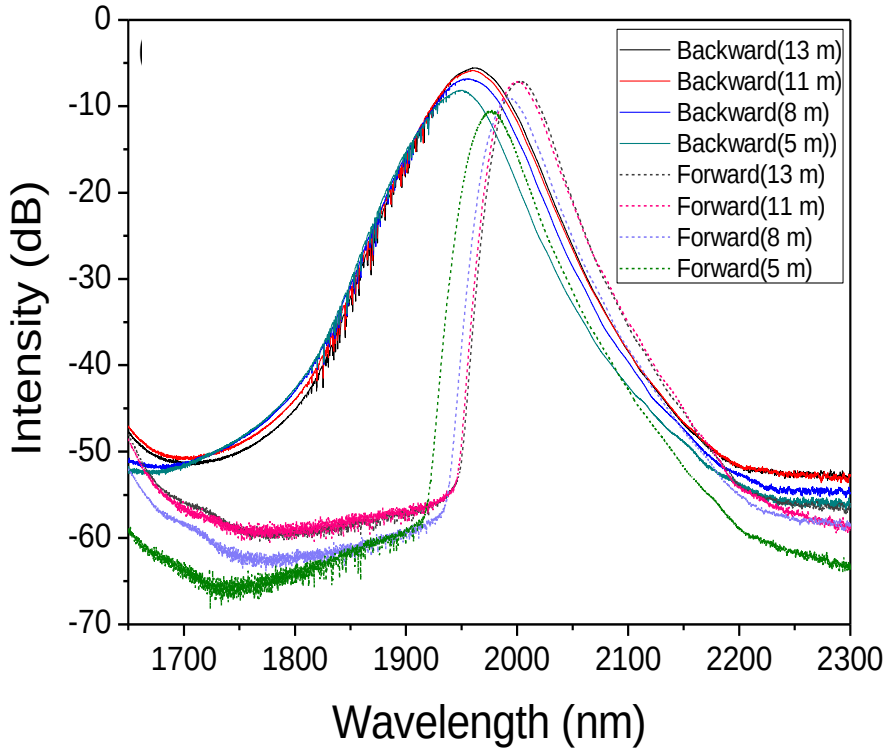

Figure 6.16 Backward ASE spectra at different fibre lengths of 13.0 m, 11.0 m, 8.0 m and 5.0 m under launched pump power of 8 W.

6.3.3 Wavelength selectable range based on FBGs

The ASE towards longer wavelength range shown above may provide the possibility of laser operation in the mid-IR 2μm region. We then investigated Tm^{3+}-doped fibre laser and the laser configurations are shown in Figure 6.17 (a) and (b), where the low reflectivity (LR) FBG and cleaved fibre end are used as the output couplers, respectively. In order to compare with previous ASE measurement which identifies the lasing wavelength limit beyond 2150 nm, we used 11.0m Tm^{3+}-doped fibre in the laser cavity. At the output end, either the fibre end facet (3.5% Fresnel reflection) (Figure 6.17 (a)] or LR FBG (Figure 6.17 (b)] was employed to provide laser feedback and also act as the output coupler. A number of FBGs were UV-inscribed with the Bragg reflection wavelengths between 1900nm and 2200nm at a span of 25 nm for the investigation. The HR FBG was designed with receptivity of > 95% and a spectral FWHM of <0.4 nm, and the LR FBG was designed with receptivity of 50% and a spectral FWHM of <0.4 nm. Because the threshold for Fresnel-reflection-based cavity might be lower than that for the FBG-based cavity at some wavelengths of small gain, the fibre end at the FBG side was angle cleaved at 8° to reduce the reflection in order to avoid the parasitic lasing.

Figure 6.17 Experimental setup of Tm^{3+}-doped silica fibre laser with counter-propagating scheme employing (a) ~3.5% reflectivity of cleaved fibre end and (b) ~50% low reflective (LR) FBG as output coupling reflectors.

By using the setup shown in Figure 6.17, the narrow width CW laser with selectable wavelength between 1975nm and 2150nm was achieved. Figure 6.18 shows the spectra of lasers centred at 1974.7nm, 1997.5nm, 2026.2nm, 2056.8nm, 2074.3nm, 2102.4nm, 2125.7nm and 2151.02nm at the maximum pumping power of 8W measured in a large spectrum range of 400nm.

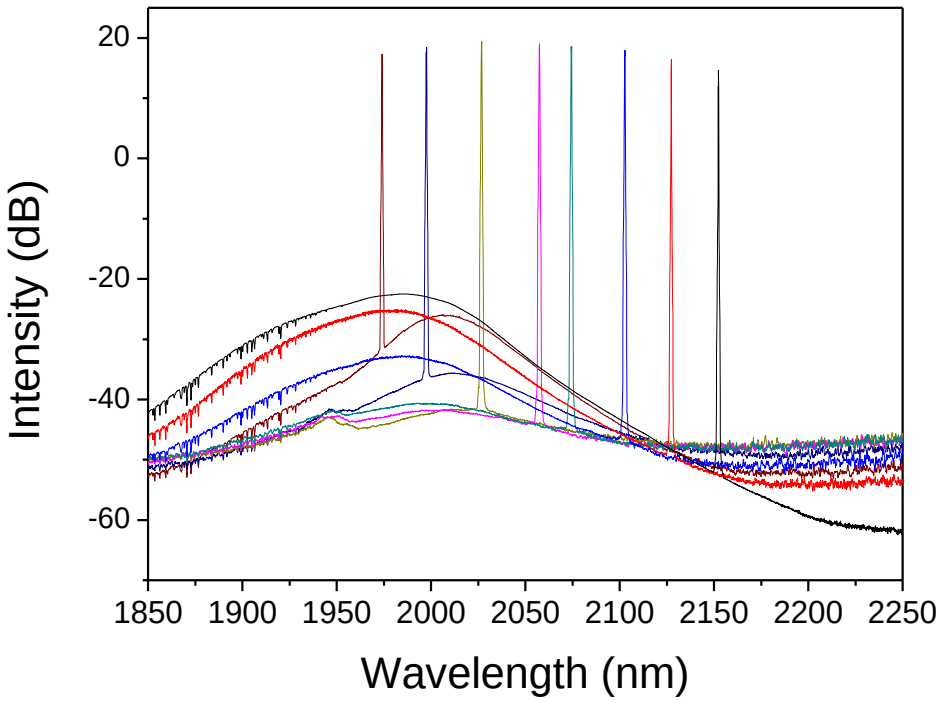

Figure 6.18 Output spectra of Tm3+-doped fibre lasers at 400 nm spectrum range for cavity constructed by perpendicular cleaved fibre end and HR FBGs.

The spectra of these mid-IR laser outputs were also measured in a 1.0nm range with a resolution of 0.02nm to investigate their spectrum characteristics, as shown in Figure 6.19. It was observed that the FWHM of laser lines were all narrower than 0.3nm suggesting the efficient spectral confining ability of the HR FBGs. Note that the spectrum gradually tended to be compressed and smoothed with increasing output wavelength owing to the weakened ground state re-absorption process at longer wavelength region. At the shorter wavelength emission region, especially below 2000nm, the spectrum was broader and exhibited more amplitude fluctuation as a result of strong ground state re-absorption and re-emission processes. After the center wavelength exceeding 2100nm, the spectrum width was essentially unchanged suggesting that the laser was almost not influenced by the re-absorption owing to the fairly low absorption cross-section of less than 0.1 $\times 10^{-25} m^2$.

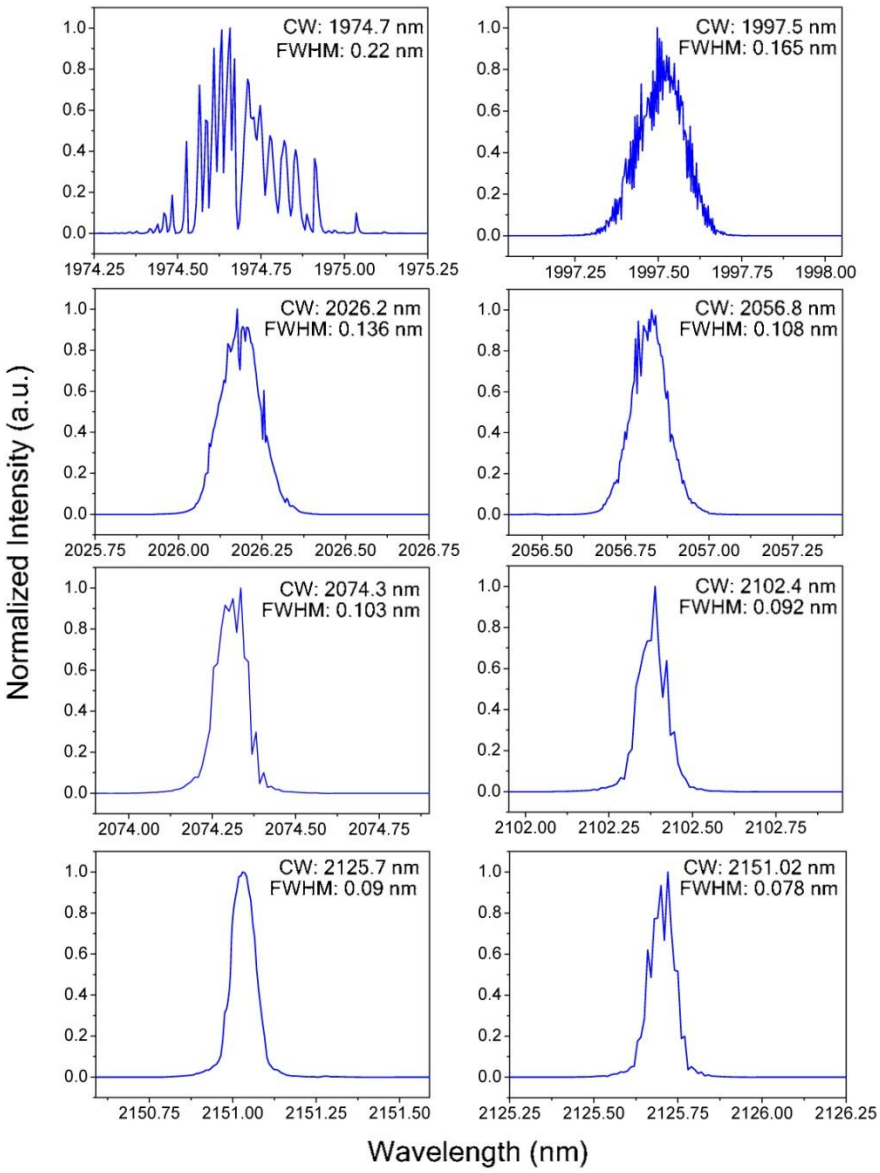

Figure 6.19 Output spectra of Tm^{3+}-doped fibre laser for the cavity constructed by perpendicularly cleaved fibre end and HR FBGs with different centre wavelengths. The scanning range and resolution were 1 nm and 0.02nm, respectively.

In order to investigate the laser wavelength operation limit of our Tm^{3+}-doped silica fibre, higher feedback was added by employing LR FBG to replace the previously cleaved fibre end as the output coupler, as shown in Figure 6.17 (b). The short and long operation wavelength edges were then extended to 1925.6nm and 2198.4nm respectively. Figure 6.20 shows the measured spectra across 400nm spectrum range at the maximum pumping power of 8.0 W.

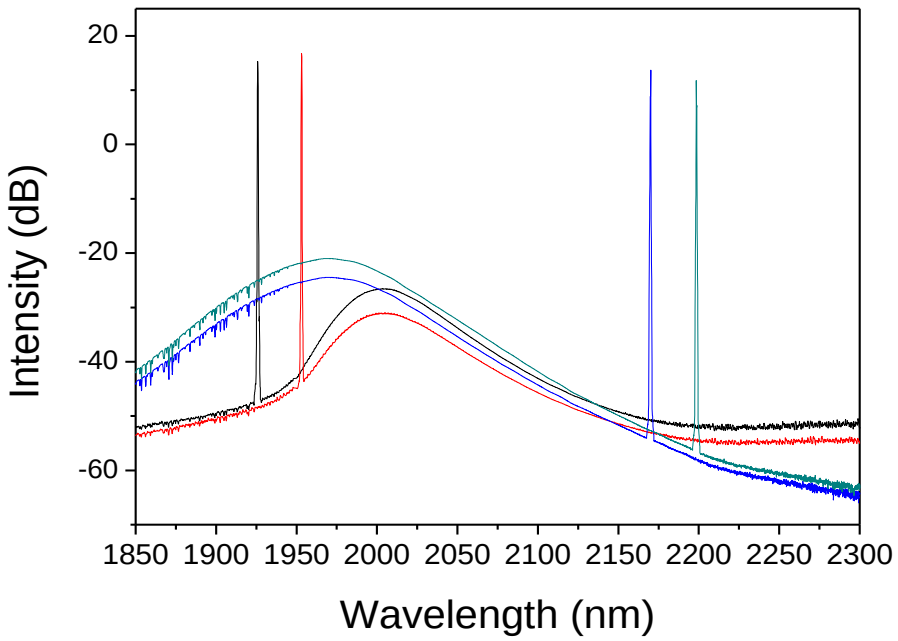

Figure 6.20 Output spectra of Tm^{3+}-doped fibre laser at 400 nm spectrum range for the cavity constructed by LR FBG and HR FBG. From left to right these centre wavelengths are at 1925.6nm, 1951.2nm, 2174.9nm, and 2198.4nm, respectively. The scanning resolution was set at 0.5 nm.

The spectra of the lasers under each LR FBG at a narrow scanning range of 1.0nm were also measured at the maximum pumping power of 8W to examine the detailed spectrum characteristics as shown in Figure 6.21 with centre wavelengths of 1925.6nm, 1951.2nm, 2174.9nm and 2198.4nm, respectively. The operation wavelength of 2198.4nm is also the longest wavelength produced from $3F^4 \rightarrow 3H^6$ transition of Tm^{3+} ions so far being demonstrated. Similar to the results as shown in Figure 6.x, the laser at 1925.6nm and 1951.2 nm still exhibited spectrum fluctuation and broadening, whereas the laser at 2174.9nm and 2198.4nm showed fixed spectrum width of 0.8nm and relatively smooth and narrow spectrum.

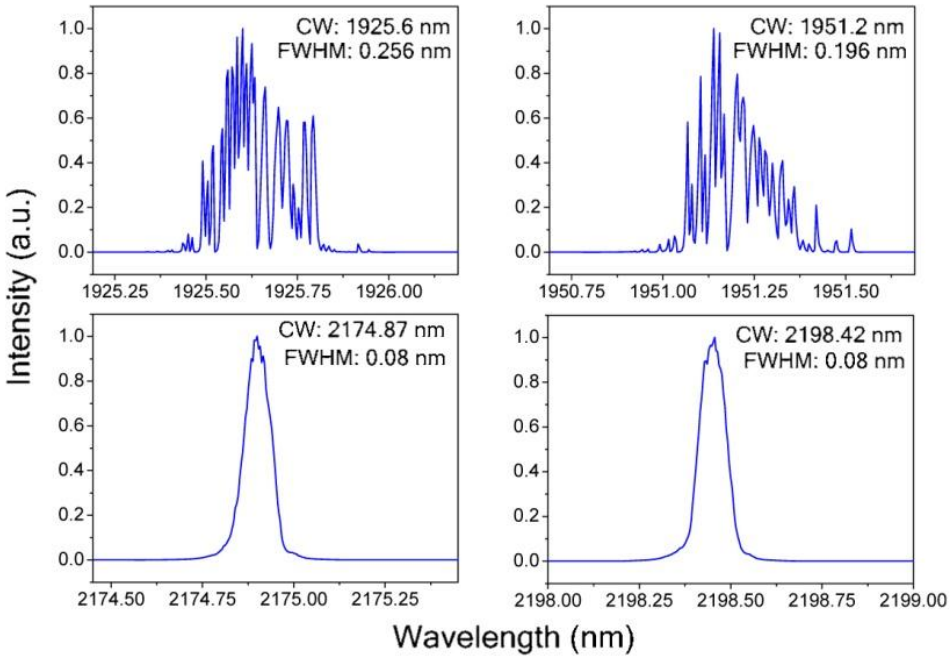

Figure 6.21 Output spectra of Tm3+-doped fibre laser for cavity constructed by LR FBGs and HR FBGs with different centre wavelengths. The scanning range and resolution were 1 nm and 0.02 nm, respectively.

6.3.4 Wavelength switchable operation based on an FBG array

It is well known that there are many methods of tuning or switching the wavelength of a fiber laser such as strain tuning an FBG, fiber etalons, external diffraction grating, and fiber coupled acousto-optic tunable filters and so on. By employing an FBG array in the laser cavity and inducing bend loss between adjacent FBGs in the array, the experiment setup of a six wavelengths switchable Tm3+- doped fiber laser was demonstrated, as shown in Figure 6. 22.

Figure 6.22 Experimental setup of multi-wavelength switchable Tm^{3+}-doped silica fibre laser.

An FBG array including 6 mid-IR FBGs centred at 1997nm, 2025nm, 2057nm, 2075nm, 2103nm and 2125nm, respectively, were fabricated and their transmission spectrum is shown in Figure 6.23. It is observed that the emission cross-section decreases with the wavelength, however, the gain and threshold are not coincidence with the emission cross-section. We arranged these FBGs in descending order, as 1997nm (FBG1), 2125nm (FBG2), 2025nm (FBG3), 2103nm (FBG4), 2075nm (FBG5) and 2057nm (FBG6). Then one end of the array was spliced to the Tm3+-doped fibre with the opposite end cleaved at 8 ° while the other end of the cavity was cleaved perpendicularly to provide 3.6% Fresnel reflection (FR) for all wavelengths. The pigtails between adjacent FBGs in the array were looped around two tubular mounts at a radius of 5cm. With this setup, the wavelength can be switched freely by increasing the distance between the two tubular mounts after the selected FBG to induce the bend loss for the suppression on all other laser modes relevant to rest FBGs. Through mode competition, the laser mode relevant to the selected FBG can win owing to its lower threshold. Figure 6.24 shows the measured spectra for the outputs at six mid-IR wavelengths, clearly demonstrated the wavelength switchable principle.

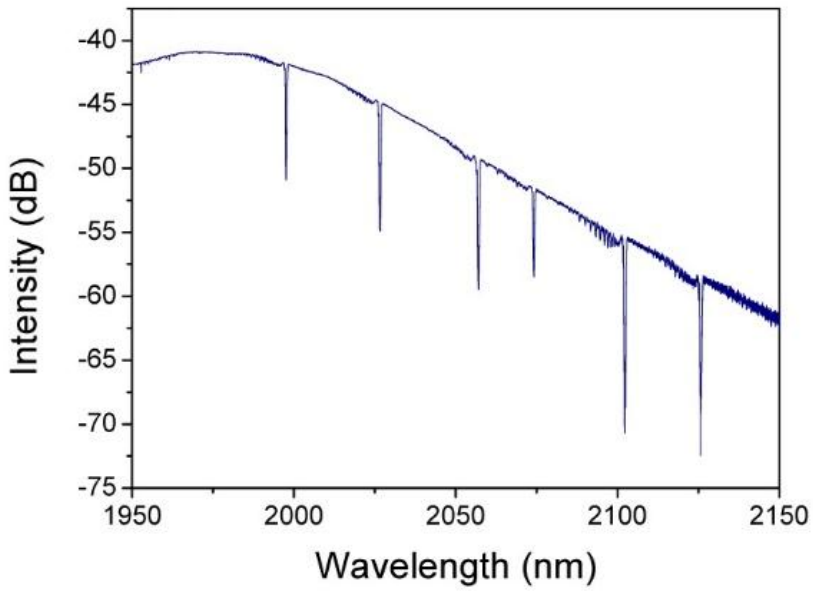

Figure 6.23 Transmission spectrum of the FBG array.

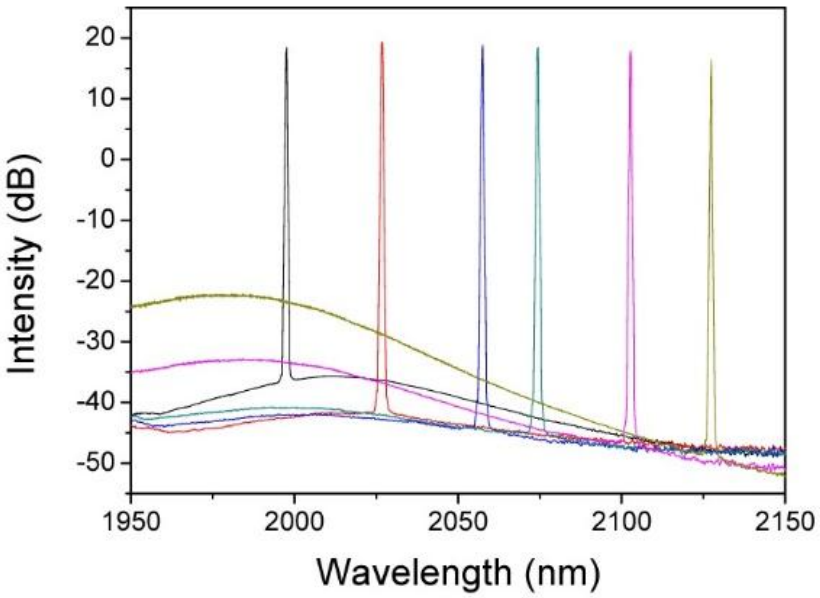

Figure 6.24 Output spectra of the multi-wavelength switchable Tm^{3+}-doped fibre laser.

6.3.5 All-fibre tuneable single-polarization fibre laser based on 45°-TFG at 2μm region

We finally investigated an all-fibre tuneable single-polarization fibre laser at 2μm region by exploring an intra-cavity polarizer based on a 45°-TFG with central response around 2μm. The experimental setup of the tuneable single-polarization fibre laser based on 45°-TFG is illustrated in Figure. 6.25. As show in the figure, a 6m length of TDF (from Nufern, SM-TDF-10P/130-HE; absorption is 3 dB/m at 793nm) is inserted into the laser cavity and pumped by 793 nm laser diode (Lumics, German), which can provide up to 8W pump power through a 980/1550 pump combiner (ITF, USA). Two Sagnac loop mirrors are located at the both ends of the cavity, which is formed by 70:30 coupler and 50:50 coupler respectively. The 50: 50 coupler is used as the output port of the fibre laser, and the two other sides form a loop to ensure a linear cavity of this laser. A 45°-TFG is inserted between the PC and the coupler to achieve single-polarization oscillation. A polarization controller (PC) is used to adjust the cavity polarization.

Figure 6.25 The configuration of linear cavity fibre laser with an intra-cavity 45°-TFG as a polariser.

Due to the comb filtering of the Sagnac loop mirror, the multi-wavelength laser may be realized by adjusting the PC. However, the multi-wavelength laser output cannot maintain operation in a stable state, the cause to the instability may due to mode competition in the cavity. Based on reference [114], while introducing an intra-cavity polarizer into a fibre laser, wide wavelength tunability may be achieved by varying the fibre birefringence with an in-line PC. In our laser system, the 45°-TFG is employed as an in-fibre polariser in the cavity. Therefore, by adjusting the PC in the laser cavity, the lasing wavelength tuning is possible to achieve. Figure 6.26 shows that the lasing wavelength can be tuned in the range of about 30nm from 1988nm to 2018nm.

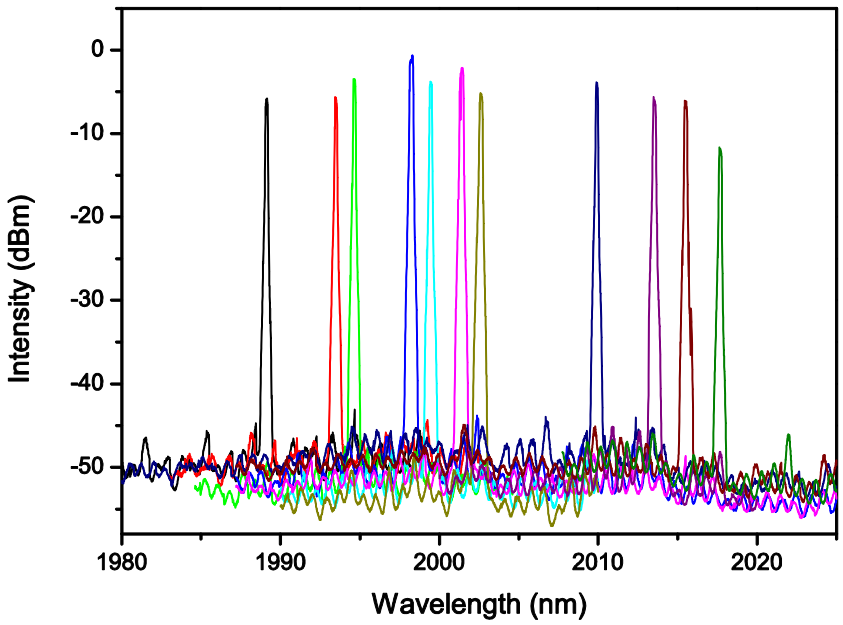

Figure 6.26 Tunable single-wavelength output between 1988nm and 2018nm from the all-fibre laser based on a mid-IR 45°-TFG and two Sagnac loop mirrors.

One unique advantage of the 45°-TFG based wavelength tuneable fibre laser is the laser output at single polarization with a high polarization dependent loss (PDL). This has been shown in 1550nm fibre lasers [117]. Figure 6.27 shows the PDL of the laser output at around 2000nm, giving a value of 34.8dB (i.e. the degree of polarization is more than 99.9%), indicating the output of the laser is almost single polarization.

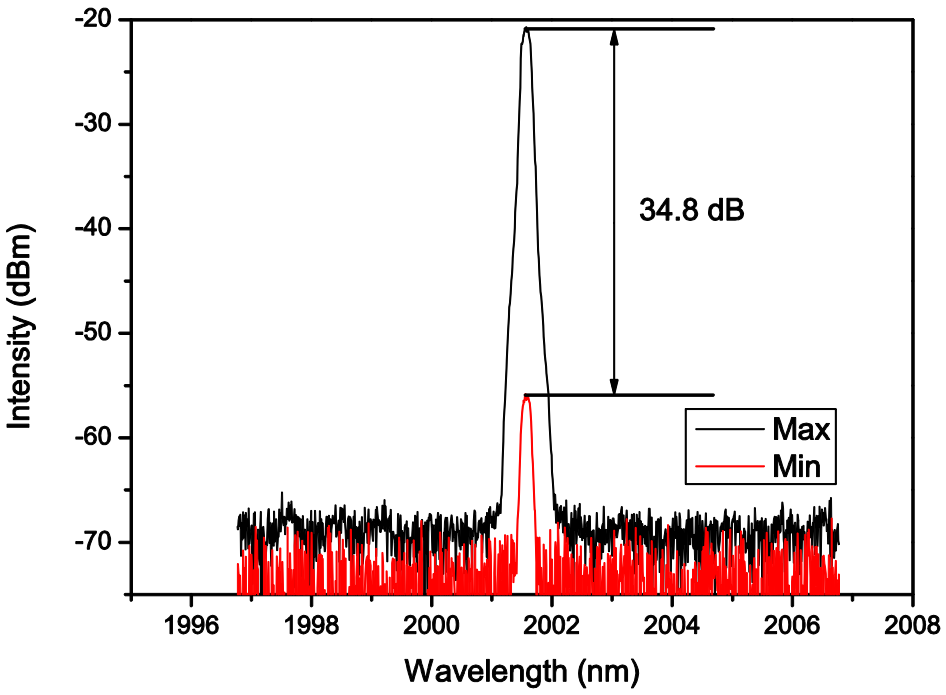

Figure 6.27 The PDL results of 45°-TFG based mid-IR fibre laser measured at ~2000nm.

6.4 Conclusions

We have successfully UV-inscribed FBGs, LPGs, and 45°-TFGs with spectral responses at mid-IR wavelength range on the standard telecom single mode SMF-28, mid-IR single mode SMF-2000 and thin cladding SM1500 fibers. Temperature and strain sensitivity characteristics for the mid-IR FBGs, temperature and refractive index response for mid-IR LPGs and polarization property for mid-IR 45°-TFGs have been investigated.

Secondly, we presented the application of mid-IR fibre gratings in selectable multi-wavelength CW and Tm^{3+}-doped tuneable fibre lasers. In the former, the laser operation at eight individual wavelengths in the range from 1925.6nm to 2198.4nm by using LR and HR FBGs was successfully demonstrated, and in the later, we have proposed and demonstrated a tuneable linear cavity fibre laser incorporating a 45°-TFG and Sagnac loop mirrors. By adjusting the PC in the laser cavity, the reported fibre laser can operate at the mode of tuneable single-wavelength lasing with a wavelength tuning range of 30nm from 1988nm to 2018nm. We have clearly demonstrated the single polarization operation of this mid-IR laser with polarization extinction ratio as high as 34.8dB, showing the degree of polarization is about 99.9%.

Chapter 7.

Conclusions and future work

7.1 Conclusions

In this thesis, a systematic investigation on the fabrication, characterisation and application of different types of optical fibre gratings (FBGs, LPGs and TFGs) with operating wavelength cover from near- to mid- IR range is presented. The main achievements can be summarized as: different types of near–IR optical fibre grating fabricated in normal telecom fibre and special designed fibre; high PDL 45º-TFGs based in-fibre polarizer and the applications on the single polarisation and mode locking fibre laser system; highly sensitive loading sensor and biosensor based on ex-TFGs with low thermal cross-sensitivity; UV-inscribed optical fibre gratings in mid-IR range and their applications as sensor and laser.

The thesis started with the literature review of fibre grating history and photosensitivity mechanism in optical fibres. Three main reported photosensitivity enhancement techniques have been brief by discussed. An introduction of mode coupling theory and phase match conditions for different type of fibre gratings is included in this thesis as well.

Three UV-inscription techniques, including two-beam holographic, phase mask scanning, and point-by-point, have been employed to fabricate the near- and mid-IR optical fibre gratings. FBG and TFG inscription techniques are mainly using the holographic and phase mask method, based on simple exposure to UV radiation periodically along a part of fibre. The phase mask inscription technique has been proved through varieties of experiments to be the efficient one. The reasons for this are good stability and the ability to write a quality grating structure. However, there are a few disadvantages to this fabrication technique including: expensive phase mask and different wavelengths needing different phase masks. The point-by-point is the most efficient and flexible method for inscribing LPGs as the period can be selected arbitrarily by simple control the UV exposure with a programmable shutter.

As for 45º-TFGs, the fabrication and characterisation have been done with the gratings inscribed in hydrogen-loaded SMF-28 fibres and PM fibres by using a tilted phase mask. One of the most important achievements is 45°-TFGs with intrinsically high PDL can be employed as ideal in-fibre polarizers. The PDL of a 45-TFG is linearly proportional to the grating length, as the experiment results have shown the PDL increases with the grating length at a rate of almost 0.986 dB/mm. For an idea in-fibre linear polarizer, 45º-TFG should be written into the PM fibre along its principal axis, which will maintain its state of polarization in the fibre. The experiment results clearly show the PDL of the 45°-TFG inscribed in PM fibre along the low-axis (30dB) is higher than along the fast axis (18dB). The 45°-TFG is also a tilted grating for side-tapping power detection due to its radiation light coupled out to the fibre perpendicularly. The power distribution over a 45°-TFG is the highest at the start position of the grating and decreasing exponentially along the grating length. Incorporating a 45°-TFG in a fibre ring laser cavity has shown significantly increased DOP of laser output to 99%, which clearly indicates that the output of the laser is highly polarized and almost single polarization. A 45°-TFG based single-polarization fibre laser has been demonstrated for loading sensing. The achieved loading sensitivities are 0.033 / ($kg \cdot m^{-1}$) and 0.042 / ($kg \cdot m^{-1}$) for the two different interaction lengths. The 45º-TFG has also be applied in the area of nonlinear photonics, which facilitates NPR based mode locking at 1.55μm region. The pulsed laser output power is at a repetition rate of 10.34MHz with 12mW output power. By using 45º-TFGs in PM fibre, the all fibre Lyot filter has been achieved, which has both polarizing and filtering function. The FSR and bandwidth of filter is inversely related to the length of PM fibre cavity.

The research work has revealed that ex-TFGs will couple the light from the core mode to the forward propagating cladding modes, which is similar to LPGs except the coupling to high order cladding modes. Although ex-TFGs have a similar property as conventional LPGs, they could not be fabricated by the point-by-point technique. Ex-TFGs reported in this thesis were fabricated by an amplitude mask with 6.6μm period. For bio-sensing applications, a high-Q glucose concentration detection biosensor has been developed based on an 81°-TFG, demonstrating the

glucose detection of the physiological range (0~3.0mg/ml) of human being. The GOD immobilization has been achieved by modifying the 81°-TFG surface with APTES. Compared to the previously reported glucose sensor based on the GOD-immobilized LPG, the 81°-TFG based sensor has shown a high RI sensitivity (168nm/RIU), lower thermal cross-talk effect (5.30pm/°C), better linearity and higher Q-factor (325) in sensing response. Finally for another sensing application, an all-fibre loading sensor based on a hybrid 45°- and 81°-TFG structure was demonstrated. Such a sensor system removes the use of the commercial polarizer and polarization controller, making the sensor system more simple and compact.

FBGs, LPGs and 45°-TFGs in mid-IR wavelength range have been successfully UV-inscribed on the standard telecom single mode SMF-28 and mid-IR single mode SM-2000 fibres. Temperature and strain sensitivity characteristics for the mid-IR FBGs, temperature and refractive index response for mid-IR LPGs and polarization property for mid-IR 45°-TFGs have been investigated. It is found that the SRI sensitivity is significantly improved by UV-inscribing LPG into the fibre with smaller cladding size. For the first time, a dual-peak LPG sensor has been produced in mid-IR range showing ultra-high SRI sensitivity. This design has made the coupled cladding modes very close to the dispersion-turning-point and small cladding size (about 40μm radius) has then been applied to shift the coupled modes even closer to the most sensitive region (dispersion-turning-point). Even large period (300μm) LPG written on small cladding SM1500 (4.2/80) fibre is able to generate the dual resonance peaks in 1500nm to 1800nm region. The SRI sensitivity has been increased by 40 times (+3722nm/RIU in the high RI range from1.404 to 1.444), compared to the same LPG on the fibre with 62.5μm cladding (82.3nm/RIU). Finally, we presented the application of mid-IR fibre gratings in selectable multi-wavelength CW and mode locking Tm3+-doped fibre lasers. In the former, the laser operation at eight individual wavelengths in the range from 1925.6nm to 2198.4nm by using mid-IR LR and HR FBGs was successfully demonstrated and in the latter, a tuneable linear cavity fibre laser incorporating a 45°-TFG and Sagnac loop mirrors have been proposed and demonstrated.

7.2 The future works

7.2.1 Optical fibre gratings fabrications for mid-IR (wavelength over 2μm)

Recently, fibre lasers and optical fibre devices operating at 2μm and 3μm region of the mid-IR spectrum have attracted growing interests owing to their applications potentially in defence, health and the environment. Due to high transmission loss beyond 2μm, we commonly use fluoride (ZBLAN) fibre as mid-IR rare earth doped fibres, which have loss as low as 3dB/km at 2.6μm [160]. Unfortunately, the optical fibre gratings cannot be written in ZBLAN fibre by UV exposure due to the non-photo sensitivity of undoped ZBLAN fibres. Thus, permanent optical grating were normally photo-induced in undoped ZBLAN fibres using femtosecond (fs) laser to physical modify the fibre structure [161]. However, the fibre structure damage by fs inscription also involves new transmission loss into the grating device comparing the UV-inscribed gratings. So far, some scientists [162] doped Ce^{3+} into ZBLAN fibre to achieve the photosensitivity and fabricate the highly reflective FBGs at 2μm in fibre core using a 248-nm excimer laser. For future work, we could propose to fabricate the different types of optical fibre grating (FBGs, LPGs and TFGs) over 2μm on Ce^{3+} doped ZBLAN fibre by using two beam holographic and phase mask technique, respectively.

7.2.2 All fibre comb-like multi-wavelength mode-locked laser

As discussed in Chapter 4, 45°-TFG based Lyot filter exhibits comb-like transmission spectra with sinusoidal shape, for which the FSR and bandwidth could be designed by using different length PM cavity. We have observed in the experiment that the Lyot filter with 100m PM fibre cavity has 57.4pm FSR and 28.7pm bandwidth, and the PDL is more than 15dB. Such a small FSR and bandwidth filter could be used in the laser system to achieve high density comb-like multi-wavelength laser. Moreover, the Lyot filter can be applied in the pulse laser system. Dr. Z. Yan [163] has demonstrated an erbium doped fibre (EDF) ring laser achieving soliton mode locking by the use of an intra-cavity Lyot filter. In his experiment, the Lyot filter has employed

as a polarised component suppressing sidebands of soliton pulse. Here, we propose an all-fibre mode-locked erbium-doped fibre laser based on nonlinear loop mirror (NOLM) with a 100 metres intra-cavity Lyot filter (see Figure 7.1). According to above discussion, the laser system in Figure 7.1 can generate multi-wavelength mode-locked laser output. The long PM fibre length of the Lyot filter also ensures enough nonlinear phase shift difference for stable mode-locking through the NOLM.

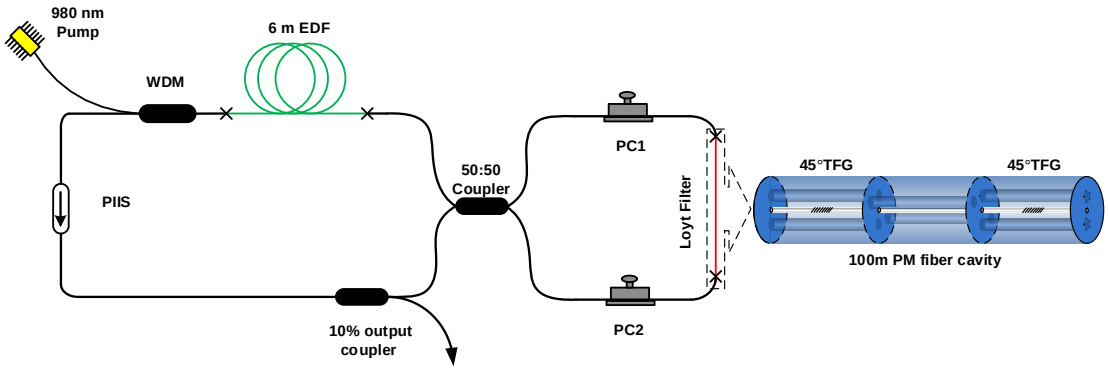

Figure 7.1 Schematic of the "figure-of-eight" mode-locked double-clad TDF laser based on NOLM incorporating an all fibre Lyot filter.

7.2.3 All fibre mode-locked laser for mid-IR wavelength range

A number of passively mode-locked lasers over 2μm have been already reported [164-170], which can be roughly classified into two major categories depending on the mode-locking mechanism. The first group can be defined as material saturable absorber (SA) based laser. The second is referred as nonlinear switching based laser, in which the transmission or reflectivity property is dependent on the nonlinear phase shift induced by nonlinear polarization evolution (NPE), nonlinear amplifying loop mirror (NALM) or nonlinear optical loop mirror (NOLM), all exhibiting the capability of pulse self-shaping that is equivalent to a real saturable absorber.

Here, we propose a new solution for thulium-doped all-fibre mode-locked laser based on NPR and optical fibre gratings. Figure 7.2 shows experimental configuration of a linear cavity Fabry-Perot system capable of generating soliton pulses with over 2μm wavelength. The advantage of this laser system compared to existing self-starting fibre soliton lasers in mid-IR wavelength range

is that an optical isolator (an expensive component) is not required. The rep1acement of the two mirrors with fibre reflection gratings (FBG and CFBG) and in-fibre polarising grating (45°-TFG) would make this configuration a truly all-fibre device. The system should be able to operate in the femtosecond short pulse regime by the adjustment of the dispersion of the laser cavity.

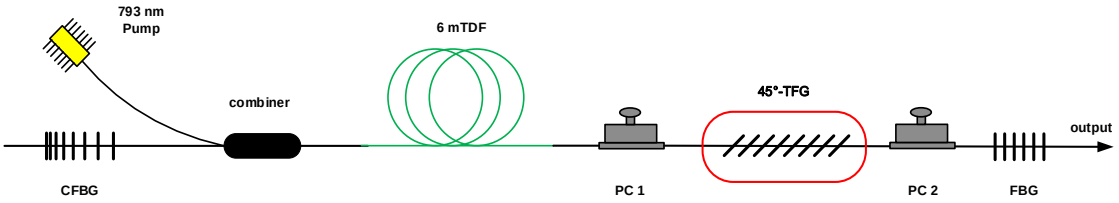

Figure 7.2 experimental configuration of linear cavity Fabry-Perot system capable of generating soliton pulses for mid-IR wavelength range.

Publications

Journal papers

1. B. Luo, Z. Yan, **Z. Sun**, J. Li, and L. Zhang, "Novel glucose sensor based on enzyme-immobilized 81° tilted fibre grating," ***Optics express* 22,** 30571-30578 (2014).

2. B. Luo, Z. Yan, **Z. Sun**, Y. Liu, M. Zhao, and L. Zhang, "Biosensor based on excessively tilted fiber grating in thin-cladding optical fiber for sensitive and selective detection of low glucose concentration," ***Optics express* 23**, 32429-32440 (2015).

3. J. Li, **Z. Sun**, H. Luo, Z. Yan, K. Zhou, Y. Liu, and L. Zhang, "Wide wavelength selectable all-fiber thulium doped fiber laser between 1925 nm and 2200 nm," ***Optics express* 22**, 5387-5399 (2014).

4. J. Li, Z. Zhang, **Z. Sun**, H. Luo, Y. Liu, Z. Yan, C. Mou, L. Zhang, and S. K. Turitsyn, "All-fiber passively mode-locked Tm-doped NOLM-based oscillator operating at 2-μm in both soliton and noisy-pulse regimes," ***Optics express* 22**, 7875-7882 (2014).

5. J. Li, Z. Yan, **Z. Sun**, H. Luo, Y. He, Z. Li, Y. Liu, and L. Zhang, "Thulium-doped all-fiber mode-locked laser based on NPR and 45°-tilted fiber grating," ***Optics express* 22**, 31020-31028 (2014).

6. M. Perry, Z. Yan, **Z. Sun**, L. Zhang, P. Niewczas, and M. Johnston, "High stress monitoring of prestressing tendons in nuclear concrete vessels using fibre-optic sensors," ***Nuclear Engineering and Design 268***, 35-40 (2014).

7. X. Wang, Z. Yan, F. Wang, **Z. Sun**, C. Mou, X. Zhang and L. Zhang "SNR Enhanced Distributed Vibration Fiber Sensing System Employing Polarization OTDR and Ultra-weak FBGs," ***Photonics Journal***, IEEE **7**, 1-11 (2015).

8. X. Wang, Z. Yan, F. Wang, J. Hua, C. Mou, **Z. Sun**, X. Zhang and L. Zhang, "An OTDR and Gratings Assisted Multifunctional Fiber Sensing System," ***Sensors Journal***, IEEE **15**, 4660-4666 (2015).

9. **Z. Sun**, C. Mou, Z. Yan, K. Zhou, X. Wang, J. Li, and L. Zhang, "Optical loading sensor based on ring-cavity fibre laser incorporating a 45°-tilted fibre polarizing grating," ***Appl Optics 54***, 4267-4272 (2015).

10. **Z. Sun**, Z. Yan, K. Zhou, Q. Sun, A. A. Badmos, and L. Zhang, "UV-Inscribed Optical Fibre Gratings in Mid-IR Range and Their Laser Applications," ***JOURNAL OF ELECTRONIC SCIENCE AND TECHNOLOGY 13***, 15 (2015).

11. **Z. Sun**, Z. Yan, C. Mou, X. Wang, J. Li, and L. Zhang, "All-Fibre Loading Sensor Based on a Hybrid 45° and 81° Tilted Fibre Grating Structure," ***Sensors Journal,*** IEEE 16, 343-348

(2016).

12. Z. Yan, **Z. Sun**, K. Zhou, B. Luo, J. Li, H. Wang, Y. Wang, W. Zhao, and L. Zhang, "Numerical and Experimental Analysis of Sensitivity-Enhanced RI Sensor Based on Ex-TFG in Thin Cladding Fibre," ***Lightwave Technology, Journal of 33,*** 3023-3027 (2015).

13. Z. Yan, C. Mou, **Z. Sun**, K. Zhou, H. Wang, Y. Wang, W. Zhao, and L. Zhang, "Hybrid tilted fiber grating based refractive index and liquid level sensing system," ***Optics Communications 351***, 144-148 (2015).

14. Z. Yan, H. Wang, C. Wang, **Z. Sun**, G. Yin, K. Zhou, Y. Wang, W. Zhao, and L. Zhang, "Theoretical and experimental analysis of excessively tilted fiber gratings," ***Optics express 24,*** 2107-2115 (2016).

15. Z. Zhang, C. Mou, Z. Yan, **Z. Sun**, and L. Zhang, "Orthogonally polarized bright-dark pulse pair generation in mode-locked fibre laser with a large-angle tilted fiber grating," ***Appl Phys B*** 122 (2016).

Conference papers:

1. C. Liu, Q. Cai, **Z. Sun**, B. Xu, J. Zhao, L. Zhang, and X. Chen, "Fibre optic chemical sensor based on graphene oxide-coated long period grating," ***Sixth European Workshop on Optical Fibre Sensors 9916*** (2016).

2. J. Li, H. Luo, Y. He, Y. Liu, B. Luo, **Z. Sun**, L. Zhang, and S. K. Turitsyn, "Semiconductor saturable absorber mirror passively Q-switched 2.97 μm fluoride fibre laser," ***Proc. SPIE 9135***, Laser Sources and Applications II, 913504 (May 1, 2014)

3. X. Wang, Z. Yan, F. Wang, C. Mou, **Z. Sun**, X. Zhang, and L. Zhang, "A distributed and key-position fiber sensing system based on LPFG and WFBG assisted OTDR," in ***Advanced Photonics***(Optical Society of America, Barcelona, 2014), p. BW3D.7.

4. **Z. Sun**, Z. Yan, C. Mou, X. Wang, J. Li, and L. Zhang, "All-fibre loading sensor based on 45° and 81° tilted fibre gratings," in ***23st International Conference on Optical Fibre Sensors (OFS23)*** 2014, pp. 91577Q-91577Q-91574.

5. **Z. Sun**, C. Mou, Z. Yan, X. Wang, and L. Zhang, "Optical loading sensor based on single polarization fiber laser incorporating an intra-cavity 45º-TFG," in ***23st International Conference on Optical Fibre Sensors (OFS23)*** 2014, pp. 91577H-91577H-91574.

6. **Z. Sun**, C. Mou, Y. Song, Z. Yan, K. Zhou, and L. Zhang, "All-fibre passively mode-locked picosecond erbium doped fibre laser using a 45-tilted fibre grating," in ***Advanced Photonics***(Optical Society of America, Barcelona, 2014), p. BW3D.4.

7. Z. Yan, **Z. Sun**, S. Xiong, C. Wang, C. Mou, C. Li, J. Li, K. Zhou, and L. Zhang, "Refractive index sensor based on a pair of hybrid 45 degree and 81degree tilted fiber gratings," in ***Advanced Photonics***(Optical Society of America, Barcelona, 2014), p. JM5A.1.

8. Z. Yan, S. Xiong, **Z. Sun**, B. Luo, C. Wang, C. Li, C. Mou, K. Zhou, and L. Zhang, "Sensitivity enhanced SRI sensor based on an Ex-TFG in thin cladding fibre," in ***Advanced Photonics***(Optical Society of America, Barcelona, 2014), p. BM4D.4

References

1. Hill, K.O., et al., *Photosensitivity in Optical Fiber Waveguides - Application to Reflection Filter Fabrication.* Applied Physics Letters, 1978. **32**(10): p. 647-649.

2. Kashyap, R., *Optical fibre Bragg gratings for applications in telecommunications.* 21st European Conference on Optical Communication - Ecoc '95, Vols 1-4, 1995: p. 23-26.

3. Kersey, A.D., et al., *Fiber grating sensors.* Journal of Lightwave Technology, 1997. **15**(8): p. 1442-1463.

4. Ventrudo, B.F., et al., *Wavelength and Intensity Stabilization of 980 Nm Diode-Lasers Coupled to Fiber Bragg Gratings.* Electronics Letters, 1994. **30**(25): p. 2147-2149.

5. Rochette, M., et al., *Gain equalization of EDFA's with Bragg gratings.* Ieee Photonics Technology Letters, 1999. **11**(5): p. 536-538.

6. Ibsen, M., et al., *Optimised square passband fibre Bragg grating filter with in-band flat group delay response.* Electronics Letters, 1998. **34**(8): p. 800-802.

7. Ouellette, F., *Dispersion cancellation using linearly chirped Bragg grating filters in optical waveguides.* Optics Letters, 1987. **12**(10): p. 847-849.

8. Meltz, G., Morey, W.W. and Glenn, W.H.. *In-fiber Bragg grating tap*. in *Optical Fiber Communication*. 1990. San Francisco, California: Optical Society of America.

9. Erdogan, T. and Sipe, J.E., *Tilted fiber phase gratings.* Journal of the Optical Society of America a-Optics Image Science and Vision, 1996. **13**(2): p. 296-313.

10. Lemaire, P.J., et al., *High pressure H_2 loading as a technique for achieving ultrahigh UV photosensitivity and thermal sensitivity in GeO_2 doped optical fibres.* Electronics Letters, 1993. **29**(13): p. 1191-1193.

11. Henderson, S.W., et al., *Eye-safe coherent laser radar system at 2.1 μm using Tm, Ho: YAG lasers.* Optics letters, 1991. **16**(10): p. 773-775.

12. Johnson, D.E., *Use of the Holmium-Yag (Ho Yag) Laser for Treatment of Superficial Bladder-Carcinoma.* Lasers in Surgery and Medicine, 1994. **14**(3): p. 213-218.

13. Sun, F.T., et al., *Application of endoscopic Ho : YAG laser incision technique treating urethral strictures and urethral atresias in pediatric patients.* Pediatric Surgery International, 2006. **22**(6): p. 514-518.

14. Sugimoto, N., et al., *Eye-safe 2.1-μm Ho lidar for measuring atmospheric density profiles.* Optics Letters, 1990. **15**(6): p. 302-304.

15. Mou, C., et al., *All-fiber passively mode-locked femtosecond laser using a 45º-tilted fiber grating polarization element.* Optics express, 2010. **18**(18): p. 18906-18911.

16. Bures, J., J. Lapierre, and D. Pascale, *Photosensitivity Effect in Optical Fibers - a Model for the Growth of an Interference Filter.* Applied Physics Letters, 1980. **37**(10): p. 860-862.

17. Lam, D.K.W. and Garside, B.K., *Characterization of Single-Mode Optical Fiber Filters.* Applied Optics, 1981. **20**(3): p. 440-445.

18. Sasaki, Y. and Ohmori, Y., *Phase-Matched Sum-Frequency Light Generation in Optical Fibers.* Applied Physics Letters, 1981. **39**(6): p. 466-468.

19. Fujii, Y., et al., *Sum-Frequency Light Generation in Optical Fibers.* Optics Letters, 1980. **5**(2): p. 48-50.

20. Stolen, R.H. and Tom, H.W.K., *Self-Organized Phase-Matched Harmonic-Generation in Optical Fibers.* Optics Letters, 1987. **12**(8): p. 585-587.

21. Farries, M., et al., *Second-harmonic generation in an optical fibre by self-written x (2) grating.* Electronics Letters, 1987. **23**(7): p. 322-324.

22. Stone, J., *Photorefractivity in Geo2-Doped Silica Fibers.* Journal of Applied Physics, 1987. **62**(11): p. 4371-4374.

23. Meltz, G., Morey, W.W. and Glenn, W.H., *Formation of Bragg Gratings in Optical Fibers by a Transverse Holographic Method.* Optics Letters, 1989. **14**(15): p. 823-825.

24. Kashyap, R., et al., *All-fibre narrowband reflection gratings at 1500 nm.* Electronics Letters, 1990. **26**(11): p. 730-732.

25. Hill, K.O., et al., *Bragg Gratings Fabricated in Monomode Photosensitive Optical-Fiber by Uv Exposure through a Phase Mask (Vol 62, Pg 1035, 1993).* Applied Physics Letters, 1993. **63**(3): p. 424-424.

26. Hill, K.O., et al. *Photosensitivity in Eu^{2+} :Al_2O_3-Doped-Core Fiber: Preliminary Results and Application to Mode Converters*. in *Optical Fiber Communication*. 1991. San Diego, California: Optical Society of America.

27. Taunay, T., et al., *Ultraviolet-enhanced photosensitivity in cerium-doped aluminosilicate fibers and glasses through high-pressure hydrogen loading.* Journal of the Optical Society of America B-Optical Physics, 1997. **14**(4): p. 912-925.

28. Malo, B., et al., *Photosensitivity in phosphorus - doped silica glass and optical waveguides.* Applied Physics Letters, 1994. **65**(4): p. 394-396.

29. Bilodeau, F., et al., *Ultraviolet-light photosensitivity in Er^{3+}–Ge-doped optical fiber.* Optics letters, 1990. **15**(20): p. 1138-1140.

30. Friebele, E.J., et al., *Optical fiber waveguides in radiation environments, II.* Nuclear Instruments and Methods in Physics Research Section B: Beam Interactions with Materials and Atoms, 1984. **1**(2–3): p. 355-369.

31. Kaiser, P., *Drawing-Induced Coloration in Vitreous Silica Fibers.* Journal of the Optical Society of America, 1974. **64**(4): p. 475-481.

32. Österberg, U. and Margulis, W., *Dye laser pumped by Nd:YAG laser pulses frequency doubled in a glass optical fiber.* Optics Letters, 1986. **11**(8): p. 516-518.

33. Anderson, D.Z. *Efficient Second-Harmonic Generation In Glass Fibers: The Possible Role Of Photo-Induced Charge Redistributiont*. 1990.

34. Österberg, U. and Margulis, W., *Experimental studies on efficient frequency doubling in glass optical fibers.* Optics letters, 1987. **12**(1): p. 57-59.

35. Anoikin, E., et al., *Photoinduced second-harmonic generation in gamma-ray-irradiated optical fibers.* Optics letters, 1990. **15**(15): p. 834-835.

36. Neustruev, V.B., *Color-Centers in Germanosilicate Glass and Optical Fibers.* Journal of Physics-Condensed Matter, 1994. **6**(35): p. 6901-6936.

37. Jackson, J.M., et al., *Preparation Effects on the Uv Optical-Properties of GeO_2 Glasses.* Journal of Applied Physics, 1985. **58**(6): p. 2308-2311.

38. Yuen, M.J., *Ultraviolet absorption studies of germanium silicate glasses.* Applied optics, 1982. **21**(1): p. 136-140.

39. Hand, D.P. and Russell, P.S., *Photoinduced Refractive-Index Changes in Germanosilicate Fibers.* Optics Letters, 1990. **15**(2): p. 102-104.

40. Fiori, C. and Devine, R.A.B., *Evidence for a Wide Continuum of Polymorphs in Alpha-SiO_2.* Physical Review B, 1986. **33**(4): p. 2972-2974.

41. Wong, D., Poole, S.B. and Sceats, M.G., *Stress-birefringence reduction in elliptical-core fibers under ultraviolet irradiation.* Optics letters, 1992. **17**(24): p. 1773-1775.

42. Attard, A.E., *Fermi Level Shift in $Bi_{12}SiO_{20}$ Via Photon-Induced Trap Level Occupation.* Journal of Applied Physics, 1992. **71**(2): p. 933-937.

43. Williams, D.L., et al. *Photosensitive index changes in germania-doped silica glass fibers and waveguides*. in *Optics Quebec*. 1993. International Society for Optics and Photonics.

44. Lawandy, N., *Light induced transport and delocalization in transparent amorphous systems.* Optics communications, 1989. **74**(3): p. 180-184.

45. Miotello, A. and Kelly, R., *Laser Irradiation Effects in Si^{+}-Implanted SiO_2.* Nuclear Instruments & Methods in Physics Research Section B-Beam Interactions with Materials and Atoms, 1992. **65**(1-4): p. 217-222.

46. Russell, P.S., et al., *Optically-Induced Creation, Transformation and Organization of Defects and Color-Centers in Optical Fibers.* International Workshop on Photoinduced Self-Organization Effects in Optical Fiber, 1992. **1516**: p. 47-54.

47. Tsai, T.-E., Friebele, E.J. and Griscom, D.L., *Thermal stability of photoinduced gratings and paramagnetic centers in Ge-and Ge/P-doped silica optical fibers.* Optics letters, 1993. **18**(12): p. 935-937.

48. Atkins, R.M. and Mizrahi, V. , *Observations of changes in UV absorption bands of singlemode germanosilicate core optical fibres on writing and thermally erasing refractive index gratings.* Electronics Letters, 1992. **28**(18): p. 1743-1744.

49. Hosono, H., et al., *Nature and origin of the 5-eV band in SiO_2: GeO_2 glasses.* Physical Review B, 1992. **46**(18): p. 11445.

50. Hosono, H., et al., *Correlation between Ge E′ Centers and Optical Absorption Bands in SiO2: GeO2 Glasses.* Japanese journal of applied physics, 1996. **35**(2B): p. L234.

51. Limberger, H.G., et al., *Compaction- and photoelastic-induced index changes in fiber Bragg gratings.* Applied Physics Letters, 1996. **68**(22): p. 3069-3071.

52. Patrick, H. and Gilbert, S.L., *Growth of Bragg Gratings Produced by Continuous-Wave Ultraviolet-Light in Optical-Fiber*. Optics Letters, 1993. **18**(18): p. 1484-1486.

53. Williams, D.L., et al., *Direct Observation of Uv Induced Bleaching of 240-Nm Absorption-Band in Photosensitive Germanosilicate Glass-Fibers.* Electronics Letters, 1992. **28**(4): p. 369-371.

54. Dong, L., et al., *Photoinduced Absorption Change in Germanosilicate Preforms - Evidence for the Color-Center Model of Photosensitivity*. Applied Optics, 1995. **34**(18): p. 3436-3440.

55. Leconte, B., et al., *Analysis of color-center-related contribution to Bragg grating formation in Ge:SiO_2 fiber based on a local Kramers-Kronig transformation of excess loss spectra.* Applied Optics, 1997. **36**(24): p. 5923-5930.

56. Fiori, C. and Devine, R., *Ultraviolet irradiation induced compaction and photoetching in amorphous, thermal SiO_2.* in *Mat. Res, Soc. Symp. Proc., Defects in Glasses, Ed. by FL Galleener, DL Griscom, MJ Weber*. 1986. DTIC Document.

57. Cordier, P., et al., *Evidence by transmission electron microscopy of densification associated to Bragg grating photoimprinting in germanosilicate optical fibers.* Applied Physics Letters, 1997. **70**(10): p. 1204-1206.

58. Sceats, M.G., Atkins, G.R. and Poole, S.B., *Photolytic Index Changes in Optical Fibers.* Annual Review of Materials Science, 1993. **23**: p. 381-410.

59. Park, Y., et al., *Residual stresses in a doubly clad fiber with depressed inner cladding (DIC).* Journal of Lightwave Technology, 1999. **17**(10): p. 1823-1834.

60. Bennion, I., et al., *UV-written in-fibre Bragg gratings.* Optical and Quantum Electronics, 1996. **28**(2): p. 93-135.

61. Starodubov, D., et al., *Bragg grating fabrication in germanosilicate fibers by use of near-UV light: a new pathway for refractive-index changes.* Optics letters, 1997. **22**(14): p. 1086-1088.

62. Lemaire, P.J., et al. *High pressure H_2 loading as a technique for achieving ultrahigh UV photosensitivity and thermal sensitivity in GeO_2 doped optical fibres*. Electronics Letters, 1993. **29**, 1191-1193.

63. Douay, M., et al., *Densification involved in the UV-based photosensitivity of silica glasses and optical fibers.* Journal of Lightwave Technology, 1997. **15**(8): p. 1329-1342.

64. Awazu, K., Kawazoe, H. and Yamane, M., *Simultaneous generation of optical absorption bands at 5.14 and 0.452 eV in 9 SiO_2: GeO_2 glasses heated under an H_2 atmosphere.* Journal of Applied Physics, 1990. **68**(6): p. 2713-2718.

65. Tanaka, S., et al., *Hydroxyl Group Formation Caused by Hydrogen Diffusion into Optical-Glass Fiber.* Electronics Letters, 1984. **20**(7): p. 283-284.

66. Stone, J., et al., *Formation of Hydroxyl Due to Reaction of Hydrogen with Silica Optical Fiber Preforms.* Applied Physics Letters, 1985. **47**(3): p. 328-330.

67. Stone, J., *Interactions of Hydrogen and Deuterium with Silica Optical Fibers - a Review.* Journal of Lightwave Technology, 1987. **5**(5): p. 712-733.

68. Bilodeau, F., et al., *Photosensitization of optical fiber and silica-on-silicon/silica waveguides.* Optics Letters, 1993. **18**(12): p. 953-955.

69. Dong, L., et al., *Enhanced Photosensitivity in Tin-Codoped Germanosilicate Optical Fibers.* Ieee Photonics Technology Letters, 1995. **7**(9): p. 1048-1050.

70. Williams, D.L., et al., *Enhanced UV photosensitivity in boron codoped germanosilicate fibres.* Electronics Letters, 1993. **29**(1): p. 45.

71. Camlibel, D.A.P., and Dabby, F. W., *Optical aging characteristics of borosilicate clad fused silica core fiber optical waveguides.* Appl. Phys. Lett. , 1975. **26**: p. 3.

72. Ky, N.H., et al., *Effects of drawing tension on the photosensitivity of Sn–Ge-and B–Ge-codoped core fibers.* Optics letters, 1998. **23**(17): p. 1402-1404.

73. Dianov, E.M., et al., *Highly photosensitive nitrogen-doped germanosilicate fibre for index grating writing.* Electronics Letters, 1997. **33**(15): p. 1334-1336.

74. Dianov, E.M., et al., *Low-Hydrogen Silicon Oxynitride Optical Fibers Prepared by Spcvd.* Journal of Lightwave Technology, 1995. **13**(7): p. 1471-1474.

75. Grand, G., et al., *Low-loss PECVD silica channel waveguides for optical communications.* Electronics letters, 1990. **26**(25): p. 2135-2137.

76. Kogelnik, H. and Shank, C.V., *Coupled-Wave Theory of Distributed Feedback Lasers.* Journal of Applied Physics, 1972. **43**(5): p. 2327-&.

77. Yariv, A., *Coupled-Mode Theory for Guided-Wave Optics.* Ieee Journal of Quantum Electronics, 1973. **Qe 9**(9): p. 919-933.

78. Erdogan, T., *Fiber grating spectra.* Journal of Lightwave Technology, 1997. **15**(8): p. 1277-1294.

79. Erdogan, T., *Cladding-mode resonances in short- and long-period fiber grating filters.* Journal of the Optical Society of America a-Optics Image Science and Vision, 1997. **14**(8): p. 1760-1773.

80. Erdogan, T., *Cladding-mode resonances in short- and long-period fiber grating filters (vol 14, pg 1760, 1997).* Journal of the Optical Society of America a-Optics Image Science and Vision, 2000. **17**(11): p. U3-U3.

81. Bhatia, V. and Vengsarkar, A.M., *Optical fiber long-period grating sensors.* Optics Letters, 1996. **21**(9): p. 692-694.

82. Lee, K.S. and Erdogan, T., *Fiber mode coupling in transmissive and reflective tilted fiber gratings.* Applied Optics, 2000. **39**(9): p. 1394-1404.

83. Anderson, D., et al., *Production of in-fibre gratings using a diffractive optical element.* Electronics Letters, 1993. **29**(6): p. 566-568.

84. Byron, K.C., et al., *Fabrication of Chirped Bragg Gratings in Photosensitive Fiber.* Electronics Letters, 1993. **29**(18): p. 1659-1660.

85. Albert, J., et al., *Moire phase masks for automatic pure apodisation of fibre Bragg gratings.* Electronics Letters, 1996. **32**(24): p. 2260-2261.

86. Zhang, L., et al., *Wide-Stopband Chirped Fiber Moire Grating Transmission Filters.* Electronics Letters, 1995. **31**(6): p. 477-479.

87. Eggleton, B.J., et al., *Long Periodic Superstructure Bragg Gratings in Optical Fibers.* Electronics Letters, 1994. **30**(19): p. 1620-1622.

88. Kashyap, R., Mckee, P.F. and Armes, D., *UV Written Reflection Grating Structures in Photosensitive Optical Fibers Using Phase-Shifted Phase Masks.* Electronics Letters, 1994. **30**(23): p. 1977-1978.

89. Hill, K.O. and Meltz, G., *Fiber Bragg grating technology fundamentals and overview.* Journal of Lightwave Technology, 1997. **15**(8): p. 1263-1276.

90. Malo, B., et al., *Point-by-Point Fabrication of Micro-Bragg Gratings in Photosensitive Fiber Using Single Excimer Pulse Refractive-Index Modification Techniques.* Electronics Letters, 1993. **29**(18): p. 1668-1669.

91. Du, D., et al., *Laser-Induced Breakdown by Impact Ionization in SiO_2 with Pulse Widths from 7 Ns to 150 Fs.* Applied Physics Letters, 1994. **64**(23): p. 3071-3073.

92. Kondo, Y., et al., *Fabrication of long-period fiber gratings by focused irradiation of infrared femtosecond laser pulses.* Optics Letters, 1999. **24**(10): p. 646-648.

93. Hindle, F., et al., *Inscription of long-period gratings in pure silica and germano-silicate fiber cores by femtosecond laser irradiation.* Ieee Photonics Technology Letters, 2004. **16**(8): p. 1861-1863.

94. Martinez, A., et al., *Direct writing of fibre Bragg gratings by femtosecond laser.* Electronics Letters, 2004. **40**(19): p. 1170-1172.

95. Mihailov, S.J., et al., *Fiber Bragg gratings made with a phase mask and 800-nm femtosecond radiation.* Optics Letters, 2003. **28**(12): p. 995-997.

96. Thomas, J., et al., *Femtosecond pulse written fiber gratings: a new avenue to integrated fiber technology.* Laser & Photonics Reviews, 2012. **6**(6): p. 709-723.

97. Boskovic, A., et al. *All-fibre diode pumped, femtosecond chirped pulse amplification system*. Electronics Letters, 1995. **31**, 877-879.

98. Grunnet-Jepsen, A., et al., *Fibre Bragg grating based spectral encoder/decoder for lightwave CDMA.* Electronics Letters, 1999. **35**(13): p. 1096-1097.

99. Cruz, J., et al., *Chirped fibre Bragg gratings for phased-array antennas.* Electronics Letters, 1997. **33**(7): p. 545-546.

100. Roman, J., et al., *Time-steered array with a chirped grating beamformer.* Electronics Letters, 1997. **33**(8): p. 652-653.

101. Fallon, R., et al., *Identical broadband chirped grating interrogation technique for temperature and strain sensing.* Electronics Letters, 1997. **33**(8): p. 705-707.

102. Ouellette, F., *Dispersion Cancellation Using Linearly Chirped Bragg Grating Filters in Optical Wave-Guides.* Optics Letters, 1987. **12**(10): p. 847-849.

103. Zi-Xiong, Q., et al., *Numerical Study of the Apodization Profile Functions, Optimal Profiles and Lengths of a Linearly Chirped Fibre Bragg Grating.* Chinese Physics Letters, 2001. **18**(2): p. 239.

104. Perry, M., et al., *High stress monitoring of prestressing tendons in nuclear concrete vessels using fibre-optic sensors.* Nuclear Engineering and Design, 2014. **268**: p. 35-40.

105. Bhatia, V., et al., *Simultaneous strain and temperature measurement with long-period gratings.* Optics Letters, 1997. **22**(9): p. 648-650.

106. Shu, X., Zhang, L. and Bennion, I., *Sensitivity characteristics of long-period fiber gratings.* Journal of Lightwave Technology, 2002. **20**(2): p. 255-266.

107. Mihailov, S., et al., *Fabrication of tilted fibre-grating polarisation-dependent loss equaliser.* Electronics Letters, 2001. **37**(5): p. 284-286.

108. Westbrook, P.S., Strasser, T.A. and Erdogan, T. *In-line polarimeter using blazed fiber gratings.* Ieee Photonics Technology Letters, 2000. **12**(10): p. 1352-1354.

109. Yan, Z. et al., *All-fiber polarization interference filters based on 45 degrees-tilted fiber gratings.* Optics Letters, 2012. **37**(3): p. 353-355.

110. Young, M., *Optics and lasers: including fibers and optical waveguides*. Vol. 5. 2000: Springer Science & Business Media.

111. Zhou, K. et al., *High extinction ratio in-fiber polarizers based on 45 degrees tilted fiber Bragg gratings.* Optics Letters, 2005. **30**(11): p. 1285-1287.

112. Yoshino, T., *Theoretical analysis of a tilted fiber grating polarizer by the beam tracing approach.* Journal of the Optical Society of America B-Optical Physics, 2012. **29**(9): p. 2478-2483.

113. Zhu, Y. et al., *A comparison of wavelength dependent polarization dependent loss measurements in fiber gratings.* Ieee Transactions on Instrumentation and Measurement, 2000. **49**(6): p. 1231-1239.

114. Yan, Z. et al., *UV-Inscription, Polarization-Dependant Loss Characteristics and Applications of 45°- Tilted Fiber Gratings.* Lightwave Technology, Journal of, 2011. **29**(18): p. 2715-2724.

115. Collett, E., *Field guide to polarization*. Vol. 15. 2005: SPIE Press.

116. Li, Y., Froggatt, M. and Erdogan, T., *Volume current method for analysis of tilted fiber gratings.* Journal of Lightwave Technology, 2001. **19**(10): p. 1580.

117. Mou, C. et al., *Characterization of 45°-tilted fiber grating and its polarization function in fiber ring laser.* Journal of the Optical Society of America B, 2009. **26**(10): p. 1905-1911.

118. Mizrahi, V., et al., *Stable single-mode erbium fiber-grating laser for digital communication.* Lightwave Technology, Journal of, 1993. **11**(12): p. 2021-2025.

119. Kersey, A.D., et al., *Fiber grating sensors.* Journal of lightwave technology, 1997. **15**(8): p. 1442-1463.

120. Lin, J.T. and Gambling, W.A., *Polarization Effects in Fiber Lasers - Phenomena, Theory and Applications.* Fiber Laser Sources and Amplifiers Ii, 1991. **1373**: p. 42-53.

121. Pureur, D., et al., *Single-polarization fiber lasers using Bragg gratings in Hi-Bi fibers.* Lightwave Technology, Journal of, 1995. **13**(3): p. 350-355.

122. Keller, U., et al., *Semiconductor saturable absorber mirrors (SESAM's) for femtosecond to nanosecond pulse generation in solid-state lasers.* Selected Topics in Quantum Electronics, IEEE Journal of, 1996. **2**(3): p. 435-453.

123. Set, S.Y., et al., *Ultrafast fiber pulsed lasers incorporating carbon nanotubes.* Selected Topics in Quantum Electronics, IEEE Journal of, 2004. **10**(1): p. 137-146.

124. Tamura, K., Haus, H. and Ippen, E.P., *Self-starting additive pulse mode-locked erbium fibre ring laser*. Electronics Letters, 1992. **28**(24): p. 2226-2228.

125. Zhang, Z., et al., *Sub-100 fs mode-locked erbium-doped fiber laser using a 45-tilted fiber grating*. Optics express, 2013. **21**(23): p. 28297-28303.

126. Fu, H., et al., *Transversal loading sensor based on tunable beat frequency of a dual-wavelength fiber laser.* Photonics Technology Letters, IEEE, 2009. **21**(14): p. 987-989.

127. Guan, B.-O., Zhang, Y.and Tam, H.-Y., *Fiber grating laser sensors*. in *Proceedings of the 2008 International Conference on Advanced Infocomm Technology*. 2008. ACM.

128. Svelto, O. and Hanna, D.C., *Principles of lasers*. 1976: Springer.

129. Suo, R., et al., *In-fibre directional transverse loading sensor based on excessively tilted fibre Bragg gratings.* Measurement Science & Technology, 2009. **20**(3).

130. Yan, Z., Zhou, K. and Zhang, L., *In-fiber linear polarizer based on UV-inscribed 45° tilted grating in polarization maintaining fiber*. Optics Letters, 2012. **37**(18): p. 3819-3821.

131. Lyot, B., *Optical apparatus with wide field using interference of polarized light.* CR Acad. Sci.(Paris), 1933. **197**: p. 1593.

132. Yan, Z. et al., *Broadband Tunable All-Fiber Polarization Interference Filter Based on 45°-Tilted Fiber Gratings.* Lightwave Technology, Journal of, 2013. **31**(1): p. 94-98.

133. Zhou, K., et al., *Optic sensors of high refractive-index responsivity and low thermal cross sensitivity that use fiber Bragg gratings of> 80 tilted structures.* Optics letters, 2006. **31**(9): p. 1193-1195.

134. Zhou, K., et al., *Low thermal sensitivity grating devices based on ex-45 tilting structure capable of forward-propagating cladding modes coupling*. Lightwave Technology, Journal of, 2006. **24**(12): p. 5087-5094.

135. Chen, X. et al., *Highly sensitive bend sensor based on Bragg grating in eccentric core polymer fiber.* IEEE photonics technology letters, 2010. **22**.

136. Yan, Z. et al., *Hybrid tilted fiber grating based refractive index and liquid level sensing system.* Optics Communications, 2015. **351**: p. 144-148.

137. Yan, Z. et al., *Numerical and Experimental Analysis of Sensitivity-Enhanced RI Sensor Based on Ex-TFG in Thin Cladding Fiber.* Lightwave Technology, Journal of, 2015. **33**(14): p. 3023-3027.

138. Wang, X.D. and Wolfbeis, O.S., *Fiber-Optic Chemical Sensors and Biosensors (2008-2012).* Analytical Chemistry, 2013. **85**(2): p. 487-508.

139. Hu, D.J.J., et al., *Photonic Crystal Fiber-Based Interferometric Biosensor for Streptavidin and Biotin Detection.* Ieee Journal of Selected Topics in Quantum Electronics, 2012. **18**(4): p. 1293-1297.

140. Topliss, S.M., et al., *Optical fibre long period grating based selective vapour sensing of volatile organic compounds.* Sensors and Actuators B-Chemical, 2010. **143**(2): p. 629-634.

141. Puckett, S.D. and Pacey, G.E., *Detection of water in jet fuel using layer-by-layer thin film coated long period grating sensor.* Talanta, 2009. **78**(1): p. 300-304.

142. Libish, T., et al., *Glucose concentration sensor based on long period grating fabricated from hydrogen loaded photosensitive fiber.* Sensors & Transducers, 2011. **129**(6): p. 142.

143. Kim, D.W., et al., *In-fiber reflection mode interferometer based on a long-period grating for external refractive-index measurement.* Applied optics, 2005. **44**(26): p. 5368-5373.

144. Deep, A., et al., *Immobilization of enzyme on long period grating fibers for sensitive glucose detection.* Biosensors and Bioelectronics, 2012. **33**(1): p. 190-195.

145. Gafsi, R. and El-Sherif, M.A., *Analysis of induced-birefringence effects on fiber Bragg gratings.* Optical Fiber Technology, 2000. **6**(3): p. 299-323.

146. Steinberg, R. and Giallorenzi, T., *Performance limitations imposed on optical waveguide switches and modulators by polarization.* Applied optics, 1976. **15**(10): p. 2440-2453.

147. Johnson, D.E., *Use of the holmium:YAG (Ho:YAG) laser for treatment of superficial bladder carcinoma.* Lasers in Surgery and Medicine, 1994. **14**(3): p. 213-218.

148. Li, J., et al., *Thulium-doped all-fiber mode-locked laser based on NPR and 45°-tilted fiber grating*. Optics Express, 2014. **22**(25): p. 31020-31028.

149. Humbach, O., et al., *Analysis of OH absorption bands in synthetic silica.* Journal of Non-Crystalline Solids, 1996. **203**: p. 19-26.

150. Chen, X., et al., *Dual-peak long-period fiber gratings with enhanced refractive index sensitivity by finely tailored mode dispersion that uses the light cladding etching technique.* Applied Optics, 2007. **46**(4): p. 451-455.

151. Leunig, A., et al., *Ho:YAG Laser Treatment of Hyperplastic Inferior Nasal Turbinates.* The Laryngoscope, 1999. **109**(10): p. 1690-1695.

152. Futao, S., et al., *Application of endoscopic Ho:YAG laser incision technique treating urethral strictures and urethral atresias in pediatric patients.* Pediatric Surgery International, 2006. **22**(6): p. 514-518.

153. Jackson, S.D. and King, T.A., *High-power diode-cladding-pumped Tm-doped silica fiber laser.* Optics Letters, 1998. **23**(18): p. 1462-1464.

154. Oh, K., et al., *Continuous-wave oscillation of thulium-sensitized holmium-doped silica fiber laser.* Optics Letters, 1994. **19**(4): p. 278-280.

155. Jackson, S.D., et al., *High-power 83 W holmium-doped silica fiber laser operating with high beam quality.* Optics Letters, 2007. **32**(3): p. 241-243.

156. Jackson, S.D., *8.8 W diode-cladding-pumped Tm^{3+},Ho^{3+}-doped fluoride fibre laser.* Electronics Letters, 2001. **37**(13): p. 821-822.

157. Walsh, B.M. and Barnes, N.P., *Comparison of Tm : ZBLAN and Tm : silica fiber lasers; Spectroscopy and tunable pulsed laser operation around 1.9 μm.* Applied Physics B, 2004. **78**(3-4): p. 325-333.

158. Sacks, Z.S., Schiffer, Z. and David, D., *Long wavelength operation of double-clad Tm:silica fiber lasers*. 2007.

159. Desurvire, E., *Analysis of gain difference between forward- and backward-pumped erbium-doped fiber amplifiers in the saturation regime.* Photonics Technology Letters, IEEE, 1992. **4**(7): p. 711-714.

160. Monerie, M. *Systems incorporating very long fluoride glass fibre optic links*. in *Hague International Symposium*. 1987. International Society for Optics and Photonics.

161. Bernier, M., et al., *Bragg gratings photoinduced in ZBLAN fibers by femtosecond pulses at 800 nm.* Optics letters, 2007. **32**(5): p. 454-456.

162. Saad, M., Chen, L. and Gu, X., *Highly reflective fiber Bragg gratings inscribed in Ce/Tm co-doped ZBLAN fibers.* Photonics Technology Letters, IEEE, 2013. **25**(11): p. 1066-1068.

163. Yan, Z., et al., *Soliton mode locking fiber laser with an all-fiber polarization interference filter.* Optics Letters, 2012. **37**(21): p. 4522-4524.

164. Wang, Q., et al., *Mode-locked 2 μm laser with highly thulium-doped silicate fiber.* Optics Letters, 2009. **34**(23): p. 3616-3618.

165. Solodyankin, M.A., et al., *Mode-locked 1.93 μm thulium fiber laser with a carbon nanotube absorber.* Optics Letters, 2008. **33**(12): p. 1336-1338.

166. Zhang, M., et al., *Tm-doped fiber laser mode-locked by graphene-polymer composite.* Optics Express, 2012. **20**(22): p. 25077-25084.

167. Wang, X., et al., *Pulse bundles and passive harmonic mode-locked pulses in Tm-doped fiber laser based on nonlinear polarization rotation.* Optics Express, 2014. **22**(5): p. 6147-6153.

168. Rudy, C.W., et al., *Amplified 2- Thulium-Doped All-Fiber Mode-Locked Figure-Eight Laser.* Lightwave Technology, Journal of, 2013. **31**(11): p. 1809-1812.

169. Li, J., et al., *All-fiber passively mode-locked Tm-doped NOLM-based oscillator operating at 2-μm in both soliton and noisy-pulse regimes.* Optics Express, 2014. **22**(7): p. 7875-7882.

170. Chernysheva, M.A., et al., *SESAM and SWCNT Mode-Locked All-Fiber Thulium-Doped Lasers Based on the Nonlinear Amplifying Loop Mirror.* Selected Topics in Quantum Electronics, IEEE Journal of, 2014. **20**(5): p. 448-455.